Electronic and magnetic properties of selected two–dimensional materials

Dissertation
zur Erlangung des Grades
„Doktor der Naturwissenschaften“
am Fachbereich Physik, Mathematik und Informatik
der Johannes Gutenberg–Universität
in Mainz

von:
Nils Richter
geboren in Tübingen
Mainz, 2017

JOHANNES GUTENBERG
UNIVERSITÄT MAINZ

Nils Richter

Electronic and magnetic properties of selected two–dimensional materials

Datum der mündlichen Prüfung: 20.02.2018

Johannes Gutenberg–Universität Mainz
AG Kläui
Institut für Physik
Staudingerweg 7
55128, Mainz

Eidesstattliche Erklärung

Hiermit erkläre ich an Eides statt, dass ich meine Dissertation selbständig und ohne fremde Hilfe verfasst und keine anderen als die von mir angegebenen Quellen und Hilfsmittel zur Erstellung meiner Dissertation verwendet habe. Die Arbeit ist in vorliegender oder ähnlicher Form bei keiner anderen Prüfungsbehörde zur Erlangung eines Doktorgrades eingereicht worden.

Mainz, den

Nils Richter

This page was intentionally left blank.

Abstract

Electronic devices, such as field–effect transistors (FETs), based on low–dimensional materials attract an immense interest as a potential inexpensive, flexible and transparent next generation of electronics. There have been considerable improvements in the accessibility of various low–dimensional materials and even the first ferromagnetic monolayers have been experimentally realized. Nevertheless, many open questions remain concerning basic physical properties of such materials. This work focusses on the electronic and magnetic properties of three carefully selected and especially interesting low–dimensional materials: Bottom–up chemically synthesized graphene nanoribbons (GNRs), nitrogen–doped graphene films and ferromagnetic chromium trihalides.

First, we investigate charge transport in bottom–up synthesized GNRs with various edge morphologies and ribbon widths. Although prototypes of FET devices based on such GNRs have recently been demonstrated, fundamental questions as for example on the dominant charge transport mechanism, or on the structure– and width–dependence of charge transport signatures in GNR devices, remain unanswered and need to be addressed experimentally. Therefore, we present the development of a reliable fabrication of GNR network FETs and their measurement. In devices with gold electrodes at micron and submicron channel lengths, we study length–dependent charge transport as a function of gate voltage and at a wide range of temperatures. First, we show that the contact resistance is low and behaves Ohmic–like. The channel current follows power laws for both temperature and drain voltage, which is explained by nuclear tunneling–mediated hopping as the dominant charge transport mechanism. In addition, we observe a large positive magnetoresistance of up to 14% at magnetic fields of 8 T at low temperatures. We find this magnetoresistance only in GNRs which have a width of five carbon dimers across the ribbon and which are expected to exhibit a particularly low band gap. With our results we provide a better understanding of the nature of charge transport and the engineering of contacts, which both is evidently crucial to bolster any further development of GNR–based devices.

Besides geometrical confinement in GNRs, we explore heteroatomic nitrogen doping as a second route of tailoring charge transport properties of graphene. Here, extended two–dimensional graphene films with substitutional nitrogen dopants are studied and compared to pristine graphene fabricated under identical conditions. By combining structural and electrical characterization methods, we elucidate the role of structural disorder and electron localization for the electronic properties of this material induced by the nitrogen dopants. We quantify the transition from weak to strong localization with doping level based on the change of the length scales for phase coherent transport. This transition is accompanied by a conspicuous sign change from positive ordinary Kohler magnetoresistance in undoped graphene to large negative magnetoresistance in doped graphene.

In addition to charge carrier properties, also spin properties depend heavily on the dimensionality, where an important ingredient for stable magnetic order in lower dimensions is magnetic anisotropy. Therefore, we investigate chromium trihalides, which are layered and exfoliable semiconductors and exhibit unusual magnetic properties. In particular, we focus on the understanding of magnetocrystalline anisotropy by quantifying the anisotropy constant of chromium iodide (CrI_3), where we find a strong change from 5 K towards the Curie temperature. We draw a direct comparison to chromium bromide ($CrBr_3$), which serves as a reference, and where we find results consistent with literature. In particular, we show that the anisotropy change in the iodide compound is more than three times larger than in the bromide. We analyze this temperature dependence using a classical model for the behavior of spins and spin clusters showing that the anisotropy constant scales with the magnetization at any given temperature below the Curie temperature. Hence, the temperature dependence can be explained by a dominant uniaxial anisotropy where this scaling results from local spin clusters having thermally induced magnetization directions that deviate from the overall magnetization.

Zusammenfassung

Elektronische Bauteile auf Basis niedrigdimensionaler Materialien, wie zum Beispiel Feldeffekttransistoren (FETs), ziehen eine enorme Aufmerksamkeit auf sich. Sie haben das Potential, die nächste Generation an kosteneffizienter, flexibler und transparenter Elektronik zu bilden. Es hat bereits eine bemerkenswerte Entwicklung in der Verfügbarkeit verschiedener niedrigdimensionaler Materialien gegeben, sodass sogar die ersten ferromagnetischen Monolagen experimentell untersucht werden konnten. Nichtsdestotrotz sind viele grundlegenden physikalischen Eigenschaften nicht erforscht. Die vorliegende Arbeit beschäftigt sich mit den elektronischen und magnetischen Eigenschaften dreier sorgfältig ausgewählter niedrigdimensionaler Materialien: Chemisch bottom–up synthetisierte Graphennanobänder (GNRs), stickstoffdotierte Graphenfilme und ferromagnetische Chromtrihalogenide.

Zuerst untersuchen wir Ladungstransport in bottom–up synthetisierten GNRs verschiedener Kantenmorphologien und Breiten. Obwohl erste FET–Prototypen basierend auf GNRs demonstriert wurden, sind einige fundamentale Fragen immer noch unbeantwortet und verlangen nach einer experimentellen Klärung. Diese Fragen betreffen zum Beispiel den Ladungstransportmechanismus oder die Struktur– und Breitenabhängigkeit des Ladungstransports. Daher präsentieren wir die technische Entwicklung einer verlässlichen Fabrikationsmethode von FETs basierend auf GNR–Netzwerken sowie die Charakterisierung dieser Bauteile. Als Funktion von Gatterspannung und für einen breiten Temperaturbereich untersuchen wir den längenabhängigen Ladungstransport mit Hilfe von FETs mit Goldelektroden und aktiven Kanälen im Bereich von einigen hundert Nanometern bis hin zu einigen Mikrometern. Dabei zeigen wir zunächst, dass der elektrische Kontaktwiderstand gering ist und sich ohmsch verhält. Desweiteren bestimmen Potenzgesetze das Verhalten des Kanalstroms in Abhängigkeit von Betriebsspannung und Temperatur, was mit Hilfe von kerntunnelnassistiertem Ladungsträgerhopping als maßgeblichen Ladungstransportmechanismus erklärt werden kann. Darüber hinaus finden wir einen ausgeprägten positiven Magnetowiderstand bis zu 14% bei Magnetfeldern von 8 T und tiefen Temperaturen. Dieser Magnetowiderstand lässt sich dabei allerdings ausschließlich in GNRs beobachten, die nur fünf Kohlstoffdimerlängen breit

sind und bei welchen eine besonders niedrige Bandlücke erwartet wird. Mit unseren Ergebnissen tragen wir signifikant zu einem tieferen Verständnis des Ladungstransportmechanismus bei und zeigen die Optimierung der elektrischen Kontakte auf. Beides ist unerlässlich, um die Realisierung zukünftiger GNR–basierter Elektronik voranzutreiben.

Neben der geometrischen Einschränkung von Ladungsträgern in GNRs, untersuchen wir Fremdatomdotierung mit Stickstoff als zweite Strategie Ladungstransport in Graphen maßzuschneidern. Dazu haben wir ausgedehnte zweidimensionale Graphenfilme mit inkorporierter Stickstoffdotierung untersucht und vergleichen sie mit reinen Graphenfilmen, welche unter identischen Bedingungen hergestellt wurden. Indem wir strukturelle und elektronische Charakterisierungsmethoden miteinander verbinden, beleuchten wir die Rolle von struktureller Ungeordnetheit sowie elektronischer Lokalisierung, welche beide durch die Stickstoffdotierung induziert werden. Wir quantifizieren hierfür den, mit zunehmendem Dotierungsniveau einhergehenden, Übergang von schwacher zu starker Lokalisierung auf Grundlage der Änderung der Längenskala von phasenkohärentem Transport. Dieser Übergang wird begleitet von einer bemerkenswerten Vorzeichenänderung des Magnetowiderstands von gewöhnlichem Kohlermagnetowiderstand in undotiertem Graphen hin zu einem großen negativen Magnetowiderstand in dotiertem Graphen.

Nicht nur die Ladungsträgereigenschaften hängen von der Dimensionalität ab, sondern auch die Eigenschaften von Spins. Hierbei ist magnetische Anisotropie ein wichtiger Faktor, um magnetische Ordnung in niedrigen Dimensionen zu gewährleisten. Daher untersuchen wir als dritten Themenbereich die magnetischen Eigenschaften von Chromtrihalogeniden. Dies sind Halbleiterkristalle mit ungewöhnlichen magnetischen Eigenschaften und einer Schichtstruktur, wodurch sie sich zu Monolagen exfolieren lassen. Wir untersuchen insbesondere die magnetokristalline Anisotropie, indem wir die Anisotropiekonstante von Chromiodid (CrI_3) als Funktion der Temperatur quantifizieren. Wir beobachten dabei eine starke Änderung der magnetokristallinen Anisotropie zwischen 5 K und der Curie–Temperatur. Diese vergleichen wir mit der von Chrombromid ($CrBr_3$), welches uns als Referenz dient, da es sich genauso verhält, wie es frühere, der Literatur entnommene, Untersuchungen erwarten lassen. Insbesondere zeigen wir, dass die Anisotropieänderung in der Iodidverbindung mehr als dreimal so stark ist wie im Bromid. Die Temperaturabhängigkeit analysieren wir mit einem klassischen Model für Spins und Spinclustern und zeigen, dass bei gegebener Temperatur die Anisotropiekonstante mit der Magnetisierung skaliert. Folglich können wir unsere experimentellen Beobachtungen mit einer dominant uniaxialen Anisotropie erklären, bei welcher die Skalierung das Resultat von lokalen Spinclustern ist, deren Magnetisierungsrichtung durch thermische Aktivierung von der Ausrichtung der Gesamtmagnetisierung abweicht.

Dedicated to

my parents

Gewidmet

meinen Eltern

Contents

Eidesstattliche Erklärung iii

Abstract v

Zusammenfassung vii

Contents xi

List of Figures xv

List of Tables xvii

Abbreviations xix

1 Introduction 1

2 Theoretical background 5
- 2.1 General effects of dimensional confinement in solid state systems 5
  - 2.1.1 Dimensional confinement of a particle 6
  - 2.1.2 Density of states 7
- 2.2 Electronic properties of selected graphene allotropes 9
  - 2.2.1 Single layer graphene 9
  - 2.2.2 Turbostratic graphene multilayers 13
  - 2.2.3 Geometrically confined graphene structures 14
- 2.3 Charge transport by charge carrier hopping 21
- 2.4 Basics of magnetism 23
  - 2.4.1 Direct exchange 23
  - 2.4.2 Itinerant ferromagnetism 24
  - 2.4.3 Superexchange 24

3 Experimental methods 27
- 3.1 Structural characterization by Raman spectroscopy 27
- 3.2 Electrical measurements 30
  - 3.2.1 Room temperature measurements 30
  - 3.2.2 Low temperature measurements 31
  - 3.2.3 Current guarding 32
  - 3.2.4 Van der Pauw technique 33

3.3 SQUID magnetometry . . . 35
3.4 Electron beam lithography . . . 35
3.5 Sputtering . . . 36

4 Development of charge transport test structures for graphene and graphene nanoribbons 37
4.1 Synthesis of carbon materials . . . 38
4.1.1 Nitrogen–doped graphene . . . 38
4.1.2 Atomically precise graphene nanoribbons . . . 39
4.1.3 Turbostratic graphene discs . . . 41
4.2 Transfer technniques . . . 42
4.2.1 Transfer of solution processable GNRs . . . 42
4.2.2 Transfer of GNRs from surfaces . . . 45
4.3 Device engineering for charge transport in bottom–up GNRs . . . 47
4.3.1 Short channel devices by lithography . . . 49
4.3.2 Short channel devices by electromigration in gold . . . 53
4.3.3 Short channel devices by electromigration in turbostratic graphene 54
4.3.4 Long channel devices . . . 59
4.4 Statistical analysis of the device yield . . . 60
4.5 Conclusion and outlook . . . 66

5 Charge transport in networks of bottom–up graphene nanoribbons 67
5.1 Experimental details . . . 68
5.2 Electrical characterization of graphene nanoribbon–network field effect transistors . . . 70
5.2.1 Current–voltage characteristics . . . 70
5.2.2 Doping effect of ambient gases . . . 76
5.2.3 Determination of the electrical contact resistance at metal/graphene nanoribbon interfaces . . . 79
5.3 Charge transport mechanism in graphene nanoribbon networks . . . 81
5.3.1 Universal scaling of charge transport . . . 81
5.3.2 Transport at low bias and low temperature . . . 85
5.4 Conclusion and outlook . . . 87

6 Magnetoresistance and charge transport in graphene governed by nitrogen dopants 89
6.1 Experimental details . . . 90
6.2 Structural investigation using Raman spectroscopy . . . 92
6.3 Transport gap and charge carrier localization in doped graphene . . . 95
6.3.1 Charge carrier density and mobility probed by the Hall effect . . . 95
6.3.2 Variable range hopping conduction in nitrogen doped graphene . . . 96
6.3.3 Positive and negative magnetoresistive effects . . . 98
6.4 Conclusion and outlook . . . 103

7 Magnetic properties of chromium trihalides 105
7.1 Magnetic properties of CrX_3 . . . 106
7.2 Experimental details . . . 106
7.3 Temperature dependence of the magnetization . . . 108

7.4 Magnetic hysteresis loops . . . 110
7.5 Magnetic anisotropy in CrI_3 and $CrBr_3$ . . . 112
7.6 Conclusions and outlook . . . 114

8 Conclusion and outlook **117**

A Additional material for Chapter 4 **121**
A.1 Raman mapping of graphene nanoribbon films on silicon dioxide . . . 122

B Additional material for Chapter 5 **123**
B.1 Raman spectra of various graphene nanoribbons . . . 124
B.2 Current–voltage characteristics of networks of various GNR species . . . 125
B.3 Gate–leakage and bias symmetry in GNR FET devices . . . 127
B.4 Determination of the field–effect mobility in GNR network FETs . . . 128
B.5 Charge transport statistics of GNR devices . . . 129
B.6 Estimation of the charge carrier density . . . 131
B.7 Doping and current annealing of GNR devices . . . 133
B.8 Gate voltage–dependence of the contact resistance . . . 135
B.9 Conductance maps . . . 136
B.10 Temperature dependence of magnetotransport . . . 137

C Additional material for Chapter 7 **139**
C.1 Additional experimental details . . . 140
C.2 Hysteresis loops of chromium trihalides . . . 141
C.3 Degradation of chromium bromide in air . . . 142

Bibliography **143**

Acknowledgements **175**

Publications List **177**

List of Figures

2.1 Graphene lattice in real and reciprocal space . . . 10
2.2 Graphene band structure . . . 12
2.3 Graphene stacks . . . 14
2.4 Armchair GNR and GNR nanowiggle . . . 16
2.5 aGNR bandstructure . . . 18
2.6 GNRNW bandstructure . . . 19

3.1 Stokes and Anti–Stokes Processes . . . 28
3.2 Raman spectrum of graphene . . . 29
3.3 Sample holder for cryostat . . . 31
3.4 Electrical measurements with driven guard . . . 32
3.5 Van der Pauw measurement schemes . . . 34

4.1 Collection of bottom–up synthesized GNR structures . . . 40
4.2 GNR films on HOPG and SiO_2 . . . 43
4.3 Optimized GNR film on SiO_2 . . . 44
4.4 Transfer of CVD–grown GNR films to a target substrate . . . 46
4.5 Schematic depiction of a GNR FET . . . 48
4.6 Flow chart of the production of lithographically defined short channel devices . . . 50
4.7 Metallic nanojunction defined by EBL . . . 51
4.8 Metallic nanojunction defined by EM . . . 54
4.9 Flow chart of the production of TG–based electromigrated short channel devices . . . 55
4.10 SEM image of a two–terminal EM device with TG disc . . . 57
4.11 EM of TG discs . . . 58
4.12 Flow chart of the production of lithographically defined long channel devices 59
4.13 Large channel device defined by EBL . . . 61
4.14 Success rates of GNR device production approaches . . . 64

5.1 Raman spectrum of aGNR 9 and aGNR 5 . . . 69
5.2 Current–Voltage–characteristics of aGNR 5 and aGNR 9 networks . . . 71
5.3 Impact of unintentional doping on the electrical properties of GNR network FETs . . . 77
5.4 Contact resistance of metal/GNR interfaces . . . 80
5.5 Temperature dependent charge transport in GNR networks . . . 82
5.6 Scaling of the current–voltage characteristics of GNR network FETs . . . 83
5.7 Transport at low temperatures and low bias voltages . . . 86

6.1 Raman spectra of undoped and doped graphene 93
6.2 Sheet resistance *vs.* temperature 97
6.3 Sheet resistance *vs.* magnetic field 99
6.4 Weak localization in undoped graphene and doped graphene 102

7.1 Image collection of CrX_3 crystals (X=I, Br, Cl) 107
7.2 Magnetization *vs.* temperature 109
7.3 Hysteresis loops 111
7.4 Magnetocrystalline anisotropy 113
7.5 Scaling of K_u 114
7.6 Exfoliation of $CrBr_3$ 115

A.1 Thin films of CVD–grown GNRs 122

B.1 Raman spectrum of aGNR 7, GNRNW (9,6),(2,15), GNRNW N–N (9,6),(2,15) and GNRNW N–S (9,6),(2,15) 124
B.2 Current–Voltage–characteristics of aGNR 7 and GNRNW (9,6),(2,15) networks 125
B.3 Current–Voltage–characteristics of GNRNW N–N (9,6),(2,15) and GNRNW N–S (9,6),(2,15) networks 126
B.4 Gate leakage and bias symmetry in aGNR 5 and aGNR 9 devices 127
B.5 Temperature dependence of charge carrier density in the aGNR 5 and the aGNR 9 devices 131
B.6 Box plot of device resistances before and after air exposure 133
B.7 Impact of current annealing on current modulation by electrostatic gating 134
B.8 Contact resistance as function of gate voltage 135
B.9 Conductance maps at low temperature for aGNR 5 and aGNR 9 136

C.1 Full hysteresis loops of CrX_3 141
C.2 Degradation of $CrBr_3$ 142

List of Tables

4.1 Overview of GNR long channel devices 65

5.1 Statistics for charge tranport parameters of GNR networks 74
5.2 Concact resistances in aGNR 5 devices 79

6.1 Raman peak positions of undoped graphene and doped Graphene 93
6.2 Overview of charge transport parameters in undoped graphene and doped graphene 102

7.1 Overview of magnetic properties of CrX_3 107

8.1 Overview of electronic properties of various graphene materials 118

B.1 Charge transport statistics aGNR 9 Chip 2 129
B.2 Charge transport statistics aGNR 5 Chip 1 129
B.3 Charge transport statistics aGNR 5 Chip 2 129
B.4 Charge transport statistics aGNR 5 Chip 4 130
B.5 Charge transport statistics aGNR 5 Chip 5 130
B.6 Charge transport statistics aGNR 5 Chip 6 130
B.7 Temperature dependence of magnetotransport in aGNR 5 137

C.1 CrX_3 crystal masses 140

Abbreviations

1D	one dimensional
2D	two dimensional
2DEG	two–dimensional electron gas
aGNR	graphene nanoribbon with armchair edges
AFM	atomic force microscopy
BLG	bilayer graphene
chGNR	graphene nanoribbon with chevron–type edges
CNT	carbon nanotube
CVD	chemical vapor deposition
DFT	density functional theory
DOS	density of states
EBL	electron beam lithography
EL	ethyl lactate
EM	electromigration
FBZ	first Brillouin zone
FET	field–effect transistor
FLG	few–layer graphene
FWHM	full width at half maximum
GNR	graphene nanoribbon
GNRNW	GNR nanowiggle
HF	hydrofluoric acid
HOPG	highly oriented pyrolytic graphite
LBM	layer breathing mode
LPE	liquid phase exfoliation
MAA	methacrylic acid

MMA	methyl methacrylate
MOSFET	metal–oxide–semiconductor FET
NMP	N–Methyl–2–pyrrolidone
PMMA	poly(methyl methacrylate)
SDS	sodium dodecyl sulfate
SEM	scanning electron microscope
SLG	single layer graphene
SQUID	superconducting quantum interference device
RBM	radial breathing mode
TA	thermal activation
TG	turbostratic graphene
THF	tetrahydrofuran
UHV	ultra–high vacuum
VDP	van der Pauw
VDW	van der Waals
VRH	variable range hopping
VTI	variable temperature inlet
zGNR	graphene nanoribbon with zigzag edges

Chapter 1

Introduction

In 2004, the pioneering experiments on graphene [1], a planar arrangement of carbon atoms in a honeycomb lattice, marked the starting point for a new paradigm in solid state physics. This paradigm of self–supported two–dimensional (2D) crystals has been fully established soon afterwards, when it was realized that layered crystals other than graphite, such as hexagonal boron nitride or transition metal dichalcogenides, can also be subjected to the method of micromechanical cleavage yielding stable monolayers [2]. Since the parental bulk crystals usually have weak interlayer bonds based on van der Waals (VDW) interactions, they are also commonly labeled VDW materials. The number of accessible monolayer materials is steadily increasing and while often they are intriguing on their own (e.g. graphene, MoS_2 [3] or black phosphorus [4]), a great potential lies in further *tailoring* their electronic, magnetic and optical properties. In this thesis, we investigate three carefully selected representatives of highly promising VDW material classes, namely atomically perfect bottom–up graphene nanoribbons, nitrogen–doped single layer graphene and chromium trihalides. The choice of these particular materials is motivated by their exceptional electronic and magnetic features which render them capable to realize such an aforementioned customization, paving the way towards new and exciting physical phenoma in reduced dimensions.

Geometrical confinement allows one to severely modify the properties a solid state system and therefore graphene nanoribbons (GNRs), which are confined graphene systems, stand in the focus of this work. In GNRs, the electronic structure depends crucially

on the width and the details of the edge morphology, where the latter knows two prototypical shapes, armchair and zigzag edges [5]. The development of charge transport devices based on such structures is of particular interest for both scientific research and industry, due to the special properties of GNRs. For example, a band gap arises which is extremely sensitive to the ribbon width. Increasing the latter by only one row of carbon atoms along an armchair GNR can result in a dramatic change of the band gap size, where the band gaps of such two GNRs can exhibit differences in the order of electronvolts [6]. Tuning this band gap opens new possibilities to approach the limits of nano–scale electronics with custom–made characteristics. Secondly, zigzag GNRs exhibit localized electronic states, which have been predicted to be magnetic [7], enabling ultra–small spintronic devices with novel functionalities. Modern chemistry allows for the bottom–up synthesis of these carbon nanostructures with precision on the atomic level and with remarkable flexibility in terms of the two aforementiond parameters, width and edge structure. In this work, we make use of this unique opportunity to synthesize and process such well–defined systems and conduct a systematic experimental study of charge transport in a variety of GNR types.

Secondly, another route to the modification of graphene's electronic properties is heteroatomic doping. Heteroatomic dopants are either incorporated in the lattice replacing carbon atoms [8], physisorbed to the graphene surface while leaving the lattice intact [9, 10], or both approaches can be combined leading to new types of devices [11]. Furthermore, heteroatomic doping even has the potential to open up a band gap [12–14]. Dopant concentrations of more than 15 % have already been reached experimentally with nitrogen and boron [15–18]. However, while the band gap increased in the boron doped graphene, the mobility decreased due to a higher amount of scattering effects [16]. This result indicates that the requirements for any device have to be carefully weighed against each other [15]. Improvements regarding one of the material's properties might lead to an undesired change of another one. In order to elucidate such alterations, we investigate in–depth how nitrogen (N) doping affects charge transport properties of graphene, where nitrogen atoms are incorporated into the lattice during the synthesis by chemical vapor deposition (CVD). Using both, electrical and structural characterization (by Raman spectroscopy), we can relate changes of charge carrier properties to changes in the structure of the material.

Finally, chromium trihalides, CrX_3 with X being a halogen ion of fluorine (F), chlorine (Cl), bromine (Br) or iodine (I), are a particular case of layered seminconductors with unusual and exciting magnetic properties. Compared to unmagnetic materials, magnetically ordered ones are largely underrepresented in the list of VDW materials [19] and recently ferromagnetism in a single CrI_3 layer has been experimentally demonstrated [20]. The synthesis of CrX_3 can be realized by CVD [21, 22] and they can be readily exfoliated using the same scotch tape technique which initially yielded graphene monolayers [1]. While CrX_3 compounds have been studied initially as bulk materials in the 1960s pioneered by Tsubokawa, Dillon and Hansen [23–26], the prospect of magnetic single layers of these materials is a source of a renewed interest. The possibility of handling single layers of various materials and combining them in arbitrary ways offers an immense flexibility and an unprecedented opportunity to create artifical designer stacks. In these stacks, exciting phenoma are emerging from the physics at the interfaces, especially when magnetic layers are integrated [27, 28]. However, magnetism of CrX_3 is still not well–understood and in order to serve as a basis for the understanding of magnetic phenomena in reduced dimensions, remaining open questions need to be addressed [22].

The thesis is organized as follows:

Chapter 2 is an introduction to the physics of two–dimensional materials, especially describing the theoretical background of graphene and graphene nanoribbons. Furthermore, the basics of magnetism are reiterated in order to build a foundation for the understanding of magnetic phenomena in chromium trihalides.

Chapter 3 presents an overview of all experimental techniques that have been used throughout this thesis to characterize GNRs, doped graphene and CrX_3 compounds. The details of the experimental setups are given in this chapter.

Chapter 4 shows the engineering process of charge transport test structures, especially to probe charge transport in GNRs. Since atomically perfect GNRs have not been available for a long time, there is no standard procedure to contact them and the achievement of a reliable device fabrication route is a major step forward in this field.

Chapter 5 is dedicated to the experiments of charge transport through GNR networks. Various types of GNRs have been measured and we compare our experimental results in this chapter, especially focussing on armchair GNRs with two different widths of five

and nine carbon atoms across the ribbon, respectively. Their electrical characterization has been extended to variable temperatures and high magnetic fields.

Chapter 6 deals with nitrogen doped graphene. A characterization of the structural integrity of CVD–grown N–doped graphene films is presented here, combined with charge transport, again at variable temperatures and at high magnetic fields. Our measurements demonstrate the relation between structure and functionality in this special graphene allotrope.

Chapter 7 presents our experimental results on the magnetic properties of chromium trihalides. Magnetometry on bulk single crystals enables us to understand the magnetocrystalline anisotropy in these compounds, which is the key to stable ferromagnetism down to the monolayer regime.

Chapter 8 finally concludes this thesis by summarizing and highlighting the major results of chapters 4 – 7. The chapter also includes an outlook of promising future research.

The results presented in this dissertation have, in parts, already been published or submitted to different journals. A list of publications is presented at the end of this thesis. Furthermore, references are included in the text wherever appropriate.

Chapter 2

Theoretical background

In a low–dimensional system the motion or arrangement of particles and other entities, such as magnetic moments, is constrained to a plane (2D) or to a chain (1D). Often new and exciting physical effects emerge from such geometrical confinement. For example, in graphene, a monolayer of carbon atoms in a hexagonal lattice, massless Dirac fermions exhibiting unusual properties are a consquence of the two–dimensional structure [29]. In this chapter, we provide a theoretical description of the effects of geometrical confinement going from two–dimensional confinement in graphene to one–dimensional confinement in graphene nanoribbons. Furthermore, we give a brief introduction to magnetic exchange effects, relevant for the magnetic coupling in chromium trihalogenides, a class of layered magnetic semiconductors.

2.1 General effects of dimensional confinement in solid state systems

Numerous physical problems are best described in three (spatial) dimensions. However, certain properties drastically change when the dimensionality of a system is confined. In solid state physics, widely discussed examples are planar spin arrangements (Ising model) [30] or low–dimensional semiconductor heterostructures [31]. Especially the latter have had a broad impact on semiconductor physics and technology as, for instance, semiconductor lasers [32] or ultrafast transistors [33] were realized using semiconductor–based quantum wells and two–dimensional electron gases (2DEGs). Founded on fundamental

quantum mechanics, a whole formalism can be developed in order to describe properties of low–dimensional semiconductor physics (see e.g. Ref. [31] for further reading) and here we recapitulate only a selection of important concepts. First, we have a closer look at the general idea of confinement and secondly, we discuss the electronic density of states in one, two and three dimensions, which is a particularly useful quantity to understand the electronic and optical properties of a system.

2.1.1 Dimensional confinement of a particle

While a completely unbound electron can propagate in all three spatial dimensions, a narrow potential well can be used to restrict this motion in one dimension to discrete energy levels. If the separation of such energy levels is large, the only energy level accessible for such an electron at low energy is the ground state and no motion will be possible in this dimension. This way electrons can be confined into two dimensions (2DEGs) or even into one dimension (quantum wires). To understand the confinement in more detail, we follow the considerations in Ref. [31] and start with the three–dimensional time–independent Schrödinger equation for one particle with mass m

$$\left[-\frac{\hbar^2}{2\,m}\,\nabla^2 + V(\mathbf{R})\right]\,\Psi(\mathbf{R}) = E\,\Psi(\mathbf{R})\,, \tag{2.1}$$

where $\mathbf{R}$ is the three–dimensional position vector, Ψ is the wave function of the particle, V denotes the potential energy, ∇ is the tree–dimensional nabla operator, $\hbar$ is the reduced Planck constant and E is the energy. We now consider a potential which confines the motion in only one dimension, i.e. in z direction. Hence, we can write $V(\mathbf{R}) = V(z)$ and the particle is still free to move along x and y direction. This motivates to write the wave function as a product of plane waves for x and y and an unknown function, $u(z)$, for z:

$$\Psi(x, y, z) = \exp\left(i\,k_x\,x\right)\,\exp\left(i\,k_y\,y\right)\,u(z)\,. \tag{2.2}$$

After substituting this into the Schrödinger equation, we can let the partial derivatives act on the exponential functions. The exponential functions then cancel from both sides and only the dependence on z remains. After sorting constant terms to the right–hand

side, we obtain

$$\left[-\frac{\hbar^2}{2\,m}\,\frac{\mathrm{d}^2}{\mathrm{d}z^2}+V(z)\right]\,u(z)=\left[E-\frac{\hbar^2\,k_x^2}{2\,m}-\frac{\hbar^2\,k_y^2}{2\,m}\right]\,u(z)=\epsilon\,u(z)\,. \tag{2.3}$$

In order to solve Eq. 2.3, we need to know the exact form of the potential energy. In either case, the energy is quantized along the z direction and the eigenenergies of the system are of the form

$$E_n(k_x,k_y)=\epsilon_n+\frac{\hbar^2\,k_x^2}{2\,m}+\frac{\hbar^2\,k_y^2}{2\,m}\,, \tag{2.4}$$

where the quantum numbers k_x, k_y and n label the states in each dimension. The infinetly deep square quantum well is the simplest example of such a confining potential and although it cannot be experimentally realized it is particularly useful to approximate finite quantum wells (e.g. in a GaAs–AlGaAs system) because of its simplicity [31]. There is a straight–forward way to extend the confinement to other dimensions. If we chose a potential of the form $V(\mathbf{R}) = V(x,y)$, the result is a quantum wire, where the particle remains free to move only along z. As we will see by the example of one–dimensional graphene nanoribbons in Sec. 2.2.3, such confinement has a significant impact on the electronic properties as large band gaps can be formed. If the potential confines the particle in all three dimensions, there is no free motion in any dimension and the result is called a quantum dot. Quantum dots exhibit then energy levels analoguous to atoms and therefore they are often called artifical atoms.

2.1.2 Density of states

The density of states (DOS) for electrons, $N(E)\,\delta E$, is one of the most important quantities to understand and describe a quantum system and its distribution of energies in an intervall $[E;E+\delta E]$. The DOS is useful in countless examples, as in magnetism (e.g. for defining the Stoner criterion, see Sec. 2.4.2) or in quantum-well lasers [31]. A general definition of the total DOS of a system with eigenenergies ϵ_n is

$$N(E)=\sum_n \delta(E-\epsilon_n)\,, \tag{2.5}$$

where $\delta(E)$ denotes the Dirac δ–distribution. In order to determine the total number of states between E_1 and E_2, Eq. 2.5 has to be integrated over this interval and then the sum has to be evaluated. We can now consider free electrons in one dimension. Their

states can be labled by their wave number k, such that Eq. 2.5 becomes

$$N(E) = 2 \sum_{k=-\infty}^{\infty} \delta[E - \epsilon_0(k)] \,, \tag{2.6}$$

where the factor 2 accounts for spin. The simplest way to treat the problem of free electrons in one dimension is to consider them being trapped in a finite box of length L and perfom the limit $L \to \infty$ at the end of the calculation. Following this route, one can readily show that the eigenstates of this system are regularly spaced in k–space with a separation of $2\,\pi/L$ [31]. Hence, for large systems, we can use a continuum approximation and replace the sum in 2.6 by an integral

$$N(E) = \frac{L}{\pi} \int_{-\infty}^{\infty} \delta[E - \epsilon_0(k)] \, \mathrm{d}k \,. \tag{2.7}$$

This integral can be easily solved by substitution using the relation $\epsilon_0(k) = \hbar^2 \, k^2/(2\,m)$ and we arrive at

$$N_{1\mathrm{D}}(E) = \frac{2\,L}{\pi\,\hbar} \int_0^{\infty} \sqrt{\frac{m}{2\,z}} \delta[E - z] \, \mathrm{d}z = \frac{L}{\pi\,\hbar} \sqrt{\frac{2\,m}{E}} \,. \tag{2.8}$$

In Eq. 2.8, we see that the DOS diverges as $E^{-1/2}$ in the limit $E \to 0$ (Van Hove singularities [34]), which is a characteristic feature of one dimension and can be found for carbon nanotubes (CNTs) and graphene nanoribbons (GNRs). In the case of parabolic band dispersion, the density of states is constant in two dimensions and $\propto \sqrt{E}$ in three dimensions. For linear bands however, the DOS is $\propto |E|$ in two dimensions (e.g. in graphene) and $\propto E^2$ in three dimensions.

2.2 Electronic properties of selected graphene allotropes

Carbon is an abundant element on earth with a large variety of allotropes [35]. In 2004, K. Novoselov et al. achieved a milestone in carbon research as the electric field effect in graphene was demonstrated [1]. These experiments were the starting point for a new and fruitful field of science. Materials beyond graphene, as for example geometrically confined graphene or graphene multilayers, exhibit further exciting properties. However, as the electronic properties of an ideal sheet of graphene are the basis to understand such more complicated systems, we start with this as an introduction.

2.2.1 Single layer graphene

A common way to derive the electronic structure of graphene [29, 36] is to employ the tight–binding method [37]. In this section, we discuss the key aspects of this approach and its results as a basis for the understanding of confined structures. The building blocks of the graphene lattice are carbon atoms which have four valence electrons participating in the formation of chemical bonds. In graphene, the atomic s orbital hybridizes with two p orbitals (sp^2 hybridization), leading to a planar arrangement of all carbon atoms. In the plane, σ bonds form an angle of 120° and π orbitals arrange perpendicular to the plane. Thus, we obtain a two-dimensional hexagonal lattice. Every carbon atom has three nearest neighbors at a distance of $a = 1.42$ Å. We choose a certain cartesian coordinate system[1] and make use of the hexagonal symmetry to find three vectors, connecting nearest neighbors:

$$\boldsymbol{\delta}_1 = \frac{a}{2}\left(1, \sqrt{3}\right)^T, \quad \boldsymbol{\delta}_2 = \frac{a}{2}\left(1, -\sqrt{3}\right)^T \quad \boldsymbol{\delta}_3 = -a\,(1,0)^T\,. \tag{2.9}$$

However, not all sites are equivalent and one can find a decomposition of the hexagonal lattice into two triangular Bravais sublattices A and B.

[1] The choice of the origin and the axes of the coordinate system is arbitrary. However, once chosen it has to be consistently used in consecutive analysis [38].

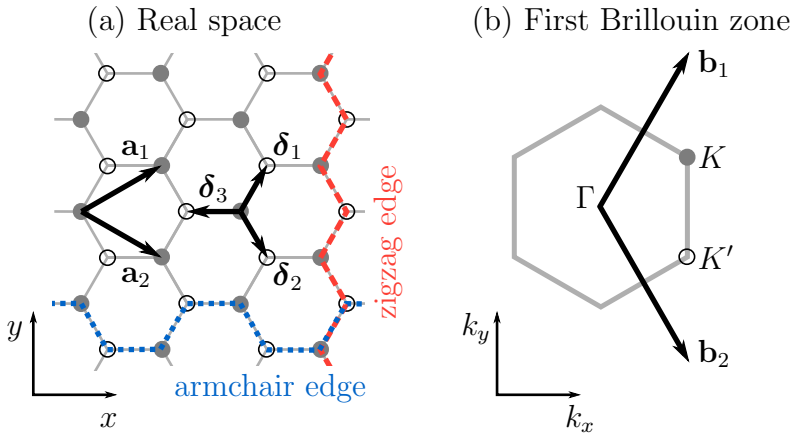

FIGURE 2.1: Graphene honeycomb lattice and its first Brillouin zone. (a) The hexagonal lattice in real space which consists of two triangular sublattices A (open dots) and B (solid dots). The vectors $\mathbf{a}_1$ and $\mathbf{a}_2$ are the primitive vectors of sublattice A and $\boldsymbol{\delta}_i$, $i = 1, 2, 3$ are the nearest neighbor vectors. Two axes of high symmetry can be found in the hexagonal lattice: armchair (blue dotted line) and zigzag (red dashed line). (b) Corresponding Brillouin zone. The vectors $\mathbf{b}_1$ and $\mathbf{b}_2$ span the reciprocal lattice. The center (Γ point) and the two inequivalent corners (K and K') of the Brillouin zone are labeled.

In the same coordinate system, the primitive vectors, e.g. of sublattice A, are given by

$$\mathbf{a}_1 = \frac{a}{2}\left(3, \sqrt{3}\right)^T, \qquad \mathbf{a}_2 = \frac{a}{2}\left(3, -\sqrt{3}\right)^T, \tag{2.10}$$

and their counterparts in reciprocal space are

$$\mathbf{b}_1 = \frac{2\,\pi}{3\,a}\left(1, \sqrt{3}\right)^T, \qquad \mathbf{b}_2 = \frac{2\,\pi}{3\,a}\left(1, -\sqrt{3}\right)^T, \tag{2.11}$$

which fulfill the condition $\mathbf{a}_i \cdot \mathbf{b}_j = 2\,\pi\,\delta_{ij}$, where $i = 1, 2$ and δ_{ij} is the Kronecker delta. Figure 2.1 schematically shows the graphene lattice in real space as well as the first Brillouin zone (FBZ) which is the first Wigner–Seitz cell [39] of the triangular lattice in reciprocal space. Neighboring corners in the FBZ are inequivalent as they are not connected by reciprocal lattice vectors and they are conventionally labeled K and K'. These crystallographic points usually coincide with so–called "Dirac" points in graphene (see below) [40]. The lattice symmetries will now help us to understand the electronic structre. As we are interested in the transport properties of graphene and its related materials, we consider only the π electrons because they are delocalized and not localized in covalent bondings. Within the tight–binding approach, we assume that an electron can hop from lattice site to lattice site, with amplitudes t when hopping between nearest

neighbors and t' when hopping between next–nearest neighbors[2]. In the language of second quantization this situation can be modeled by introducing annihilation (creation) operators $a_{i,\sigma}$, $b_{j,\sigma}$ ($a^\dagger_{i,\sigma}$, $b^\dagger_{j,\sigma}$) which annihilate (create) an electron with spin σ ($\sigma = \uparrow, \downarrow$) at lattice sites $\mathbf{R}_i$ and $\mathbf{R}_j$ of the sublattices A and B, respectively:

$$H = -t \sum_{\langle i,j\rangle,\sigma} \left(a^\dagger_{\sigma,i}\, b_{\sigma,j} + \text{H.c.} \right) - t' \sum_{\langle\langle i,j\rangle\rangle,\sigma} \left(a^\dagger_{\sigma,i}\, a_{\sigma,j} + b^\dagger_{\sigma,i}\, b_{\sigma,j} + \text{H.c.} \right) . \tag{2.12}$$

The sum in the first term runs over all nearest-neighbor sites $\langle i,j\rangle$, while the sum in the second term considers the next–nearest neighbor sites $\langle\langle i,j\rangle\rangle$. The symbol H.c. denotes the Hermitian conjugate of the preceding term. Without loss of generality, we restrict the following calculation to nearest–neighbor hopping and perform a Fourier transformation of the annihiliation (creation) operators such that

$$a_{i,\sigma} = \frac{1}{N} \sum_{\mathbf{k}} e^{i\,\mathbf{k}\,\mathbf{R}_i}\, a_{\mathbf{k},\sigma}, \quad b_{j,\sigma} = \frac{1}{N} \sum_{\mathbf{k}} e^{i\,\mathbf{k}\,\mathbf{R}_j}\, b_{\mathbf{k},\sigma} \,. \tag{2.13}$$

Here, we choose the same phase factor for the two sublattices [38] and N is the number of unit cells. Reintroducing these operators into the Hamiltonian (Eq. 2.12) and computing the sum over the lattice sites, we find the Hamiltonian in momentum space

$$H = -t \sum_{\sigma,\mathbf{k}} \left(\gamma_{\mathbf{k}}\, a^\dagger_{\sigma,\mathbf{k}}\, b_{\sigma,\mathbf{k}'} + \gamma^*_{\mathbf{k}}\, b^\dagger_{\sigma,\mathbf{k}}\, a_{\sigma,\mathbf{k}'} \right) , \tag{2.14}$$

where we have used $\gamma_{\mathbf{k}} = \sum_{i=1}^{3} e^{i\mathbf{k}\cdot\boldsymbol{\delta}_i}$. In a final step of algebraic transformation, we rewrite Eq. 2.14 in a matrix and spinor notation,

$$H = \sum \Psi^\dagger_{\mathbf{k}\sigma} \cdot A \cdot \Psi_{\mathbf{k}\sigma} \,, \tag{2.15}$$

with $A = \begin{pmatrix} 0 & -t\,\gamma_{\mathbf{k}} \\ -t\,\gamma^*_{\mathbf{k}} & 0 \end{pmatrix}$ and $\Psi_{\sigma,\mathbf{k}} = \begin{pmatrix} a_{\sigma,\mathbf{k}} \\ b_{\sigma,\mathbf{k}} \end{pmatrix}$. In order to derive the energy spectrum we now calculate the eigenvalues ϵ_k of the matrix A. The result is given by

$$\epsilon_k = \pm t \cdot |\gamma_k| \,. \tag{2.16}$$

[2]The value t is approximately 2.8 eV [29], while t' is not well known. From *ab initio* calculations a range of $0.02\,t \leq t' \leq 0.2\,t$ is predicted [41]. A tight-binding fit to cyclotron resonance experiments finds $t' \approx 0.1$ eV [42].

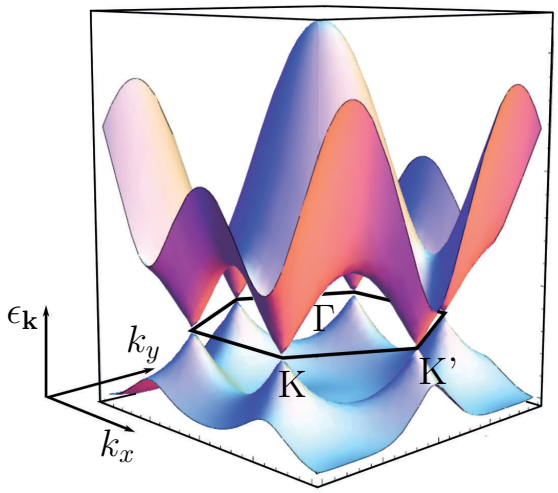

FIGURE 2.2: Plot of the full graphene band structure (Eq. 2.19) with the choice $t' = 0.1\,t$. Characteristic points (see main text) in the FBZ are marked.

An explicit expression for $|\gamma_{\mathbf{k}}| = \gamma_{\mathbf{k}} \cdot \gamma_{\mathbf{k}}^*$ can readily be calculated by using Euler's formula and the symmetries in the sine and cosine functions

$$|\gamma_k| = \sqrt{3 + f(\mathbf{k})}\,, \tag{2.17}$$

with

$$\begin{aligned} f(\mathbf{k}) &= 2 \sum_{1<j} \cos\left(\mathbf{k} \cdot (\boldsymbol{\delta}_i - \boldsymbol{\delta}_j)\right) \\ &= 2 \left[\cos\left(\sqrt{3}\, k_y\, a\right) + 2\, \cos\left(\frac{3}{2}\, k_x\, a\right)\, \cos\left(\frac{\sqrt{3}}{2}\, k_y\, a\right)\right]. \end{aligned} \tag{2.18}$$

If we account for the next–nearest neighbor contribution ($t' \neq 0$) the symmetry between valence and conduction band is broken:

$$\epsilon_k = \pm t \cdot |\gamma_k| - t' \cdot f(\mathbf{k})\,. \tag{2.19}$$

In Fig. 2.2, we show an image of the full band structure (Eq. 2.19). The conduction (π^*) and the valence (π) bands touch at the points K and K'. Considering small electron momenta q around these points, we can expand Eq. 2.19 in a Taylor series. The first order of this expansion shows that the spectrum becomes linear in q resembling the dispersion of massless relativistic particles, such as photons, where the Fermi velocity $v_F = 10^6$ m/s replaces the speed of light c [29]. In a continuum theory of the low–energy

excitations it can be shown that a two–dimensional Dirac equation is able to describe the physics in this regime appropriately [29, 43]. This result is also robust towards the influence of next–nearest neighbor hopping because all further corrections lead to higher order terms in the expansion beyond the dominating linear one [44].

2.2.2 Turbostratic graphene multilayers

The unusual electronic structure of graphene monolayers as discussed in the previous section is altered when graphene layers are stacked and form bi– or multilayer systems. However, the stacking order is crucial as it determines in which way the electronic properties change [29]. Starting with a first graphene layer (A) at a fixed position, a second layer (B) is usually displaced by a nearest neighbour vector of the honeycomb lattice $\boldsymbol{\delta}_i$, $i = 1, 2, 3$ (see Eq. 2.9). As a consequence of this translation, half of the atoms in B are directly above the atoms of one sublattice of A and the other half sits on top of the hexagon centers of the first layer as depicted in Fig. 2.3 (a). To describe the electronic properties of such bilayer graphene, further tight–binding parameters can be introduced to the model Hamiltonian in Eq. 2.14 in order to account for interlayer hopping. The adapted model leads to a quadratic energy dispersion around the K points instead of the linear Dirac cone [29] and this result does not depend on the choice of $\boldsymbol{\delta}_i$ for the translation of the second layer. However, stacks with a large number of layers can be arbitrarily complex in their stacking order and analytical expressions for the electronic bands can only be obtained for the highly ordered cases. In the most common arrangement the sign of the translation alternates, i.e. $\boldsymbol{\delta}_i$, $-\boldsymbol{\delta}_i$, $\boldsymbol{\delta}_i$, $-\boldsymbol{\delta}_i$, ... leading to ABA or Bernal stacking (α-graphite). Here, the established model for the band structure was developed by Slonceswki and Weiss [45] and McClure [46] which does not give rise to the massless Dirac fermions of graphene monolayers. Nevertheless, there is a way to preserve the linear dispersion around the Dirac point, which is by introducing a twist angle between adjacent graphene layers, so–called turbostratic graphene (TG) [47]. From a theoretical point of view, the constant rotation of graphene layers with respect to adjacent ones leads to the restoration of the fourfold band-structure degeneracy at the Dirac point with an energy interval around it, where the linear dispersion is kept intact. The superlattice, which is a moiré lattice as exemplified in Fig. 2.3 (b), is characterized by the rotation angle φ which therefore is crucial for the electronic properties. The rotation angle can be calculating using the lattice vector of the unrotated layer $\mathbf{a}_1$ and

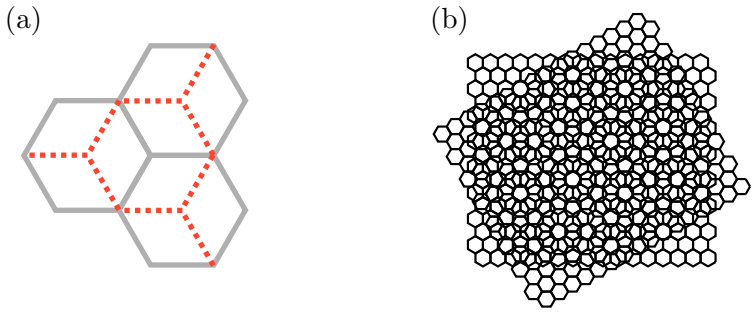

FIGURE 2.3: (a) shows the usual stacking of two graphene layers. If one takes the grey honeycomb as reference, then the red dashed honeycomb is shifted by a nearest neighbour vector $\boldsymbol{\delta}_i$, $i = 1, 2, 3$. (b) shows schematically the occurrence of a moiré pattern by rotating two layers with respect to each other. The rotation in this example is $\varphi = 30°$.

the rotated layer $\mathbf{a'}_1$:

$$\cos(\varphi) = \frac{\mathbf{a}_1 \cdot \mathbf{a'}_1}{|\mathbf{a}_1|\,|\mathbf{a'}_1|}\,. \tag{2.20}$$

The moiré periodicity D can be then deduced by

$$D = \frac{a}{2\sin(\varphi/2)}\,. \tag{2.21}$$

While for rotation angles of 30°, the linear energy interval is in the order of electron volts, it shrinks down to milli-electron volts for angles of 1.47° or smaller [47]. In this situation, the graphene layers are strongly coupled.

2.2.3 Geometrically confined graphene structures

In Sec. 2.2.1, we have discussed the electronic properties of an infinite graphene sheet. A confinement of such a sheet along one lateral dimension results in elongated and narrow stripes, so–called graphene nanoribbons (GNRs) which can be classified according to their edge structure and width. Carbon atoms situated along the periphery of a GNR have unpaired electrons because they are surrounded by only two instead of three other carbon atoms. Such dangling bonds are energetically unfavorable and the system will tend to form covalent bonds with other atomic or molecular specimen, e.g. oxygen or hydrogen (termination) [48]. In this thesis, we investigate two different types of (hydrogen terminated[3]) GNRs shown in Fig. 2.4, one having armchair edges and the

[3]The hydrogen termination is in this case dictated by the precursor molecule used for the bottom–up synthesis of the GNRs (compare Sec. 4.1.2)

other exhibiting a so–called chevron structure. The electronic properties of a GNR depend crucially on both, its width and its edge structure, and various techniques have been invoked to calculate the energy bands, such as the tight–binding method [5, 41, 49, 50], solutions of the Dirac equation [51–53] as well as density functional theory (DFT) and *ab initio* calculations [41, 54–57]. However, all solutions have in common that they must satisfy the boundary conditions dictated by the GNR structure, namely the electron wave function vanishes at the borders of the ribbon.

2.2.3.1 Armchair and zigzag GNRs

In the hexagonal graphene lattice, there are two distinct types of edges, armchair and zigzag, which are formed when we imagine the lattice to be cut along certain directions. If we choose the horizontal x–axis in Fig. 2.1 to mark zero degrees, we find armchair edges at angles $\theta_{\mathrm{a}} = 0°$, $60°$ and $120°$, while we can follow a zigzag edge at angles $\theta_{\mathrm{z}} = 30°$, $90°$ and $150°$. The electronic properties of armchair GNRs (aGNRs) are remarkebly different from those of zigzag GNRs (zGNRs) and both show clear distinctions to the electronic structure of an extended graphene sheet. Especially, zGNRs host localized electronic edge states with energies close to the Fermi level E_F residing exclusively on one sublattice and absent in two–dimensional graphene as well as in aGNRs [5, 49, 50]. Their existence can be demonstrated for example analytically, considering a semi–infinite graphene sheet with a zigzag edge, or on the level of a nearest–neighbor tight binding ansatz for the π electrons [29, 49, 53]. As a consequence of these states, particular features in the energy spectrum and the DOS emerge. The highest valence band and the lowest conduction band are associated to the edge states and become (partially) flat in the region $2\pi/3 \leq k \leq \pi$. Even on the basis of more sophisticated calculations, these bands are degenerate as long as the spin degree of freedom is not considered, rendering zGNRs generally metallic [54–56]. Such flat bands are linked to a sharp increase of the DOS around E_F which is in contrast to the non–confined case, where the DOS vanishes at E_F. With this enhanced DOS, magnetic ordering of electron spins has been predicted where the coupling is ferromagnetic along one edge and antiferromagnetic for opposite edges [49, 58–61]. A staggered potential resulting from the magnetic ordering can lift the degeneracy of the flat band in the antiferromagnetic ground state and a band gap opens up, while a state where spins on opposite edges are parallel remains metallic [6, 54, 58, 62, 63]. However, at finite temperatures, a long range magnetic order is not

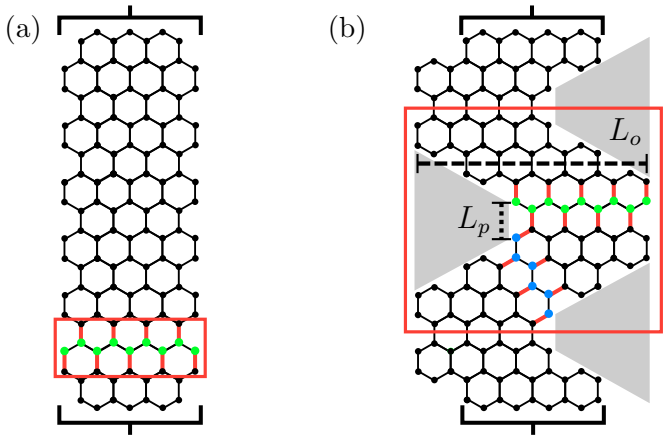

FIGURE 2.4: Prototypical aGNR (a) and GNRNW (b) structure. For both structures the basic repeating unit to construct the one–dimensional crystal (unit cell) is enclosed by a red rectangle. The aGNR has a width of 9 carbon dimer lines across the ribbon (marked in red), or 9 carbon atoms (marked in green), respectively. The GNRNW is composed of a parallel aGNR 9 segment (dimers marked in red, carbon atoms in green) and an oblique aGNR 6 segment (dimers marked in red, carbon atoms in blue). The dashed line indicates the length of the oblique part L_o and the dotted line marks the length of the parallel part L_p. Edge atoms terminating the structure are not shown.

possible in one– and two–dimensional systems [64] and at maximum a certain spin–correlation length can be expected. At room temperature the spin–correlation length is estimated to be approximately 1 nm [7, 63]. Furthermore, deviations from half–filled bands can significantly disturb the magnetic order [65]. Armchair edges are lacking such localized edge states, and in sufficiently narrow aGNRs, a band gap is always present [6, 52–55, 66–68]. It is convenient for the further discussion to use the number of carbon dimer lines N across the ribbon (compare Fig. 2.4) as a measure for the width W and we introduce the notation "aGNR N" in order to refer to aGNRs with a given N. If necessary, we can calculate W explicitly via

$$W = \frac{1}{2}\sqrt{3}\,a\,(N-1)\,, \tag{2.22}$$

where a is the nearest neighbor distance (see 2.2.1). To analyze the electronic structure of aGNRs, we start again by considering a simple tight–binding model describing nearest neighbor hopping of electrons in π orbitals. Analogous to Sec. 2.2.1 we use the language

of second quantization to set up an appropriate model Hamiltonian [69]:

$$H = -t \sum_{l} \left[\sum_{m \in \text{odd}} a_l^\dagger(m) b_{l-1}(m) + \sum_{m \in \text{even}} a_l^\dagger(m+1) \right] + \text{H.c.} \\ - t \sum_{l} \sum_{m=1}^{N-1} \left[b_l^\dagger(m+1) a_l(m) + a_l^\dagger(m+1) b_l(m) \right] + \text{H.c.}\,. \tag{2.23}$$

Herein, $a_l(m)$ and $b_l(m)$ ($a_l^\dagger(m)$ and $b_l^\dagger(m)$) are the annihilation (creation) operators of an electron at sublattice site A and B of the mth dimer and in the lth unit cell. The first line describes hopping of electrons along the ribbon (longitudinal) while the second line accounts for hopping across the ribbon (transverse). Wakabayashi et al. provide a detailed calculation of the eigenvalues for Eq. 2.23 in Ref. [69] and here, we just summarize the result. The boundary conditions lead to the discretization of the electron momentum in the transverse direction:

$$p = \frac{r\,\pi}{N+1}, \quad r = 1, 2, \ldots, N\,, \tag{2.24}$$

while the longitudinal momentum k is continuous for infinitely long ribbons. The spectrum can be derived explicitly:

$$E = \pm t \sqrt{1 + 4 \left(\cos(p) \cos\left(\frac{k}{2}\right) + \cos^2(p) \right)}\,. \tag{2.25}$$

Most importantly, we note that based on Eqs. 2.24 and 2.25 there are three groups of aGNR N, such that $N_1 = 3\,m$, $N_2 = 3\,m+1$ or $N_3 = 3\,m+2$, $m \in \mathbb{N}$, which differ by the size of their direct band gap Δ_i, $i = 1, 2, 3$ at the Γ point in the FBZ. Within the tight–binding model the group aGNR N_3 has $\Delta_3 = 0$ and is consequently always metallic while for N_1 and N_2, Eq. 2.25 yields $\Delta_1 > \Delta_2$ [5, 50, 53, 67, 69–71]. However, more complex treatments of the problem, e.g. DFT and Green's function approaches, reveal that quantum confinement and lattice distortion effects lead to band gaps in all three groups with a gap size hierachy $\Delta_2 > \Delta_1 > \Delta_3$ [6, 52, 54, 55, 66–68].[4] We further note that due to this hierarchy, there is a non–monotonous behavior of the band gap with W, but per family an inverse scaling $\Delta_i \propto 1/N_i$ is found, characteristic to quantum confinement [54]. Moreover, it is enlightening to compare the bands obtained by the tight–binding method with the original graphene band structure. A zone–folding

[4] If one accounts for third–nearest neighbors and lattice distortions the tight–binding method leads to results in agreement with first–principle calculations, too [72].

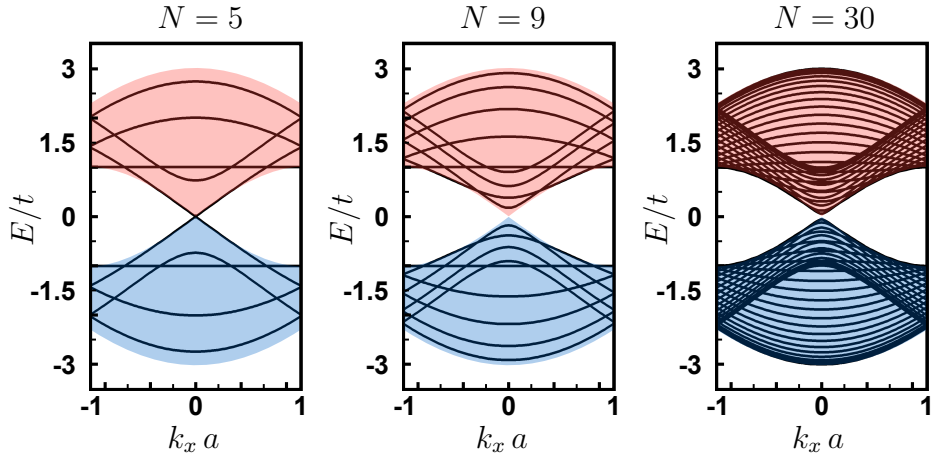

FIGURE 2.5: Tight–binding energy bands of aGNR 5, aGNR 9 and aGNR 30. While the $N = 5$ ribbon is metallic, there is a gap in the $N = 9$ and $N = 30$ cases. The projected valence band (blue) and conduction band (red) of a two–dimensional extended graphene sheet are shown in each plot as colored overlay, illustrating the agreement of the dispersions in the limit $N \to \infty$.

technique can be applied, where we project the two–dimensional graphene band strucutre (Eq. 2.16) onto the armchair direction in the hexagonal FBZ (see Fig. 2.5) [5, 69, 70]. The linear dispersion around the K point gives rise to the valence band and conduction band of the aGNR touching at $k = 0$ in the one–dimensional FBZ. On the other hand, towards the borders of the FBZ, the bands move apart leading to large gaps at $k = \pm\pi$. As discussed, the direct gap opens in the FBZ central region for small N, while for large N, the resemblance to the projection becomes more and more obvious (see Fig 2.5).

2.2.3.2 Chevron GNRs

Besides the regular armchair and zigzag edge patterns, more complicated morphologies are possible, for example by fusing armchair or zigzag segments in a kinked fashion, by introducing a chirality or by adding (periodic) functionalizations along the edge. In this way, GNRs with cove–type edges [73, 74], chiral GNRs [75–78], or chevron–like GNRs (chGNRs) [79–82] can be obtained. The latter comprises a multitude of subclasses with structural variations, such as jagged GNRs [83], sawtooth GNRs [84], W–shaped GNRs [85], or so–called nanowiggles [86], and theory predicts intriguing thermoelectric [87, 88] electronic and magnetic properties [81, 86] resulting from the non–straight topologies. The fundamental difference of fused GNR blocks of different width and straight GNRs is

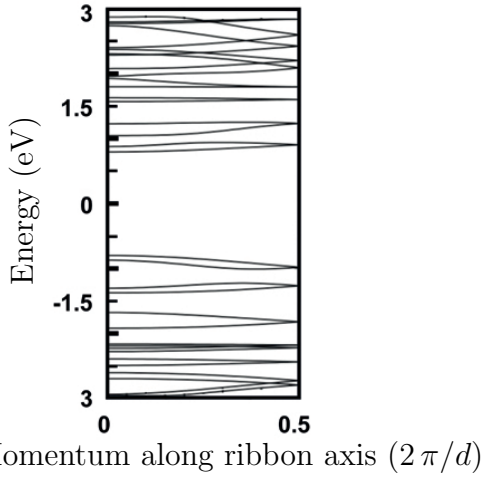

FIGURE 2.6: Energy bands of GNRNW $(9, 6), (2, 15)$ obtained by DFT calculations. The symbol d denotes the length of the unit cell in real space. Adapted and reprinted by permission from Macmillan Publishers Ltd: Nature **466**, 470. Copyright 2010 (Ref. [79]).

the occurence of a new periodicity in the system, which defines a superlattice. Superlattices can lead to a strong modulation of the energy gap in real space resulting in quantum well structures or series of quantum dots [89]. Hence, designing the periodicity of the superlattice opens up another opportunity to tailor the electronic properties of GNRs [88, 90] as it has been done very successfully in conventional semiconductors [91, 92]. Due to the aformentioned variety of structures there is no general classification scheme covering all possible chGNRs. Only within chGNR subfamilies certain regularities can be found such that often a small number of parameters defines the ribbons contained in the respective subfamily.

Here, we focus on GNR nanowiggles (GNRNWs) with lattice structures which can be viewed from two different perspectives. On the one hand, we can describe them as successive repetitions of parallel and oblique aGNR and/or zGNR segments, seamlessly stitched together. On the other hand, we can imagine a wide aGNR/zGNR from which trapezoidal wedges are carved out on alternating edges. The GNRNW structure depicted in Fig. 2.4 is the relevant one for this thesis and it is assembled from two aGNR segments of different width. To exemplify the alternative picture, we mark the "removed" parts of a wide GNR as shaded areas in Fig. 2.4 as well. A set of four parameters is uniquely associated with any allowed GNRNW structure, if certain regularity conditions are applied [86]. These parameters are the lengths (L_p, L_o) and the widths (W_p, W_o) of the parallel

and the oblique domains, respectively. For the width of each segment we count the carbon dimer lines in the usual way and obtain $(W_p, W_o) = (9, 6)$. The length L_o is defined as the width of the (imaginary) wedge–healed aGNR and the length L_p is the number of carbon–carbon distances a expanding along the smallest basis of the trapezoids, which yields $L_o = 15$ and $L_p = 2$ for our case. The electronic structure of GNRNWs is accurately described in the tight–binding framework [86]. However, the majority of calculations available in literature are based on first principles. In Fig. 2.6, we show an example of a DFT calculation of the energy bands in the GNRNW $(9, 6), (2, 15)$. The band gap derived in the DFT framework is approximately 1.6 eV consistent throughout the literature [79–81, 93, 94]. Although DFT is most often qualitatively accurate, the obtained band gap can often not reproduce experimental observations, especially if there are enhanced electron–electron interactions in low-dimensional nanostructures [6, 95]. Other methods, such as a many–body Green's function approach with screened Coulomb interaction are more accurate and yield larger gaps of approx. 3.6 eV for the freestanding structure [93, 94, 96].

2.3 Charge transport by charge carrier hopping

In disordered solids like polycrystalline or amorophous (organic as well as inorganic) semiconductors the wavefunction of charge carriers is not delocalized over the whole volume. In this case, transport of charge carriers is dominated by the transition between localized sites via tunneling or overcoming potential barriers instead of the wave–like propagation found in crystalline and structurally ordered materials. The hopping transition rate k_{ij} from an occupied site i to an empty site j is typically described either by the Miller–Abrahams formalism or by Marcus theory [97–99]. However, the theory of nuclear tunneling, which is based on tunneling in an asymmetrically biased double quantum well, is able to give a unified description of charge transport in virtually all important organic semiconductors [100, 101]. Here, the nuclear vibrations are coupled to the charges and drive the charge transfer from site to site. Assuming a purely dissipative situation, Fisher and Dorsey, and Grabert and Weiss [102, 103] derived an analytic expression for the transfer rate

$$\begin{aligned} k_{ij} =& \frac{H_{ij}^2}{\hbar^2\,\omega_c}\left(\frac{\hbar\,\omega_c}{2\,\pi\,k_\mathrm{B}\,T}\right)^{1-2\,\alpha^*}\left|\Gamma\left(\alpha^* + i\left(\frac{\epsilon_{ij}}{2\,\pi\,k_B\,T}\right)\right)\right|^2 \\ & \times \Gamma(2\,\alpha^*)^{-1}\,\exp\left(\frac{\epsilon_{ij}}{2\,k_\mathrm{B}\,T}\right)\exp\left(-\frac{|\epsilon_{ij}|}{\hbar\,\omega_c}\right)\,, \end{aligned} \tag{2.26}$$

where H_{ij} is the electronic coupling between initial and final state, ϵ_{ij} is the difference in energy between donor and acceptor states, α^* is the Kondo parameter describing the coupling strength between charge and bath, ω_c is the characteristic frequency of the bath, k_B is the Boltzmann constant, T is the temperature and Γ is the complex gamma function. Following the considerations in Ref. [100], the macroscopic electric current in such a system can be calculated based on Eq. 2.26 by comparing forward and backward hopping events

$$I \propto k_\mathrm{forward} - k_\mathrm{backward} = k(\epsilon_{ij}) - k(-\epsilon_{ij})\,. \tag{2.27}$$

Under the assumption of equal hopping steps, the energy difference of the states i and j in Eq. 2.27 can be written in terms of the applied bias potential V, the hopping distance L_{ij} and the total distance L which the charge carrier has to traverse

$$\epsilon_{ij} = L_{ij}\,e\,V/L = \gamma\,e\,V\,, \tag{2.28}$$

where we define $\gamma^{-1} = L/L_{ij}$ as the number of hopping events performed by charge carriers to cover the full distance between the electrodes and e is the elementary charge. We now substitute Eqs. 2.26 and 2.28 into Eq. 2.27, define $\alpha = 2\,(\alpha^* - 1)$ and consider the limit $|\epsilon_{ij}| \leq \hbar\,\omega_c$. This yields an analytic formula for the expected current density [100]

$$J = J_0\,T^{1+\alpha}\,\sinh\left(\frac{\gamma\,e\,V}{2\,k_B\,T}\right)\left|\Gamma\left(1+\frac{\alpha}{2}+i\,\frac{\gamma\,e\,V}{2\,\pi\,k_B\,T}\right)\right|^2 . \tag{2.29}$$

There are two limiting cases that can be drawn from Eq. 2.29: In the low–voltage Ohmic range, the current density is given by

$$\lim_{V\to 0} J = \frac{J_0\,\gamma\,e}{2\,k_B\,T}\,\left|\Gamma\left(1+\frac{\alpha}{2}\right)\right|^2\,T^{\alpha}\,V\,. \tag{2.30}$$

Furthermore, the opposite limit of high voltages results in a temperature independent power law for the current density

$$\lim_{V\to\infty} J = J_0\,\pi^{-\alpha}\left(\frac{\gamma\,e}{2\,k_B}\right)^{\beta}\,V^{\beta}\,. \tag{2.31}$$

Within the framework of nuclear tunneling theory, the exponents α and β of Eqs. 2.30 and 2.31 are connected as $\beta = \alpha + 1$. Equations 2.29, 2.30 and 2.31 play important roles in the analysis of charge transport in Sec. 5. Furthermore, the charge carrier mobility in hopping systems can be approximated using a modified Einstein relation [104]

$$\mu = \frac{e\,a^2}{k_{\mathrm{B}}\,T}\,k\,, \tag{2.32}$$

where a is the intermolecular (hopping) distance and k is the charge transfer or hopping probability per unit time. Equation 2.32 shows clearly, that the mobility in the case of hopping is governed by the hopping rate in contrast to the case of delocalized band transport, where the mobility scales with the average scattering time τ [105]. As a consequence, the mobility is typically much lower in hopping systems than in crystalline systems [104].

2.4 Basics of magnetism

In Sec. 7 of this thesis, we investigate the magnetic properties of chromium trihalogenides, a class of layered materials. The following paragraphs summarize briefly the most important concepts to understand magnetism in solids. Magnetic phenomena arise due to the subtle and complex interplay of elementary magnetic moments. These magnetic moments are caused by the electron's angular momentum that is comprised of the electron's orbital motion and its spin. The angular momentum and the magnetic dipole moment of electrons are linked as follows:

$$\boldsymbol{\mu} = -\frac{\mu_B}{\hbar}\left(\mathbf{L} + g\mathbf{S}\right) . \tag{2.33}$$

In Eq. 2.33, $\mu_B = e\,\hbar/2\,m_e$ denotes the Bohr magneton with m_e the electron mass. The g–factor is $g \approx 2$ for the electron [106]. The dipolar fields created by these moments are typically too weak to account for long range magnetic order and only so–called exchange interactions, based on quantum mechanical principles, lead to the ordering of magnetic moments [106].

2.4.1 Direct exchange

Arising from Pauli's exclusion principle for fermions, exchange is a purely quantum mechanical phenomenon. The spins of electrons with wavefunctions $\psi_a\left(\mathbf{r}_1\right)$ and $\psi_b\left(\mathbf{r}_2\right)$ located at positions $\mathbf{r}_1$ and $\mathbf{r}_2$ can either couple into a singlet ($S = 0$) or a triplet state ($S = 1$), which implies that the spin configuration is either antiparallel or parallel, respectively. Depending on the energy difference between both states, one or the other alignment will be preferred [106]

$$J_{a,b} = E_S - E_T = 2\int \psi_a^*\left(\mathbf{r}_1\right)\psi_b^*\left(\mathbf{r}_2\right)\hat{\mathcal{H}}\psi_a\left(\mathbf{r}_2\right)\psi_b\left(\mathbf{r}_1\right)\mathrm{d}\mathbf{r}_1\mathrm{d}\mathbf{r}_2 . \tag{2.34}$$

The symbol $\psi_{a/b}^*$ denotes the complex conjugate of the wave function. If $J_{a,b} > 0$, we have $E_S > E_T$ and the triplet state is favoured. In a (magnetic) solid an interaction of the form Eq. 2.34 applies between all neighboring spins and a general Hamiltonian can be written as [106]

$$\hat{\mathcal{H}} = -\sum_{i,j} J_{i,j}\mathbf{S}_i\mathbf{S}_j . \tag{2.35}$$

2.4.2 Itinerant ferromagnetism

In some cases magnetic order in metals is associated with delocalised $3d$–electrons that move freely through the material (itinerant electrons). If it becomes energetically favorable for some electrons with energies within ΔE around the Fermi edge to flip their spin from down to up and thus create an imbalance in the spin population, ferromagnetic ordering is established [106]. The new densities are then given by $n_{\uparrow/\downarrow} = 1/2\,(n \pm g\,(E_F)\,\Delta E)$ with $g\,(E_F)$ the density of states at the Fermi level. This gives rise to a net magnetization $M = \mu_B\,(n_\uparrow - n_\downarrow) \neq 0$.

In this situation two energy terms are competing. On the one hand the electrons gain kinetic energy $E_{\text{kin}} = \frac{1}{2} g\,(E_F)\,(\Delta E)^2$. On the other hand there is also a reduction of energy which is due to the interaction of the magnetization with the molecular field:

$$E_{\text{pot}} = -\int_0^M \mu_0 \lambda M' \mathrm{d}M' = -\frac{1}{2}\mu_0 \lambda M^2\,. \tag{2.36}$$

The parameter λ expresses how large a molecular field is obtained for a given magnetization. The quantity $U = \mu_0 \mu_B^2 \lambda$ is then a measure of the Coulomb energy. The condition for ferromagnetism becomes

$$E_{\text{kin}} + E_{pot} = \frac{1}{2} g\,(E_F)\,(\Delta E)^2\,(1 - U g\,(E_F)) \leq 0\,, \tag{2.37}$$

which leads to the so–called Stoner criterion for ferromagnetism [107]

$$U\,g\,(E_F) \geq 1\,. \tag{2.38}$$

Hence, ferromagnetism requires strong Coulomb effects and a high density of states at the Fermi energy.

2.4.3 Superexchange

The term "superexchange" describes the phenomenon of magnetically coupled cations, whose interaction is mediated by an anion. In such cases, the spatial distance between the cations is large, typically in the order of Ångströms, and several atomic orbitals are involved. The concepts and the theory behind this phenomenon have been introduced

first by H. Kramers [108], and were then fully developed mainly by P. W. Anderson [109–111], J. B. Goodenough [112, 113] and J. Kanamori [114]. The superexchange effect in ionic insulators, with the antiferromagnet MnO being one of the most famous examples, can be derived from quantum mechanical perturbation theory in a one–electron Hartree–Fock approach. This electron is considered to be the "magnetic" electron, typically occupying a d shell, while all other, s and p, electrons are core electrons. An intermixing of the magnetic d electron wave with the p electron wave of the non–magnetic anion is then the primary mechanism of superexchange [115]. If the magnetic electron is delocalized over the whole structure it has the chance to lower its kinetic energy (at the cost of Coulomb energy U). The exchange constant is then

$$J \propto -\frac{b^2}{U}\,, \tag{2.39}$$

where b denotes the electron transfer integral accounting for its kinetic energy [115]. In general, superexchange leads to antiferromagnetic coupling and only in rare cases ferromagnetic coupling occurs. A set of semi–empirical rules were developed by Goodenough and Kanamori which are very useful to rationalize the magnetic properties of superexchange coupled materials on a qualitative level [112–114]. We summarize these rules in the form given by Anderson in Ref. [115]. In order to predict the magnetic coupling in an ionic material, one firstly determines which of the d orbitals contains the magnetic electrons according to ligand field theory. The two rules are then:

A. Two ions with magnetic orbital lobes pointing towards each other in such a way that the orbitals would have a large overlap integral, the superexchange is antiferromagnetic. Herein, we can find three subcases:

   1. The lobes are of d_{z^2}–type in the octahedral case and they are in a 180° position, such that they point directly toward the mediating anion and toward each other. Then the antiferromagnetic superexchange interaction is large.
   2. The lobes are of d_{xy}–type and are in a 180° position. Then the antiferromagnetic superexchange interaction is large.
   3. On one ion, the electron occupies a d_{z^2} orbital and on the other ion, the electron occupies a d_{xy} orbital and they are in a 90° position. Then the $p\pi$ orbital is the $p\sigma$ for the other and the antiferromagnetic superexchange interaction is large

B. The magnetic orbitals are arranged such that they are in contact but the overlap integral is comparatively small. This would be the case if on one ion, the electron occupies a d_{z^2} orbital and on the other ion, the electron occupies a d_{xy} orbital and they are in a 180° position. Then the ferromagnetic superexchange interaction is large (nevertheless, not as strong as the antiferromagnetic one in the other cases).

Chapter 3

Experimental methods

For the characterization of the materials investigated within this thesis, a multitude of experimental methods were employed. This chapter introduces the most important techniques which were used to access and quantify structural and electrical properties of these materials. We begin with Raman spectroscopy, which is a powerful tool to determine the structural integrity of carbon materials. Furthermore, charge transport measurements at variable temperatures and high magnetic fields require dedicated setups, which involve helium cryostats, superconducting magnets and appropriate source–measure devices. In order to extract material specific quantities, such as resistivity or charge carrier mobility, the geometry of the current path must be known or the van der Pauw (VDP) method must be applied. Finally, the magnetic properties of chromium trihalides were determined by a superconducting quantum interference device (SQUID).

3.1 Structural characterization by Raman spectroscopy

Raman spectroscopy [116] is one of the most common techniques to characterize the structure of graphene–based systems. It can be used to unambigiuously identify CNTs, single and multilayer graphene and GNRs based on their specific Raman spectra, which serve as unique fingerprints [117]. Raman spectroscopy relies on the (inelastic) Raman scattering [118, 119] of photons (with an energy of $\hbar\omega$) in a crystal under the creation or annihilation of excitations such as phonons or magnons (with energy $\hbar\Omega$). The scattering generally involves intermediary electronic states. If the incoming photon *creates*

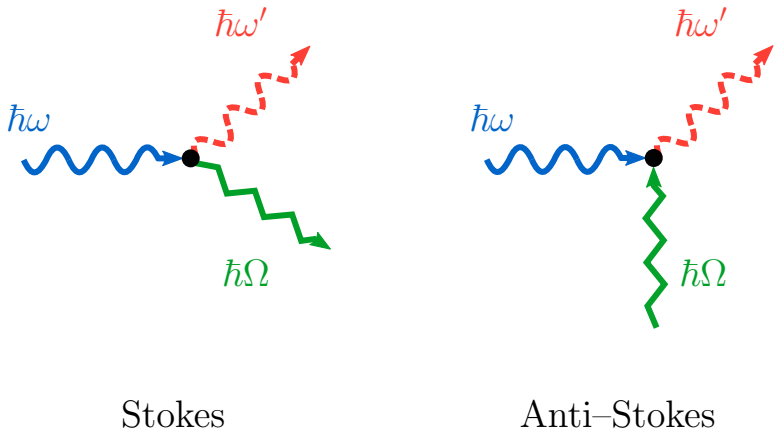

FIGURE 3.1: Stokes and Anti–Stokes scattering of an incoming photon $\hbar\omega$ with a phonon $\hbar\Omega$ in a crystal. The scattered phonon carries an energy of $\hbar\omega'$.

a phonon (Stokes), the scattered phonon carries a lower energy $\hbar\omega' = \hbar\omega - \hbar\Omega$. In the opposite case of *annihilation* (Anti–Stokes), the scattered phonon has an increased energy of $\hbar\omega' = \hbar\omega + \hbar\Omega$. Both processes are diagrammatically depicted in Fig. 3.1. The Stokes process is much more probable than the Anti–Stokes [105] and hence, Raman spectra are usually plotted with the difference between incident and scattered photon energy (Raman shift) on their abscissa. Often, the Raman shift is given in units of cm^{-1} which can be converted to meV via the relation $1\,\mathrm{meV} = 8.0655447\,\mathrm{cm}^{-1}$.

Both, the absence of an electronic band gap as well as the linear energy dispersion around the K point in the Brillouin zone have important implications for the Raman spectrum of graphene, such as the fact that any given excitation energy leads to resonant scattering processes. As a consequence and due to electron–electron and electron–phonon interactions, the Raman spectrum of graphene consists of only very few intense features, which are, in contrast to many other materials, not related to the phonon density of states. [120–122]. We briefly discuss the most prominent peaks in the spectrum of single layer graphene, which are typically analyzed for structural characterization[1]. In Fig. 3.2 a representative Raman spectrum is shown, where we find the so–called G peak at approximately $1580\,\mathrm{cm}^{-1}$, the D peak at approximately $1350\,\mathrm{cm}^{-1}$ and the $2D$ peak at approximateley $2700\,\mathrm{cm}^{-1}$. Quantum mechanical pertubation theory is able to describe the scattering processes building the basis for these (and for all other) peaks. It allows

[1] Numerous publications, such as Ref. [117], discuss these and other peaks in much greater detail.

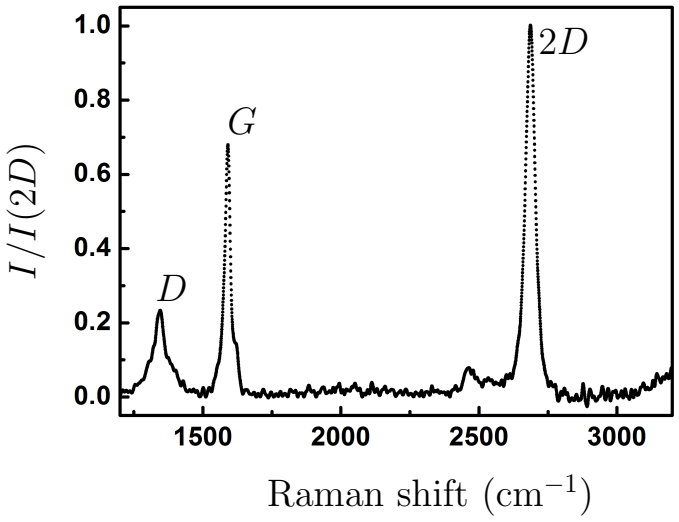

FIGURE 3.2: Raman spectrum of a defective graphene monolayer.

one to calculate the Matrix element for n–phonon processes [117]. However, for the G, D and $2D$ peaks only one– and two–phonon processes are relevant.

The G peak can be traced back to a one–phonen process giving rise to an E_{2g} mode[2] at the Γ point of the Brillouin zone. In this mode, carbon atoms of different sublattices vibrate in–plane along anti–parallel axes. In the quantum mechanical calculation of the corresponding matrix element, quantum interference effects of the involved electron waves play an important role. From this follows that doping, which effectively controls the occupation of electronic states, can change the intensity of this peak [123–125]. The D peak is another one–phonon mode which is usually not Raman–active in defect–free samples. This peak arises from a breathing mode of the carbon hexagon which needs a defect for its activation. Here, the total momentum conservation can be satisfied by an additional electron–defect scattering event. Finally, the $2D$ peak involves a two–phonon process and is an overtone of the D peak. Interestingly, the $2D$ peak is always visible in the spectrum, because the momentum conservation is satisfied by two phonons with opposite wave vectors and hence, no defects are required for its activation.

Edges in a graphene sample, as for example in GNRs, can be seen as line defects. While the translational symmetry is preserved along the edge, it is broken in the direction normal to it. Consequently, the occurence of the D peak would be expected. However, a detailed analysis shows that perfect zigzag edges do not result in a D–peak activation

[2]The notation "E_{2g}" refers to the irreducible representation of the underlying point group D_{6h} and thus reflects the symmetry of the phonon mode.

[126–128]. On the other hand, perfect armchair edges lead to an angular dependence of the D peak intensity $I(D)$ on the polarization of the incident light, because the electronic momentum has to be perpendicular to the edge in order to contribute. If linearly polarized light is oriented at an angle Θ with respect to the edge and an analyzer, parallel to the polarizer is used, one finds $I(D) \propto \cos^4(\Theta)$. The ratio $I(D)_{min}/I(D)_{max}$ is then a measure of the edge imperfection when disordered edges are present with armchair and zigzag contributions [127]. Furthermore, the modification of the G peak can be used to discriminate between perfect armchair and perfect zigzag edges, as the former results in $I(G) \propto \sin^2(\Theta)$ and the latter in $I(G) \propto \cos^2(\Theta)$ [129]. Additionally, the low–energy spectrum, where the so–called radial breathing mode (RBM) is located, contains information about the structure (width, morphology and functionalization) of GNRs [79, 130–134]. The position of the RBM can be used to determine the width of a GNR as the wave vector of the RBM is proportional to the inverse of the ribbon width [131, 134].

3.2 Electrical measurements

For the charge transport measurements described in this thesis (Secs. 4 – 6), different setups and techniques have been used. In the following section, we describe briefly the two different experimental setups for electrical measurements at room temperature and at variable temperatures. Moreover, we explain the technique of current guarding, which is important when measuring resistances higher than megaohms. The VDP method allows for the determination of material specific charge transport parameters for samples with arbitrary lateral shape.

3.2.1 Room temperature measurements

For the electrical measurements of graphene nanoribbons at room temperature, a setup from Dr. W. P. at the Max Planck Institute for Polymer Research was available. The setup comprises a three–terminal probe station integrated in an inert gas glove box with nitrogen atmosphere. Graphene and related materials are very sensitive to adatomic doping originating from their environment [135] and in order to guarantee stable experimental conditions, all room temperature measurements have been carried out in the

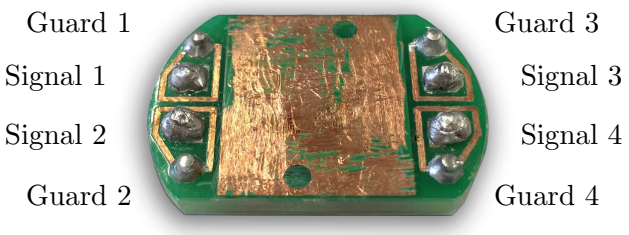

FIGURE 3.3: Cryostat sample holder suitable for the measurement of highly resistive samples. Since the holder is designed for guarded measurements using triaxial connections, it has four signal pins and additionally four guard pins (see Sec. 3.2.3).

glove box. Typically, the glove box contains ≤ 3 ppm of molecular oxygen and ≤ 0.1 ppm of water. The probe station is connected to a Keithley 4200 semiconductor characterization system which contains three independent source–measure units and allows for the electrical characterization of test devices.

3.2.2 Low temperature measurements

Variable temperature measurements have been carried out in a bath cryostat equipped with a dynamic variable temperature insert (VTI) at the bottom of the sample space which allows for the control of the sample temperature. Stable temperatures within approx. 0.1 K are obtained by balancing the cooling power of a liquid helium flow against the heating power of a electrical resistive heating element. The liquid helium is drawn from the main reservoir through a needle valve which is adjusted manually. Temperatures below 4.2 K are obtained by reducing the vapour pressure of the liquid helium in the sample space by mechanical pumping. Furthermore, the setup contains a superconducting magnet, capable of applying unidirectional magnetic fields up to 9 T. Electrical measurements are enabled with a Keithley 238 source–measure unit or using a combination of a Keithley 224 current source and a Keithley 182 voltmeter. A measurement computer allows for a remote control of the setup. While in a probe station setup as in the room temperature measurements metallic needles establish an electrical connection positioned on the sample surface with the help of micromanipulators, for measurements in the cryostat, the sample has to be glued to a sample holder. In Fig. 3.3 a sample holder is shown, which has four signal connections each protected by a

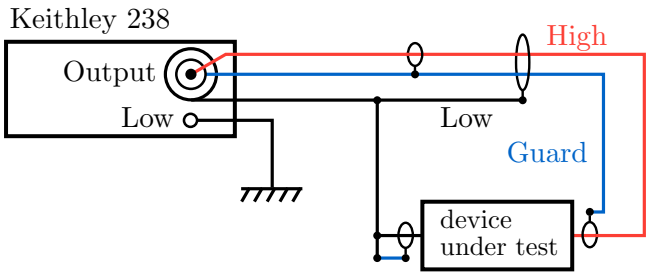

FIGURE 3.4: Schematic depiction of the setup for electrical measurements using a driven guard supplied by the Keithley 238 source–measure unit as used within this work. I thank Prof. Dr. G. J., who developed and provided the setup.

guard line (see Sec. 3.2.3). The electrical connection from the sample holder to the sample is established by metallic wires, which are attached to the sample surface either using silver paste or by ultrasonic–assisted wire bonding.

3.2.3 Current guarding

Current guarding is a technique, which is commonly used when very high resistances or very low currents and voltages are to be measured [136]. For the measurement of high resistances in the range of Gigaohms or more, special care has to be taken in order to avoid leakage currents which can obfuscate the signal of interest. The use of triaxial cables and guarding is able to eliminate the impact of leakage currents on the measured signal as explained in the following. In the triaxial configuration, there is an inner conductor for the signal, an inner and an outer shield. If the inner shield is put to the same voltage as the inner conductor, their voltage difference is zero and no current can leak in or out. Consequently, the test current flows completely through the inner conductor and on to the measurement's input. On the other hand, any leakage current flowing finds its path from the guard to the grounded outer shield. An additional effect is that it speeds up measurement times, since it avoids RC circuits with large time constants, which are effectively formed in coaxial cables between the signal carrying conductor and the grounded shield. In Fig. 3.4, the measurement setup for highly resistive samples as used within this work is depicted schematically [136].

3.2.4 Van der Pauw technique

The van der Pauw (VDP) technique is a common method to measure the sheet resistance R_S and the Hall voltage U_H of arbitrarily shaped thin films where the thickness is small compared to its lateral dimensions and where the following conditions are fulfilled [137]:

1. The sample should be homogenous and isotropic with uniform thickness.
2. There must not be any holes inside the sample area.
3. The contact area of any individual contact should be at least one order of magnitude smaller than the area of the entire sample. The error introduced by the contact size can be estimated based on the geometry and corrected [138].

For a VDP measurement, four electrodes electrodes at the perimeter of the sample are required in order to separate the current and the voltage circuits. Figure 3.5 shows the measurement schemes in order to determine the resistances $R_{ij,kl}$ which are defined as

$$R_{ij,kl} = \frac{U_{kl}}{I_{ij}}\,, \tag{3.1}$$

where $i, j, k, l \in \{1, 2, 3, 4\}$ correspond to the numbers of the electrodes in Fig. 3.5. The sheet resistance can be derived by numerically solving Eq. 3.2:

$$\mathrm{e}^{-\frac{\pi R_a}{R_S}} + \mathrm{e}^{-\frac{\pi R_b}{R_S}} = 1\,, \tag{3.2}$$

where R_a and R_b are the averaged measured resistances

$$\begin{aligned} R_a &= \frac{1}{4}\left(R_{13,24} + R_{31,42} + R_{24,13} + R_{42,31}\right)\,, \\ R_b &= \frac{1}{4}\left(R_{12,34} + R_{21,43} + R_{34,12} + R_{43,21}\right)\,. \end{aligned} \tag{3.3}$$

For the Hall voltage U_H the current is applied diagonally through the sample and the voltage is measured perpendicular to the current flow. A magnetic field B is applied perpendicular to the plane. Similar to the measurements of R_S, an averaging procedure is required for the Hall measurements. First, all measurements should be carried out for both magnetic field directions, upwards and downwards. Secondly, all polarities should be switched and averaged. Finally, the charge and voltage paths should be interchanged.

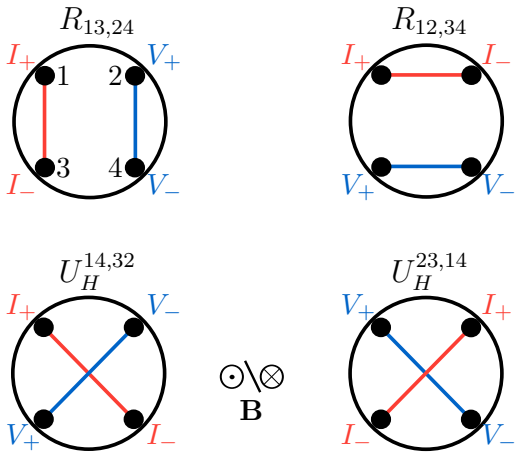

FIGURE 3.5: Sketch of VDP measurement geometries. An example for each configuration to determine R_S and U_H is shown. In order to reach maximum accuracy in the measurement, it is necessary to switch polarities for the current and voltage or to interchange current and voltage leads as described in the main text. Hall measurements require an additional magnetic field **B** perpendicular to the plane.

The overall Hall voltage is then determined by

$$U_H = \frac{1}{4}\left(U_H^{14,32} + U_H^{41,23} + U_H^{23,14} + U_H^{32,41}\right) , \tag{3.4}$$

with the four Hall voltages

$$\begin{aligned}
U_H^{14,32} &= \frac{1}{2}\left(U^{14,32}(+B) - U^{14,32}(-B)\right) , \\
U_H^{41,23} &= \frac{1}{2}\left(U^{41,23}(+B) - U^{41,23}(-B)\right) , \\
U_H^{23,14} &= \frac{1}{2}\left(U^{23,14}(+B) - U^{23,14}(-B)\right) , \\
U_H^{32,41} &= \frac{1}{2}\left(U^{32,41}(+B) - U^{32,41}(-B)\right) .
\end{aligned} \tag{3.5}$$

Here $U_H^{ij,kl}(\pm B)$ denotes the detected voltage between contacts k and l with a constant current between i and j and at the same magnetic field value B pointing up- (+) and downwards (−).

3.3 SQUID magnetometry

The superconducting quantum interference device (SQUID) is able to measure small changes in a magnetic flux with high precision by making use of quantum interference effects in Josephson junctions [139, 140]. While so–called dc SQUIDs are based on a superconducting loop with two Josephson junctions, rf SQUIDs contain only one of such junctions. A detailed description of the operating principles can be found in Refs. [140, 141], while we refer only to the main results here. The SQUID loop itself is a flux–to–voltage transducer where the output voltage is modulated by the magnetic flux enclosed by the loop with a certain periodicity set by the fundamental magnetic flux quantum $\Phi_0 \approx 2.07\,\mathrm{T\,m^2}$. The SQUID loop can be coupled inductively to superconducting detection coils via a so–called flux transformer. In a second–order gradiometer configuration of the detection coils, not the total flux density is measured but the spatial derivative, which allows for significant noise reduction and thus for the measurement of very small signals [141]. Here, the magnetic sample has to be moved mechanically through the pickup coils and the stray field produced by its magnetic moment couples inductively to the SQUID loop. Now, a feedback loop can be used to keep the magnetic flux in the SQUID constant. In this case, the measurement signal is the feedback current.

In this work we use a Quantum Design MPMS XL which is able to detect magnetic moments as small as $10^{-12}\,\mathrm{A\,m^2}$ [142]. This SQUID is calibrated to the stray field of a point–like magnetic dipole. If the stray field of the sample differs significantly from this ideal situation, the measurement has to be corrected accounting for the shape of the sample. Geometrical correction factors have been calculated and can be used for this purpose [143].

3.4 Electron beam lithography

In electron beam lithography (EBL) [144], the basic idea is to use a focused electron beam of a scanning electron microscope (SEM) to write the desired structure first into a radiation sensitive polymer, often called “resist”, and to transfer it then from the resist directly to the substrate/sample by etching, milling or lift–off. For this thesis, so–called positive resists have been chosen, where those parts exposed to the electron beam

undergo a chemical reaction enhancing their soluability compared to the unexposed parts. In the development step, an appropriate solvent creates then a polymeric mask on the sample. This mask determines the areas on the sample which are directly covered with metal in a subsequent metallization step (Sec. 3.5). By dissolving the polymer, the material on the mask is taken away and the desired structure is left behind on the sample surface (lift–off). With EBL, lateral feature sizes down to the nanometer range and virtually any pattern can be obtained. The basic underlying physical processes in EBL are not repeated here as they can be found in literature [144] and have been summarized in my diploma thesis [145]. Nevertheless, for each experiment in this thesis, the fabrication is detailed in the respective section, including the EBL recipes.

3.5 Sputtering

In this work, the method of sputtering has been employed to realize metallic contacts on the surface of silicon/silicon dioxide (Si/SiO_2) substrates. Sputtering is based on glow discharge in order to evaporate a target material by the bombardment with ions and atoms [146]. A glow discharge is ignited in an argon gas atmosphere by applying several hundred volts between the material reservoir (target) and the substrate which is to be coated with the metal film. As a result, a stable plasma is formed and gas ions are transported towards the cathode. These gas ions impinge on the target directly or release a collision cascade with neutral gas atoms which eventually hit the target, too. If the energy transfer to the target overcomes the enthalpy of sublimation, the bombardment causes an ejection of atoms. The release of target atoms is omnidirectional and some will reach the substrate, where a thin film starts to grow. Further details about this technique can be found in Ref. [146].

Chapter 4

Development of charge transport test structures for graphene and graphene nanoribbons

This chapter deals with the technical side of the development of electrical circuits on a carrier substrate, which allow for charge transport experiments in graphene and especially in GNRs. In the following, we will refer to any such test circuit as a "device" and a substrate equipped with devices is called a "chip". For conventional semiconductors, there are established and reliable standard fabrication routes and in the recent years such a knowledge base has been built up for the fabrication of devices based on graphene flakes and films as well. In contrast, the technology of bottom–up synthesized GNRs is still in an early stage, and there is not yet an established standard protocol for the GNR device fabrication and therefore, we test several different approaches. First, we describe in detail the initial growth of the graphene nanoribbons, their transfer to a substrate and the development of appropriate electrical contacts. Secondly, in Sec. 4.4, we introduce certain success rates, which we define for different stages of the whole device production process. Based on these success rates we find a reliable way to fabricate devices to probe charge transport in GNR networks in a systematic way.

4.1 Synthesis of carbon materials

We start with a description of the synthesis of the different carbon materials which have been used. The focus lies on the fabrication of nitrogen doped graphene films by chemical vapor deposition (CVD) and the bottom–up synthesis of GNRs. Furthermore, within this work, TG discs have been used for electromigration experiments (see Sec. 4.3.3), while charge transport in TG discs has been extensively studied by us previously in Refs. [145, 147].

4.1.1 Nitrogen–doped graphene

Doping of graphene is a broadly used term and often used in various contexts, ranging from electrostatic doping using an external electric fields generated by gate electrodes [148], to adatomic charge transfer doping [9, 10] and finally to heteroatomic doping by implanting a second atomic species in the graphene crystal lattice [18, 149–158]. In this work, we focus exclusively on the latter. Different fabrication methods can be used to incorporate a dopant into the graphene lattice. Hyperthermal ion implantation is an example for first growing pristine graphene and integrating the dopants in a second step [159]. However, ion implantation is a poorly controlled stochastic process, where the quality of the obtained doped graphene depends critically on the implantation beam energy and dose. Growing doped graphene in only one step, for example by CVD, is advantageous due to the reduced number of fabrication steps and the potentially higher throughput. CVD is an efficient method to produce single layer graphene [160], where a precursor molecule in gas phase condenses on a catalytic substrate and forms a graphene crystal. Copper is widely used as a substrate in the CVD synthesis of graphene [161]. While in the early stages of CVD grown graphene, the crystal quality was not competitive with mechanically exfoliated graphene, this process has been optimized nowadays, enabling charge carrier mobilities of up to $350,000\,\mathrm{cm^2V^{-1}s^{-1}}$ in undoped graphene, by minimizing lattice defects and optimizing the transfer processes [160]. Furthermore, heteroatomic dopants can easily be integrated by using additional precursors like NH_3 or pyrrole if nitrogen doping is to be obtained [149]. Following this approach, doping with nitrogen [18, 149–151], boron [152, 153], sulfur [154–156], phosphorus [157] and silicon [158] atoms has thus far been demonstrated. Among these different dopants, nitrogen is often a natural choice due to its comparable size to carbon while it has an additional

valence electron leading to n (electron) doping when carbon atoms are replaced by nitrogen atoms (so called graphitic defects) [162]. Interestingly, p (hole) doping is possible as well, if other types of defects are formed, which involve the formation of vacancies in surrounding hexagon rings or distortions of these rings (e.g. so–called pyrrolic, pyridinic or nitrilic defects) [162]. Direct visualizations of nitrogen doped graphene grown by CVD shows that graphitic defects are occuring predominantly [163].

4.1.2 Atomically precise graphene nanoribbons

For the fabrication of GNRs, top–down and bottom–up techniques have been developed and reported. In a top–down approach, an existing structure is modified to yield a GNR in the end. Established techniques are liquid phase exfoliation (LPE) [164], EBL patterning [165], electron beam sculpting [166], and unzipping of CNTs [167, 168]. LPE and CNT unzipping have their advantages in terms of low cost and high throughput, and EBL offers the highest degree of flexibility for the resulting structure. However, top–down methods are generally lacking the deterministic control over the edge structure and ribbon width at the atomic level [164]. The bottom–up method remedies this shortcoming as both, edge morphology and GNR width, are accurately tailored by the design of precursor molecules which serve as building blocks to assemble long ribbons.

In this work, we investigate GNRs resulting from surface–assisted synthesis [79, 169, 170] as well as GNRs from solution–mediated [171–174] synthesis. Both are processes which have been developed and established at the Max Planck Institute for Polymer Research in Mainz.[1] In the solution–mediated approach, the polymerization of the precursors into linear polyphenylenes is followed by oxidative cyclodehydrogenation ("graphitization"). The polymerization is the key step, which determines the final structures of the GNRs as well as their length. Cove–type GNRs with high longitudinal extension over 600 nm can be obtained by AB–type Diels–Alder polymerization [174, 175]. An example of such a cove–type GNR, which is relevant for this work, is shown in Fig. 4.1 and the fabrication scheme can be extended to obtain other GNR structures, which are, however, not investigated in this work. Among them are aGNRs [173, 176], various cove–edge GNRs [74] and chGNRs [80, 177] have been reported. The solution–mediated approach is particularly interesting as it offers liquid–phase–processable GNRs on a bulk scale with the

[1] I thank Dr. A. N. and Dr. Z. C., who have been pioneering the research in this field of chemistry. They are part of the group of Prof. Dr. K. M. and kindly provided the supply with GNRs.

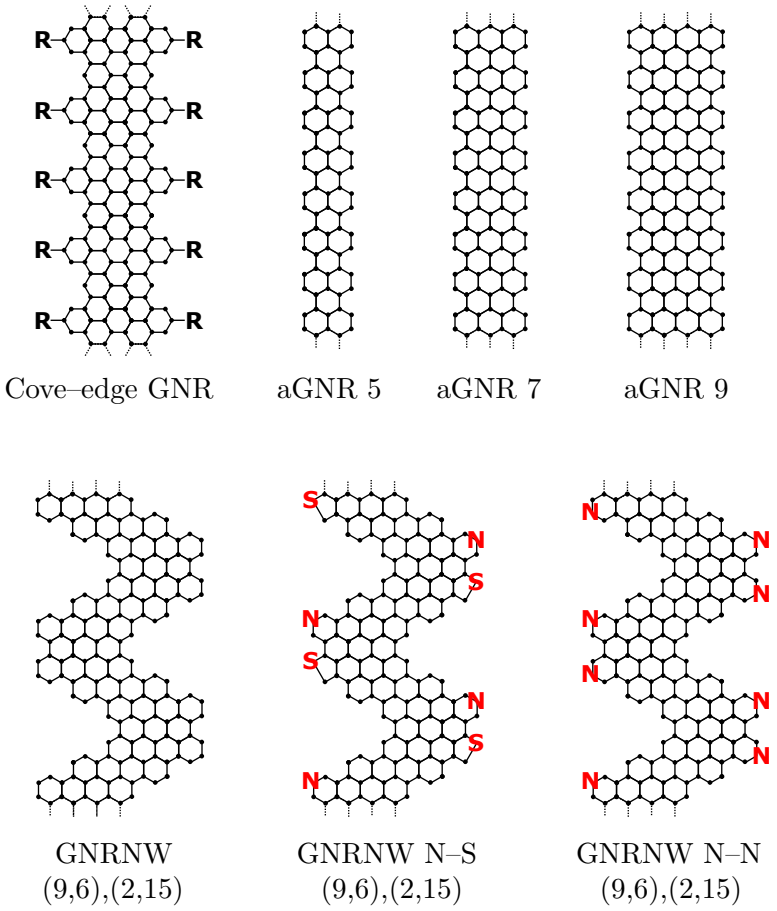

FIGURE 4.1: Collection of schematic drawings of bottom–up synthesized GNRs which are relevant for this work. The cove–edge GNR on the top left is synthesized using a solution–based polymerization [174]. The alkyl chains along the periphery (R) are either a single dodecyl chains ($R = C_{12}H_{25}$) or branchend 2-decyltetradecyl chains ($R = R_1+R_2$, $R_1 = C_{12}H_{25}$, $R_2 = C_{10}H_{21}$). All other GNR structures are synthesized using the CVD process described in the main text. Open bonds are saturated by hydrogen atoms (not drawn) as determined by the precursor molecules used for the synthesis.

potential of enormeous flexibility towards applications. Section 4.2.1 describes how thin films of these GNRs on surfaces can be obtained. GNRs synthesized on a metal surface naturally form a thin film resulting from the underlying chemical processes. Such a GNR film can be transferred from the catalytic substrate to virtually any desired target substrate (see Sec. 4.2.2). As we demonstrate and discuss in the following sections, these GNRs yield a higher amount of functional devices and are therefore in the focus of the charge transport experiments presented in Sec. 5. In the surface–catalyzed approach, monomers substituted with halogen groups are coupled into linear polyphenylenes via radical polymerization. A subsequent cyclodehydrogenation yields GNRs of different topologies and widths, such as aGNRs 5 [178], aGNRs 7 [79], aGNRs 13 [179], chGNRs

[79], zGNRs 6 [180], GNR heterojunctions [169] and even heteroatom–doped GNRs [181–183]. Initially, this fabrication method has been developed in an ultra–high vacuum (UHV) environment, which facilitates the *in–situ* characterization by scanning tunneling microscopy. However, if lateral charge transport experiments are the aim, the elaborate and costly UHV equipment is inconvenient because it restricts the large–scale fabrication and further use of the GNRs. Therefore, in chapter 5, we make use of GNRs which have been fabricated in a CVD process developed by Chen et al. allowing for the inexpensive and high–throughput bottom-up synthesis of structurally well–defined GNRs. Using this system, the fabrication of chGNRs, doped GNRs (N–doping and N, S–co–doping) and aGNRs 7 over large areas even under ambient-pressure conditions has been achieved [82]. Notably, the CVD–grown GNRs exhibit structural quality and properties comparable with those synthesized under UHV conditions as shown by various characterization methods as for example Raman spectroscopy. The CVD method can furthermore yield aGNRs of different widths by using different precursor monomers [184, 185]. Hence, with the capability of tailoring the monomer building blocks by modern synthetic chemistry [186], the bottom-up approach yields access to atomically perfect GNRs with engineered chemical and electronic structures which are currently out of reach for the top–down approach. Figure 4.1 shows an overview of all CVD–grown GNRs which have been investigated within this work.

4.1.3 Turbostratic graphene discs

Turbostratic graphene (TG) is a multilayer system of graphene where adjacent layers are rotated by a certain angle. While already in Bernal–stacked bilayer graphene the energy dispersion becomes quadratic around its K points [29], such a rotational stacking leads to a restoration of the linear band structure within a certain energy window [187]. Thus, in contrast to graphite, TG retains two–dimensional charge–transport properties with high charge carrier mobilities on the order of $10^4\,\mathrm{cm^2\,V^{-1}\,s^{-1}}$ and the multilayer structure of TG discs renders them more resilient than single layer graphene against environmental influences [147] such as adatoms or charged impurities on the substrate [188]. The TG discs which have been used for the electromigration experiments described in Sec. 4.3.3 were commercially bought from nTec AS, Oslo[2]. Their fabrication is based on the decomposition of hydrocarbons by exposing them to the heat of an inert gas plasma,

[2] http://www.n-tec.no/

which can be carried out on an industrial scale in a plasma-arc reactor. The resulting carbon material consists of fullerenes, CNTs, open conical carbon structures (also called micro-cones) and TG micro-discs, which are predominantly flat [189]. The TG discs can be separated from this mixture of materials by means of sonication, centrifugation and filtration and subsequently transferred to a substrate as described in Ref. [147].[3]

4.2 Transfer technniques

For the integration of GNRs into electronic circuits it is necessary to transfer them to a target substrate. A homogeneous distribution of flat–lying, straight GNRs is desirable for a reliably high yield of functional devices. In the following sections (Secs. 4.2.1 and 4.2.2), we describe the development of techniques to obtain such thin GNR films for both types, liquid–phase processable GNRs and CVD–grown GNRs.

4.2.1 Transfer of solution processable GNRs

The main advantage of liquid–phase processable GNRs is that their handling is comparatively easy. Dispersed in a liquid, their storage and transport is simple and in principle they can be readily integrated in device fabrication processes. However, certain preconditions must be fulfilled, i.e. that they show sufficient dispersibility to form stable dispersions on the one hand, and on the other hand that they form homogenous films when brought to a surface. In my diploma thesis (Ref. [145]) it has been shown that cove–edge GNRs dispersed in tetrahydrofuran (THF) form a self–arranged, homogeneous and flat film on the surface of highly oriented pyrolytic graphite (HOPG) (see Fig. 4.2 (a)). The film was readily obtained by drop casting a volume of a few microliters on the HOPG sample and letting the solvent evaporate at ambient conditions. Using atomic force microscopy (AFM) [190], the film can be visualized and the regular arrangement of GNRs is clearly demonstrated (see Fig. 4.2). However, the same approach does not yield any comparable result on a SiO_2 surface. Here, the GNRs coagulate instead and form large clusters with no internal order (Fig. 4.2 (b)). For example, resulting from the hydrophobic carbon surface, bundling and aggregation is known in the case of CNTs

[3] I thank Dr. Y. H. who provided purified powders of TG discs during my whole project and whenever they were needed. She also showed me how to deposit these discs on the surface of a substrate by using a sticky tape–stamp transfer method.

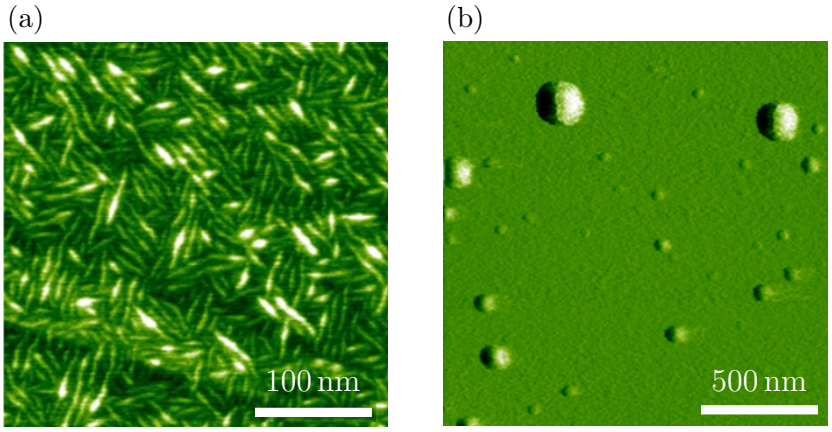

FIGURE 4.2: AFM images of solution–processible GNRs on two different surfaces. In (a), we show GNRs on a HOPG surface where they lie flat and straight. On a SiO_2 surface large and separated clusters of GNRs are visible (b). The images have been adapted from Ref. [145] and have been originally taken by S. K. in the group of Prof. Dr. A. K. at the Johannes Gutenberg University Mainz.

[191] in aqueous media and on hydrophilic interfaces. To enhance their dispersibility, the GNRs are already functionalized during their synthesis by adding bulky alkyl chains (dodecyl or 2-decyltetradecyl [174]) along the periphery of the ribbons. By optimizing the dispersion and deposition parameters, we aim to improve the formation of thin films further. Therefore, we have carried out a systematic **(i)** variation of the liquid in which GNRs are to be dispersed; **(ii)** variation of the GNR concentration in this medium; and **(iii)** variation of the deposition technique. In order to measure the success of the different approaches, we perform Raman spectroscopy, which allows to scan a large area very efficiently, while AFM is time consuming and covers only small areas.

The requirements towards the liquid are twofold. On the one hand, it should lead to a dispersion where GNRs are well–separated for a long time without precipitating. On the other hand, when drop cast to a surface it must be volatile enough to evaporate quickly and leave behind the GNR film. Therefore, we test tetrahydrofuran (THF), N–Methyl–2–pyrrolidone (NMP) and water with the surfactant sodium dodecyl sulfate (SDS). The solvent THF has a particularly high vapor pressure with 170 hPa at 20° C [192] leading to rapid evaporation already under ambient conditions. NMP is more polar and has at the same temperature a much lower vapor pressure of approximately 0.4 hPa [193]. Finally, water with SDS has been tested being a standard choice for dispersing CNTs [191]. We initialize the experiments by mixing 1 mg of GNR powder with the liquid and disperse the GNRs using a tip sonicator for 2 h. In a second step, the dispersion

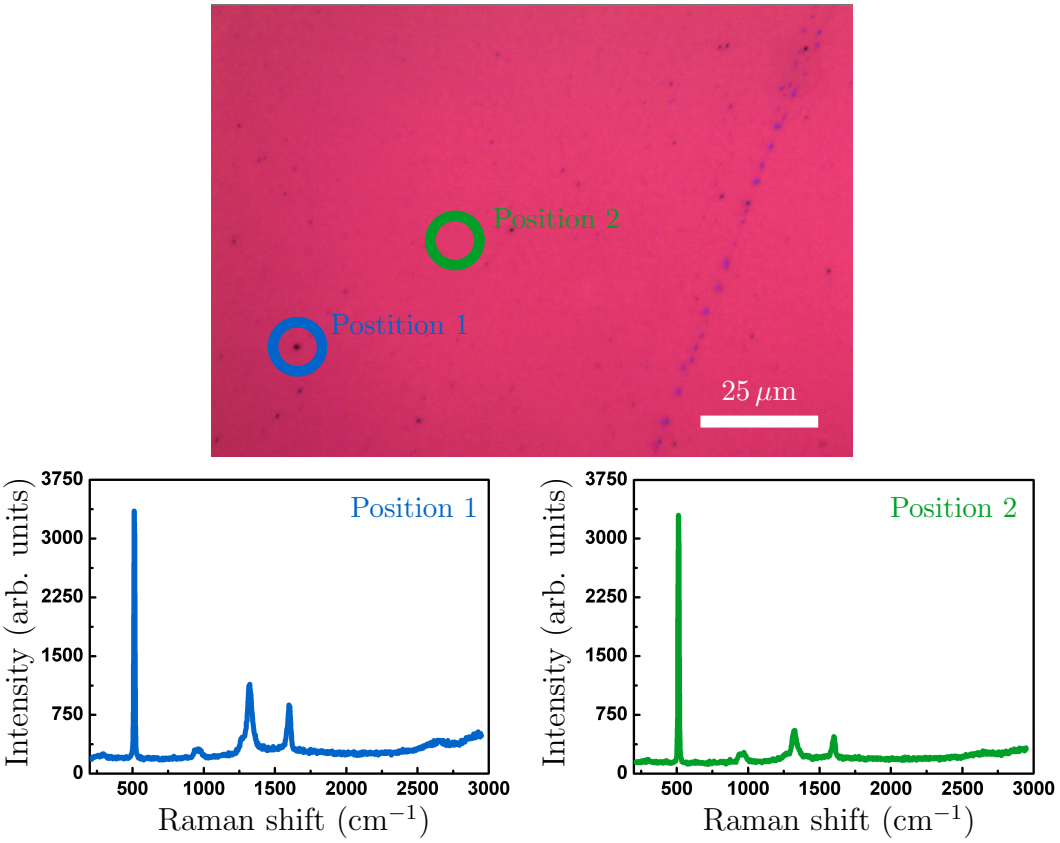

FIGURE 4.3: Solution–processable GNRs deposited as a thin film on a SiO_2 surface. Under the microscope, large GNR bundles are visible (e.g. at position 1) distributed over the whole area. Focusing a laser spot on such a bundle yields a large Raman intensity for the G peak. After the optimization of the dispersion and deposition parameters, a lower but clearly visible G intensity can be measured between the GNR aggregations, e.g. at position 2, showing that GNRs cover the whole surface. In the non–optimized case only isolated aggregations were observable.

is centrifuged at 1500 rpm for 1 min. Finally, the supernatant is extracted and diluted to 1/2, 1/3, ..., 1/10 of the initial concentration. Following this recipe, purple–colored dispersions are obtained where the GNRs are not visible as solid material (compare also Refs. [174, 175] for photographs and absorption spectra of such dispersions). These dispersions have been stable over days, when stored at ambient conditions, where NMP and water with SDS showed slightly less precipitated material after the same amount of time. However, for the deposition experiments, we always used the freshly prepared dispersions. Here, we try four different approaches: Simple drop casting on a substrate, drop casting on a heated substrate, spin casting, where we vary the rotation speed from 1000 rpm to 5000 rpm and incubation of the substrate for 24 h. While by drop casting we can make sure to deposit all GNRs within a droplet, the spin casting may lead to more homogeneous distributions of GNRs over the whole substrate surface, if

the adhesion of GNRs is strong enough. Indeed, we obtain the best result for GNRs dispersed in THF at the lowest concentration (1/10), drop cast on a substrate at a temperature of 120° C. In Fig. 4.3, we show that in this case, we obtain a strong Raman signal all over the substrate surface and especially at locations, where there are no GNR aggregates visible under the microscope. Based on our observations, we conclude, that the GNRs are coagulating too rapidly to form films of the same quality on SiO_2 as on HOPG. Especially when the relative concentration is increasing during the evaporation process of the solvent, the bundling of GNRs into aggregates is facilitated. Heating the substrate introduces thermal energy which can keep individual GNRs apart and reduces the possible interaction time for GNRs to aggregate as the solvent evaporates faster. Either further functionalization of the GNRs themselves or of the substrate surface will be necessary to obtain a higher level of internal order in the GNR film.

Hence, despite the remarkable progress of the solution–mediated synthesis, processing of the resulting GNRs is still a major difficulty due to their limited solubility and tendency to aggregate in dispersions which also compromises the performance of the electronic devices based on them. As a result, only very limited modulation of the electrical resistance with a gate voltage has been observed in our own measurements (compare [145]) and in other experiments, reported in literature [194–196].

4.2.2 Transfer of GNRs from surfaces

The surface–assisted growth of GNRs by CVD presented in Sec. 4.1.2 as well as the CVD fabrication of single layer graphene described in Sec. 4.1.1 require a metallic substrate which catalyzes the reaction. Such metallic surfaces are not suitable for charge transport experiments due to their high conductivity which would shunt any attempted lateral charge transport through the graphene immediately. Thus, certain techniques have been developed to transfer GNR [82, 197] and graphene [160, 198–202] films to arbitrary substrates. The transfer can be conducted with or without a sacrificial polymer layer such as poly(methyl methacrylate) (PMMA). A PMMA layer provides additional mechanical stability and facilitates the transfer of intact films over a large area (see Fig. A.1 (Appendix A) and Ref. [82]). Without PMMA, however, contamination by non–dissolvable residues on the GNR film can be avoided, which can make electrically contacting graphene–based materials difficult [203]. In Fig. 4.4 we depict the transfer

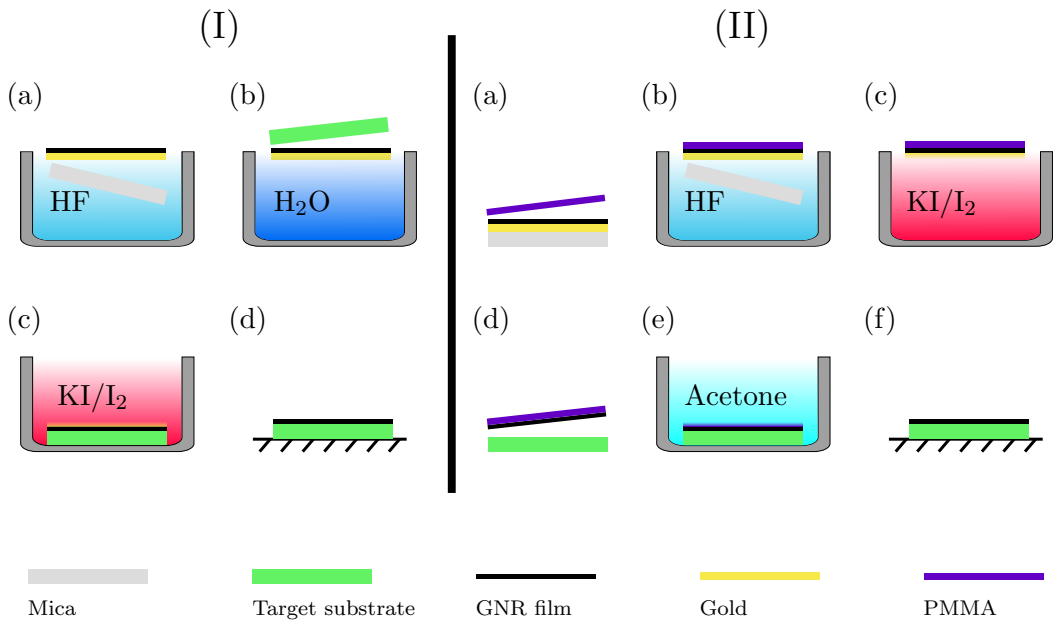

FIGURE 4.4: Schematic depiction of two transfer techniques for GNR films to arbitrary target substrates. Procedure (I) does not employ a sacrificial PMMA layer and avoids therefore PMMA residues on the transferred GNR film. Procedure (II) uses PMMA to enhance the mechanical robustness which leads to a lower density of ruptures in the transferred GNR film.

of GNRs grown on a gold/mica substrate to an arbitrary target substrate schematically in both versions, with and without PMMA, and in the following we describe them step by step.

(I) (a) Floating of the GNR/gold/mica stack on concentrated hydrofluoric acid (HF) for several hours in order to delaminate the GNR/gold film from the mica slab by dissolving the mica interfacial layer.

(b) Careful transfer of the GNR/gold film to a (deionized) water bath, which rinses the film and is a safe medium to collect it with the target substrate.

(c) Gold etching using a typical gold etchant such as a potassium iodide solution.

(d) GNR film successfully transferred to the desired target substrate.

(II) (a) Spin coating of a PMMA layer onto the GNR/gold/mica stack in order to provide additional mechanical robustness.

(b) Floating of the PMMA/GNR/gold/mica stack on concentrated HF for several hours in order to delaminate the PMMA/GNR/gold film from the mica slab.

(c) Gold etching using a typical gold etchant such as a potassium iodide solution.

(d) Transfer of the PMMA/GNR film to the target substrate. This step can take place either in a water bath, like in (I) or in a dry environment.

(e) Careful transfer of the PMMA/GNR/target substrate stack to an acetone bath, which dissolves the PMMA layer. After the removal of the PMMA a rinsing step using isopropanol can be introduced before one lets the GNR film dry (not shown).

(f) GNR film successfully transferred to the desired target substrate.

Our standard transfer of single layer (doped) graphene films grown by CVD on copper substrates is very similar to procedure (II) for the GNRs. The copper as catalytic metal can have a thickness in the range of 10^1–$10^2\,\mu$m and consequently it is stiff enough to be handled freestanding without the need for mica as a carrying substrate. Consequently, step (II.b) is not required. The only difference is then to use the appropriate etchant for the copper, such as iron nitrite or ammonium persulfate. Because of the described analogies, we do not detail the transfer of single layer graphene here and refer the reader to the literature, where the process is well documented (e.g. Refs. [198, 199] which describe exactly the transfer method employed by M. R. for the fabrication of samples in Sec. 6).

4.3 Device engineering for charge transport in bottom–up GNRs

In the following section, we detail the development of short channel electrodes and long channel electrodes and furthermore describe the general schemes of the GNR device fabrication. The classifications "long" and "short" refer to the separation L of the electrodes, which is larger than the average length of a GNR in the long channel case. The lengths of solution–processable GNRs range between 100 and 600 nm [174] while in the CVD case the average length is about 30 nm [184]. These electrodes are designed to probe charge transport in GNR networks, while short channel devices ultimately aim to inject current into single GNRs. In both cases, we inject and measure electrical current in a two–point configuration between a source and a drain electrode, through the GNRs

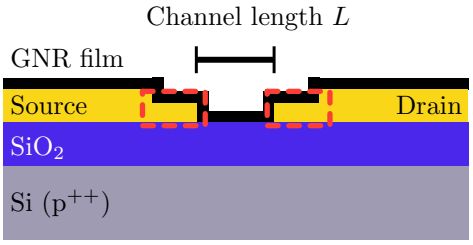

FIGURE 4.5: Schematic depiction of a GNR FET in cross–sectional view. The device current flows between the metallic (Au) source and drain electrodes through the GNR channel. In long channel devices L is larger than the average length of a GNR and in short channel devices vice versa. The GNR film covers the whole substrate surface. Nevertheless, since the films show generally large resistivities, we assume that electrical cross talk between devices and shunting through the GNR film is negligible. Therefore, we can determine GNR resistivities based on the device geometry. The areas enclosed in the red, dashed boxes mark the contact area, where charges are injected into the GNRs. The drawing is not to scale.

as channel medium. The substrate is a commercially available, degenerately doped silicon (Si) wafer, which is covered by a silicon dioxide (SiO_2) layer. The conductive Si can serve as a global back gate electrode and the SiO_2 forms an insulating back gate barrier. This structure allows for the application of an electric field and hence, offers the functionality of a field–effect transistor (FET). The thinner we choose the gate oxide, the more charge carriers can be generated per volt of applied gate voltage. However, the probability of an electrical breakdown of the barrier, which destroys the device, is also enhanced for thinner oxide layers. Therefore, we usually choose a thickness of approximatley 300 nm for the SiO_2 layer, allowing for the application of gate voltages on the order of 100 V while leakage currents remain negligble compared to typical currents through the GNRs. Figure 4.5 shows a schematic depiction of such a GNR FET. In this work, we choose gold (Au) as a material to realize source and drain electrodes. Gold is an inert noble metal with high conductivity, which forms good electrical contacts on graphene [204]. However, together with semiconducting materials such as GNRs, a metal can either form an Ohmic contact or a Schottky barrier, depending on their work function difference [105]. The work function of GNRs is not known and a systematic study of the metal–GNR junction as a function of the metal species is beyond the scope of this work. Hence, Au has been used as a starting point, while some tests have been performed using palladium (Pd) as a material for the nanojunction of short channel devices. Furthermore, as indicated by the high–quality GNR films on HOPG surfaces (see Sec. 4.2.1), graphene–based materials are promising to form high–quality interfaces

for Ohmic contacts. This motivates the electromigration study in Sec. 4.3.3 in TG discs, to form source–drain nanojunctions.

4.3.1 Short channel devices by lithography

Short channel devices are suitable to contact nanoscopic structures like individual GNRs or magnetic molecules. Consequently, a gap between source and drain must not be larger than a few nanometers for molecules to fit in, or tens of nanometers for the larger systems such as GNRs. We explore two possible fabrication approaches for such a nanojunction. Direct patterning by EBL and the formation of a nanogap by electromigration. We start with the description of the lithographically defined nanojunctions. Figure 4.6 is a flow chart of the process, which comprises the following steps:

1. Initial cleaning

   - Wafer pieces with a size of approximately $1 \times 1\,\mathrm{cm}^2$ are cleaned by immersing into acetone, isopropanol and distilled water for 1 min each. Afterwards, the substrates are blow dried by a nitrogen gun and further residual water is removed from the surface by annealing for 5 min on a hot plate at 130° C.

2. First EBL step

   - Spin coating of the copolymer methyl methacrylate and methacrylic acid in ethyl lactate (MMA(8.5)MAA EL6) onto the substrate using a prespin of 500 rpm for 2 s (acceleration $500\,\mathrm{rps}^2$) and a mainspin of 3000 rpm for 60 s (acceleration $3000\,\mathrm{rps}^2$). A baking step follows on the hot plate for 90 s at 180° C.
   - Spin coating of the resist PMMA 950K A4 onto the substrate using a prespin of 500 rpm for 1 s (acceleration $500\,\mathrm{rps}^2$) and a mainspin of 3000 rpm for 60 s (acceleration $3000\,\mathrm{rps}^2$). Baking on the hot plate for 90 s at 180° C.
   - Electron beam exposure with a dose of $170\,\mu\mathrm{C/cm}^2$ at an acceleration voltage of 10 kV and a beam current of approximately 2.9 nA. For large structures, such as contact pads and alignment markers, a coarse step size, e.g. 30 nm, is sufficient.

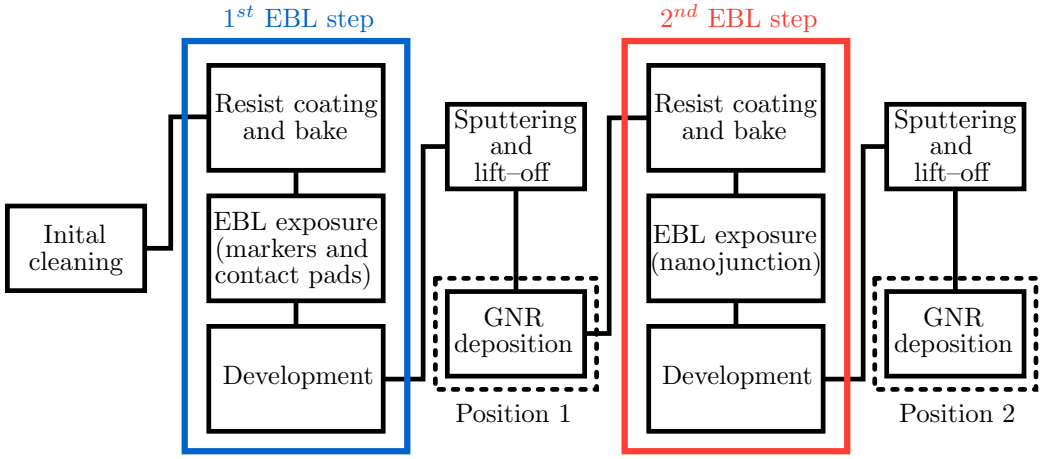

FIGURE 4.6: Flow chart representation of the production of lithographically defined short channel devices. The GNR deposition can take place at any of the two indicated positions in the process.

- Development of the structures by immersing the substrate fully into a mixture of methyl isobutyl ketone and isopropanol (1 : 3) for 30 s and subsequently into pure isopropanol for 30 s.

3. Sputtering and lift–off

   - The metalization is realized by sputter evaporation (see Sec. 3.5). To establish appropriate sputtering conditions a vacuum chamber is pumped for several hours down to a pressure of approximately 10^{-7} mbar and then filled with argon gas until a pressure of approximately 5×10^{-2} mbar is reached. For the contact pads and markers, we choose a film thickness of $t_{Au} \approx 50$ nm with a chromium seed layer (thickness $t_{Cr} \approx 5$ nm) to improve adhesion on the SiO_2 surface. For the lift–off the substrate is immersed into acetone for several hours. A pipette can be used to establish a gentle flow of the solvent over the surface accelerating the procedure.

4. First possibility to deposit GNRs.

5. Second EBL step

   - Spin coating of the resist PMMA 950K A4 onto the substrate using a prespin of 500 rpm for 2 s (acceleration 500 rps^2) and a mainspin of 4000 rpm for 60 s (acceleration 4000 rps^2). Baking on the hot plate for 90 s at 180° C.

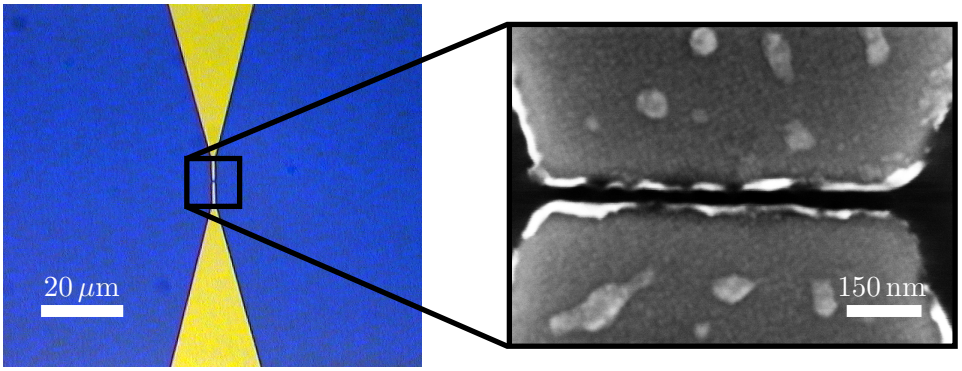

FIGURE 4.7: Optical micrograph of short channel device. The SiO_2 surface appears blue, while the metallic contacts are golden. Using scanning electron microscopy, we zoom into the center of the boxed area and magnify the nanojunction (black contrast in the inset) which has a gap of approximately 24 nm in this case.

- Electron beam exposure for the nanojunction with a dose of 360 μC/cm^2 at an acceleration voltage of 20 kV and a beam current of approximately 17 pA. The step size should be set as small as possible and we usually choose 2 nm.
- Development of the structures by immersing the substrate fully into a mixture of methyl isobutyl ketone and isopropanol (1 : 3) for 45 s and subsequently into pure isopropanol for 30 s.

6. Sputtering and lift–off
   - Metallization by sputtering a Cr/Au film ($\approx$ 5 nm/20 nm) under the same conditions as before. Here, we also tested Pd ($\approx$ 15 nm) for some chips as an alternative. Lift–off by immersing into acetone for several hours. A pipette can be used to establish a gentle flow of the solvent over the surface accelerating the procedure.
7. Second possibility to deposit GNRs.

In this process, the first EBL step makes use of a double–layer resist system, which allows for large metal film thicknesses ($\geq$ 100 nm). We choose a gold thickness such that conductivity is maximized while at the same time a large mismatch compared to the thickness of the second part of the electrodes, which forms the nanojunction, is avoided. The second EBL step comprises only a single resist layer which is necessary to reach the required resolution for feature sizes of a few nanometers. However, the reduced resist

layer thickness puts constraints on the metal film thickness. The EBL recipe has been under constant development throughout this work and here we detail its latest version for which gaps between source and drain electrode can be as small as 10 to 15 nm over a width of 700 nm.[4] Figure 4.7 shows an optical microscopy image of the electrodes with the nanojunction lying in the center of the boxed area. The junction, which has a length of approximately 24 nm, is shown on the right, magnified by SEM. Critical steps in this process are the exposure and development of the nanojunctions. Shortcuts between the electrodes can occur due to overexposure or due to overdevelopment. However, we have optimized the parameters to minimize the spread of widths and thus maximize the yield of nanojunctions. Furthermore, closed connections can be opened afterwards by electromigration, which can generate gaps with a length even below of what is achievable by pure lithography.

There are two possibilites to include the deposition of GNRs in this process. If the deposition takes place at position 1, between the two EBL steps, the GNRs are clamped between the substrate and the metallic part of the source and drain electrodes (top electrodes). However, in that case the GNRs are exposed to all chemicals involved in the second half of the process as well as to the electron beam and to highly energetic metal atoms during the sputtering. Resist residues and damage caused by the electron beam or the sputtered metal can lead to device degradation such as a reduced mobility, as known from graphene research [203, 205, 206]. GNR deposition at position 2 therefore yields cleaner devices, where GNRs are contacted from the bottom as schematically shown in Fig. 4.5. In Secs. 4.4 and 5 we show that this approach has led reliably to a larger number of functional devices in this work. Nevertheless, by further optimizing the process conditions, the results for top electrodes may be improved as well, for example, by encapsulating the GNRs before carrying out the fabrication step for such top electrodes.

[4] I thank S. K. for his major contribution to the EBL process development.

4.3.2 Short channel devices by electromigration in gold

The technique of electromigration (EM) offers an alternative approach to obtain nanojunctions suitable to act as source–drain electrodes for charge transport experiments using GNRs. In EM, atoms are moving due to high electrical current densities and the method has been used to study transport properties of atomic point contacts in non–magnetic [207, 208] and in magnetic materials [209–211]. Furthermore, it found application in molecular electronics [212–214] and molecular spintronics [215–217]. For the displacement of an ion from its position in a conductor, the ion must be subjected to a force, which is larger than the restoring force given by the chemical binding. This force arises due to the electric field inside the material $\mathbf{E}$ and is given by $\mathbf{F} = Z^* e \mathbf{E}$, where Z^* is the effective charge number of an ion in EM [218]. The displacement force consists of the direct action of the applied electric field and the momentum exchange between charge carriers (electrons) and the ion. Joule heating further promotes the displacement. Due to screening, the contribution of momentum exchange is typically much larger than the direct contribution in metals. Consequently the displacement is directed on average along the electron flow.

The experimental setup for EM, which has been used in this work, was built by Dr. R. R. and consists of a Keithley 2400 sourcemeter controlled by a National Instruments LabVIEW computer programme originally written in the group of Dr. R. H.–V. at the Karlsruhe Institute for Technology. Starting from a certain initial level V_0, the voltage is incrementally increased up to a target voltage V_T being applied to the device which is to be electromigrated. At this point, the software reduces the voltage automatically back to V_0. Such a loop is called "electromigration cycle". In order to avoid uncontrolled breaking of the device, certain protection limits have to be set. The break–off point, G_{BO} stops the process immediately, when a critical resistance is reached and furthermore, if the change of resistance is too large, the applied voltage is reduced, depending on a chosen power decrease parameter. A more detailed description of the working principle can be found in Ref. [219]. In Ref. [145] we describe the electromigration of gold electrodes for the purpose of GNR device fabrication. In Fig. 4.8 an example of an electromigrated nanojunction is shown. The process is more time consuming and less reliable than defining nanojunctions by lithography (see Sec. 4.3.1). However, smaller

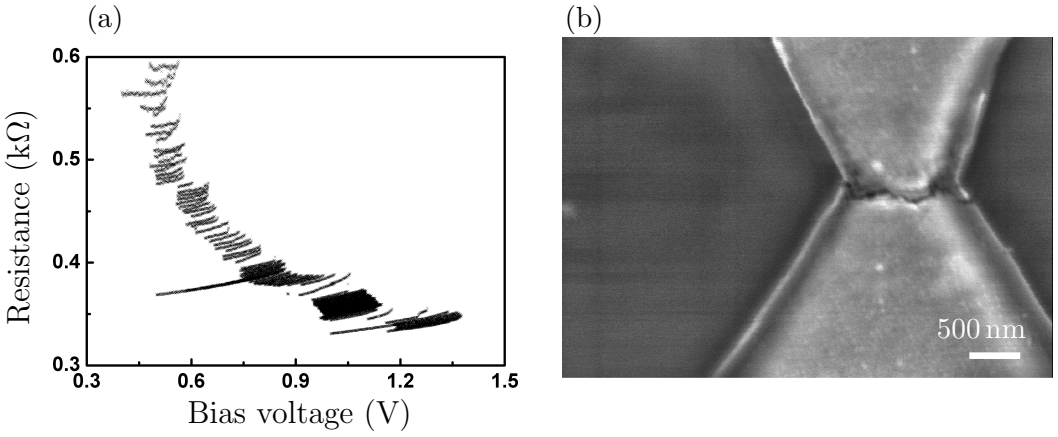

FIGURE 4.8: (a): Change of resistance as monitored during the electromigration process. (b): Resulting gap between two Au leads that can be bridged with GNRs. Image adapted from Ref. [145].

electrode spacings of less than 10 nm can be obtained and the process can be applied to carbon–based electrodes as well, as presented in the following section.

4.3.3 Short channel devices by electromigration in turbostratic graphene

The fabrication of high-quality electrical contacts to semiconductors is key to their use in electronic devices and scientific charge-transport experiments. In two–dimensional semiconductors, the reduced dimensionalty adds a further degree of complexity, since established ways to reduce the contact resistance are not applicable. Surface-cleaning by reactive ion etching as well as the formation of metal–semiconductor alloys in the interface area by high–temperature annealing modifies the two–dimensional materials usually to an untolerable extent or even completely destroys it. A way to reduce the contact resistance R_C for the electrical characterization of GNRs are graphene-based electrodes [220]. One possibility to obtain the required nanogap is by cutting a graphene film into two. Using EBL, such gaps can be created lithographically. However, ultimately small gaps are formed by employing electromigration. In this section, we present the electromigration of nanogaps in turbostratic graphene discs. The main results have been also published in Ref. [221].

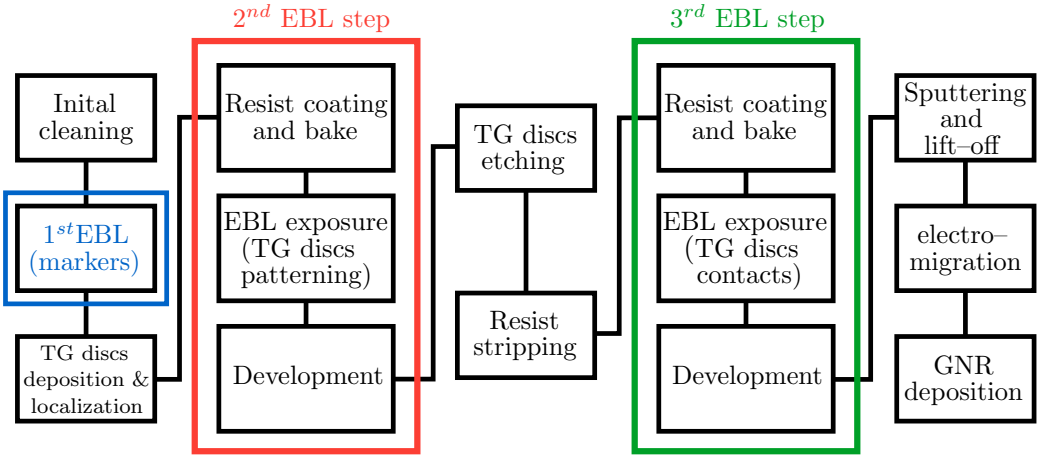

FIGURE 4.9: Flow chart representation of the production of electromigrated TG–based short channel devices.

4.3.3.1 Device production

For the production of GNR short channel devices based on electromigrated graphene electrodes, the device fabrication is more complex than the previously described scheme since TG discs have to be included and processed. Figure 4.9 shows the modified process, which requires three steps of EBL.

1. Initial cleaning
   - Standard cleaning procedure as described in Sec. 4.3.1.
2. First EBL step
   - Creation of arrays of alignment markers on the substrate surface, which allows for orientation on the surface of the substrate (see below). This step comprises spin coating, EBL exposure, development and sputtering and lift–off using the same parameters as the marker creation in Sec. 4.3.1.
3. TG discs deposition and localization
   - The TG dics are available in the form of powder. Using adhesive tape, the dics are collected and transferred to a Si/SiO_2 substrate by pushing it gently onto the surface. After rinsing with acetone and isopropanol, typically hundreds of discs are distributed randomly on the SiO_2 (typcial density of discs is

approximately $10^4\,\mathrm{mm}^{-2}$) where they can be located with the help of the marker arrays using optical microscope. Afterwards, these discs are inspected more thoroughly in an SEM, and we choose flat discs which are large in diameter and thus suitable for further processing.

4. Second EBL step and etching

   - Patterning of the discs in an hourglass–like shape as indicated in Fig. 4.10. The etching is done by exposing the dics to an reactive oxygen plasma for approximately 2 minutes. Such long etching time requires a very thick layer of PMMA ($\geq 800\,\mathrm{nm}$) to protect the remaining parts of the discs.

5. Resist stripping

   - The remaining resist is removed from the substrate surface by immersing the substrate into acetone for several hours.

6. Third EBL step and sputtering

   - Two–terminal contacts are defined on the TG dics (see Fig. 4.10) to enable charge injection. A double–layer resist with exposure parameters analogous to the recipe in Sec. 4.3.1 can be used. After the development and immediately before the metal evaporation, a short ($< 10\,\mathrm{s}$) plasma step removes resist residuals and ensures good ohmic contacts on the discs. Thicknesses of $10\,\mathrm{nm}/100\,\mathrm{nm}$ are used for the Cr/Au films.

7. Electromigration

   - Electromigration of TG discs to form nanogaps.

8. GNR deposition

The fabrication process of the devices has been developed in collaboration with the CNR Istituto Nanoscienze at the University of Modena (Italy) and the device production has been carried out in their facilities, while the EM experiments described in the following section have been performed at the University of Mainz.[5]

[5]I thank Dr. A. C. for the preparation of the samples and for his support during the experiments.

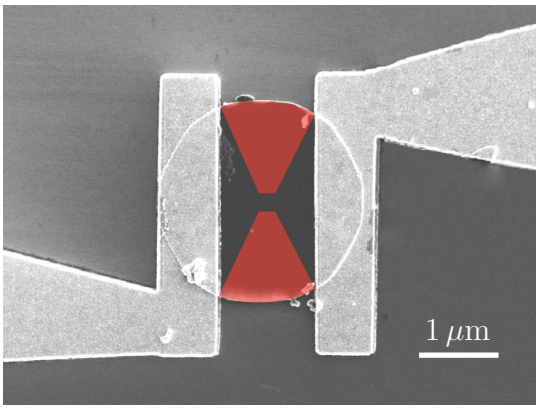

FIGURE 4.10: TG disc contacted with gold electrodes in a two–point configuration. In order to create a preferred location for the EM to take place, we pattern the discs into an hourglass–like shape. For this purpose, the areas marked in red in the image are etched away by reactive oxygen plasma treatment.

4.3.3.2 Formation of nanogaps in turbostratic graphene by electromigration

The EM experiments were performed under ambient conditions using the same setup as described in Sec. 4.3.2. The characterization of the nanogap was afterwards perfomed by recording I–V characteristics with a Keithley 6430 Sub–Femtoamp source–meter. To obtain a high current density in the interior of the discs, the hourglass–like shape was necessary in our experiments. The resulting constriction leads to large current densities at the narrowest spot of the disc and facilitates the EM process to start from there. In contrast, for unpatterned discs, the process starts usually at the metal–TG interfaces (see also [221]). We find that the EM process in the devices is well–controlled up to resistances of around 16 kΩ. At this point, the formation of a gap starts to set in and the resistance eventually jumps to higher values showing that one can obtain controlled contact dimensions. In Fig. 4.11 (b) we show how the resistance evolves over several EM cycles, where a cycle is defined as the increase of bias voltage until either a target voltage is reached or the resistance increases by a certain percentage and then starting again from a voltage level that corresponds to a defined fraction of dissipated power in the device. The resulting gap is located at the desired position close to the disc center rather than at the contacts as shown in Fig. 4.11 (a). In total, EM has been exemplified in four different discs and all of them showed a similar behavior. We verify the presence of a nanogap by comparing the I–V characteristics of such a device before (Fig. 4.11 (c)) and after (Fig. 4.11 (d)) electromigration. While the disc has initially a low electrical resistance of approximately 250 Ω, after EM, a bias voltage of 1 V results typically in a current of

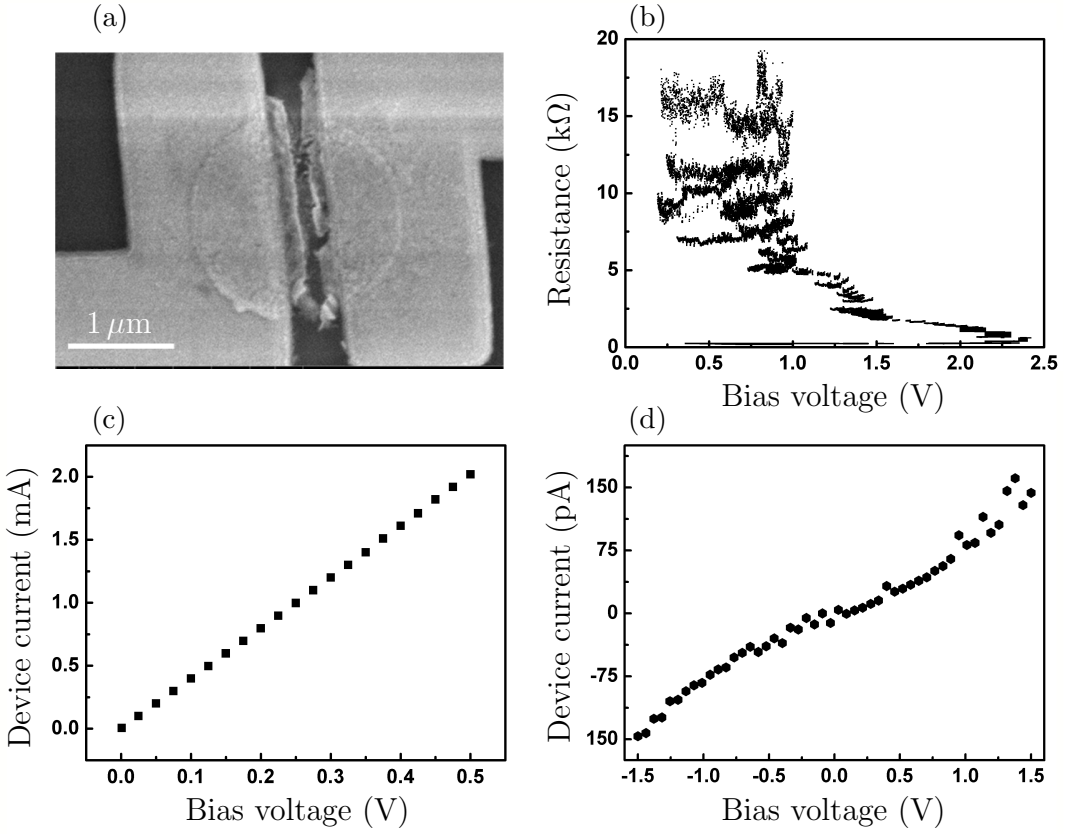

FIGURE 4.11: (a): Scanning electron microscope image of patterned disc after the EM process showing intact metal contacts while a breaking is visible in the disc. (b): EM cycle for a patterned TG disc (see text) showing the transition to high–ohmic (approximately 16 kΩ) behavior, which indicates the opening of a gap. (c): I–V characteristic of an intact TG device. The current follows Ohm's law with a low resistance of approximately 250 Ω. (d): I–V characteristic of electroburned TG device. A tunneling current is visible, demonstrating the presence of an open gap in the range of a few nanometers only.

approximately 80 pA, showing a typical tunneling current through the gap in the disc. The scheme of EM can be applied to other carbon–based systems as well. EM has been reported in graphene, and CNTs for example and in Ref. [221], we have tested EM also in mechanically exfoliated few–layer graphene and in turbostratic graphene grown on silicon carbide (SiC). This work suggests that the oxygen pressure is a key factor in the EM process but also other factors such as the type of graphene stacking, the morphology of the edges and the specific graphene/substrate system play an important role. Further studies will focus on tuning the partial oxygen pressure during the electromigration to determine the optimal working conditions for the different types of device.

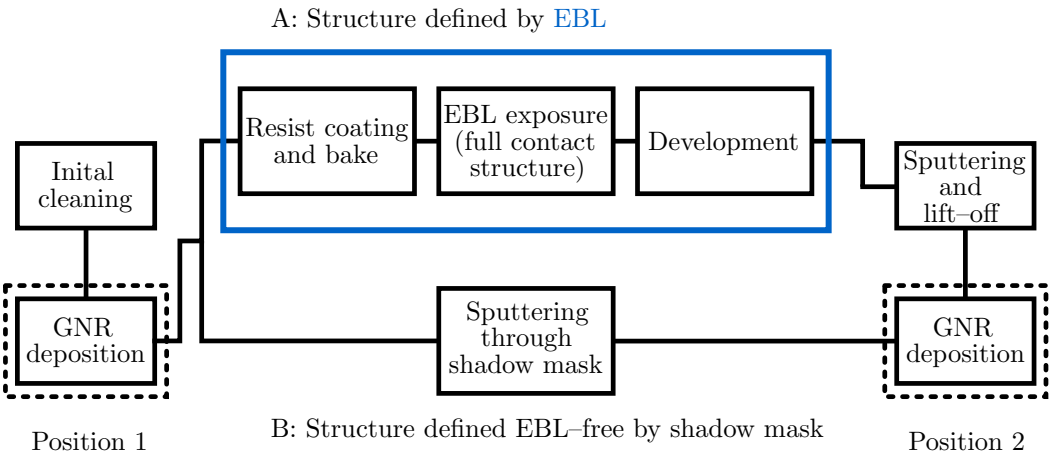

FIGURE 4.12: Flow chart representation of the production of long channel devices. The GNR deposition can take place at any of the two indicated positions in the process. The large feature sizes of the devices allow to choose between EBL–defined contacts or contacts defined EBL–free by a shadow mask.

4.3.4 Long channel devices

Complementary to the short channel devices discussed in the previous sections, we have fabricated long channel devices where the source electrode and the drain electrode are separated by a distance which is larger than the average length of a GNR and therefore probe charge transport through GNR networks. The fabrication process can be simplified to comprise only one step of EBL. Alternatively, the throughput can be furthermore enhanced by using a predefined mechanical shadow mask. In this approach, the desired pattern is carved into a material (e.g. a sheet of stainless steel) and these holes in the shadow mask determine where the sample surface gets metallized. In Fig. 4.12 these options are represented as two parallel branches in the flow chart labled A and B. We now describe the process steps in detail:

1. Initial cleaning
    - Standard cleaning procedure as described in Sec. 4.3.1.
2. First possibility to deposit GNRs.

3.A. Structure defined by EBL

- Spin coating of double–layer resist as described in 4.3.1.

- Electron beam exposure with a dose of 170 μC/cm^2 at an acceleration voltage of 10 kV. For the large contact pads a large beam current of approximately 2.9 nA can be chosen to reduce the writing time. The part of the electrodes which form the junction require a better accuracy which is reached with a lower current of approximately 0.7 nA.
- Development of the structures by immersing the substrate fully into a mixture of methyl isobutyl ketone and isopropanol (1 : 3) for 30 s and subsequently into pure isopropanol for 30 s.
- Metallization and lift–off under the same conditions as described in 4.3.1. Thicknesses of 5 nm/100 nm are used for the Cr/Au films.

3.B. EBL–free shadow mask sputter evaporation of Cr/Au films to form the electrodes.

4. Second possibility of GNR deposition.

The main advantages of the shadow mask approach are cleanliness and speed. Compared to EBL, the GNR samples are not exposed to chemicals and resist residues on the sample surface are avoided. Furthermore, the time consuming serial writing of all structures is replaced by the parallel evaporation of the metal for all structures on the chip. In this way a high throughput can be achieved. On the other hand, the structures cannot be varied easily and the minimal spacing of electrodes is limited to a few micrometers (5 μm was the smallest spacing for the shadow mask used in this work). EBL offers virtually unlimited flexibility to change and adapt structure geometries and a wider range of electrode spacings can be accessed. Similar to our discussion in the short channel case (see Sec. 4.3.1), there are two possibilites to include the deposition of GNRs in this process, marked with dashed boxes at position 1 or position 2, respectively. Figure 4.13 shows an example of a large channel device.

4.4 Statistical analysis of the device yield

We now assess the device yield of the presented fabrication approaches in a statistical manner in order to find the most promising way forward in the development of GNR devices. Throughout the process, we can identify quasi–deterministic steps as opposed

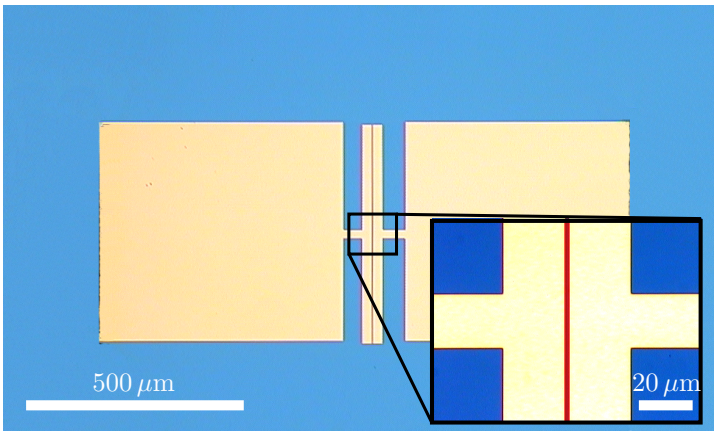

FIGURE 4.13: Optical micrograph of a large channel device. The SiO_2 surface appears blue, while the metallic contacts are golden. The inset shows a zoom into the center of the boxed area magnifying the channel region where charge current flows through GNR networks (marked in red). The junction has a separation of approximately 500 nm in this case.

to steps, which involve a certain stochasticity. As an example, lithography of large structures is typically a very well–controlled technique and has an excellent reproducibility of the result. In contrast, the integration of the GNRs adds a stochastic element to the device fabrication since the synthesis and deposition of GNRs is not controlled on the level of individual ribbons. Instead, we produce and process always a large number of GNRs in parallel and their position, orientation and individual structural integrity are random when they are deposited on the substrate surface, although the synthesis is perfect on the atomic level dictated by the underlying chemical reaction.

The fabrication of the source and the drain electrodes, which build the backbone for any GNR device, relies to a large extent on EBL. As already pointed out, there is basically no randomness in the lithography process as long as the feature sizes are large. Hence, a yield of up to 100 % satisfactory electrode structures can be obtained for the long channel devices. The situation changes for the short channel devices. On the scale of a few nanometers, which is the required separation of the electrode leads of the nanojunction, the EBL resolution becomes limited by the structure of the resist (e.g. size of polymer-chains or height corrugations across the film) and the interaction volume when electrons impinge. Hence, there is a certain spread in the obtained electrode gaps where some can even be connected. Based on more than 2000 attempted lithographies, we achieved a success rate of 70 % for devices with a spacing on the order of 15 to 20 nm. Connected devices, however, can be subjected to EM as described in Sec. 4.3.2. EM is much less

controlled than EBL and it is time consuming, where the EM of a single junction can take hours. Six out of ten tested devices (60 % success rate) yielded nanogaps on the order of a few nanometers, while the remaining four ended in an uncontrolled destruction of the device. Due to the small number of attempted EMs in TG, the success rate is not representative and is therefore not further discussed here. More detailed information about EM in TG and other graphene allotropes are given in Ref. [221].

The integration of GNRs as the channel medium of the FET devices described in the previous sections is one of the most delicate parts of the whole process. In Secs. 4.2.1 and 4.2.2 we presented the methods for GNR deposition on a surface, where Raman spectroscopy is a versatile tool to judge the quality of the resulting GNR films. Especially using the transfer techniques for CVD–grown GNRs, homogenous films can be obtained which show uniform Raman signals over an area of more than 100 mm^2 (see Fig. A.1 (Appendix A) and Ref. [82]). However, to measure the success of the device integration, we define two further figures of merit. In a first stage, the conductivity of the device should increase drastically compared to an open device, where only tunnel currents or leakage currents through the substrate might flow. If this is not the case, charges are not efficiently injected into the GNRs and the device is unusable. Secondly, due to the semiconducting nature of the GNRs, we expect to observe an electric field effect, i.e. the modulation of a source–drain current using a gate voltage. Finally, even after successful device patterning and GNR deposition, a device can still be compromised if a leakage current between gate and drain electrode is too large. For the following discussion of the yield of solution–processable and CVD–grown GNR devices, we subsume lithography failures and gate leakages under a total fabrication failure rate (or success rate, respectively) and contrast this number to the amount of devices with a measurable (and gate–tunable) conductivity. The ratio of these two rates indicates whether the device yield is limited by the former or the latter.

In the case of the solution–processable GNRs, around 1000 short channel devices were measured, where we transferred cove–edge GNRs onto previously fabricated junctions (according to the process diagram in Fig. 4.9 or position 2 of the process diagram in Fig. 4.6). After the application of GNRs, a fraction of approximately 0.5 % of all devices displayed resistances lower than the open nanojunction, however with a large spread ranging from Megaohms to Gigaohms and without significant tunability by a gate voltage. The device yield is clearly limited by the efficiency of charge injection

into the GNRs and not by fabrication failures. Secondly, roughly 1000 further short channel devices with CVD–grown (undoped) GNRNWs have been tested. In this case, approximately 1 % of all devices showed a measurable current with a similar distribution of resistances as for the cove–edge GNRs, where, again, the gate dependence was negligible. The device yield did not depend on the position of the GNR transfer in the process (transfer before or after defining contacts) and was furthermore also independent on Au or Pd as contacting material. Many reports attempting to fabricate FETs based on a single or only few GNRs discuss the issue of Schottky–like energy barriers at the metal/GNR interfaces, which inhibit the current flow and are thus one major limitation of charge injection [82, 197, 222]. Such barriers due to band mismatch between channel and contact metal degrade the transistor performance and lead to limited gate modulation. A second factor influencing the electric field effect is the ratio of channel length and gate barrier thickness. For a thick gate barrier oxide of 300 nm the metallic leads screen a large fraction of the electric field, if the channel length is in the range of only a few nanometers. In a situation where the device resistance is already limited by Schottky–barriers, no field effect can be observed. These results have also been detailed in Ref. [82], where furthermore a comparison is drawn between metallic short channel devices, metallic long channel devices[6] and graphene–based short channel devices[7].

Indeed, the situation is drastically different for long channel devices with (CVD–grown) GNRNWs. The process as depicted in Fig. 4.12 offers four different ways to produce a device as there are two possible positions for the GNR deposition and two methods to realize the metallic source–drain electrodes. We have tested two out of these four combinations. In the first one, the GNR deposition takes place at position 1, where we use the transfer technique without a supporting PMMA layer. The electrodes are sputtered through a metallic shadow mask. We choose this combination (1.B) because it allows to eliminate any contamination due to resist residues from the process. Secondly, we test a fabrication route where the GNR deposition takes place at position 2 and EBL is used to define contacts. This combination (2.A) allows only for a GNR transfer with a supporting PMMA layer, because otherwise the electrodes would be destroyed in the

[6]For this publication, the measurements on chGNR long channel devices have been carried out by the collaborating group of Prof. Dr. C. Z. at the University of Southern California, Los Angeles.

[7]For this publication, the measurements on chGNR graphene–based short channel devices have been carried out by the collaborating group of Prof. Dr. M. A. at the University of Modena. Since this group focuses on the graphene–based electrodes and our focus lies on devices with metallic electrodes, we do not detail the success statistics for graphene–based devices here. Very detailed information and statistical analyzes can be found in Refs. [196, 223].

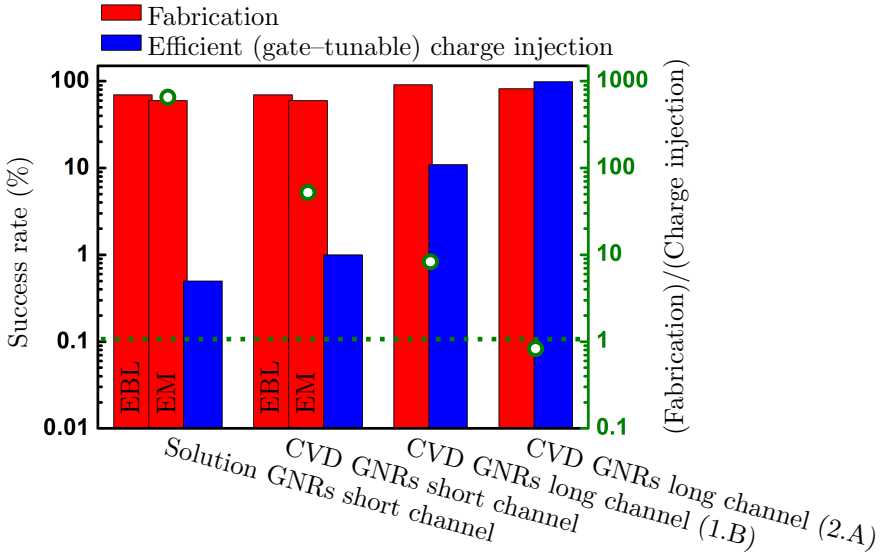

FIGURE 4.14: Overview of GNR long channel and short channel device production success (see main text). The histograms belong to the left axis (logarithmic scale) and show the success rates of contact fabrication (red) and successful charge injection (blue). Gate–tunable conductivities were only measured in long channel devices. The dots (green border and white filling) belong to the right axis (logarithmic scale) and show the ratio of fabrication success to charge injection success. Only for the fabrication route 2.A for CVD GNR long channel devices this ratio is < 1, indicating that the device yield is limited by the fabrication of devices and not anymore by ineffective charge injection (the dashed line marks the threshold). In the case of short channel devices the numerator of this ratio is calculated by taking the average of success rates for EBL and EM.

gold–etching step. Nevertheless, the risks of contamination are minimized by shifting the GNR deposition to position 2 in the process, which is after the EBL step. A total amount of 14 chips (240 devices) have been produced and Fig. 4.14 shows the device yield of these approaches in comparison with the yield for short channel devices. The fabrication success rate is particularly high, exceeding 90 %, for fabrication route 1.B as we would expect by eliminating all lithography steps. More importantly, the amount of devices that show measurable conductivities rises up to 10 %, which is an order of magnitude more than for the CVD GNR short channel devices. Moreover, the conductivities were gate–tunable throughout all devices. These charge injection success rates are high enough to extend the measurements to doped GNRNWs (pure N doping and N-S codoping), aGNRs 7 and aGNRs 9. In Tab. 4.1, we show an overview of all GNR long channel devices (including also fabrication 1.B). While the overall charge injection success rate stays approximately constant (11 % counting all devices), the measured conductivities depend on the type of GNR, already indicating that we test properties inherent to the

Structure	Chip	Layers	Success rate (total)	Fabrication	L (μm)
aGNR 5 (350)	1	1	10/16	2.A	$0.5-5$
aGNR 5 (350)	2	1	9/12	2.A	$0.5-5$
aGNR 5 (400)	3	1	13/16	2.A	≈ 1
aGNR 5 (400)	4	1	15/16	2.A	$0.5-5$
aGNR 5 (400)	5	1	15/16	2.A	$0.5-5$
aGNR 5 (600)	6	1	15/16	2.A	$0.5-5$
aGNR 7	1	1	3/20	1.B	$5-25$
aGNR 9	1	1	2/20	1.B	$5-25$
aGNR 9	2	2	8/16	2.A	≈ 2
aGNR 9	3	2	12/12	2.A	≈ 2
GNRNW (9,6),(2,15)	1	1	1/20	1.B	$5-25$
GNRNW (9,6),(2,15)	2	3	2/20	1.B	$5-25$
GNRNW N-N (9,6),(2,15)	1	1	1/20	1.B	$5-25$
GNRNW N-S (9,6),(2,15)	1	1	3/20	1.B	$5-25$

TABLE 4.1: Overview of GNR long channel devices for both fabrication routes. In total 240 devices on 14 chips have been produced. The first column indicates the tested GNR structure. The number in parantheses for aGNRs 5 denotes the annealing temperature (in °C) in the CVD process. The second column numbers the chips consecutively for each GNR structure. The third column shows how many GNR layers have been transferred onto the respective chip. The success rate in the fourth column is given by all operational devices on a chip over all available devices on a chip. Hence it includes fabrication and charge injection success. In the last column, the electrode separation lengths L are listed.

respective GNR using the presented approach (see Sec. 5 for the detailed device analysis). Finally, we tested fabrication 2.A beginning with the aGNR 9 structure which has shown the largest conductivities among the GNRs measured so far.[8] Using this route, $\geq 99\,\%$ of all devices show a gate–tunable conductivity, while the fabrication success stays satisfyingly high with $82\,\%$. Consequently, the fabrication/charge injection–ratio drops eventually below 1 to a value of 0.83, which means that an efficient charge injection is reached and a reliable fabrication method is found.[9] Using fabrication 2.A, furthermore aGNRs 5 have been investigated which show conductivities which are orders of magnitude larger than in the case of aGNRs 9 (see Sec. 5).

[8]Only for aGNR 5, we measure larger conductivities. However this structure has been tested only after the fabrication route 2.A has been established.

[9]Note that the term "charge injection efficiency" bears a certain ambiguity. For the current discussion, we simply mean the existence of a gate–tunable conductivity, regardless whether the contact is Ohmic or Schottky–like. A detailed discussion about the contacts is subject of the following chapter.

4.5 Conclusion and outlook

To achieve the vision of nano– or molecular electronics, which offer novel functionalities, several technological challenges need to be overcome. In particular the question how to embed nano–scale objects such as a graphene nanoribbons in electronic circuits in a reliable way suitable for the mass production of devices needs to be solved. In this chapter we presented the methods and techniques to synthesize different GNRs and integrate them in short channel and long channel field effect transistor test structures.[10] There are fundamentally two different approaches to obtain atomically perfect GNRs, which are Diels–Alder polymerization in solution and metal–catalyzed CVD. For their device integration, the GNRs have to be transferred to a substrate with an insulating surface (e.g. SiO_2). We showed that the formation of thin solution–processable GNR films is limited by their tendency to agglomerate (even already in a liquid medium). This leads to coarse grained dispersions and the risk of GNR bundle formation instead of a homogenous thin film on a SiO_2 surface. A satisfying result has been obtained using a heated target substrate and optimized deposition conditions. A promising path for the improvement of the GNR dispersibility is side–chain engineering [174]. On the other hand, the optimization of device integration can be tackled in two ways. Firstly, graphitic electrodes can be used, where π-π interactions facilitate the alignment of GNRs. Secondly, the homogeneity of thin films can be improved by functionlization of the GNRs themselves and of the substrate surface. Together with optimized deposition techniques of solution–processable GNRs as discussed in Sec. 4.2.1, further advances will become possible. Besides the discussed techniques, also alternatives to deposit GNRs should be systematically investigated, as for example the electrospray method [196] which has not been considered in this work. Furthermore, in the case of CVD–grown GNRs, a thin film is naturally formed during their synthesis. This film can be transferred to a target surface which offers a straight–forward way for device integration. By engineering this process, we have found a reliable way to fabricate long channel FET devices with a device yield approaching 100 %. This result finally enables the systematic study of the electronic properties in graphene nanostructures as a function of their width, edge structure and functionalization (e.g. heteroatomic doping).

[10] The synthesis was developed in the Max Planck Institute for Polymer Research while the device engineering is an integral part of this work.

Chapter 5

Charge transport in networks of bottom–up graphene nanoribbons

Graphene nanoribbons, synthesized bottom–up by chemical methods, are the ideal test systems for a variety of theoretical predictions and expectations concerning the electronic and magnetic properties of such ultra–narrow and atomically perfect carbon structures [5–7]. Experimental work so far has been largely focussed on spectroscopic techniques [79, 169, 180], while lateral charge transport remains a challenge. Although first short–channel device prototypes show promising performance [195, 197, 222], a thorough investigation of the underlying charge transport mechanism is so far missing. Due to the difficulties in fabricating single–ribbon devices (Sec. 4, Refs. [197, 222]) many simple but important experiments are impeded, e.g. testing the channel length dependence of the charge transport, or the extraction of the Schottky–barrier heights, when large energy barriers are claimed to be the dominant origin of the observed current–voltage signatures [197, 222]. With the reliable device fabrication of long channel devices being established as presented in Sec. 4.3.4, these fundamental tests become possible for the first time and their results are presented in this chapter. Herein, the role of contacts is clarified by a transmission line method, where we find Ohmic contacts which do not limit the charge injection in our devices in contrast to the Schottky–barrier dominated contacts in previouse studies [197, 222]. As the most important result, we demonstrate a universal scaling of the channel current over a wide range of bias voltages and temperatures, showing that charge hopping is the dominant transport mechanism, which sets limits to the conductivity and mobility in devices where the channel is comprised of more

than one single ribbon. In addition, we find an intriguing positive magnetoresistance in aGNR 5, which is absent in aGNR 9 and is in contrast to previous experimental work that shows negative magnetoresistance in top–down fabricated GNRs [224].

5.1 Experimental details

All GNR films discussed in the following have been synthesized following the CVD method as detailed in Sec. 4.1.2. While the general procedure was identical for the growth of all films, the choice of the precursor molecule yielded different types of GNRs. The transfer from the Mica/Au substrate to a wafer of highly doped Si with a $t_{\mathrm{Ox}} = 300\,\mathrm{nm}$ thick SiO_2 layer was carried out according to Sec. 4.2.2 and after the chip fabrication was complete, we performed Raman spectroscopy on the films in order to confirm the structural integrity and rule out any severe alterations of the GNRs due to the transfer.[1] In Fig. 5.1 we present representative Raman spectra taken on films of aGNR 9 and of aGNR 5 (see Fig. B.1 in Appendix B for Raman spectra of all other GNR species listed in Tab. 4.1). All measurements were performed with a Bruker RFS 100/S Raman spectrometer using a laser beam with an excitation wavelength of 532 nm.

Comparing these spectra with literature reports [82, 184, 185], we find an excellent agreement for all GNR species confirming that the GNRs are still intact after the transfer. The width of the GNRs which are composing the films can be identfied with the help of the RBM in the Raman signature (compare Sec. 3.1). For aGNR 9, we find the RBM peak at approximately $311\,\mathrm{cm}^{-1}$. In the Raman spectrum of the aGNR 5 film, we find two RBM lines, one at approximately $533\,\mathrm{cm}^{-1}$ and the other at approximately $283\,\mathrm{cm}^{-1}$. While the former is associated to GNRs with 5 carbon atoms across the ribbon, the latter indicates the presence of GNRs that are twice as wide (10 carbon atoms). We attribute the occurrence of this peak to a small fraction of aGNR 10 contained in the film, which are produced by a lateral fusion process of two aGNR 5 units. Such fusion depends on the annealing temperature and at the 400 °C only a small number of GNRs fuse together [185], such that we can neglect their contribution to any charge transport experiment in the following sections. At room temperature, these charge transport experiments have been performed using the electrical characterization setup in a nitrogen glove box described in Sec. 3.2.1, while the variable temperature measurements

[1] I thank Dr. Z. C. for the growth of the GNR films and for performing Raman spectroscopy on them.

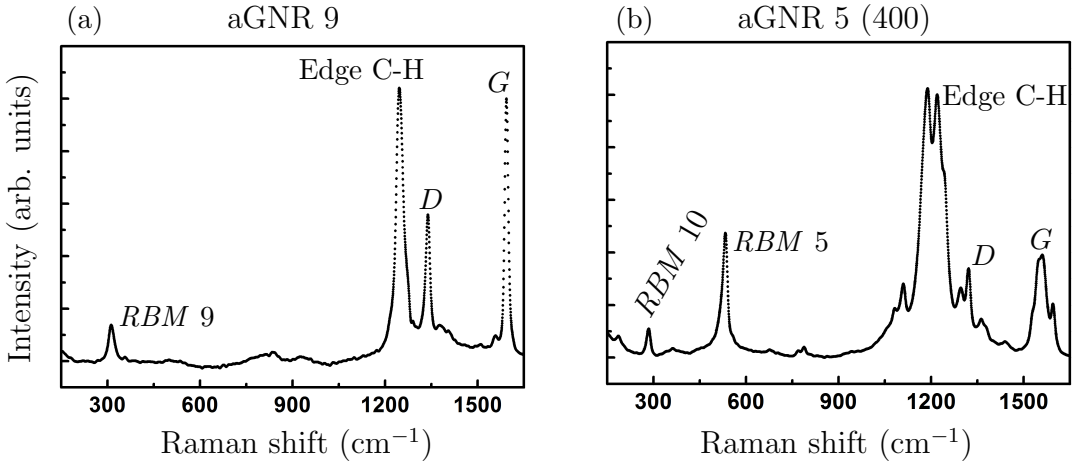

FIGURE 5.1: Raman spectrum of an aGNR 9 film (a) and of an aGNR 5 film (b), both on a Si/SiO_2 surface. The spectra exhibit strong D (at approximately $1340\,cm^{-1}$) and G (between $1565\,cm^{-1}$ and $1595\,cm^{-1}$) peaks at the typcial positions of crystalline sp^2 carbons. The peak at approximately $1220\,cm^{-1}$ indicates the presence of carbon–hydrogen (C–H) bonds which are expected to be located along the periphery of all ribbons. The low–energy lines can be attributed to the width–dependent RBMs (see main text and Refs. [184, 185]).

have been carried out in a helium bath cryostat, where the current guarding technique was necessary to avoid spurious leakage currents in the electrical wiring (compare Secs. 3.2.2 and 3.2.3). We focus here especially on those devices in Tab. 4.1, which have been fabricated following route 2.A, since in this case, the device yield allowed us to test a large enough number of devices to enable statistical analysis, demonstrating that the results are robust and reproducible. However, based on qualitative similarities between the electrical characterization at room temperature (see Sec. B.2), we expect that the results apply also to all other GNRs.

5.2 Electrical characterization of graphene nanoribbon–network field effect transistors

5.2.1 Current–voltage characteristics

We biased all devices listed in Tab. 4.1 with voltage sweeps between source and drain electrodes across the GNR network channel and tested for modulation of the resulting current by applying a voltage to the gate electrode.[2] The drain voltage was swept from 100 mV to 20 V and back while the source electrode was grounded and the current at the drain terminal I_D was measured. In three–terminal devices as investigated in this study, parasitic leakage currents through the gate oxide can occur. Therefore, the current at the drain terminal I_D is composed of the current through the channel I_{DS} and of the current flowing between the source electrode and the gate electrode I_{DG}:

$$I_D = I_{DS} + I_{DG} \,. \tag{5.1}$$

If I_{DG} is small enough, the measured current at the source terminal is equal to the channel current $I_D \approx I_{DS}$. In order to quantify the impact of leakage currents, we measure the current at the gate electrode $I_G = I_{DG} + I_{SG}$, where I_{SG} is the current flowing between the source electrode and the gate electrode. At small voltages V_G applied to the gate electrode, the gate current is small compared to the drain current and its dependence on V_D is negligible and only at large V_G, the leakage starts to affect I_D (see B.3). However, since I_G does not change with V_D, we correct for its influence by simply subtracting I_G from the curves, such that $\lim_{V_D \to 0} I = 0$. For aGNR 5 and aGNR 9 devices, a representative set of the resulting I–V curves at six different gate voltages is presented in Fig. 5.2 on a double logarithmic scale (see B.2 for the other GNR species). At low voltages, the transport is Ohmic and linear in bias while at larger voltages the current grows superlinear with V_D, following a power law $I_{DS} \propto V_D^{\beta}$. Since the transport is symmetric in bias (compare B.3), we only show the measurements for positive bias voltages here.

[2] All measurements in this section are done at room temperature in a nitrogen glove box unless stated otherwise.

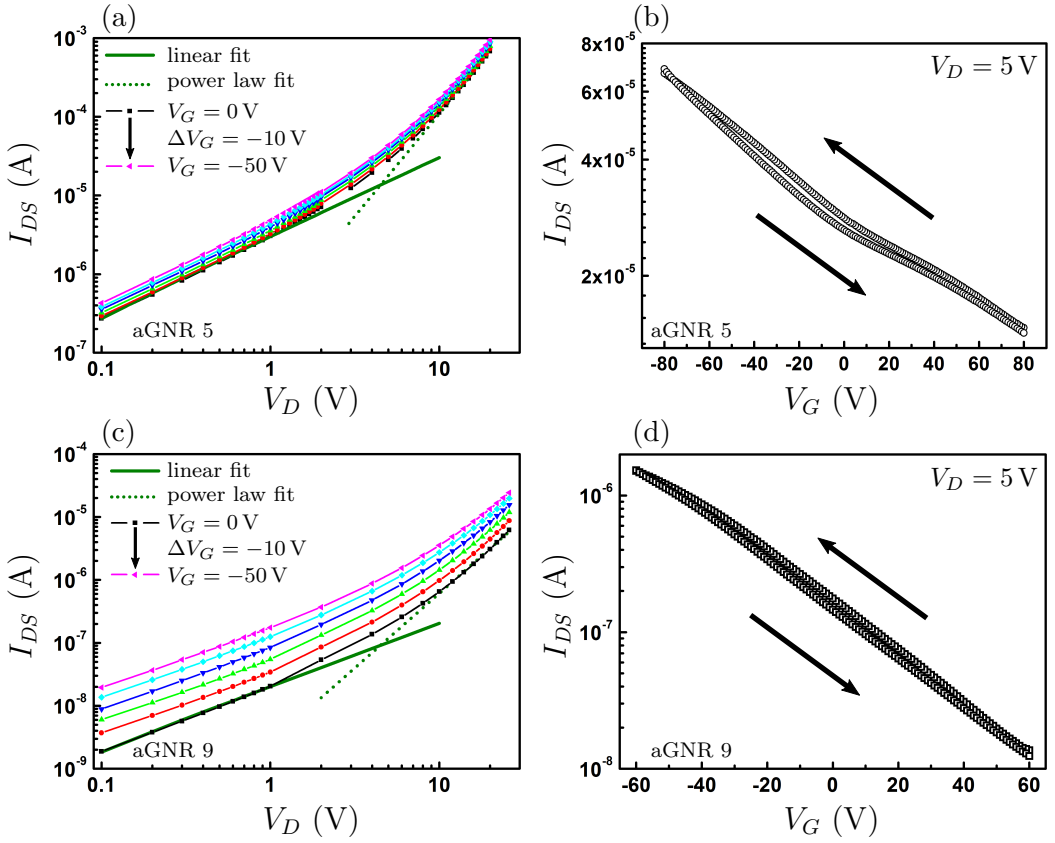

FIGURE 5.2: I–V and transfer curves of aGNR 5 ((a), (b)) and aGNR 9 ((c), (d)) gated across 300 nm SiO_2. The channel current I_{DS} responds in an Ohmic–like fashion at low V_D ($V_D \leq 1\,V$). Solid dark green lines are linear fits to the $V_G = 0\,V$ data in (a) and (c). At larger bias voltages ($V_D \geq 10\,V$), a power law $I_{DS} \propto V^{\beta}$ describes the data and dotted dark green lines are the fits to the $V_G = 0\,V$ data, where we obtain $\beta = 2.6$ for the aGNR 5 device and $\beta = 2.4$ for the aGNR 9 device. The arrows in (b) and (d) indicate the sweep direction. Lines are guides for the eye.

The gate modulation of the current leaves these functional dependencies unchanged, while decreasing V_G increases the conductance of the system, indicating a hole–dominated (p–type) transport. To analyze the current modulation further, we take so–called transfer curves, where we fix V_D and sweep the gate voltage (typically, we limit the gate voltage to $V_{G,max} = \pm 80\,V$ in order to keep the gate leakage acceptably small). We show two representative transfer curves in Fig. 5.2 (b) (aGNR 5) and (d) (aGNR 9). A small correction to the transfer curves has been applied analogous to the correction for the I–V curves. In the aGNR 9 case, the transfer curve appears linear on a logarithmic scale over the whole range of gate voltages, while there are two slopes in the curve of the aGNR 5 devices with a transition around $V_G \approx 0\,V$. At small drain bias, one expects two different regimes in the transfer curve of conventional FET devices (e.g. n–type in metal–oxide–semiconductor FETs (MOSFETs)) [225]: Below a certain threshold voltage

$V_G < V_T$, the current rises exponentially and the transistor operates in the subthreshold regime. Above threshold, the current eventually rises linearly with increasing V_G. Using this threshold voltage we find in ideal transistors that the gate voltage has the full control over I_{DS} and the influence of the drain voltage becomes insignificant, when the condition $V_{DS} \geq (V_G - V_T)$ is met (current saturation) [225]. As visible from Fig. 5.2 (b) and (d), the saturation regime is not reached in our tested devices and the devices always operate subthreshold. Therefore, an important figure of merit for transistors, the $I_{\mathrm{on}}/I_{\mathrm{off}}$–ratio is not well–defined in this case. The $I_{\mathrm{on}}/I_{\mathrm{off}}$–ratio compares the current in the saturation regime (on–state) with the current in the subthreshold regime (off–state). In order to still be able to quantify the impact of the gate voltage, we therefore use two alternative figures. First, we define a current modulation ratio $IM_{V_{G,1},V_{G,2}} = I(V_{G,1})/I(V_{G,2})$, where we compute the ratio of channel current at specific gate voltages and second, we determine the exponential slope in the range of negative gate voltages. The latter is also known as subthreshold slope and its inverse is the subthreshold swing [225]

$$SS = \left(\frac{\partial \log_{10} I_{DS}}{\partial V_G} \right)^{-1} . \tag{5.2}$$

The subthreshold swing indicates how much gate voltage is required to change the channel current by a factor ten (one decade $\equiv 1\,\mathrm{dec}$). Furthermore, the transfer curves allow for the determination of a field–effect mobility μ_{FE} according to Ref. [226] as

$$\mu_{\mathrm{FE}} = \frac{g}{V_D\, C_{\mathrm{Ox}}} \frac{L}{W} . \tag{5.3}$$

In Eq. 5.3, $g = \frac{\partial I_{SD}}{\partial V_G}$ is the transconductance, L is the channel length, W is the channel width and $C_{\mathrm{Ox}} = \epsilon\, \epsilon_0 / t_{\mathrm{Ox}} \approx 1.15 \times 10^{-4}\,\mathrm{F/m^2}$ is the geometrical capacitance density assuming that the channel and the gate electrode form a parallel plate capacitor.[3] We use these definitions to determine $IM_{-80\mathrm{V},+80\mathrm{V}} \approx 5$ ($IM_{-60\mathrm{V},+60\mathrm{V}} \approx 120$), $SS \approx 199\,\mathrm{V/dec}$ ($SS \approx 56\,\mathrm{V/dec}$) and $\mu_{\mathrm{FE}} \approx 2 \times 10^{-2}\,\mathrm{cm^2\,V^{-1}\,s^{-1}}$ ($\mu_{\mathrm{FE}} \approx 1 \times 10^{-3}\,\mathrm{cm^2\,V^{-1}\,s^{-1}}$) for the aGNR 5 (aGNR 9) device shown in Fig. 5.2 (see Sec. B.4 for more details on the determination of μ_{FE}). We note that we ascertain the channel current to be always much larger than the gate leakage current in order to avoid artifacts such as transient off–currents that dip below the gate current and lead to inflated current modulation ratios.

[3] Here, we use $t_{\mathrm{Ox}} = 300\,\mathrm{nm}$ as mentioned above, the relative permittivity of SiO_2 $\epsilon = 3.9$ and the vacuum permittivity $\epsilon_0 \approx 8.854\,\mathrm{F/m}$.

While for aGNR 5 there is no literature available on lateral charge transport experiments, the current modulation for aGNR 9 is comparable to what has been observed previously [222], although our study does not aim to maximize the device performance. From a device engineering point of view, there are alternatives to the 300 nm thick SiO_2 gate barrier to drastically improve the electrostatic coupling between the gate electrode and the GNR channel by increasing the electric field at the contacts and improve the transmission through the barriers. Such alternatives can be found in ionic liquids (e.g. N, N-diethyl-N-(2-methoxyethyl)-N-methylammonium bis(trifluoromethylsulfonyl-imide)) or a gate barrier material with a large relative permittivity (e.g. Hafnium dioxide HfO_2). In Ref. [222], Llinas et al. have shown for aGNR 9 that the gate modulation can be increased from a level comparable to what we find up to a current modulation ratio of 10^5. The hysteresis that is present in the transfer curves (Fig. 5.2 (b) and (d)) is also comparable to previous studies in GNR– or CNT–based devices. Such hysteresis often arises from charge transfer between carbon materials and charge traps at the silicon dioxide/ambient interface [227, 228]. While a detailed analysis is beyond the scope of the present work, it can be found in Ref. [229] and in the following we use averaged curves of back and forward sweeps for any further analysis. Hysteresis in the I–V curves (Fig. 5.2 (a) and (c)) was negligible throughout all measurements.

The optimization of the fabrication process (described in the previous section, Sec. 4) eventually enabled us to produce a larger number of functional devices, in total 97. Therefore, a comparison of all devices, which have been produced following the fabrication route 2.A, is possible and we can corroborate the reproducibility and uniformity of the GNR films as seen by Raman spectroscopy (see Fig. A.1). The statistical analysis of the electrical characterization furthermore allows us to discriminate between charge transport signatures which appear systematically and hence are likely to be significant, and those signatures which occur randomly, for example in the case of local inhomogeneities in the GNR film, resulting in a degraded device performance. In Tab. 5.1, we present the statistics for chip 3 of the aGNR 5 series together with the statistics of chip 3 of the aGNR 9 series.[4]

[4]I thank A. T. for his support with the room temperature measurements, increasing the statistical sample and rendering the statistics more robust.

GNR type	ρ (Ω)	β	μ_{FE} ($\mathrm{cm^2\,V^{-1}\,s^{-1}}$)	$IM_{-50\mathrm{V},+50\mathrm{V}}$	SS (V/dec)
aGNR 9	2.0×10^{11}	2.7	4×10^{-4}	164	42
	2.3×10^{11}	2.7	4×10^{-4}	153	44
	(1.2×10^{11})	(0.1)	(2×10^{-4})	(51)	(5)
aGNR 5	8.3×10^{7}	2.7	0.03	2.6	154
	8.0×10^{7}	2.7	0.03	2.5	189
	(4.8×10^{7})	(0.2)	(0.01)	(0.5)	(82)

TABLE 5.1: Overview of median (first row), mean value (second row) and standard deviation (third row in parantheses) for five important charge transport parameters. Resistivity, mobility and the current modulation parameters are determined at a drain bias of $V_D = 5\,\mathrm{V}$ and at zero gate voltage. The statistics are based on seven devices for aGNR 9, and thirteen devices for aGNR 5.

We summarize median, mean value and standard deviation of the following five transport parameters: The resistivity ρ at a low bias voltages and zero gate voltage, the exponential slope β of the I–V-curve at high bias voltages and zero gate voltage, the field effect mobility μ, the current modulation ratio $IM_{-55\mathrm{V},+55\mathrm{V}}$ and the subthreshold swing SS.

The median is a statistical parameter which is exteremly robust against outliers in a data set and hence, a large difference between arithmetical mean and median indicates the presence of such outliers. In this case, the median is better suited to represent a typical value of the data set. By comparing mean value and median, and weighing all single measurements against the third quartile, we were able to identify three devices on the aGNR 9 chip, where the charge transport parameters differ strongly from the rest of the statistical sample (e.g. we find a much higher resistance) and which we therefore regard as outliers. On the aGNR 5 chip such outliers were not present. The (outlier–corrected) mean values and medians (listed in Tab. 5.1) are then equal within the standard deviation. Especially, the small standard deviation of β with only 5 % (6 %) for aGNR 9 (aGNR 5) is remarkable and underlines the high network uniformity and reproducibility. Since β is directly connected with the underlying charge transport mechanism (as we show in Sec. 5.3), this small spread of values corroborates the assumption that the charge transport mechanism is equal throughout all tested GNR network devices. Larger standard deviations, especially occurring for the resistance and in the field–effect mobility can arise easily as these two parameters are strongly influenced by the doping level (i.e. the number of accessible charge carriers for transport, see Sec. 5.2.2). Nevertheless, we still find standard deviations $\lesssim 20\,\%$ in most cases (compare also statistics in Sec. B.5), indicating the high quality of the GNR films.

Based on this analysis, we find a significant difference in the resistance, the mobility and the current modulation between aGNR 9 and aGNR 5 devices, where we calculate the resistivity as $\rho = (V_D/I_{DS})\,(\tilde{n}\,W/L)$, with $\tilde{n}$, the number of transferred layers, W (L), the width (length) of the device channel and $V_D = 5\,\mathrm{V}$. On the basis of Raman spectroscopy and reported scanning tunneling microsopy images [184, 185], we can assume the aGNR 5 and aGNR 9 networks to be structurally comparable, i.e. the GNRs have on average the same length and are similarly distributed. Furthermore, the extrinsic charge carrier density provided by dopants will be similar, since the fabrication process and substrates are equal. Then, the most relevant expected difference between them is the electronic structure (compare Sec. 2.2.3.1), e.g. the band gap. Density functional theory predicts a difference of 400 meV between the band gaps Δ of aGNR 9 ($\Delta \approx 2.1\,\mathrm{eV}$) and aGNR 5 ($\Delta \approx 1.7\,\mathrm{eV}$) [6]. Using the conventional exponential dependence of thermally activated (intrinsic) charge carriers

$$n \propto \exp\left(-\frac{\Delta}{2\,k_\mathrm{B}\,T}\right), \tag{5.4}$$

this difference translates to a factor of 10^3 at room temperature between the intrinsic charge carrier densities of the two GNR species (k_B is the Boltzmann constant). A large difference in the charge carrier density is experimentally supported by the gate voltage–induced current modulation, for which we can calculate the induced charge carrier density as

$$n_\mathrm{ind} = \frac{C_\mathrm{Ox}\,V_G}{e}, \tag{5.5}$$

where e is the elementary charge. At $V_G = 50\,\mathrm{V}$, Eq. 5.5 yields $n_\mathrm{ind} \approx 3.6 \times 10^{12}\,\mathrm{cm}^{-2}$ and in the aGNR 9 devices, since the current modulation is large, this gate voltage–induced charge carrier density must be dominant over the background charge carrier density.[5] On the other hand, $IM_{-50\mathrm{V},+50\mathrm{V}}$ for aGNR 5 devices is much smaller and therefore, the induced carrier density can only impose a small change relative to the total charge carrier density. In Sec. B.6, we directly estimate the total charge carrier density using the linear part of the I–V curve and Ohm's law, corroborating this reasoning. Nevertheless, at room temperature (300 K), we still have $1.7\,\mathrm{eV} \gg k_B\,T \approx 26\,\mathrm{meV}$, and hence, it appears unintuitive that a charge carrier density in the order of $10^{12}\,\mathrm{cm}^{-2}$ is provided intrinsically, as even the zero–band gap material graphene has not more than $10^{11}\,\mathrm{cm}^{-2}$ intrinsic carriers at room temperature [230]. To explain our observations, two

[5] This statement is only true, if the contact resistance plays no role. See Sec. 5.2.3 for the influence of the contacts.

different reasons may hold. Firstly, the theoretical band gap could be an overestimation and in aGNR 5 devices we have indeed a large intrinsic charge carrier density at room temperature. As a matter of fact, controversial experimental and theoretical results can be found in literature concerning the band gap, especially for aGNR 5 [71, 178]. Secondly, the activation energy of impurities to provide additional charge carriers could be lower for the aGNR 5 devices than for the aGNR 9 devices. Possibly, the interaction of aGNR 5 and aGNR 9 systems with extrinsic dopants is different or there are different extrinsic dopants present in the aGNR 5 and aGNR 9 devices. However, a significantly different reactivity is not expected, since the two systems have the identical chemical composition, edge morphology and edge termination. Furthermore, fabrication, processing and environment have been the same for all chips and devices, leaving the reason for possible large differences in the composition of extrinsic dopants unclear. Besides the charge carrier density, there are further large disparities between the resistivity and mobilities in the different GNRs, with factors of $\geq 10^3$ for the resistivity and $\approx 10^2$ for the mobility. To gain a deeper understanding here, we require knowledge about the charge transport mechanism in the investigated devices. The latter will be elucidated in Sec. 5.3 and therefore, the discussion will be continued there.

5.2.2 Doping effect of ambient gases

In the last section, we briefly mentioned the impact of unintentional doping by adatoms stemming from the environmental atmosphere, which is well–known to be significant in carbon–based devices [203]. To test systematically the influence of changes in the environment, we exposed chip 2 of the aGNR 9 series to air on purpose. In Fig. 5.3 (a) we present a time series of resistance measurements ($V_D = 5\,\mathrm{V}$) for one device on this chip. The large changes of the resistance, especially directly after the exposure on day 15 and day 32 can be unambiguously attributed to the storage of the chip in either nitrogen or air, as these changes appeared systematically and at the same time for all tested devices on the chip (see Fig. B.6 for a box plot that summarizes the measurement results of several devices). The chip was kept in the glove box already for 7 weeks before we started measurements on it (day 0) and after further 14 days, the resistance remained nearly unchanged. On day 15, we removed the chip for 10 minutes from the glove box and exposed it to the environmental air in the laboratory. We then put it back into the glove box and remeasure immediately, where we observe a drastically

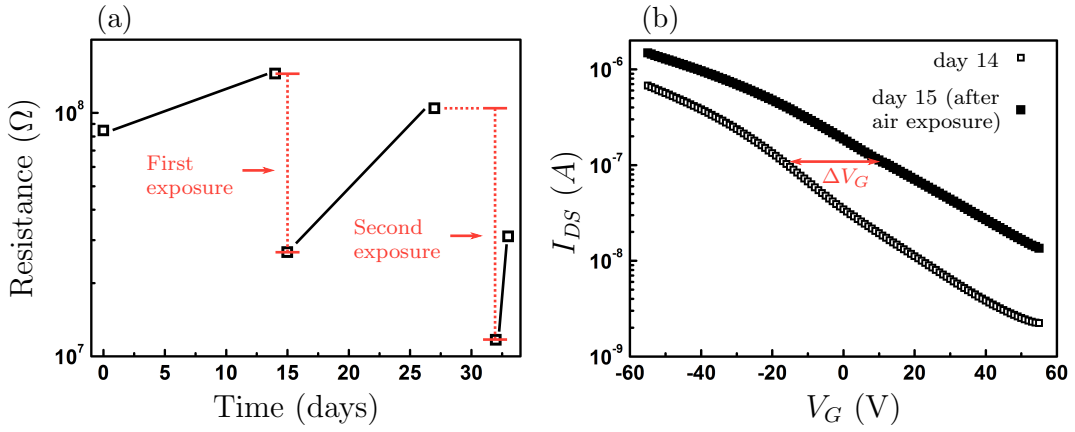

FIGURE 5.3: Impact of ambient doping on the electrical properties of GNR network FETs. In (a), we plot the resistance of a aGNR 9 device as a function of time. The jumps in the resistance can unambiguously traced back to the exposure to air. With the help of the change in the transfer curves, shown in (b), we estimate the change of charge carrier density to $\Delta n \approx 1.8 \times 10^{12}\,\mathrm{cm}^{-2}$. Lines are guides for the eye.

enhanced current, about 18 times as large as before, i.e. a much lower resistance. After 12 additional days, the pre-exposure value of the device resistance is nearly restored. On day 32, we again remove the chip from the glove box and this time, we expose it for 5.5 hours to the laboratory air. Remeasuring shows that again the resistance is lowered (approximately by a factor of 12). However, the reverse process, presumably associated with the desorption of adatoms in the inert gas atmosphere, has begun immediately after the air exposure ended, as shown by the fact that the resistance has nearly tripled 24 hours after ending the exposure to air.

By looking at the transfer characteristics before and after exposure (see Fig. 5.3 (b)), we can estimate how many charges have been introduced due to the air exposure. For that, we shift the post exposure curve by $\Delta V_G \approx 25\,\mathrm{V}$ such that it coincides with the pre–exposure curve. Via Eq. 5.5, this difference in gate voltage translates into a change of the surface charge carrier density of $\Delta n \approx 1.8 \times 10^{12}\,\mathrm{cm}^{-2}$, resulting in larger conductances. Especially at large positive gate voltages, where we induce electrons and deplete holes, the ratio $I_{\mathrm{post-exp}}/I_{\mathrm{pre-exp}}$ (at constant V_G and V_D) grows. As a consequence, the current modulation ratio and the subthreshold swing are notably affected, where the former drops from $IM_{-55\mathrm{V},+55\mathrm{V}} \approx 3 \times 10^2$ to $IM_{-55\mathrm{V},+55\mathrm{V}} \approx 1 \times 10^2$ and the latter rises from $SS \approx 41\,\mathrm{V/dec}$ to $SS \approx 52\,\mathrm{V/dec}$.

The presented results of our experiments are extremenly important to understand how unintenional doping can affect the device performance in any charge transport experiment with graphene nanoribbons. Some parts of the fabrication process usually take place in the laboratory or in a cleanroom, where it is not possible to exactly control the environmental gas composition. Different gaseous species contained in normal air, such as oxygen and water, can contaminate the sample surface during and after the fabrication and typically result in p–type doping [203]. Hence, in an ideal fabrication process, the GNRs should never be exposed to air. However, meeting this requirement is technologically complex and usually costly, although performing fabrication and measurements in a controlled inert gas atmosphere is fundamentally possible. As an alternative, annealing, e.g. by passing large current densities through the device [231] or heating in a gas mixture of hydrogen and argon has been suggested and tested in charge transport experiments in graphene–based devices [203]. However, employing the deposition process as discussed in Sec. 4.2.2, adsorbates can be trapped between the substrate and GNR film and in this case, annealing will not necessarily lead to a removal of these impurities. In Fig. B.7, we show that current annealing is possible with our devices. However, the major scope of this work is to shed light on the fundamental charge transport properties. Hence, we leave room for follow–up studies to further engineer the device fabrication process and annealing procedures towards the minimization of unintentional doping, while we focus on the in–depth analysis of the underlying charge transport mechanisms in our devices in the following sections.

5.2.3 Determination of the electrical contact resistance at metal/-graphene nanoribbon interfaces

For the process of charge injection into solids, the contacts play a crucial role. Before we further analyze the current–voltage curves presented in Sec. 5.2.1, it is therefore important to characterize the metal/GNR junctions and determine whether the measured transport characteristics are governed by the contacts. To this end, we use the transmission line method [232], a technique that has been successfully applied to determine the contact resistance in CNT network devices [233–235]. The chips 1, 2 and 5 in the aGNR 5 series have been designed for this purpose and contain devices with varying channel length L (between approximately 0.5 and 5 μm). We use the Ohmic low–V_D part of the I–V curves to determine the device resistance R_{on} as the slope of a linear model via a least squares fit. Similiar to the measurements in Fig. 5.2, we vary the gate voltage between $V_G = \pm 60\,\mathrm{V}$, here, in steps of $\Delta V_G = 10\,\mathrm{V}$. The data points for each gate voltage were again linearly fitted (least square fit) to extract the total contact resistance (source + drain) R_C from the intercept of the fit curve with the ordinate–axis at zero channel length (Fig. 5.4 (a)). In Tab. 5.2, we list R_C and channel resistances (i.e. the slopes of the linear R_{on} versus L fits) at $V_G = -60\,\mathrm{V}$, where the channel is fully turned on (see Sec. B.8 for details on the gate–voltage dependent contact resistance). The values for the contact resistances are comparable to what has been found in devices based on organic semiconductors and CNT networks [232, 233, 236]. Furthermore, the width–normalized inverse channel resistance $m = (\partial R/\partial L)^{-1}/W$ at different gate voltages (Fig. 5.4 (b)) can be used to determine the contact resistance–corrected charge carrier mobility [232]:

$$\mu_{RC} = \frac{1}{C_{\mathrm{Ox}}} \frac{\partial m}{\partial V_G}\,. \tag{5.6}$$

Following this method, any apparent channel–length dependence of the mobility originating from contact resistance at the source and drain electrodes is eliminated. However, the comparison of the values listed in Tab. 5.2 with the field–effect mobility extracted

Chip	R_C (MΩ) ($V_G = -60\,\mathrm{V}$)	R_{channel} (Ω/m) ($V_G = -60\,\mathrm{V}$)	R_C/R_{total} ($V_G = -60\,\mathrm{V}$)	R_C/R_{total} ($V_G = 0\,\mathrm{V}$)	μ_{RC} ($\mathrm{cm^2\,V^{-1}\,s^{-1}}$)
1	0.17 ± 0.05	$(5.8 \pm 0.2) \times 10^{11}$	0.25	0.1	$(5.0 \pm 0.3) \times 10^{-3}$
2	6 ± 1	$(3.4 \pm 0.4) \times 10^{12}$	0.56	0.50	$(8 \pm 1) \times 10^{-4}$
5	0.4 ± 0.2	$(6.2 \pm 0.6) \times 10^{11}$	0.40	0.19	$(3.4 \pm 0.2) \times 10^{-3}$

TABLE 5.2: Summary of contact and channel resistances extracted from length– and gate–dependent charge transport measurements for three chips of the aGNR 5 series.

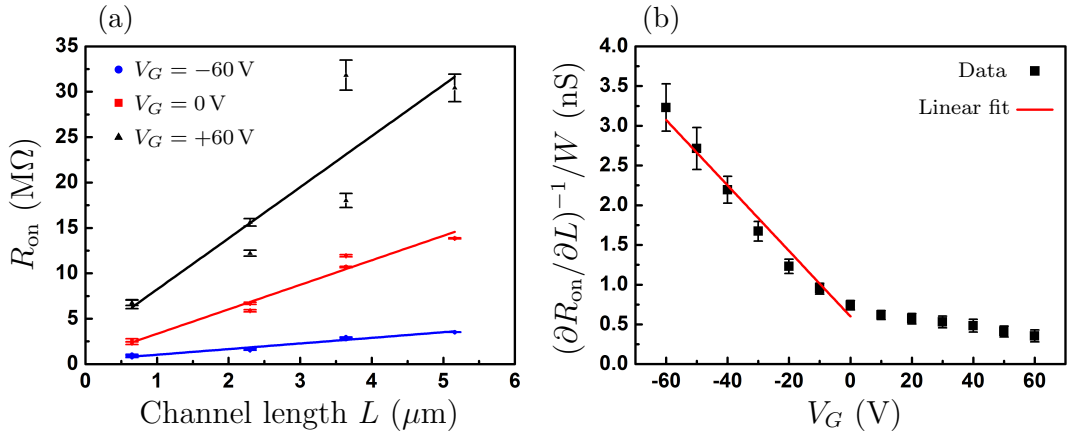

FIGURE 5.4: Contact resistance of metal/GNR interfaces measured on chip 5. (a) Total device resistance (channel and contact resistance) R_{on} as a function of channel length for contact resistance extraction at different gate voltages. (b) Width–normalized reciprocal slopes of the total resistance depending on gate voltage allowing for the determination of a contact resistance–corrected charge carrier mobility.

from the transfer curves (see Tabs. 5.1 and in Appendix B.5), shows that the difference is small. Additionally, the ratio of contact resistance versus total device resistance is in either case $< 15\,\%$ at a channel length of 500 nm. Therefore, we conclude that contact resistance is not the dominant factor and we do not require further corrections for contact resistance effects. Instead, we perform the following analyses using the as–measured data and suggest for future studies to use Kelvin force microscopy [237], capable of directly measuring the voltage drop across the contacts. This technique can reveal in the most direct way the influence of the contact resistance and improve the possibilities of accounting for it.

5.3 Charge transport mechanism in graphene nanoribbon networks

5.3.1 Universal scaling of charge transport

We can now attempt a thorough analysis of charge transport in aGNR 5 and aGNR 9 networks.[6] A priori the charge transport mechanism is not clear in our systems. The GNRs themselves are crystalline units and in crystalline materials, charge carriers are delocalized, where Bloch waves in the band structure picture are a proper description. On the other hand, dealing with *networks* of GNR units, where charge carriers have to cross ribbon–ribbon junctions, suggests that hopping between GNRs should be considered alternatively to be the dominant transport mechanism, very similar to the situation in most organic semiconductors [104]. Generally, the temperature dependence of charge transport can help to identify the appropriate mechanism. Therefore, we measure one aGNR 5 device and one aGNR 9 device in a cryostat (see Sec. 3.2.2), where we vary the temperature between 260 K and approximately 3 K and take I–V curves at various fixed temperatures as shown in Fig. 5.5 (a) and (b). In the double logarithmic plot of the I–V curves, we observe two general trends: The current decreases monotonously with decreasing temperature, and the transition voltage from linear to superlinear behavior decreases with decreasing temperature. At large biases, the functional dependence remains a power law, however the exponent β changes and extrapolation to $T \to 0$ yields values of $\beta = 4$ ($\beta = 8$) for the aGNR 5 (aGNR 9) device. Similar power laws have been obsverved for a large range of semiconducting polymers [100, 101] and can be explained by nuclear tunneling mediated hopping as the dominant charge transport mechanism. In nuclear tunneling, the coupling of the electronic charges to their nuclear environment sets the potential landscape for the movement of the charges. As detailed in Sec. 2.3, an analytic expression for the expected current (Eqs. 2.29, 2.30 and 2.31) can be derived if all hopping events are assumed to be equivalent, which is the case when energetic disorder is suppressed by high charge carrier densities. However, it is important to note that there are other physical models which yield Eq. 2.29. Among these models we can rule out Luttinger Liquid [238] since it requires impurity–free purely one–dimensional systems, and Coulomb blockade, which we expect for transport through a low–capacitance

[6] I sincerely thank Dr. K. A. and Prof. Dr. P. B. for the stimulating discussions about the data analysis presented in this chapter.

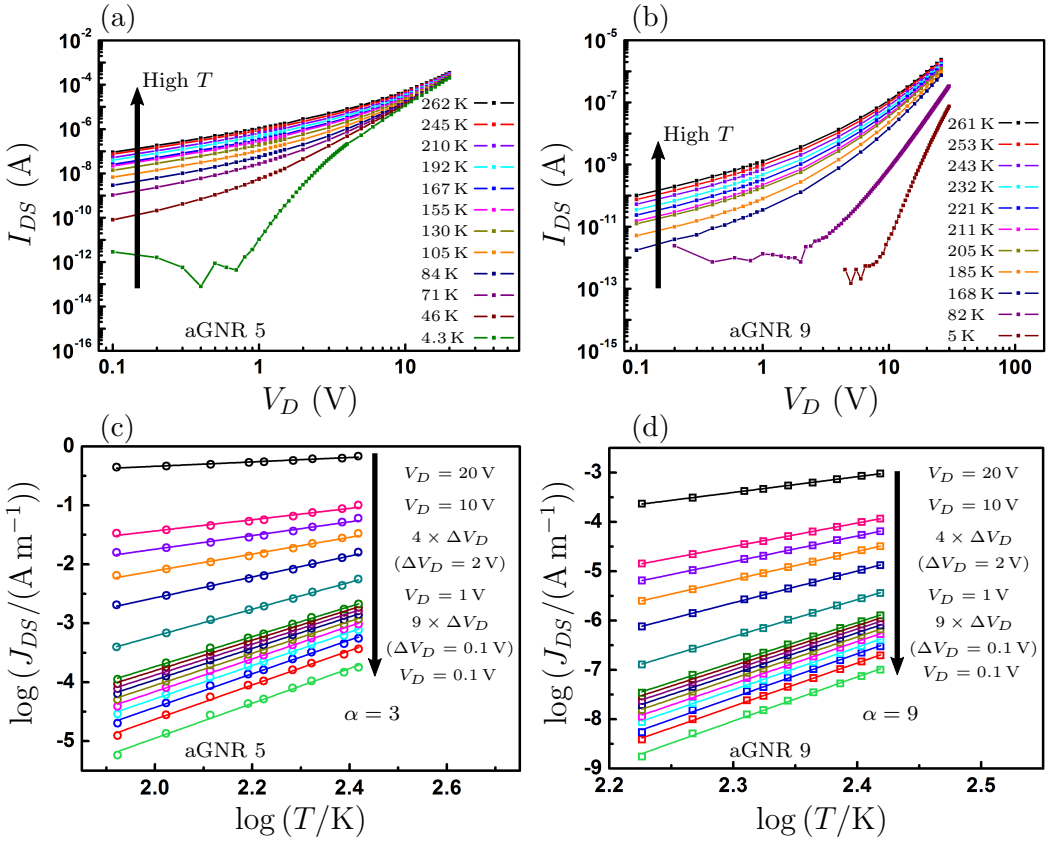

FIGURE 5.5: Temperature dependence of charge transport in aGNR 5 and aGNR 9 networks. (a) and (b) show the evolution of I–V curves with temperature. Measurement accuracy is approximately 10^{-13} A which becomes visible at the lowest temperature in the low–V_D regime. Lines are guides for the eye. In (c) and (d), we show cuts through the I–V curves for fixed drain voltages. Here, lines represent linear fits through the data used to determine the exponent of a power law $I_{DS} \propto T^{\alpha'}$. In the limit of drain voltage to zero, we find the exponent $\alpha = 3$ for aGNR 5 and $\alpha = 9$ for aGNR 9.

tunnel junction, e.g. through a quantum dot [239] (see also Sec. B.9). Finally, variable range hopping (VRH) can also lead to a similar expression for current as a function of voltage and temperature [240] and more knowledge is required to discriminate between VRH and nuclear tunneling mediated hopping (see below in Sec. 5.3.2). In order to be able to describe charge transport based on nuclear tunneling with Eqs. 2.29 – 2.31, energetic disorder must be suppressed, since single hopping steps become inequivalent in the presence of energetic disorder [241]. At high charge carrier densities, carriers hop between sites with narrow energetic spreading and hence the energetic states are similar. The GNR devices under test are dominated by extrinsic charge carriers due to environmental doping (see Secs. 5.2.2 and B.6) and therefore this precondition is fulfilled. Consequently, we can assume that energetic disorder is suppressed and if the model of nuclear tunneling is able to describe our data, we expect that all measurements of I_{DS} at

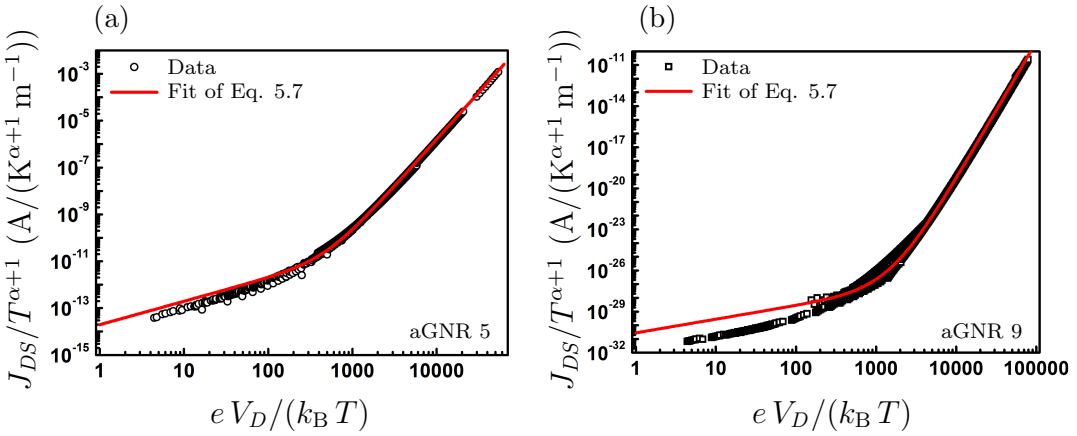

FIGURE 5.6: Scaled channel current density $J_{DS}/T^{\alpha+1}$ as a function of relative energy $e\,V/k_B\,T$ for the aGNR 5 device (a) and the aGNR 9 device (b). The values of α are determined from the temperature dependence of the current density at a drain voltage of $V_D = 0.1\,\mathrm{V}$. Solid red lines are fits to Eq. 2.29 showing excellent agreement with the measurement.

different temperatures and voltages can be collapsed to a single curve if scaled correctly. In order to determine the exponent α, we make use of Eq. 2.30 and plot $\log(J_{DS})$ as a function of $\log T$ at different drain voltages in Fig. 5.5 (c) and (d), where $J_{DS} = I_{DS}/W$. We evaluate α' as the slope of a linear model by a least squares fit and find α in the limit of vanishing drain voltage to be $\lim_{V\to 0} \alpha' = \alpha = 3$ for aGNR 5 and $\alpha = 9$ for aGNR 9. For aGNR 5, we find excellent agreement with the constraint $\beta = \alpha + 1$ (see Sec. 2.3), while for aGNR 9 this condition is experimentally not equally evident. Most likely, the latter is a shortcoming of the fact that we determine β only in a restricted fitting range at 5 K (see also discussion below in Sec. 5.3.2). We now use α to scale the current density as $J_{DS}/T^{\alpha+1}$ and plot this quantity as a function of relative energy $e\,V/k_B\,T$ in Fig 5.6. These plots consist of 2633 data points for the aGNR 5 device and 3414 data points for the aGNR 9 device and contain all I–V curves above 4 K (5 K for the aGNR 9 device). In Fig. 5.5 it is clearly visible that the I–V curves at these low temperatures have two different slopes in the double logarithmic plot. While the slope at high bias voltages fits the picture of nuclear tunneling mediated hopping, the first slope possibly arises due to charge traps [242]. In the following section (Sec. 5.3.2), we discuss this regime in more detail. Therefore, we include only the high–bias ($V_D \geq 10\,\mathrm{V}$) data points of the I–V curves at 4 K (5 K). Furthermore, we performed temperature sweeps at high bias voltages ($V_D = 5\,\mathrm{V}$, $V_D = 10\,\mathrm{V}$ for the aGNR 5 device and $V_D = 10\,\mathrm{V}$, $V_D = 30\,\mathrm{V}$ for the aGNR 9 device) between 258 K and 3.3 K, which are also included in Fig. 5.6. By fitting Eq. 2.29 with J_0 and γ as the only free fitting parameters, we find excellent agreement

using $J_0 = (1.44 \pm 0.05) \times 10^{-12}\,\mathrm{A/(K^{\alpha+1}\,m^{-1})}$, $\gamma = (7.66 \pm 0.09) \times 10^{-3}$ for the aGNR 5 device and $J_0 = (2.1 \pm 0.1) \times 10^{-32}\,\mathrm{A/(K^{\alpha+1}\,m^{-1})}$, $\gamma = (4.84 \pm 0.04) \times 10^{-3}$ for the aGNR 9 device. The parameter γ is expected to be dependent on channel length [100], while α and J_0 are expected to be constant. Studying these parameters as a function of L will help to further pin down the details of charge transport, e.g. to test VRH against nuclear tunneling mediated hopping.

After having established that charge hopping is likely the dominant charge transport mechanism, we can again look at the values for the mobility as determined in Sec. 5.2.1. Although a degradation of the charge carrier mobility with larger band gaps is expected, theory predicts still much larger values for the mobility in the order of $10^2\,\mathrm{cm^2\,V^{-1}\,s^{-1}}$ for GNRs with a band gap of comparable size [243]. Using terahertz spectroscopy, comparable values have been experimentally observed in aGNR 9 samples [184]. However, in the field of semiconducting polymer devices, mobilities in the range of $10^{-1}\,\mathrm{cm^2\,V^{-1}\,s^{-1}}$ to $10^{-4}\,\mathrm{cm^2\,V^{-1}\,s^{-1}}$ are typically observed [244], where hopping is regularly the dominant charge transport mechanism. In this case the current (i.e. the resistivity) as well as the mobility are determined by the hopping rates (compare Eq. 2.32 in Sec. 2.3). The rate equation in the dissipative case of nuclear tunneling has been derived in Sec. 2.3 and hence, instead of scattering events of delocalized electron waves, the microscopic parameters in Eq. 2.26 determine the mobility and resistivity. The experimentally determined parameter α is a scaled version of the Kondo parameter as described in Sec. 2.3 and we see that based on this parameter, the coupling between charges and bath is stronger in aGNR 9 ($\alpha = 9$) than in aGNR 5 ($\alpha = 3$). The other quantities in Eq. 2.26 can be accessed eventually by further measurements beyond the scope of this work as, for example, the energy difference between donors and acceptors ϵ_{ij} is directly related to the channel length dependence of γ (compare also Eq. 2.28 in Sec. 2.3). To substantiate the generality of this analysis, these experiments should be repeated with other types of GNRs, e.g. aGNR 7 or aGNR 13, which belong the aGNR $N = 3\,m+1$ family in contrast to aGNR 5 and aGNR 9 which belong to the $3\,m+2$ and $3\,m$ families, respectivley (see also Sec. 2.2.3.1). Then we expect a renormalization of the $I(V,T)$ characteristics according to Eq. 2.29 will collapse for all GNR species onto a single curve. For this renormalization, although beyond the scope of this work, the dimensionless parameter $e\,V_{\mathrm{hop}}/(k_{\mathrm{B}}\,T)$, with $V_{\mathrm{hop}} = \gamma\,V$, representing the applied bias divided by the number of hops can be used in analogy to Ref. [100].

5.3.2 Transport at low bias and low temperature

As mentioned in the previous section, the I–V curves of both, the aGNR 5 and the aGNR 9 device, show at 4 K and 5 K a qualitative difference to the I–V curves at more elevated temperatures. For low bias voltages, there is a different slope in the $\log I_{DS}$ vs. $\log V_D$ data at such low temperatures as shown in Fig. 5.7 (a) and (b). Such an additional slope in the I–V characteristic is typical for the presence of charge traps [242]. The second slope at large drain voltages fits again the trend of the I–V curves at higher temperatures. For the aGNR 5 device, we find a peculiar dependence of the resistance on a perpendicularly applied magnetic field (see Fig. 5.7 (c) and (d)). At low bias voltages, we observe an increase of the resistance with magnetic field B up to a relative change of 14 % at $B = 8\,\mathrm{T}$ which can be perfectly described by a quadratic function $\Delta\rho/\rho = a\,B^2$. Although, this behavior is reminiscent of the ordinary Kohler magnetoresistance in metals [245], this model is inadequate as it is based on delocalized band transport and the transport mechanism here is clearly charge carrier hopping.

To investigate this effect further, we study it as a function of temperature and bias voltage. Increasing these parameters leads to a decrease of the effect. In Fig. 5.7 (d), we see that no magnetic field dependence can be seen anymore above $T = 50\,\mathrm{K}$. Furthermore, when we increase the bias voltage and approach the regime of nuclear tunneling mediated hopping, the effect also goes down, as shown in Fig. 5.7 (c), where we present magnetic field sweeps at two different drain voltages of $V_D = 5\,\mathrm{V}$ and $V_D = 10\,\mathrm{V}$. A model to explain these intriguing findings is elusive and our result is contrary to previous studies, which found a large negative magnetoresistance effect in graphene nanostructures [224]. However, the experiments of Bai et al. in Ref. [224] deal with top–down patterned single ribbon devices operating in a Coulomb blockade regime. In contrast, hopping transport is in general compatible with a positive magnetoresistance where, however, an exponential dependence of the resistance with magnetic field is expected instead of a power law [246]. Hence, in order to understand the effect in more detail, further measurements are required. First, the parameter space of bias voltage, temperature and magnetic field should be scanned with higher precision, which allows to follow better the transition of the nuclear tunneling regime into the magnetoresistance regime. Second, the measurements should be extended to higher magnetic fields, to test different predictions for the magnetoresistance [246].

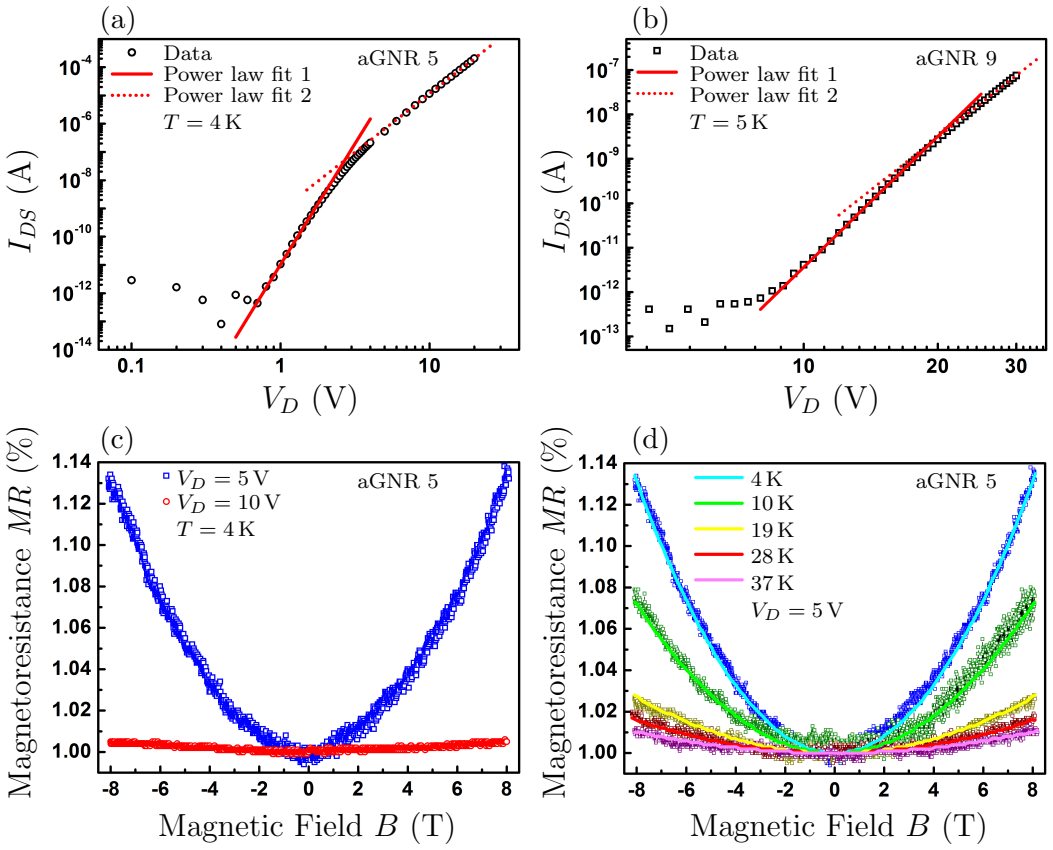

FIGURE 5.7: Transport at low temperatures and low bias voltages. In (a) and (b), we demonstrate that we can distinguish two slopes in the double logarithmic plot of the I–V curves at $T = 4\,\mathrm{K}$ for the aGNR 5 device and at $T = 5\,\mathrm{K}$ for the aGNR 9 device. The low–bias slope is $\beta_1 = 8.6$ ($\beta_1 = 9.8$) for the aGNR 5 device (for the aGNR 9 device). The high–bias slopes are $\beta_2 = 4$ and $\beta_2 = 8$, respectively. In the low–bias transport regime, a positive magnetoresistance arises for the aGNR 5 sample, which is absent in aGNR 9. In (c), we show that the magnetoresistance effect vanishes at high drain voltages (e.g. $V_D = 10\,\mathrm{V}$), while at low drain voltages ($V_D = 5\,\mathrm{V}$) it is a sizeable effect up to 14 %. (d) shows the temperature dependence of the magnetoresistance. At temperatures $T \geq 50\,\mathrm{K}$ the magnetoresistance as well as the difference between the two high–bias slopes in the log(I)–log(V) curve (see Fig. 5.5) vanishes. Lines are fits of a quadratic model of the form $\Delta\rho/\rho = a\,B^2$ to the data, where we find $a \approx 0.002\,\mathrm{T}^{-2}$ at 4 K (see Tab. B.7 for an overview of all temperatures).

5.4 Conclusion and outlook

In conclusion, we have shown that for aGNR 5 and aGNR 9 network FET devices at high charge carrier densities, the $I(V,T)$ characteristics over a wide range of temperatures and bias voltages can be described by the unified description developed for semiconducting polymers, which includes the hopping rates derived by the model of nuclear tunnelling. For both types of GNRs, aGNRs 5 and aGNRs 9, the $I(V,T)$ characteristics showed a power law dependence on both temperature and voltage which can be renormalized to a single curve. This universal curve integrates all measurements at temperatures between 3 and 260 K and at drain voltages swept over two orders of magnitude. This study shows that the mechanism that drives charge transport in all organic polymer devices is also operational in devices based on GNR networks.

However, there are still open questions calling for further experimental and theoretical work beyond the current work. These open questions for example concern the actual band gap for lateral charge transport or the role of charge traps for the large positive magnetoresistance in aGNR 5. By analyzing the hysteresis of the transfer curves, it will be possible to infer the number of charge traps in the devices (this is subject of a follow–up study in Ref. [229]). However, their role to influence the effect of a magnetic field is unclear at the moment. Furthermore, due to the current state–of–the–art GNR fabrication, the final transport properties of each sample are determined by a number of extrinsic factors which cannot be controlled directly. As a consequence, there is always a random element in the fabrication of GNR FET devices, for instance resistance, charge carrier mobility or the current modulation ratio of two GNR samples fabricated together under exactly the same conditions may differ by as much as a factor of two. Consequently, it is an absolute necessity to repeat the experiments on several samples to exclude sample–dependent artifacts and uncertainties. For future experiments, we suggest to rely on encapsulated GNR samples, e.g. sandwiched between sheets of hexagonal boron nitride, a technique which is nowadays common for devices based on graphene sheets [247].

Additionally, we suggest it to be worthwhile to optimize the device production further towards single–ribbon devices. Firstly, based on the results of our study, charge transport signatures in short–channel devices can now be interpreted much more facile, especially in the case of an uncertain number of ribbons forming the conductive channel. Secondly, with aGNR 5, we have found the most conductive GNR species so far, which will drastically increase the yield of functional short–channel devices.

Chapter 6

Magnetoresistance and charge transport in graphene governed by nitrogen dopants

Substitutional nitrogen doping of graphene is a viable route for the tailoring of charge carrier properties in graphene. We elucidate the nature of this doping by combining Raman spectroscopy to obtain structural information, and charge transport measurements, which additionally reveal the influence of charged impurities on the electronic properties. In a thorough electrical characterization of undoped graphene and nitrogen doped graphene at variable temperatures and in magnetic fields up to 8 T, we find a sixfold increase in the charge carrier concentration with varying nitrogen content, indicating highly effective doping. Additionally, the formation of a charge transport gap is revealed by variable range hopping conduction. The magnetotransport exhibits a conspicuous sign change from positive Kohler magnetoresistance in undoped graphene to a large negative magnetoresistance that we can attribute to the doping induced disorder. The presented experiments have been the basis of a bachelor thesis (Ref. [248]) and a publication (Ref. [249]) and the majority of the measurements was performed together with M. R.. For the following discussion, the analysis of the data has been thoroughly revised and extended. With these more accurate and new results, we quantify the transition from weak to strong localization in doped graphene based on the change of the length scales for phase coherent transport and localization.

6.1 Experimental details

For the experiments on doped graphene, ten samples were produced in total and the three samples with the highest quality were used for measurements. Samples 1 and 2 were provided by the Max Planck Institute for Polymer Research, and are not doped. Sample 3 stems from a collaboration with an industrial partner and is doped with nitrogen. Since the undoped samples are qualitatively similar [248], we show the results of only one of them (sample 2). All samples have been fabricated by CVD as described in Sec. 4.1.1. For the doped sample, the nitrogen atoms were incorporated in the lattice following the approach described in Ref. [149]. For the realization of charge transport test devices, different approaches have been tested. One possible fabrication strategy is to transfer the graphene first and define the contacts afterwards. This fabrication route suffers from mainly two disadvantages: The patterning procedure by EBL generally leaves resist residues on the graphene surface and can degrade the quality of the sample. Furthermore, the graphene crystals can get damaged in the metalization process, especially when sputtering is used, where metal atoms impinge with high energy on the graphene surface. Hence, in order to perform charge transport measurements, silicon/silicondioxide (Si/SiO_2) substrates have been prepared with sets of four metallic contact pads which build the corners of a square with side lenghts between 100 and $800\,\mu$m. These contact pads were made of gold (thickness $t_{Au} \approx 50\,$nm), where we used a chromium seed layer (thickness $t_{Cr} \approx 5\,$nm) to improve adhesion to the SiO_2 surface. The metals have been sputter evaporated onto the SiO_2 surface. Prior to the sputtering, the structures have been defined by EBL. Here, a resist double layer of MMA(8.5)MAA EL6 and PMMA 950K A3 has been used, facilitating the lift–off procedure compared to single–layer resist approaches. The fabrication steps in detail are the following:

1. Sample Preparation

   - Standard cleaning procedure of Si/SiO_2 substrates (highly doped p^{++} Si with $(300 \pm 5)\,$nm SiO_2) as described in Sec. 4.3.1.
   - Spin coating of MMA(8.5)MAA EL6 onto the substrate using a prespin of 500 rpm for 5 s and a mainspin of 2000 rpm for 60 s (acceleration of 2000 rps^2). Baking on the hot plate for 90 s at 180° C.

- Spin coating of PMMA 950K A3 onto the substrate using a prespin of 500 rpm for 3 s and a mainspin of 2500 rpm for 60 s (acceleration 2000 rps^2). Baking on the hot plate for 90 s at 180° C.

2. EBL step

   - Electron beam exposure with a dose of 170 $\mu\mathrm{C/cm}^2$ at an acceleration voltage of 10 kV.
   - Development of the structures by immersing the substrate fully into a mixture of methyl isobutyl ketone and isopropanole (1 : 3) for 30 s and subsequently into pure isopropanole for 30 s.

3. Metallization by sputtering a Cr/Au film ($\approx$ 5 nm/50 nm) under the same conditions as described in Sec. 4.3.1.

4. Lift–off by immersing the sample into acetone for some hours. Using a pipette to establish a gentle flow over the surface can accelerate the procedure.

Further details of the fabrication can be found in Ref. [248]. The graphene has not been further patterned and instead the samples have been measured using the VDP method (see Sec. 3.2.4). The charge transport experiments have been performed in a helium bath cryostat using a Keithley 224 current source and a Keithley 182 voltmeter for the resistance measurements. The theory of the VDP method assumes point–like contacts and the error induced by the size of the contacts has been considered and is described in detail in Ref. [248].

6.2 Structural investigation using Raman spectroscopy

The fabrication of graphene using CVD is an established method and has been signifiantly optimized over the recent years to yield graphene crystals of high structural integrity and with very good electrical properties as for example demonstrated by a large values for the charge carrier mobility [160]. On the other hand, the synthesis of doped graphene species, as described in Sec. 4.1.1, is more difficult to control which results in a lower reproducibility of sample quality. To ascertain the impact of the CVD doping procedure, we combine electrical transport and structural investigation by Raman spectroscopy for each sample. We start with the discussion of the Raman spectra of the doped and of an undoped graphene sample. For both samples 225 spots on the sample have been tested (compare Ref. [248]) to check for homogeneity and in Fig. 6.1 we show two representative spectra. The theoretically expected line shape of the peaks follows a Lorentzian profile. In practice however, the resolution of the measurement apparatus can lead to additional Gaussian broadening and therefore, a convolution of a Lorentzian and a Gaussian distribution function describes the data more accurateley [250]. Such a convolution is called a Voigt profile and is given by

$$V(x,\sigma,\gamma) = \int_{-\infty}^{\infty} G(x',\sigma)\, L(x-x',\gamma)dx' \,, \tag{6.1}$$

$$G(x,\sigma) = \frac{1}{\sigma\sqrt{2\,\pi}}\, e^{-t^2/2\,\sigma^2} \,, \quad L(x,\gamma) = I_0 \frac{1}{1+\left(\frac{2\,(x-x_0)}{\gamma}\right)^2} \,. \tag{6.2}$$

where $G(x,\sigma)$ denotes a Gaussian distribution with a standard deviation σ and $L(x,\gamma)$ is the Lorentzian Raman line profile centered at x_0 and with a full width at half maximum (FWHM) γ. Evaluating this convolution is computationally expensive and for this reason the fit to the Raman spectra has been done using an approximation [251] which has a maximum deviation from Eq. 6.1 of 10^{-13}. The obtained peak positions are summarized in Tab. 6.1 together with the FWHM of the fit and the peak height normalized to the G peak. We first analyze these data with respect to the number of layers (N) because the CVD growth can lead to mixtures of single layer graphene (SLG), bilayer graphene (BLG) or few–layer graphene (FLG) samples, although the process is self–limited as soon as the reactive copper surface is covered and the contact with the precursor is blocked [252]. Albeit Raman spectra of SLG and graphene stacks share some fundamental peaks like the D, G or $2D$ peak, shear and layer breathing modes (LBM) are only possible

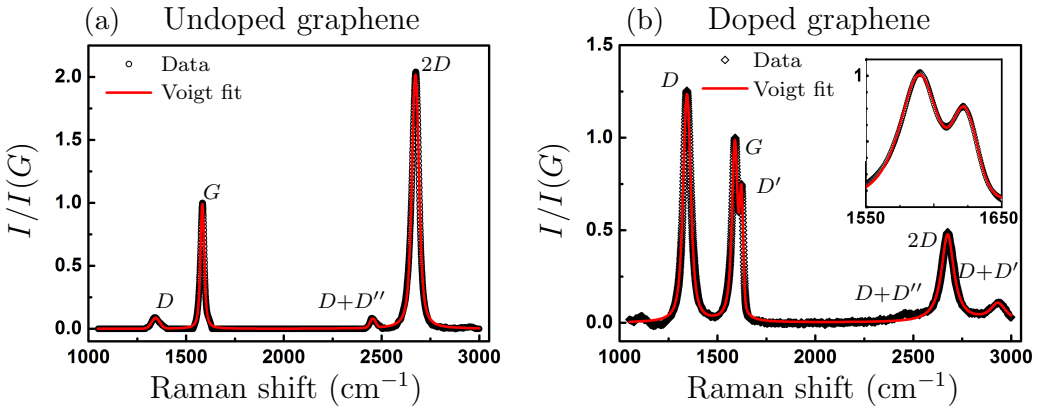

FIGURE 6.1: Raman spectrum of undoped graphene (a) and nitrogen-doped graphene (b). The larger defect peak (D) in the doped case together with the D' peak indicate an increase of scattering centers due to the doping procedure. The red lines are a fit to Voigt profiles as given in Eq. 6.1. The inset shows in a close–up that the G and D' peaks merge in the doped case.

in the latter due to relative motions of the planes themselves, either perpendicular or parallel to their stacking direction. Consequently, the presence and position of these modes are a direct probe of N. For example, the position of the C peak due to a shear mode varies with N as $\propto \sqrt{1+\cos \pi/N}$ in Bernal stacked systems [117]. However, the C peak occurs for bilayer graphene at a frequency of approximately $31\,\mathrm{cm}^{-1}$ [117], which is below the accessible wave vector range of the used the Raman spectrometer (Bruker RFS 100/S). The LBMs on the other hand are located at $1655\,\mathrm{cm}^{-1}$, $1730\,\mathrm{cm}^{-1}$ and $1765\,\mathrm{cm}^{-1}$ [253]. None of these peaks are visible in our spectra, neither for the doped sample, nor for the undoped sample. A second indication is given by the $2D$ peak, which is not only sensitive to defects but also to N as there is a clear change in shape and intensity evolving with the stacking induced change of the electronic bands. While in SLG the $2D$ peak consists of a single Lorentzian line, it is comprised of four compononents in BLG and of two components in the limit $N \to \infty$ [117]. A very careful

Sample	Quantity	D	G	D'	$D+D''$	$2D$	$D+D'$
2	Position	1344 ± 1	1584 ± 1	/	2455 ± 1	2674 ± 1	/
	FWHM	48 ± 10	24 ± 2	/	34 ± 10	43 ± 1	/
	Height	0.09	1	/	0.08	2.04	/
3	Position	1344 ± 1	1589 ± 1	1623 ± 1	≈ 2455	2676 ± 1	2933 ± 2
	FWHM	46 ± 1	36 ± 1	20 ± 1	/	77 ± 3	98 ± 23
	Height	1.25	1	0.75	/	0.48	0.11

TABLE 6.1: Raman peak parameters of undoped graphene and doped graphene obtained from Voigt fits to the spectra.

analysis is necessary here because a single Lorentzian fit could also be consistent with TG [117] and hence this is not a direct evidence for SLG on its own. In this case, a significant broadening is expected with an FWHM of more than $50\,\mathrm{cm}^{-1}$, roughly two times larger than in SLG [117]. Looking at the $2D$ peak in the spectrum of the undoped sample (Fig. 6.1 (a)) such a broadening is not discernible (i.e. the measured peaks have a sharp maximum and no shoulder features) and a single Voigt line yields a good fit. The FWHM of this line is $(43 \pm 1)\,\mathrm{cm}^{-1}$, where the inherent Lorentzian contribution has an FWHM of $(23 \pm 1)\,\mathrm{cm}^{-1}$. While the Lorentzian FWHM is in good agreement with the expected value for SLG, the overall line width is larger but still below the value expected for TG. Structural disorder in the sample can cause an enhanced FWHM, as well as the Gaussian component induced by the measurement apparatus. Such disorder is definitely present in the sample as can be inferred from the presence of a D peak. The same reasoning holds for the $2D$ FWHM of the doped sample. Here, again a single Voigt line describes the data resonably well and the FWHM is $(77 \pm 3)\,\mathrm{cm}^{-1}$, where a strong disorder broadening is expected from the large D peak as detailed below. In summary, while the described Raman features give a good indication that our samples are predominantly SLG, minor patches of BLG or FLG cannot be excluded, especially in the doped case. One of the most direct evidence of SLG would be for example the observation of SLG–like anomalous quantum Hall effect in a clean sample [254].

Further information about the structural integrity of the samples can be drawn from the Raman spectra and in particular from the D peak. In Ref. [255] a three stage model is introduced describing different levels of crystallinity in carbon–based systems and how this is reflected in the Raman spectrum. Stage 1 comprises single crystals and polycrystalline specimens (down to nanocrystallites) in sp^2 configuration. In stage 2, we find nanocrystallites down to low sp^3 amorphous carbon. Finally, high sp^3 amorphous carbon is classified in stage 3. Each stage can be identified by their Raman signature. The D peak reveals immediately, that the doped sample is more defective than the undoped one, since this peak is the most prominent one in the spectrum. Furthermore, a strong D' shows up, nearly as high as the G peak together with a $D + D'$ at $(2933 \pm 2)\,\mathrm{cm}^{-1}$: These two peaks evolve with a growing number of defects. In order to decide whether a sample is still in stage 1, the FWHM of the D, G and $2D$ peaks can be used, which should be below $75\,\mathrm{cm}^{-1}$, $42\,\mathrm{cm}^{-1}$ and $150\,\mathrm{cm}^{-1}$ [256]. As this is the case for the doped sample, we assume that there is no significant sp^3 amorphization. Besides

this qualitative analysis, we can use the ratio of the D and G peak intensities in order to quantify the average distance between two (Raman active) defects or their density respectively via

$$I(D)/I(G) = K\,\lambda^4/L_D^2\,, \tag{6.3}$$

where $K = (1.8 \pm 0.5) \times 10^{-9}\,\mathrm{nm}^{-2}$ is an empirical constant and λ is the wavelength of the excitation laser in nm [256]. We used a wavelength of 532 nm and obtain $L_D = (40 \pm 6)\,\mathrm{nm}$ for the undoped sample. For the doped case, we arrive at $L_D = (11 \pm 2)\,\mathrm{nm}$ which is close to the validity limit at $L_{D,min} = 10\,\mathrm{nm}$ for Eq. 6.3. These values correspond to defect densities of $n_{D,undoped} = 10^{14}\,\frac{\mathrm{cm}^{-2}}{\mathrm{nm}^2}/\pi\,L_D^2 = (2.0 \pm 0.6) \times 10^{10}\,\mathrm{cm}^{-2}$ and $n_{D,doped} = (2.8 \pm 0.7) \times 10^{11}\,\mathrm{cm}^{-2}$. Here, we only consider Raman active defects, e.g. point defects or grain boundaries. Charged impurities, which do not contribute to the D peak are not detected. Their influence however can be probed in transport measurements.

6.3 Transport gap and charge carrier localization in doped graphene

6.3.1 Charge carrier density and mobility probed by the Hall effect

We measure the charge transport properties of sample 3 to further investigate the influence of the nitrogen doping on the electronic properties of graphene. The undoped samples have been measured to serve as a reference and we discuss the results in comparison to this reference system. Nitrogen dopants in the graphitic configuration are expected to be electron donors and we expect this configuration to be predominant (compare Sec. 4.1.1). In order to test this, we deduce the charge carrier concentration n and mobilities μ from Hall effect measurements as given by

$$n = \frac{1}{R_H\,e}\,, \quad \mu = \frac{1}{e\,R_S\,n}\,, \tag{6.4}$$

where R_H is the Hall constant derived from the slope of the Hall resistance as a function of the applied magnetic field, R_S is the sheet resistance and e is the elementary charge. In the undoped sample, we find a charge carrier mobility of $(1014 \pm 4)\,\mathrm{cm}^2\,V^{-1}\,\mathrm{s}^{-1}$ with a charge carrier density of $(6.42 \pm 0.03) \times 10^{12}\,\mathrm{cm}^{-2}$ at 279 K. At 2.5 K the mobility is $(1122 \pm 32)\,\mathrm{cm}^2\,V^{-1}\,\mathrm{s}^{-1}$ and the density $(6.22 \pm 0.03) \times 10^{12}\,\mathrm{cm}^{-2}$. Such a weak

dependence on temperature has been reported for graphene and it is often goverened by extrinsic sources, such as lattice defects, charged impuritites and interfacial phonons of the supporting substrate [257]. In case of the nitrogen-doped sample, we measure at 279 K a charge carrier mobility of $(23 \pm 4)\,\mathrm{cm}^2\,V^{-1}\,\mathrm{s}^{-1}$ with a charge carrier density of $(39.3 \pm 0.2) \times 10^{12}\,\mathrm{cm}^{-2}$. The latter shows an increase of more than a factor six compared to the undoped case while the mobility is drastically reduced. These observations can be readily explained by the doping: The modification of the graphene lattice with additional nitrogen atoms increases the charge carrier density significantly as each nitrogen atom provides an additional electron. Furthermore, these defects form additional scattering centers and decrease the mobility. Finally, at 2.5 K we obtain $\mu = (11 \pm 3)\,\mathrm{cm}^2\,V^{-1}\,\mathrm{s}^{-1}$ and $n = (22.0 \pm 0.2) \times 10^{12}\,\mathrm{cm}^{-2}$ respectively, which is a much stronger change with temperature as compared to the undoped sample.

6.3.2 Variable range hopping conduction in nitrogen doped graphene

To elucidate this temperature dependence, we monitor the sheet resistance over the whole temperature range from room temperature down to 2.5 K (Fig. 6.2). For the undoped sample there is again a very weak dependence and the temperature scan reveals a broad minimum at around 100 K, as shown in the inset of Fig. 6.2. This nonmonotonicity of $R_S(T)$ is a result of competing effects and has been reported in CVD–grown graphene before [257]. The increase of R_S with T, $dR_S/dT > 0$, in the range $T \geq 100$K can be understood as a result of thermally weakened screening and enhanced electron–phonon scattering. In graphene on SiO_2, the only intrinsic phonon mode which plays a role is an acoustic phonon giving rise to a linear dependence in T. However, charge carriers can also couple to remote optical surface phonons of the SiO_2 substrate with energies $\hbar\omega_{SP1} = 63\,\mathrm{meV}$ and $\hbar\omega_{SP2} = 116\,\mathrm{meV}$ [257]. The opposite behavior, $dR_S/dT < 0$, at low temperatures results from thermal activation in the presence of electron–hole puddles. For samples with a charge carrier mobility $\mu \lesssim 1000\,\mathrm{cm}^2\,\mathrm{V}^{-1}\mathrm{s}^{-1}$, this activated behavior becomes dominant over the usually observable temperature range of approximately $[2 - 300]$ K [257]. Looking at the doped graphene sample, a monotonic increase of R_S with decreasing T is observed, similar to the behavior of a gapped semiconductor. However, following the argumentation above, this behavior can be also be caused by a disorder induced transport gap instead of a energy band gap and hence, we need additional criteria to differentiate between both. Prestigiacomo et al. suggest that the

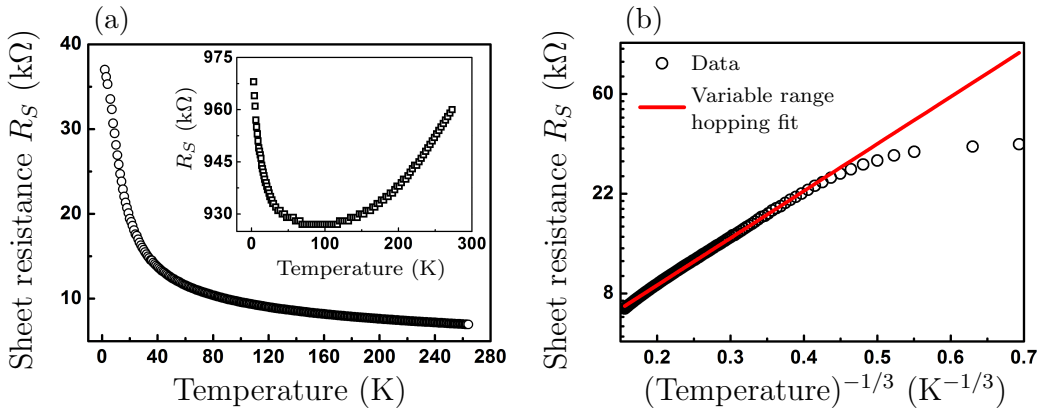

FIGURE 6.2: Temperature dependence of the sheet resistance R_S in the nitrogen–doped sample. In (a), we show the data in a normal scaling, whereas in (b) both axes have been scaled according to Mott's variable range hopping law. The red line is a fit to Eq. 6.5, showing the excellent agreement of our data with theory for all temperatures between 279 K and approximately 10 K. At lower temperatures, the sheet resistance deviates from the range hopping model, indicating another conduction mechanism to become important in this range. The inset shows the temperature dependence of R_S for the undoped sample as a reference. Error bars are small ($\leq 10\,\Omega$) and omitted in the plots in order to improve the readability.

former is typically accompanied by a drop of the mobility when moving towards low temperatures along with the presence of VRH conductivtiy [258]. The VRH conductivtiy is given by

$$\sigma_{\mathrm{VRH}}(T) \propto e^{-\left(\frac{T_0}{T}\right)^p}, \tag{6.5}$$

where the exponent $p = 1/(d+1)$ depends on the charge transport dimensionality d [259]. As already pointed out, the mobility decreases by a factor of 2 at low temperature and to test additionally for the presence of VRH, we plot our data on a logarithmic scale versus $(1/T)^p$ in Fig. 6.2 (b). Here, we set $d = 2$, because graphene is a two–dimensional material. This choice results in a good fit for the whole temperature range down to 10 K and we extract an activation temperature of $T_0 = (105 \pm 2)\,\mathrm{K}$ corresponding to $E_0 = (9.1 \pm 0.2)\,\mathrm{meV}$. At even lower temperatures, the sheet resistance grows significantly slower than expected from VRH, indicating the presence of another conduction mechanism working in parallel. Often, a combination of VRH and thermal activation (TA) is considered to describe $R_S(T)$ data [159], where the TA is of the form $\propto \exp\left[-E_G/(2\,k_B\,T)\right]$. In our case, a low excitation energy of $E_G < 1\,\mu\mathrm{eV}$, leading to a nearly constant TA term (in the observed temperature range), can qualitatively explain our data while a least–squares fitting procedure did not yield satisfactory results. The physical origin of such a thermally activated behavior in semiconductors is usually found

in the transition of charge carriers from a valence band to a conduction band over a band gap. In graphene, a band gap is absent and although in literature, the formation of a gap is discussed for doped graphene [16], TA is also consistent with strongly localized charge carriers which are excited to delocalized states in the same band [260].

6.3.3 Positive and negative magnetoresistive effects

If the behavior of R_S as a function of temperature is a result of localization and disorder, we expect to find further evidence for charge carrier localization in the magnetic field[1] (B) dependence of the sheet resistance. In Fig. 6.3, we plot the magnetoresistance ratio MR against the magnetic field, where we define

$$MR = \frac{R_S(B) - R_S(0)}{R_S(0)} \cdot 100\,\%\,, \tag{6.6}$$

and B is applied perpendicular to the plane of current flow. At 279 K the MR increases monotonically in the undoped graphene while at 2.5 K, the MR first decreases at low magnetic fields (< 0.5 K) before it also starts to increase similarly to the high–T case with a crossover to positive MR at 2.35 T. Magnetoresistance effects in graphene are governed by different physics depending on the charge carrier density. While in the low–density regime, the simultaneous presence of holes and electrons leads to a pronounced MR [261], the high–density limit is metallic and transport is Drude–like. In a single–carrier Drude model, however, no MR is expected. Nevertheless, in theories beyond the free–electron model, the influence of non–spherical Fermi surfaces is considered and generally, in non–magnetic conductors, the MR is a strictly positive function (f) of the product $\tau\,B$, with τ the relaxation time [245]. Since the conductivity σ is proportional to τ one has

$$MR = f(\sigma(0)\,B) = f\left(\frac{B}{R_S(0)}\right)\,. \tag{6.7}$$

Equation 6.7 is known as "Kohler's rule" and for many metals it takes the form [245]

$$MR = \left(\frac{\sigma(0)}{2\,n\,e}\right)\,B^2 \cdot 100\,\% = \left(\frac{\mu\,B}{2}\right)^2 \cdot 100\,\%\,, \tag{6.8}$$

[1] The magnetic field in the interior of our samples is not known and hence, the most concise way of referring to the applied magnetic field in teslas would be $\mu_0\,H$, with μ_0 the vacuum permeability and H the magnetic field in A/m. However, for the sake of brevity, we use the symbol B in this chapter to refer to this field.

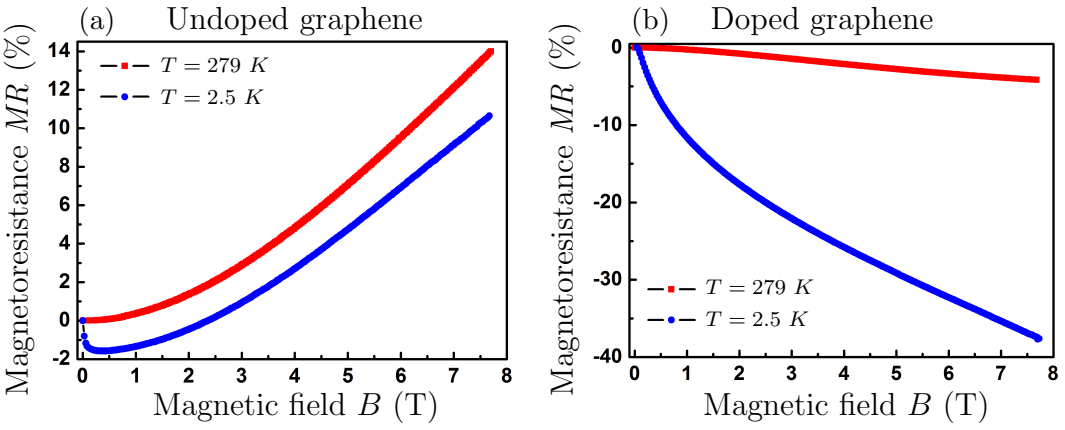

FIGURE 6.3: Magnetoresistance (MR) of undoped graphene (a) and doped graphene (b) where the magnetic field B was applied perpendicular to the sample plane at 279 K and 2.5 K. The measurements were symmetric with respect to the polarity of B and have been averaged. In the undoped case, the weak localization peak is clearly visible at low temperature and zero field. Ordinary Kohler magnetoresistance, according to Eq. 6.8, describes the field range up to $B = 2$ T. At higher fields a deviation from Kohler's rule can be caused by spatial mobility fluctuations as described in the main text. (b) shows the same measurements for the doped case where the sign and the shape of the curves change compared to the pristine graphene. Error bars are small ($\leq 0.1\%$) and omitted in the plots in order to improve their readability.

if the magnetic field strength is sufficiently low ($\mu B \ll 1$). With the Hall mobility of this sample, we estimate the limiting field to be around 10 T and a least–square fit in this range results in a mobility of approximately 1200 $\mathrm{cm^2\,V^{-1}\,s^{-1}}$, in very good agreement with the Hall value. Here, we restrict the fitting procedure to field values below 2 T because at higher fields the data deviate from that model in a very similar way as observed in Ref. [262], which can be explained by spatial inhomogeneities of the mobility, e.g. due to defects, throughout the sample. In the low–T case, the occurence of the additional local maximum around zero is a typical indication for weak localization, a quantum correction to the resistance due to self–interferring electron waves in low–dimensional materials, which we discuss in more detail below. We now turn to the nitrogen–doped graphene sample, which shows a sign change of the MR, persisting even at elevated temperatures (Fig. 6.3 (b)). This observation is especially surprising, given that the previously discussed ordinary MR mechanism generally leads to a positive MR. At 279 K, the sheet resistance at zero field is $R_S(0) = 7\,\mathrm{k\Omega}$, and we find a 4 % decrease at 8 T. At 2.5 K the relative change is significantly larger (38 %) as the sheet resistance drops from $R_S(0) \approx 36\,\mathrm{k\Omega}$ to $R_S(8\,T) \approx 25.9\,\mathrm{k\Omega}$. This observation of negative MR and a strong temperature dependence shows, that the nitrogen doping completely changes the nature of the transport. Comparing available studies (including this one),

which all observe a similar negative *MR*, suggests that this effect in graphene is strongly correlated with doping together with localization and disorder [159, 263–265]. However, the underlying mechanism is an open question. We want to attempt to understand the negative *MR* by comparing our experimental data with predictions of different models. To begin with, we consider the magnetic polaron model [264, 266]. Dopant atoms can lead to the formation of local magnetic moments and the details of the resulting *MR* depend on their interaction. We have *a priori* no good reasons to assume a large interaction between such spins in our doped graphene sheet and if present, further effects should emerge, such as a resistive hysteresis as a function of the magnetic field, which was not observed in our measurements. However, in the case of non–interacting spins, this model predicts an opposite temperature dependence to our experimental findings and hence, we rule out the contribution of magnetic polarons.

Next, we consider diffusive scattering at defects [264, 267] which should be highly enhanced by the nitrogen atoms. The magnetic field forces the charge carriers to follow a cyclotron trajectory with a radius $r_c \propto B^{-1}$ [247]. Higher magnetic fields lead to smaller radii and thus to less scattering at defect boundaries, which in turn decreases the resistance. The magnitude of the effect will increase with decreasing temperature, just as observed for our nitrogen-doped graphene sample. However, the theoretical calculations predict a magnetoresistance that depends on the square of the magnetic field [267, 268], while we observe a roughly linear dependence of the *MR* at higher fields for both room temperature and low temperatures.

Finally, localization effects of charge carriers can be a the source of a negative *MR*, and we have mentioned weak localization already for the undoped case. In the case of weak localization, the largest impact is expected at low temperatures and low magnetic fields, typically $< 1\,\mathrm{T}$. With no sign of saturation approaching 8 T, neither at 2.5 K, nor at 279 K, we exclude weak localization as a main mechanism behind our experimental results for magnetic fields above approximately 1 T. Whith no single model explaining our observation, we now consider a superposition of different mechanisms. Following the approach of Zhang et al. in Ref. [268], localization and diffusive boundary scattering may result in a linear, negative *MR*, where the weights of this superposition are temperature dependent. However, for the measurement at high temperature, we expect localization effects to diminish, and as a consequence this approach does not fit to our data at 279 K. Altogether, our observations can be explained in parts by the combined effect of different

MR mechanisms. However, a unified explanation for the low and high temperature regime together is elusive. Our results are hence calling for further theoretical work to describe a linear negative *MR* in a nitrogen–doped graphene system at all temperatures.

6.3.3.1 Crossover from weak to strong localization in doped graphene

The aforementioned signature of localization in the *MR* allows for a deeper and quantitative analysis of the degree of localization in the doped graphene sample and the undoped graphene samples. We start with a simplified model describing weak localization in graphene, where we neglect small corrections due to trigonal warping and intravalley scattering in order to allow for an easy understanding of the effect [269]. In this case, the quantum correction to the resistivity due to weak localization is given by

$$\Delta R_S = -\frac{2\,e^2\,R_S^2}{\pi\,h}\left[F(d\,B\,\tau_\phi) - F(d\,B\,\tau)\right] , \tag{6.9}$$

where τ_ϕ is the phase coherence time and we define $\tau^{-1} = \tau_\phi^{-1} + 2\,\tau_i^{-1}$. The scattering rate τ_i^{-1} describes intervalley scatttering and neglecting the intravalley contribution, we determine the elastic scattering time $\tau_e = 1/2\,\tau_i$ [265, 270]. Furthermore, we define $F(z) = \ln(z) + \Psi(1/2 + 1/z)$, with Ψ the digamma function and $d = 4\,e\,D/\hbar$ with e the elementary charge, $\hbar$ the reduced Planck constant and D the diffusion constant. The interplay between the two time scales of phase coherence and scattering leads to a reduction in the resistance for applied fields: With increasing field strenghts, electron waves gather additional phases when moving in the system. This phase leads to decoherence and reduces the destructive interference. Via this mechanism the enhanced backscattering due to weak localization is lifted already in moderate magnetic fields, thus leading to a decrease of the resistivity. To fit the model to our data, we subtract a smooth background, for which we assume that it does not originate from localization. This is done by fitting a quadratic model (compare Eq. 6.8) to the high–field data of the undoped sample and a linear model to the high–field data of the doped sample. The resulting magnetoresistance is then solely due to localization and is given by

$$\Delta R_{S,WL}(B) = R_S(B) - R_S^*(B) - (R_S(0) - R_S^*(0)) . \tag{6.10}$$

Here $R_S(B)$, $R_S(0)$ denote the measurement data and $R_S^*(B)$, $R_S^*(0)$ denote the back-

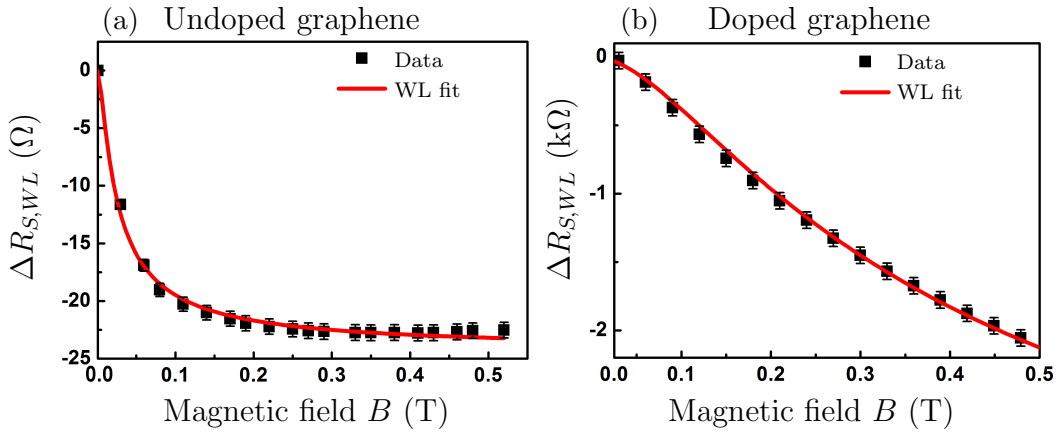

FIGURE 6.4: Background–corrected *MR* at low magnetic fields, originating from localization for the undoped sample (a) and doped sample (b). The red lines are fits of Eq. 6.9.

ground resistance as described above. The results are shown in Fig. 6.4 and using the Einstein relation for the diffusion constant $D = v_F^2\,\tau_e$ [270], we estimate the phase coherence time and the elastic scattering time (see Tab. 6.2). In order to determine the type and strength of the localization, we furthermore calculate the phase relaxation length L_ϕ and the localization length L_D based on the fit–extracted scattering times [265]:

$$L_\phi = \sqrt{D\,\tau_\phi}\,, \tag{6.11}$$

$$L_D = L_e \exp\left(\frac{\sigma_D}{e^2/h}\right)\,. \tag{6.12}$$

Herein, we use the elastic scattering length $L_e = \sigma_D\,h/(2\,e\,\sqrt{\pi\,n})$ and the Drude conductivity $\sigma_D = e\,\mu\,n$ at high temperature which we calculate using the values for n and μ derived from the Hall measurements. The values for the elastic length are both below the average defect distances obtained from the Raman spectroscopy measurements ($\Delta L \approx 10\,\text{nm}$ for both samples) because the movement of electrons is influenced not only by short range scattering centers but also by (charged) long range impurities in contrast

Sample	τ_ϕ (fs)	τ_e (fs)	D (m^2/s)	L_ϕ (nm)	L_e (nm)	L_D (nm)	Localization
2	164.9 ± 0.1	274 ± 9	0.274 ± 0.002	212 ± 1	29.5 ± 0.2	/	weak
3	16.45 ± 0.03	130 ± 6	0.130 ± 0.001	46.2 ± 0.2	1.3 ± 0.2	10 ± 4	strong

TABLE 6.2: Overview of charge transport parameters in undoped graphene (sample 2) and doped graphene (sample 3) as obtained from fits to the localization model (Eq. 6.9) and further deduced from Eqs. 6.11, 6.12. Charge carrier scattering is drastically increased and strong localization takes place in the doped case as can be inferred from these parameters (see main text).

to the Raman D peak. The ratio of phase coherence length to localization length indicates whether a system is in the weak ($L_\phi/L_D < 1$) or in the strong localization regime ($L_\phi/L_D > 1$). If this ratio is approximately unity, a system is in the transition from weak to strong localization. In the undoped case, the Drude conductivity is much larger than e^2/h rendering the expression in Eq. 6.12 meaningless and indicating clearly that charge carriers are only weakly localized. In the nitrogen–doped device however, we find an orders of magnitude change in the phase coherence time, and the scattering time, which results in $L_\phi/L_D \approx 4.5$. Hence the doped sample falls into the strong localization regime. We attribute this transition from weak to strong localization to the nitrogen defects, which form additional scattering centers and thus decrease the mean free path of charge carriers. This quantitative result also explains the strongly reduced mobility of the charge carriers that we measure for nitrogen-doped graphene compared to undoped graphene and shows that we obtain a consistent picture of the effect of doping on the charge carrier transport in graphene.

6.4 Conclusion and outlook

With our experiments, we demonstrate and quantify the significant impact of nitrogen doping on the graphene lattice structure as probed by Raman spectroscopy and on the charge carrier transport properties as probed by transport measurements at variable temperatures and magnetic fields. Samples of doped graphene and undoped graphene were fabricated by identical CVD and transfer processes and consequently, the charge transport measurements performed on undoped CVD–graphene are directly comparable to the results obtained for nitrogen-doped graphene and we can trace back the observed changes to the doping. Hall effect measurements reveal a sixfold increase of the charge carrier density due to the doping. Furthermore, the strong temperature dependence of the resistance is reminiscent of semiconductors, and fitting with Mott's variable range hopping model indicates the formation of a transport gap. A positive and largely temperature–independent high field *MR* is found for undoped graphene which we attribute to ordinary magnetoresistance mechanisms typical for metallic conduction. In contrast, a negative *MR* is observed for doped graphene persisting over the whole measured temperature range between 2.5 and 279 K and with a maximum observed change of up to 38 % at low temperatures. While this indicates a correlation between

disorder induced localization and such a large negative MR, there is no single theory, which can consistently explain the combination of our observations for the measured temperature and magnetic field range. Hence, our experimental findings call for further theoretical work on the large negative MR, also at elevated temperatures. For low temperatures and low magnetic fields, we find that fitting a weak localization model yields excellent agreement with the measurement data. Based on the extracted phase coherence times and elastic scattering times, we can quantify the strength of the localization by looking at the length scales of phase coherence and localization. Here, we find the doped sample to clearly fall in the strong (Anderson) localization regime. The deduced transport coherence times, which are directly correlated to the amount of short– and long–ranged defect scattering centers, are reduced by orders of magnitude in doped graphene as compared to undoped graphene. In summary, we find that the doping consistently increases the charge carrier density, opens a transport gap, reverses the magnetoresistance, and enhances charge carrier localization. Given the identical fabrication processes, we can attribute all these observed effects unambiguously to the additional dopants in the graphene, showing that nitrogen doping is a viable route for effectively tailoring the charge transport in doped graphene. Following this path, further exciting experiments become possible. For example, there is another approach of doping graphene by physisorbing dopants onto the graphene surface while leaving the lattice intact [9, 10]. This method is complementary to the substitutional doping presented here, where carbon atoms in the crystal lattice are replace by heteroatoms. Combining both approaches, allows for tunable and flexible transitions between n– and p–type doping in the same crystal, which demonstrates the versatility of changing the electronic properties in graphene by controlling the degree of doping [11].

Chapter 7

Magnetic properties of chromium trihalides

Chromium trihalides (CrX_3 as introduced in Sec. 1) are layered semiconductors which exhibit ferromagnetic coupling in each layer plane mediated by superexchange. We have studied the three compounds CrI_3, $CrBr_3$ and $CrCl_3$ carefully by SQUID magnetometry and moreover, we demonstrate that few–layer crystals can be readily obtained by mechanical exfoliation. We find an unusual temperature dependence of the magnetization, which we further analyze by quantifying the temperature evolution of the magnetocrystalline anisotropy constant K_u. In the iodide, we find it strongly changes from $K_u = (300 \pm 50)\,\mathrm{kJ/m^3}$ at 5 K to $K_u = (43 \pm 7)\,\mathrm{kJ/m^3}$ at 60 K, close to the Curie temperature. We draw a direct comparison to $CrBr_3$, which serves as a reference, and where we find results consistent with literature. In particular, we show that the anisotropy change in the iodide compound is more than 3 times larger than in the bromide. A further analysis using a classical model shows that the anisotropy constant scales with the magnetization at any given temperature below the Curie temperature. This scaling results from local spin clusters having thermally induced magnetization directions that deviate from the overall magnetization, and it indicates that the temperature dependence of the magnetization can be explained by a dominant non–constant uniaxial anisotropy. These results have great signficance for the understanding of the predicted magnetic coupling in monolayer crystals of these materials. The analysis of CrI_3 and $CrBr_3$ has also been detailed in a manuscript [21].

7.1 Magnetic properties of CrX_3

Magnetism in chromium trihalides arises from magnetic superexchange coupling of the Cr^{3+} ions mediated via X^- ions. The Goodenough–Kanamori–Anderson rules (see Sec. 2.4.3) can be applied to CrX_3 systems predicting a strong ferromagnetic intralayer coupling for all three compounds, CrI_3, $CrBr_3$ and $CrCl_3$. This is suprising as it is in contrast to many other semiconductors and insulators, where superexchange leads to antiferromagnetism and only a few other non–metallic systems show ferromagnetism, such as EuS, EuO, ferrites and some garnets. A detailed description of possible superexchange paths can be found in Refs. [23, 271]. In order to apply the GKA rules correctly, it is necessary to know the crystal structure of these trihalides. The CrX_3 crystals exist in two different phases, namely in a monoclinic structure ($AlCl_3$–type) with space group $C2/m$ at elevated temperatures and at lower temperatures in a trigonal structure (BiI_3–type) with space group $R\bar{3}$. While for CrI_3 and $CrBr_3$ there is a consensus in literature about these symmetry groups [22], there is controversy for $CrCl_3$ [272]. In either case, the layers extend in the ab plane and are stacked along the c axis. The phase transition occurs at approximately 180 K for CrI_3 and the two phases coexist for a significant temperature range [22]. For $CrBr_3$ the transition takes place at temperatures around 420 K and for $CrCl_3$ at around 240 K [273]. Besides the coupling of magnetic ions within the layer planes, there is also a much weaker coupling between the layers (see Tab. 7.1). While for CrI_3 and $CrBr_3$ the interlayer coupling is also ferromagnetic [274], in $CrCl_3$ it is antiferromagnetic [272, 274, 275]. In Tab. 7.1 we summarize the magnitudes of intralayer (J) and interlayer (J') coupling in CrI_3, $CrBr_3$ and $CrCl_3$.

7.2 Experimental details

The compounds CrI_3, $CrBr_3$ and $CrCl_3$ were prepared directly from the elements in an evacuated quartz tube using a CVD method as described in Ref. [21] resulting in plate–like crystals that have lateral extension of millimeters while being hundreds of micrometers thick (see Fig. 7.1).[1] For the measurement of their magnetic properties we have used a SQUID magnetometer (QuantumDesign MPMS XL).[2] Samples of each

[1] I thank D. W. in the group of Prof. Dr. B. L. at the Max Planck Institute for Solid State Research in Stuttgart for providing the samples.

[2] I thank F. R., who helped to carry out a large part of the presented measurements and who was a helping hand in processing all measurement data.

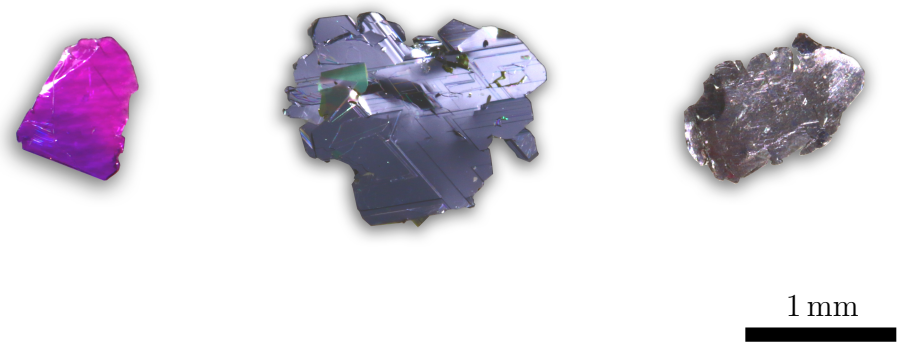

FIGURE 7.1: Collection of pictures of CrX_3 crystals. From left to right: $CrCl_3$, $CrBr_3$, CrI_3. I thank P. K. for his support in photographing the crystals and processing the images.

compound have been loaded into the SQUID in two configurations. Firstly, such that the magnetic field H is aligned in parallel to the stacking direction (i.e. parallel to the crystallographic c axis and perpendicular to the crystal planes) and secondly, such that H is perpendicular to the stacking direction (i.e. perpendicular to the c axis and parallel to the crystal planes). Here, we measure H in A/m and the conversion into teslas is done by multiplying with μ_0, the vacuum permability. Mechanical support for the loading procedure is granted by clamping the crystals between two halfs of a small (length $< 5\,\mathrm{mm}$) bisected cigarette filter, which adds a negligible diamagnetic moment to the measurement signal. For the calculation of the volume magnetization, we weigh the crystals after the magnetometry measurements, using a laboratory balance (Kern ABT 220-5DM). The small size of the crystals implies a low mass (typically in the milligram regime), resulting in this quantity to yield the largest contribution to the

type	J (meV)	J' (meV)	T_{crit} (K)
CrI_3	1.16	0.15	68 [274], 61 [22]
$CrBr_3$	0.71	4.27×10^{-2}	32.7
$CrCl_3$	0.45	-1.54×10^{-3}	16.8

TABLE 7.1: Exchange coupling strengths and critical temperatures for magnetic ordering T_{crit} of the compounds CrI_3, $CrBr_3$ and $CrCl_3$. For the ferromagnetic iodide and bromide, $T_{crit} = T_C$, the Curie temperature, while for the antiferromagnetic chloride, $T_{crit} = T_N$, the Néel temperature. The magnitudes of the interlayer coupling have mainly been derived from field dependent susceptibility, magnetization or magnetic torque measurements. If not otherwise stated, the values are taken from Ref. [274].

absolute measurement error. However, the measurements of the magnetic moments of a sample exhibit comparatively low errors due to the good signal to noise ratio, allowing us to deduce robust conclusions for instance about the temperature dependence. Masses and mass densities are listed in Appendix A.

7.3 Temperature dependence of the magnetization

After preparing and loading the samples into the SQUID, we measure the projection of the magnetic moment along the (vertical) z direction at variable temperatures. In Fig. 7.2 we present the magnetization M of all investigated compounds as a function of temperature and for the two different measurement configurations ($H \parallel c$ and $H \perp c$) at three different field magnitudes (0.1 T, 1 T and 5 T). Below the Curie temperatures (see Tab. 7.1), we observe with further decreasing temperature an increase of M which saturates eventually at liquid helium temperatures. When we apply a field of 5 T, M saturates always at the same value, irrespective of whether we apply $H \parallel c$ or $H \perp c$. For CrI_3 the saturation value is $M_{S,5\,T} = (206.1 \pm 10.3)\,\mathrm{kA/m}$ which corresponds to a magnetic moment of $(3.00 \pm 0.15)\,\mu_B/F.U.$, where μ_B denotes the Bohr magneton and *F.U.* stands for formula unit. The latter is in excellent agreement with the expected spin–only saturation moment of Cr^{3+} ions $\mu_{\mathrm{sat}} = g\,S = 3\,\mu_B$, where S is the total spin quantum number and g the electron Landé factor [22]. However, for a smaller field of 1 T, M saturates at the same value only in the $H \parallel c$ configuration, while in the $H \perp c$ configuration, M remains at a significantly smaller saturation value of $M^{perp}_{S,1\,\mathrm{T}} = M^{parallel}_{S,1\,\mathrm{T}} - \Delta M = (94.7 \pm 3.5)\,\mathrm{kA/m}$. Obviously, 1 T field strength is not sufficient to align all spins in the layer plane. Generally, such a difference ΔM can be attributed to the effect of the magnetocrystalline anisotropy[3] and here, the c axis is found to be the easy axis. Surprisingly, for $H \perp c$ there is an additional sign change in dM/dT at approximately 53 K which cannot be explained by constant magnetocrystalline anisotropy and requires a more complex analysis as detailed below.

In $CrBr_3$, the c axis is found to be the easy axis, too, while the anisotropy is clearly smaller. For the bromide 1 T is sufficient to saturate M in both configurations at $M_{S,5\,\mathrm{T}} = (271.1 \pm 21.1)\,\mathrm{kA/m}$ (equivalent to $(3.09 \pm 0.24)\,\mu_B/F.U.$). This saturation value is not reached anymore when we apply magnetic fields as low as 100 mT and we

[3] Due to the (macroscopic) size of the crystallites, we can neglect shape anisotropy.

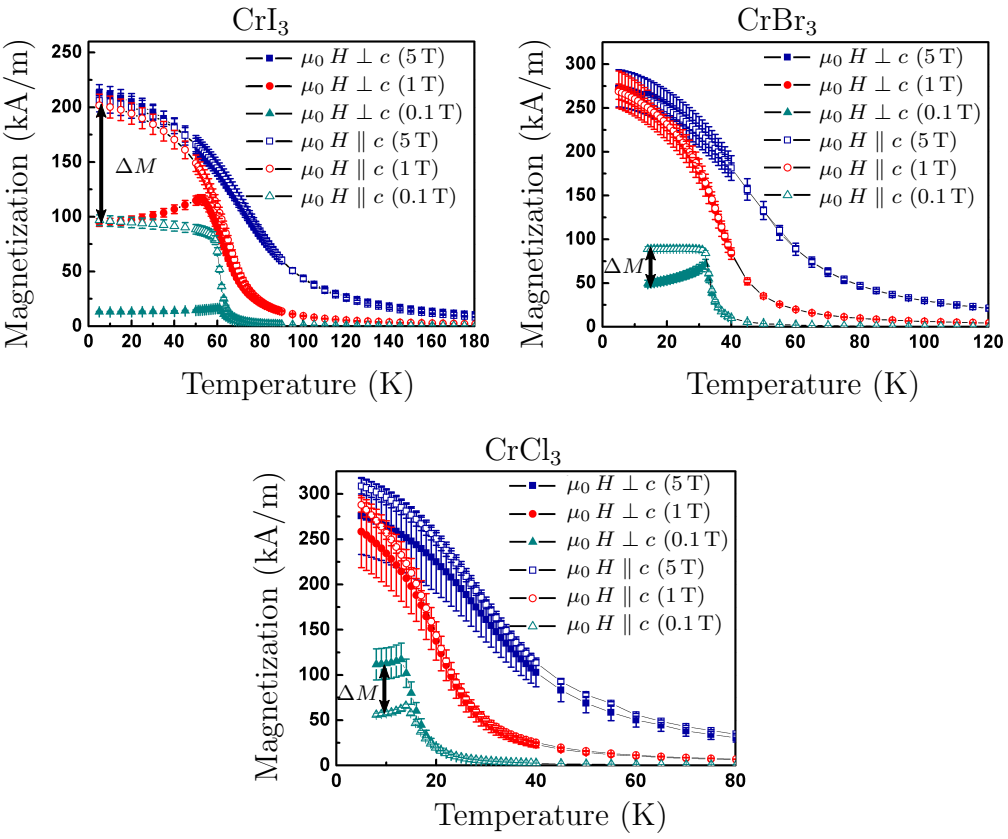

FIGURE 7.2: Magnetization of CrX_3 as a function of temperature measured at different magnetic fields and in two different configurations: $\mu_0 H \perp c$ and $\mu_0 H \parallel c$. For small fields the magnetocrystalline anisotropy leads to a strong difference ΔM of the effective saturation value for the different configurations. Lines are guides for the eye.

observe a discrepancy of $\Delta M \approx 39\,\mathrm{kA/m}$ between the different configurations. Qualitatively similar to the iodide, dM/dT changes sign at approximately 30 K for $\mu_0 H = 0.1\,\mathrm{T}$.

In $CrCl_3$, we find a maximum saturation value of $M_{S,5\,\mathrm{T}} = (308.7 \pm 8.5)\,\mathrm{kA/m}$ (equivalent to $(2.96 \pm 0.10)\,\mu_B/F.U.$) and fields $\geq 1\,\mathrm{T}$ yield identical values (within their uncertainties). Looking at the 100 mT data however, we observe an opposite behavior as compared to the iodide and the bromide. Here, the $H \perp c$ configuration leads to larger magnetization values than the $H \parallel c$ configuration and the change in sign of dM/dT is present in both configurations, probably resulting from a complex interplay of antiferromagnetic ordering and temperature dependent anisotropy. Hence, we cannot unambiguously identify the c axis as an easy axis anymore.

7.4 Magnetic hysteresis loops

In order to explain the unusual magnetization behavior discussed above that cannot be reproduced with the conventional assumption of temperature independent magnetic properties, such as the anisotropy, we ascertain the impact of the magnetocrystalline anisotropy[4] now in detail by focusing on magnetic hysteresis loops, which are a standard technique to characterize magnetic properties, such as magnetic remanence and coercivity. For a full cycle, we ramp the magnetic field to a maximum value of $\mu_0 H = +5\,\mathrm{T}$ in order to saturate the magnetization of the sample. We then decrease the field step–wise and take three consecutive measurements at fixed field values until $\mu_0 H = -5\,\mathrm{T}$ is reached. Subsequently, we measure in the same way reversing the field again up to $\mu_0 H = +5\,\mathrm{T}$ before we ramp the field back to zero. The maximum remanence we observe is approximately 0.75 % of M_S accompanied by a low coercive field of $H_c \lesssim 10.3\,\mathrm{kA/m}$ for CrI_3 in the $H \parallel c$ configuration at 5 K. While the crystallites produce measurement signals much larger than the intrinsic measurement accuracy of the SQUID, remanent magnetization and coercive field are vanishing at higher temperatures in CrI_3, and neither are they detectable at any temperature for the other two compounds. Hence, we can use all data points for every field step to build the average and use the standard deviation as the error for the magnetization measurements. The closed hysteresis loops suggest that chromium trihalides are magnetic extraordinarily soft materials, where the magnetization follows the applied magnetic field direction virtually instantaneously during reversal. This observation is consistent with previous reports [22] and we propose that the reason lies in the small interlayer exchange coupling for the these compounds (see Tab. 7.1). For CrI_3 this energy scale is a factor 2.7 lower than T_{min}/k_B, where $T_{min} = 5\,\mathrm{K}$ is the lowest measurement temperature and k_B is the Boltzmann constant. This leads to a vanishing interlayer coupling and thus to an immediate randomization of the magnetization throughout the layers when the field is relaxed back to zero, even though, the intralayer coupling is strong. In order to observe a remanent net magnetic moment and the resulting coercive field, the low-field regime should be revisited, ideally using remanence-free Helmholtz coils instead of superconducting ones and measured at millikelvin temperatures, which is however beyond the scope of this work and not possible with our currently used setup. We repeat the hysteresis loops in the $H \perp c$

[4] I would like to thank in particular Prof. Dr. H.–J. E. for his stimulating input in the discussion of the $M(T)$ curves.

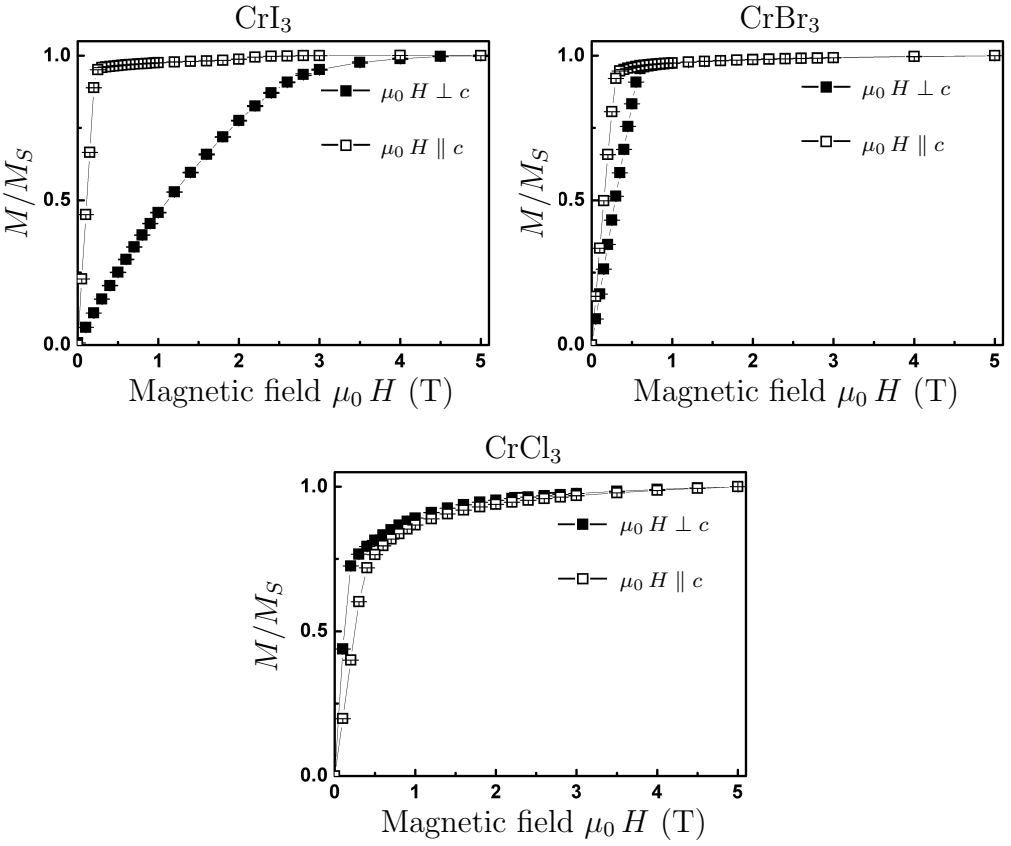

FIGURE 7.3: Positive branch of magnetic hysteresis loops for all CrX_3 compounds at a temperature of 10 K in both measurement configurations. The field at which the magnetization starts to saturate, H_{sat} is extracted from these curves and used to calculate the magnetocrystalline anisotropy (see main text). Lines are a guide for the eye.

configuration, which show distinct differences as compared to the parallel configuration. In Fig. 7.3 we show the averaged magnetization normalized to the saturation magnetization for all three compounds and in both measurement configurations at a temperature of $T = 10\,\mathrm{K}$.[5] If we apply $H \parallel c$, we observe a sharp rise of the magnetic moment in the iodide and bromide with increasing field, followed abruptly by a state of saturation when a certain magnetic field H_{sat} is reached. In contrast, in the $H \perp c$ configuration, the slope of $M(H)$ in the low–field, i.e. the magnetic susceptibility $\chi = dM/dH$, is smaller and H_{sat} shifts to higher field values. For $CrCl_3$ the behavior is reversed with respect to the magnetic field direction, similar to the temperature dependent measurements. Due to this more complex behavior of the chloride, a further analysis would go beyond the scope of this thesis and we focus on CrI_3 and $CrBr_3$ in the following discussion of the magnetocrystalline anisotropy.

[5]Full hysteresis loops are shown in Appendix B.

7.5 Magnetic anisotropy in CrI_3 and $CrBr_3$

The saturation field H_{sat}, which can be observed in the measurements in the $H \perp c$ configuration is a direct measure of the magnetocrystalline anisotropy. The magnetocrystalline anisotropy contributes to the micromagnetic energy density with a term

$$E_A = K_u \sin^2(\theta - \phi) \tag{7.1}$$

In this formula, K_u denotes the uniaxial anisotropy constant, θ the direction of the preferred magnetization and ϕ the direction in which the magnetization points. If we consider the sample being fully magnetized above H_{sat}, the single domain state becomes a valid approximation for CrI_3 and $CrBr_3$, which can be described by the Stoner–Wohlfarth model [276]. Within this model, the anisotropy constant can be derived via

$$\frac{2\,K_u}{M_S} = \mu_0\, H_{\mathrm{sat}}\,. \tag{7.2}$$

We extract H_{sat} from the hysteresis loops by determining the point of maximal curvature of the hysteresis curve directly below the region of saturation. In order to obtain the acurate value for the saturation magnetization, we correct for a small paramagnetic contribution in the saturation region by subtracting the slope of a linear fit in the field intervals $|H| > |H_{\mathrm{sat}}|$. Measuring hysteresis loops for various temperatures allows us then to deduce the anisotropy constant as a function of temperature for both compounds, CrI_3 and $CrBr_3$, as shown in Fig. 7.4. The temperature dependence of $CrBr_3$'s anisotropy has been reported in the early stages of CrX_3 research by Dillon [24, 277] and in Fig. 7.4 (b), we plot our measurement together with the temperature dependence extracted from Ref. [24]. For the whole temperature range, we find an excellent agreement, corroborating the validity of using Eq. 7.2, where the low–temperature anisotropy amounts to $K_u = (86.1 \pm 6.0)\,\mathrm{kJ}/m^3$. For CrI_3 on the other hand, this is to the best of our knowledge the first determination of a temperature dependence in K_u. As in $CrBr_3$, the anisotropy decreases towards T_C. At 5 K, the experimental value is $K_u = (301 \pm 50)\,\mathrm{kJ/m^3}$. We now compare this with numerical calculations of the CrI_3 system based on density functional theory.[6] The details of the calculation are described

[6] I thank Dr. N. S. in the group of Prof. Dr. U. S. at the Materials Science and Engineering and Physical Sciences and Engineering Division of the King Abdullah University of Science and Technology (KAUST) in Thuwal for providing these calculations.

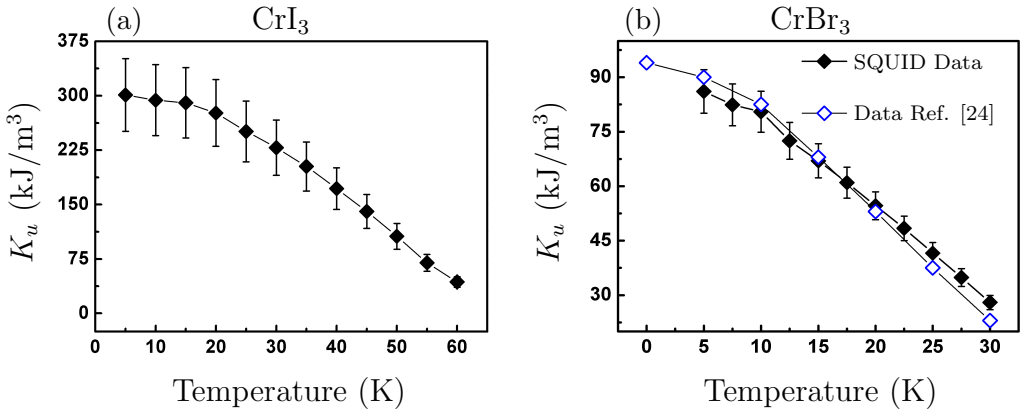

FIGURE 7.4: Temperature dependence of K_u. For CrI_3 (a) as well as for $CrBr_3$ (b) a decrease of K_u is clearly visible as T is increased towards T_C. For comparison, we have extracted from Ref. [24] the temperature dependence for the anisotropy in $CrBr_3$ and we find an excellent agreement with our measurement. Lines are a guide for the eye.

in Ref. [21]. In the calculation, the magnetic anisotropy energy is determined as the difference between the total energies obtained for magnetization along the a and c axes, resulting in 0.5 meV, with c being the easy axis. Dividing by the volume of the unit cell of CrI_3 then yields K_u^{theo}. We find that the experimental value coincides with the theoretically expected value of $K_u^{theo} = 290\,kJ/m^3$ showing the validity of this approach. To analyze the observed temperature dependence of our anisotropy data, we consider that the magnetic anisotropy is a product of the interplay between the spontaneous magnetization and the crystal lattice. Often, the temperature dependence of the anisotropy is found to be stronger than that of the spontaneous magnetization. In a simple classical theory, anisotropy and magnetization are linked by the relation

$$\left\langle K^{(n)} \right\rangle \propto M_S^{n(n+1)/2}, \tag{7.3}$$

where $\left\langle K^{(n)} \right\rangle$ is the anisotropy expectation value for the n^{th} power angular function [278, 279]. In case of uniaxial anisotropy, we obtain $n = 2$ and in case of cubic anisotropy $n = 4$, leading to an exponent of 3 and 10, respectively. To check whether this model can describe our temperature dependence, we show in Fig. 7.5 the experimentally determined temperature dependences plotted as $K_u/K_u(5\,K)$, $M_S/M_S(5\,K)$, $(M_S/M_S(5\,K))^3$, $(M_S/M_S(5\,K))^{10}$. The comparison clearly shows, that the scaling $K_u(T)/K_u(5\,K) = ((M_S(T))/M_S(5\,K))^3$ is the most appropriate fit. This is in line with the predominant uniaxial anisotropy found from the magnetometry and thus explains the temperature dependence of the uniaxial anisotropy in both systems, CrI_3 and

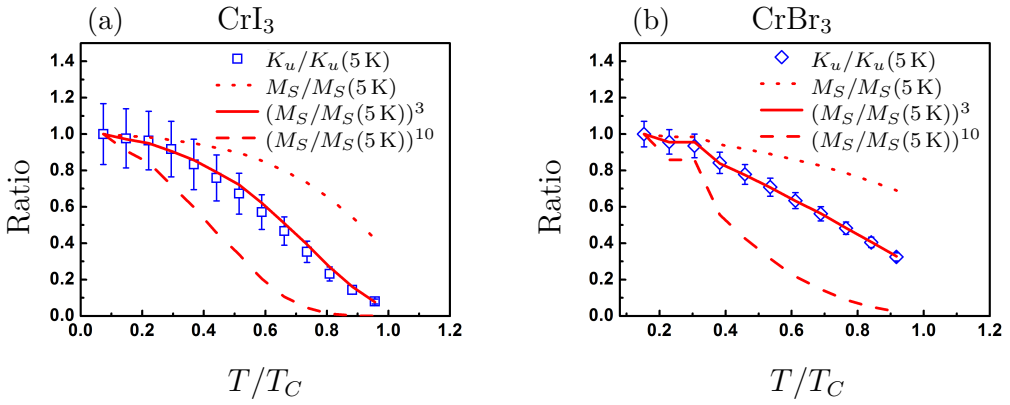

FIGURE 7.5: The ratio $K_u/K_u(5\,\mathrm{K})$ for CrI_3 (a) and $CrBr_3$ (b) plotted in comparison to the ratio $((M_S(T))/M_S(5\,\mathrm{K}))^{(n(n+1)/2)}$, where $n = 1$,2, and 4. For both compounds, the anisotropy scales to the third power of $((M_S(T))/M_S(5\,\mathrm{K}))$, in line with theoretical expectations for a predominant uniaxial anisotropy (leading to $n = 2$). Error bars of the $((M_S(T))/M_S(5\,\mathrm{K}))$ ratios are omitted for the sake of clarity. We use $T_C = 68\,\mathrm{K}$ for CrI_3 and $T_C = 32.7\,\mathrm{K}$ for $CrBr_3$.

$CrBr_3$. However, it is noteworthy to mention, that in this theory by Zener and Carr, the anisotropy constants are explicitly independent of temperature and only the crystallographic symmetries determine the anisotropy. The observed decrease of K_u with increasing temperature arises from solely from a large number of local spin clusters, fluctuating randomly around the macroscopic magnetization vector, activated by the non–zero thermal energy. These insights into the nature of the magnetocrystalline anisotropy are key for the understanding of possible ferromagnetism in CrX_3 compounds with a drastically reduced number of layers. While in pure isotropic two–dimensional systems, no magnetic order is expected [64], mechanical corrugations and magnetic anisotropy are possible pathways to establish stable ferromagnetism nevertheless in quasi–two–dimensional single CrX_3 layers, so that the determination of the anisotropy is a key step.

7.6 Conclusions and outlook

In summary, we carried out an in–depth analysis of the magnetocrystalline anisotropy in CrI_3 and in $CrBr_3$ revealing that the complex magnetization dependence on temperature results from temperature dependence of the magnetocrystalline anisotropy. While for $CrBr_3$, the agreement with previous experiments is excellent, we find a more than three times stronger temperature evolution of K_u in CrI_3. The experimentally obtained

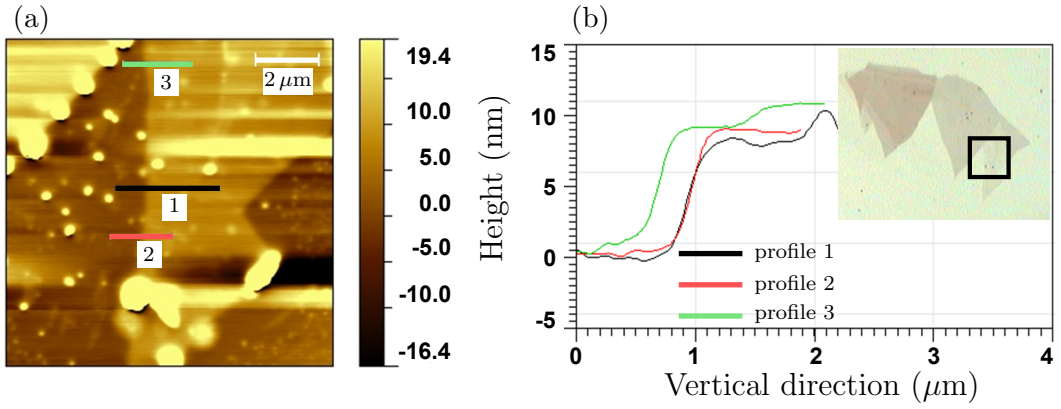

FIGURE 7.6: Exfoliated $CrBr_3$ flake on a GaAs substrate. In (a) an AFM image of the thinnest part of the flake is shown. Three line scans are performed to measure the height of the flake as shown in (b). The extracted height of approximately 8.5 nm corresponds to twelve layers. The inset shows an optical microscopy image of the same flake. The area marked by the black box is the location where the AFM image was taken.

value at low temperature $K_u = (301 \pm 50)\,\mathrm{kJ/m^3}$ is within the error identical to a theoretically derived value $K_u = 290\,\mathrm{kJ/m^3}$ for 0 K and agrees with a value determined by FMR. We find that the temperature dependence can be explained based on a classical model leading to a scaling of the temperature dependence with a critical exponent that results from a dominant uniaxial anisotropy combined with thermal activation effects that locally lead to magnetization deviating from the ensemble value. Even with this understanding of the bulk compounds, our results show that the phenomenology of magnetism in CrX_3 compounds still awaits further exploration. For example, despite the strong ferromagnetic coupling within layers of CrX_3, significant magnetic remanence of the whole sample is regularly absent. We explain this absence with the low interlayer coupling and calling for magnetometry in tailored set-ups, e.g. capable of reaching millikelvin temperatures. To understand the bulk magnetic properties of chromium trihalide compounds is furthermore a key first step to using these compounds as single layers in spintronic applications. Our calculations on CrI_3, which also covered the monolayer limit, show a drastic increase of the Curie temperature to 138 K and recently Wang et al. suggested that the critical temperature can be further tuned upwards by carrier doping [280]. We have tested to obtain such single layers by mechanical exfoliation using sticky tape In Fig. 7.6 we show an example of an exfoliated $CrBr_3$ flake. The different optical contasts correspond to different layer thicknesses, where darker contrast means a larger number of layers. Atomic force microscopy reveals that the thinnest part of the

flake has a thickness of approximately (8.5 ± 0.5) nm which corresponds to twelve layers. Finally, the experiments show, that most of the obtained crystals are not stable under ambient atmosphere, with a possible degradation mechanism according to the reaction: $CrX_3 + x\,H_2O \rightarrow CrX_3 \cdot x\,H_2O$. An illustration of this degradation process in $CrBr_3$ can be found in the Appendix B. While we have found $CrCl_3$ to be the most stable compound, we suggest to conduct the exfoliation procedure of the other two compounds under inert gas atmosphere and use encapsulation techniques, e.g. with hexagonal boron nitride similar to encapsulation of graphene layers [281]. Only then, this exciting materials class will be able to show its full potential for ultra–thin spintronics.

Chapter 8

Conclusion and outlook

In summary, we studied in–depth three different low–dimensional materials, namely bottom–up synthesized graphene nanoribbons, nitrogen–doped graphene and magnetic semiconducting chromium trihalides, which all have exciting properties. First, we have demonstrated, how we can make use of the versatile GNR synthesis by a simple ambient–pressure CVD method. This technique is capable of high–throughput and scalable growth of various GNR structures at low cost [82, 184]. After the optimization of the device fabrication described in Sec. 4, these GNR structures are readily integrated in electronic devices, such as GNR network FETs, enabling the fundamental charge transport experiments presented in Sec. 5. Here, we measured six different GNR structures, which were aGNR 5, aGNR 7, aGNR 9, GNRNW $(9,6),(2,15)$, and the doped species GNRNW N–N $(9,6),(2,15)$ and GNRNW N–S $(9,6),(2,15)$. Among these six structures, aGNR 5 and aGNR 9 are predicted by theory to exhibit comparably low band gaps, and we have carried their characterization to a wide range of temperatures, electric fields and magnetic fields. These experiments enable us to pin down charge carrier hopping as the dominant charge transport mechanism. By applying a scaling of the channel current density as $J/T^{\alpha+1}$ (α being the exponent of a power law $J \propto T^{\alpha}$ at low bias) on the basis of a nuclear–tunneling assisted hopping model, we find for each of the two structures a single curve onto which all $J(V,T)$ data collapses. The structural similarity of the devices and the fact that charge transport signatures at room temperature are comparable, strongly suggest that the same charge transport mechanism is operational in any GNR–based electronic device whenever carriers have to cross inter–ribbon junctions. Understanding the physics of charge transport is extremely relevant for the

Material	μ ($\mathrm{cm^2\,V^{-1}\,s^{-1}}$)	n ($\mathrm{cm^{-2}}$)	Δ (eV)	Conduction mechanism
aGNR 5	0.01 [*]	$\geq 10^{12}$ [*]	1.7 [6]	hopping [*]
aGNR 7	10^{-5} [*]	n/a	3.8 [6]	hopping [*]
aGNR 9	10^{-4} – 10^{-3} [*]	$\geq 10^{11}$ [*]	2.1 [6]	hopping [*] tunneling [222]
GNRNW $(9,6),(2,15)$	10^{-4} [*]	n/a	1.6 [79]	hopping [*]
SLG	$\geq 10^{3}$ [*]	$\geq 10^{12}$ [*]	0 [29]	band–like [*]
SLG encapsulated	$\geq 10^{5}$ [160]	$\geq 10^{11}$ [160]	0 [29]	band–like [160]
Doped SLG	$\geq 10^{1}$	$\geq 10^{13}$ [*]	≈ 0.09 [*]	hopping [*] and [159]
Epitaxial graphene	$\approx 10^{4}$ [282]	$\geq 10^{12}$ [282]	0 [187]	band–like [282]
TG	$\geq 10^{4}$ [147]	$\approx 10^{11}$ [147]	0 [187]	band–like [147]

TABLE 8.1: Overview of electronic properties of various graphene materials. The mobilities are extracted from gate dependent transport measurements and Hall measurements. Charge carrier densities in unprotected devices are typically dominated by extrinsic doping. The transport gaps for the GNRs, (encapsulated) SLG, epitaxial graphene and TG are theoretically expected band gaps. The transport gap of doped graphene is the one determined in Sec. 6 and in this system mobility and charge carrier density stronlgy depend on the doping level. Note that there is a large variety in epitaxial graphene, depending on the growth conditions and number of layers. The values marked by [*] are from this work. This overview and references herein are not exhaustive.

interpretation of any experiment dealing with GNR–based devices and for the future development of GNR–based electronics. In order to give an overview of key parameters of charge transport, we summarize state–of–the–art values for charge carrier mobility μ, charge carrier density n, transport gap (e.g. band gap) Δ and the dominant charge transport mechanism for various graphene materials in Tab. 8.1. Here, we can see that hopping transport is regularly accompanied by low values of μ, and large mobilites are only possible in protected SLG and TG systems with delocalized electron transport. Therefore, based on our results, we understand the disparity of mobilities measured in lateral transport experiments (this work) compared to mobilities estimated from terahertz spectroscopy, which are in the order of $10^2\,\mathrm{cm^2\,V^{-1}\,s^{-1}}$ for aGNR 9 samples [184]. The performances of FET devices fabricated are limited by inter–ribbon hopping processes, limiting the possible intrinsic transport properties of the single GNRs. Despite the advances in the understanding of bottom–up GNR–based electronic devices, where we contribute with this work by elucidating the charge transport mechanism in

an important class of such devices, we see that this field is still in its early stages. In particular, the growth of longer GNRs through optimization of the CVD process will enable the engineering of electrical contacts for single crystalline GNR units. This is an important prerequisite to reach the realm of delocalized band transport. Together with the development of wider GNRs with smaller band gaps, the availability of band transport dominated devices will be key for a possible use of GNRs in future electronics. Up to now, the band gaps of the bottom–up GNRs used for device studies are several hundred millielectronvolts above the technologically relevant silicon band gap of approximately 1.1 eV [31]. In parallel, we started to explore graphitic electrodes (see Sec. 4.3.3), where carbon–carbon interactions improve the electrical contact, which will also facilitate transport experiments on chemically derived GNRs. Finally, extended research on SLG showed that encapsulation and atomically flat substrates (e.g. hexagonal boron nitride) [160] will eventually be required to maximize device performance of such sensitive low–dimensional systems. Following these routes, GNRs may provide practical solutions to the current challenges for nano–electronic, optoelectronic, and photonic devices in the future.

In Sec. 6, we demonstrated that substitutional doping of graphene, e.g. by nitrogen, is an alternative pathway towards low–dimensional materials with tailor–made charge transport properties. In our experiments, we find that increasing the level of N-doping leads to a gradual change in the shape of the magnetoresistance accompanied with a sign change from positive to negative magnetoresistance. Further studies combining structural and electrical investigation will complete the picture of the electronic structure changing with the configuration and arrangement of the nitrogen dopants in graphene. As an example, it has been shown that photochemical doping allows one to tune the Fermi level of graphene locally with complex and controllable spatial doping profiles opening the way for novel applications such as optically defined p–n–junctions [11].

Lastly, we investigated pathways towards monolayer materials with ferromagnetic order in Sec. 7. Ferromagnetic monolayers of CrI_3 have been demonstrated only recently [20]. In this work, we focussed in particular on the magnetic anisotropy of CrI_3 and $CrBr_3$ tackling a key open question, which is the stabilization of ferroic order in these layered two dimensional systems. The magnetocrystalline anisotropy is a possible ingredient that can allow one to overcome the limitations set by the Mermin-Wagner theorem [64], which prohibits magnetic ordering in two or less dimensions. In this work, we find for CrI_3 that

the magnetocrystalline anisotropy constant strongly changes from $K_u = (300 \pm 50)\,\mathrm{kJ/m^3}$ at 5 K to $K_u = (43 \pm 7)\,\mathrm{kJ/m^3}$ at 60 K, close to the Curie temperature and compare this change with the temperature evolution of K_u in $CrBr_3$. Our analysis shows that the temperature dependence of the magnetization in these compounds can be explained by a dominant uniaxial anisotropy. Additionally, theoretical calculations show not only qualitative, but even quantitative agreement. Therefore, we find the anisotropy to be a key aspect to understanding the magnetism in this class of materials paving the way towards the exploration of unexpected and new phenomena such as spin–filtered light emitting diodes [28].

Appendix A

Additional material for Chapter 4

A.1 Raman mapping of graphene nanoribbon films on silicon dioxide

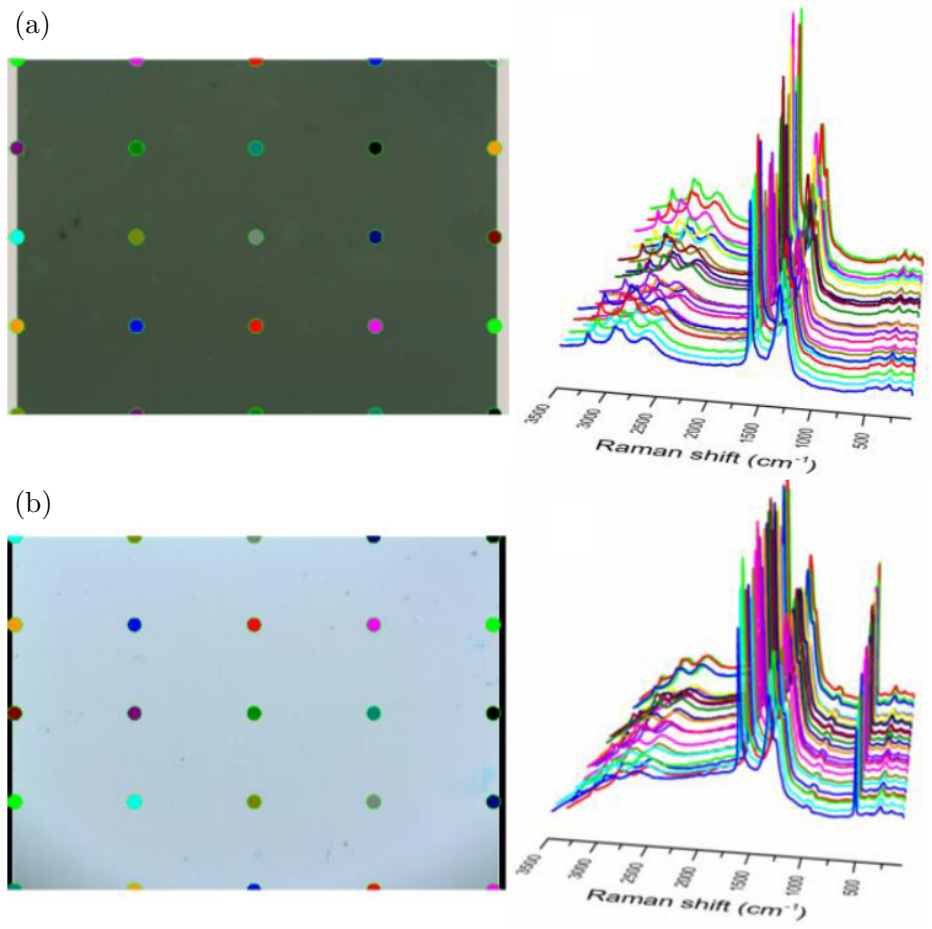

FIGURE A.1: Optical microscope images and Raman mapping of chevron-type GNRs transferred on fused silica (a) with a field of view of $50 \times 65\,\mu$m and on a silicon wafer (b) with a field of view of $50 \times 330\,\mu$m, respectively. Adapted and reprinted with permission from Ref. [82]. Copyright 2016 American Chemical Society.

Appendix B

Additional material for Chapter 5

B.1 Raman spectra of various graphene nanoribbons

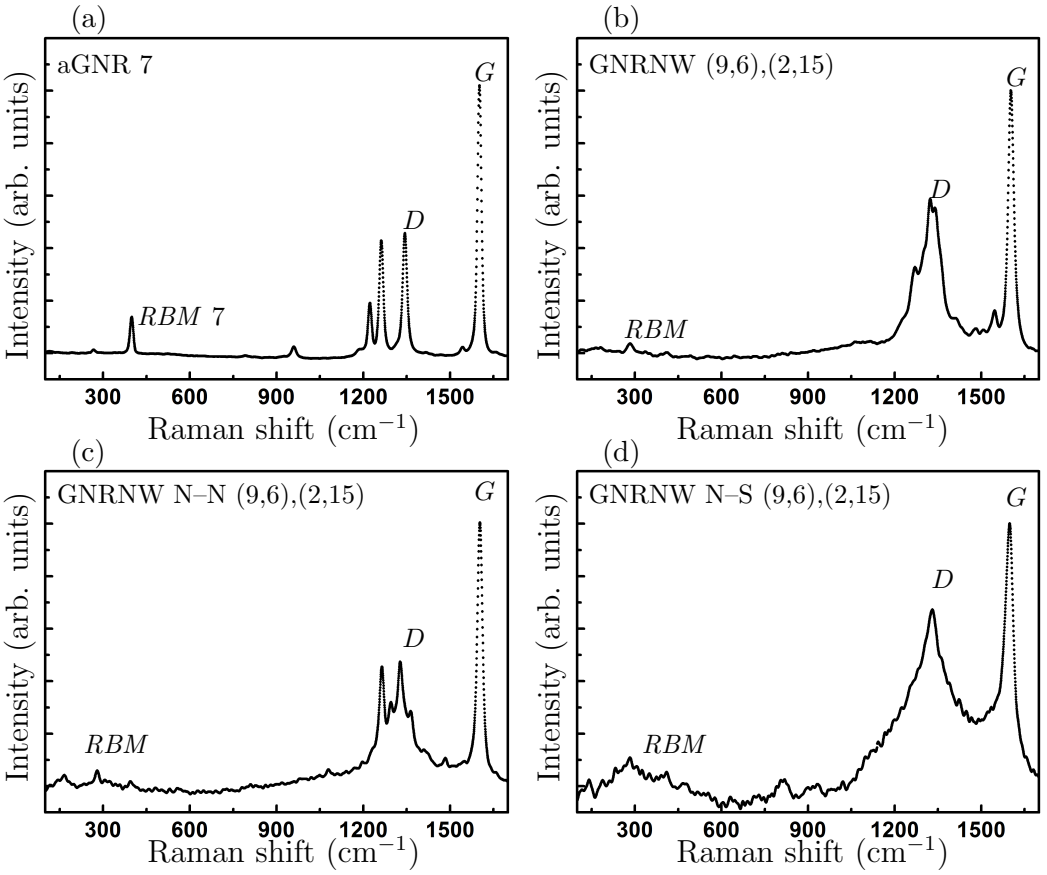

FIGURE B.1: Raman spectrum of an aGNR 7 film (a), a GNRNW (9,6),(2,15) film (b), a GNRNW N–N (9,6),(2,15) film (c) and a GNRNW N–S (9,6),(2,15) film, all on a Si/SiO_2 surface. Analogous to the case of aGNR 5 and aGNR 9, the low–energy lines can be attributed to the width–dependent RBMs (see Ref. [82]). For aGNR 7, we find the RBM at approximately 399 cm^{-1} and for GNRNW (9,6),(2,15), GNRNW N–N (9,6),(2,15) and GNRNW N–S (9,6),(2,15) at approximately 280 cm^{-1}.

B.2 Current–voltage characteristics of networks of various GNR species

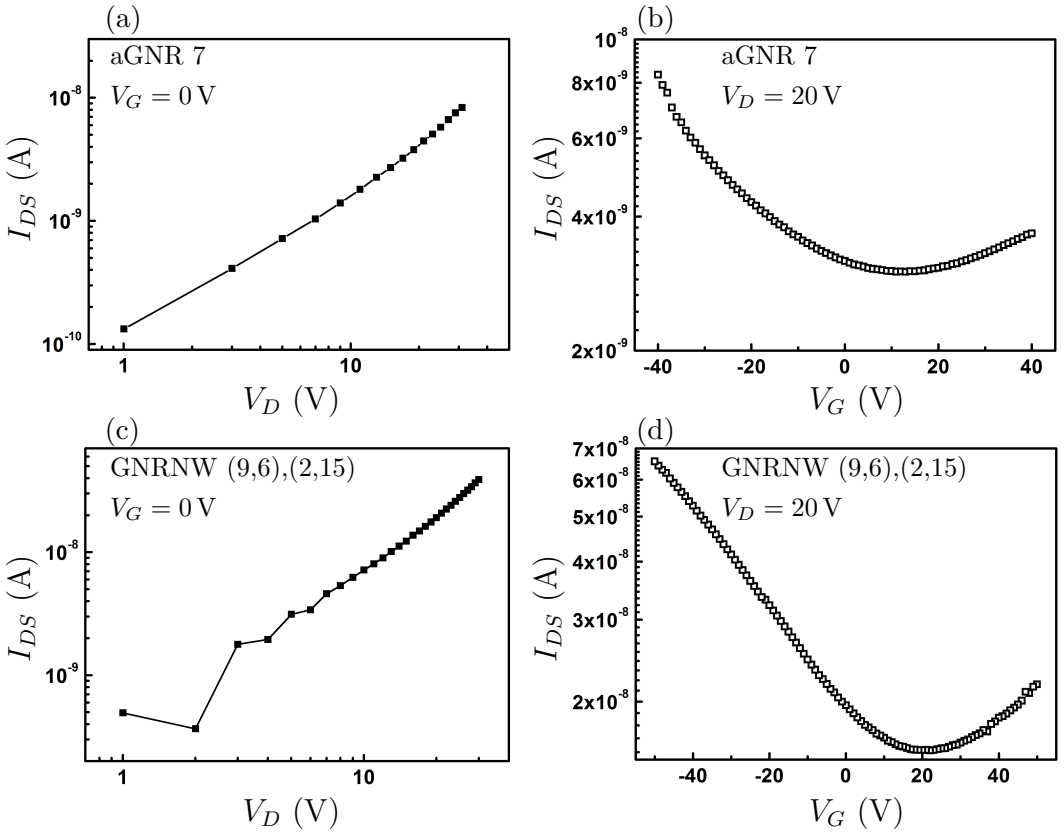

FIGURE B.2: I–V and transfer curves of aGNR 7 ((a), (b)) and GNRNW (9,6),(2,15) ((c), (d)) gated across 300 nm SiO_2 with a channel length of $L = 10\,\mu$m. The channel current follows a power law similar to the case of aGNR 5 and aGNR 9. However, the response to the gate voltage is smaller. Lines are guides for the eye.

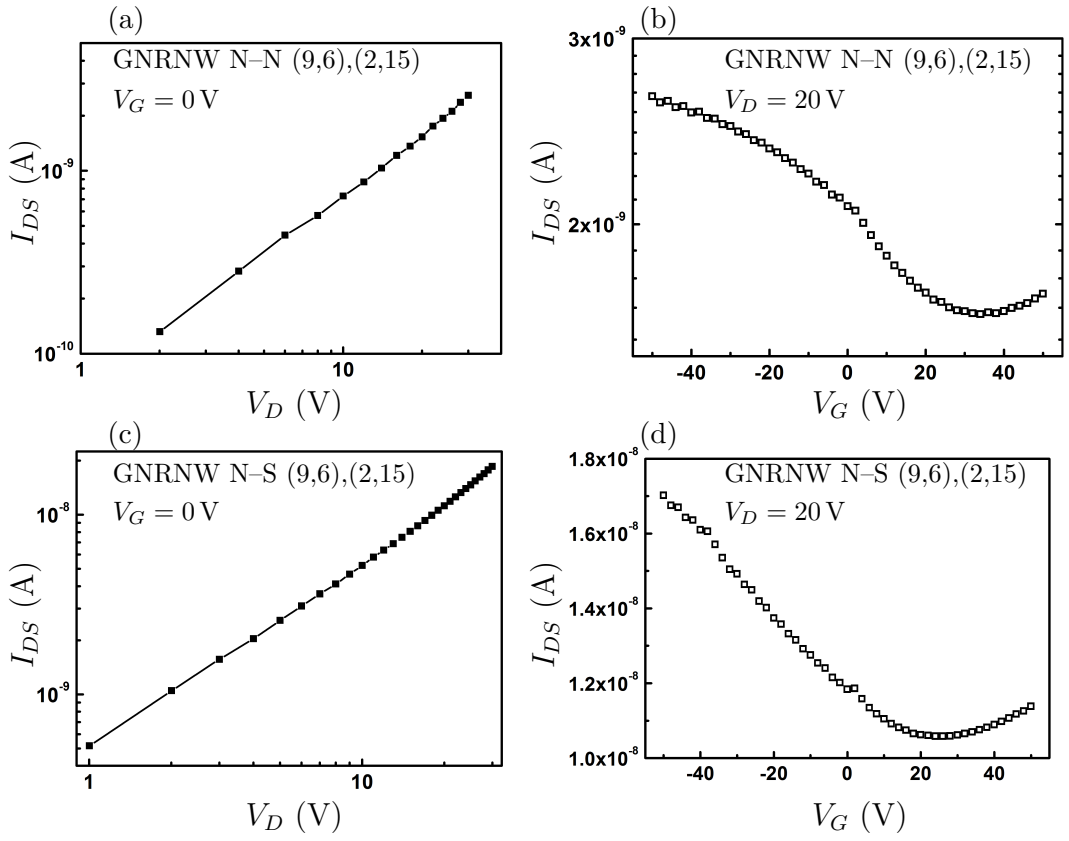

FIGURE B.3: I–V and transfer curves of GNRNW N–N (9,6),(2,15) ((a), (b)) and GNRNW N–S (9,6),(2,15) ((c), (d)) gated across 300 nm SiO_2 with a channel length of $L = 15\,\mu$m. The channel current follows a power law similar to the case of aGNR 5 and aGNR 9. However, the response to the gate voltage is smaller. Lines are guides for the eye.

B.3 Gate–leakage and bias symmetry in GNR FET devices

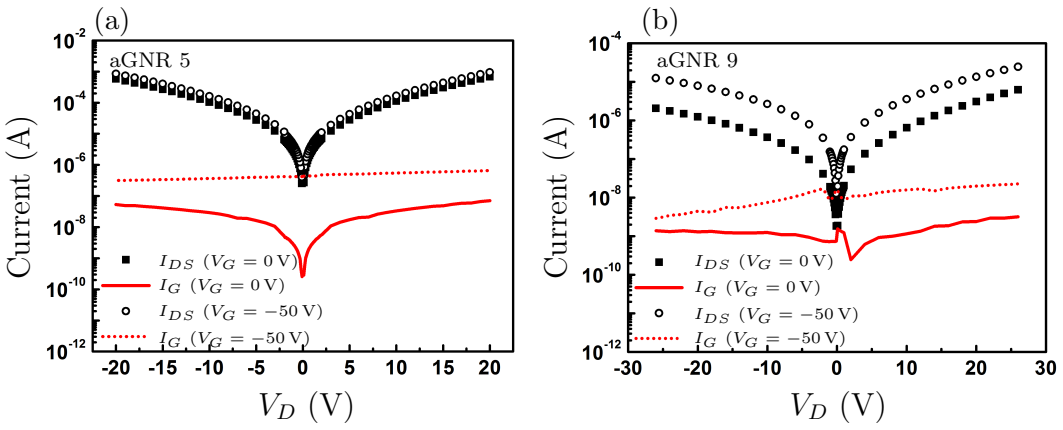

FIGURE B.4: Gate leakage current and bias symmetric channel current for a representative aGNR 5 (a) and aGNR 9 (b) device presented in a semi–logarithmic plot. The gate current is orders of magnitude below the channel current and does not depend on bias voltage. We plot the absolute value of the channel current in order to provide a facile comparison of positive and negative bias. Although the current at negative drain voltages is systematically lower than the current at positive drain voltages, this difference is very small. Hence, the use of only positive bias data in Sec. 5 is justified.

B.4 Determination of the field–effect mobility in GNR network FETs

The field–effect mobility can generally be extracted from the transfer curve according to Ref. [226] via

$$\mu_{\mathrm{FE}} = \frac{g}{V_D\, C_{\mathrm{Ox}}} \frac{L}{W}\,, \tag{B.1}$$

where $g = \frac{\partial I_{SD}}{\partial V_G}$ is the transconductance, L is the channel length, W is the channel width and $C_{\mathrm{Ox}} = \epsilon\,\epsilon_0/t_{\mathrm{Ox}} \approx 1.15 \times 10^{-4}\,\mathrm{F/m^2}$ is the geometrical capacitance density assuming that the channel and the gate electrode form a parallel plate capacitor. Here, we use $t_{\mathrm{Ox}} = 300\,\mathrm{nm}$, the relative permittivity of SiO_2 $\epsilon = 3.9$ and the vacuum permittivity $\epsilon_0 \approx 8.854\,\mathrm{F/m}$. Ideally, the transconductance is determined in the linear regime of the transfer curve. However, with the GNR network FET devices investigated in Sec. 5 a linear regime is not reached. Therefore, we use a linear approximation of the curve in the range $V_G \leq -40\,\mathrm{V}$. In the linear regime of transfer curves, the channel current is usually much larger than in the subthreshold regime and therefore the transconductance which we extract in this way leads to a systematic underestimation of μ_{FE}. Hence, the values given for μ_{FE} in Sec. 5 are estimates. However, the contact resistance–free mobilities as determined in Sec. 5.2.3 are of the same magnitude showing that the systematic error in the field–effect mobility is small and hence these values represent a realistic approximation of the charge carrier mobility in the devices. Furthermore, we use μ_{FE} in Sec. B.6 for the calculation of the charge carrier density as a function of temperature. The systematic error in the mobility of course propagates to the charge carrier density. Nevertheless, the temperature dependence of the transfer curves is captured correctly in the field–effect mobility and therefore the statements in Secs. 5 and B.6 are robust against these systematic uncertainties.

B.5 Charge transport statistics of GNR devices

Chip 2 of the aGNR 9 series:

ρ (Ω)	β	μ_{FE} ($\mathrm{cm^2\,V^{-1}\,s^{-1}}$)	$IM_{-50\mathrm{V},+50\mathrm{V}}$	SS (V/dec)
6.2×10^8	3.3	8×10^{-5}	56	55
7.4×10^8	3.3	8×10^{-5}	69	54
(5.7×10^8)	(0.1)	(5×10^{-5})	(34)	(7)

TABLE B.1: Overview of (outlier–corrected) median (first row), mean value (second row) and standard deviation (third row in parantheses) for five important charge transport parameters for chip 2 of the aGNR 9 series. Of the eight functional devices on the chip, two were classified as outliers and six are the basis for the presented statistics. Outliers are defined in the main text of Sec. 5.2.1.

Chip 1 of the aGNR 5 series:

Channel length (μm)	R_{Ohm} (MΩ)	β	μ_{FE} ($V_D = 5\,\mathrm{V}$)	$IM_{-50\mathrm{V},+50\mathrm{V}}$	SS (V/dec)
5.2	2×10^7	1.9	8×10^{-3}	4	124
	2×10^7	1.9	8×10^{-3}	4	124
	(9×10^6)	(0.01)	(4×10^{-3})	(0.1)	(6)
3.9	7×10^6	2.0	0.01	4	137
	9×10^6	2.1	0.01	4	134
	(4×10^6)	(0.03)	(2×10^{-3})	(0.1)	(10)
2.2	4×10^6	2.3	0.02	3	159
	4×10^6	2.3	0.02	3	159
	(2×10^4)	(0.02)	(6×10^{-4})	(0.1)	(0.1)
0.7	1×10^6	2.8	0.02	2	294
	1×10^6	2.8	0.02	2	312
	(1×10^5)	(0.1)	(3×10^{-3})	(0.2)	(35)

TABLE B.2: Overview of median (first row), mean value (second row) and standard deviation (third row in parantheses) for five important charge transport parameters for chip 1 of the aGNR 5 series. Of the ten functional devices on the chip, none was classified as outlier and all ten are the basis for the presented statistics.

Chip 2 of the aGNR 5 series:

Channel length (μm)	R_{Ohm} (MΩ)	β	μ_{FE} ($V_D = 5\,\mathrm{V}$)	$IM_{-50\mathrm{V},+50\mathrm{V}}$	SS (V/dec)
4.8	1.2×10^8	2.1	2×10^{-3}	5	95
	1.4×10^8	2.0	2×10^{-3}	5	99
	(1.0×10^8)	(0.2)	(3×10^{-4})	(1)	(14)
3.3	8×10^7	2.2	2×10^{-3}	4.5	99
	1×10^8	2.2	2×10^{-3}	4.4	101
	(6×10^7)	(0.2)	(2×10^{-5})	(0.6)	(10)
1.9	9×10^7	2.7	2×10^{-3}	4	106
	9×10^7	2.7	2×10^{-3}	4	106
	(1×10^6)	(0.01)	(3×10^{-5})	(0.2)	(2)

TABLE B.3: Overview of median (first row), mean value (second row) and standard deviation (third row in parantheses) for five important charge transport parameters for chip 2 of the aGNR 5 series. Of the nine functional devices on the chip, none was classified as outlier and all nine are the basis for the presented statistics.

Chip 4 of the aGNR 5 series:

	$L = 5.2\,\mu$m	$L = 3.7\,\mu$m	$L = 2.1\,\mu$m	$L = 0.6\,\mu$m
Max. resistance (Ω)	3×10^8	3×10^8	3×10^8	2×10^8
Min. resistance (Ω)	4×10^5	7×10^6	9×10^5	9×10^4

TABLE B.4: Device performance of chip 4 of the aGNR 5 series. Although charge injection was successful for 15 of 16 devices on the chip, the resistance varied strongly within each series of devices with same channel length. Furthermore, the resistance was in most cases larger than for devices of other, comparable chips. Therefore, we present here a comparison of highest and lowest resistance for each channel length instead of median, mean value and standard deviation. The reason for the low device performance could be an unintentional damage of the GNR film.

Chip 5 of the aGNR 5 series:

Channel length (μm)	R_{Ohm} (MΩ)	β	μ_{FE} ($V_D = 15\,$V)	$IM_{-50\mathrm{V},+50\mathrm{V}}$	SS (V/dec)
5.2	1.4×10^7	2.0	0.01	6	114
	1.8×10^7	2.0	0.01	5	121
	(1×10^7)	(0.1)	(2×10^{-3})	(0.6)	(17)
3.6	1.0×10^7	2.1	0.01	5	126
	1.1×10^7	2.1	0.01	5	122
	(7×10^5)	(0.08)	(1×10^{-3})	(0.6)	(10)
2.3	7×10^6	2.4	0.02	4	129
	7×10^6	2.4	0.01	4	131
	(1×10^6)	(0.01)	(4×10^{-3})	(0.3)	(15)
0.7	3×10^6	3.2	0.03	2	285
	3×10^6	3.2	0.03	2	286
	(4×10^5)	(0.1)	(7×10^{-3})	(0.2)	(37)

TABLE B.5: Overview of median (first row), mean value (second row) and standard deviation (third row in parantheses) for five important charge transport parameters for chip 5 of the aGNR 5 series. Of the 15 functional devices on the chip, three were classified as outliers and 12 are the basis for the presented statistics. Outliers are defined in the main text of Sec. 5.2.1.

Chip 6 of the aGNR 5 series:

	$L = 5.2\,\mu$m	$L = 3.5\,\mu$m	$L = 2.3\,\mu$m	$L = 0.7\,\mu$m
Max. resistance (Ω)	8×10^9	4×10^9	1×10^9	1×10^7
Min. resistance (Ω)	1×10^9	7×10^8	8×10^8	3×10^5

TABLE B.6: Device performance of chip 6 of the aGNR 5 series. Although charge injection was successful for 15 of 16 devices on the chip, the resistance varied strongly within each series of devices with same channel length. Furthermore, the resistance was in most cases larger than for devices of other, comparable chips. Therefore, we present here a comparison of highest and lowest resistance for each channel length instead of median, mean value and standard deviation. The reason for the low device performance could be an unintentional damage of the GNR film.

B.6 Estimation of the charge carrier density

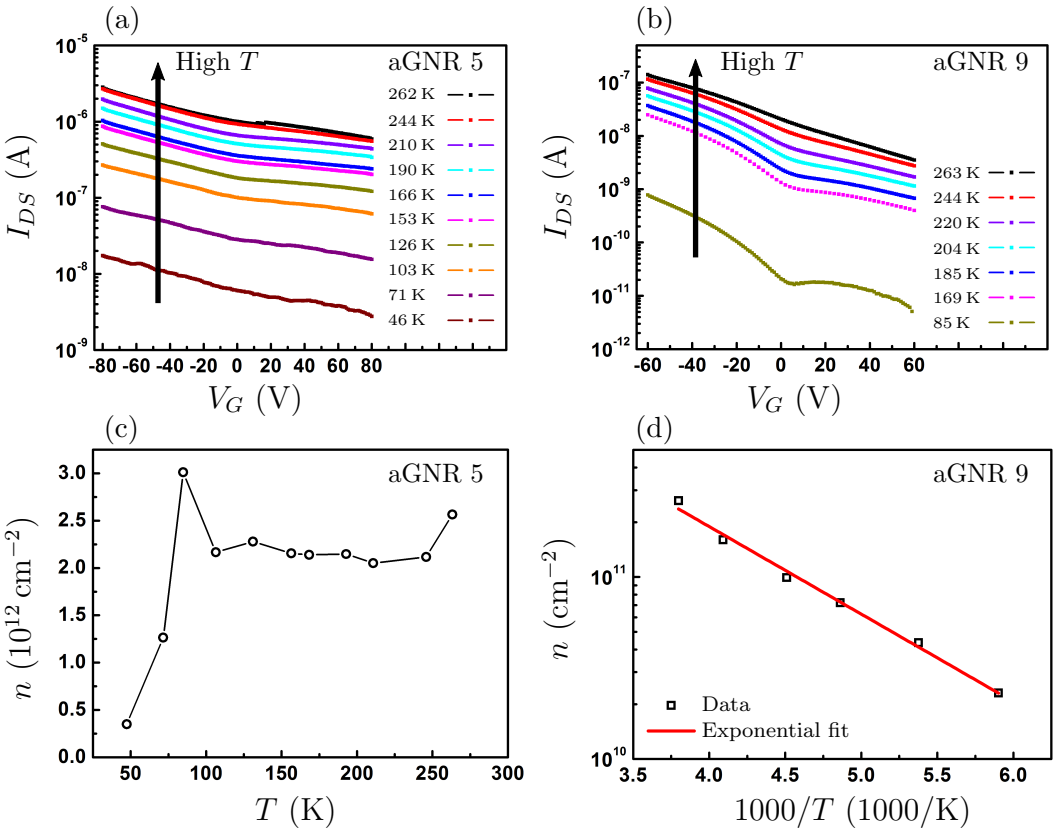

FIGURE B.5: Temperature dependence of charge carrier density in the aGNR 5 and the aGNR 9 devices. In (a) and (b), we present the temperature evolution of the transfer curves for the aGNR 5 device and the aGNR 9 device, respectively. The transfer curves were taken at a drain voltage of $V_D = 1\,\mathrm{V}$ (aGNR 5) and $V_D = 5\,\mathrm{V}$ (aGNR 9). The field–effect mobility is extracted from these curves according to Sec. B.4 and used to estimate the charge carrier density. As shown in (c), the charge carrier density in the aGNR 5 device is constant over a wide temperature range between 100 K and 260 K. In this temperature range, the charge carrier density in the aGNR 9 device shows an activated behavior as the Arrhenius plot presented in (d) shows. Lines in (a), (b) and (c) are guides for the eye.

The resistance of a conductor can be calculated if charge carrier density n and charge carrier mobility μ are known [105] according to

$$R = (e\,\mu\,n)^{-1}\,. \tag{B.2}$$

By using the Ohmic part of the I–V curves of aGNR 5 and aGNR 9 devices and $\mu \equiv \mu_{\mathrm{FE}}$, we can solve Eq. B.2 for n and estimate the total charge carrier density. Since we also measured transfer curves at variable temperatures (see Fig. B.5 (a) and (b)), we furthermore find the temperature evolution of the charge carrier density, shown in

Fig. B.5 (c) and (d) for aGNR 5 and aGNR 9, respectivley. Since we are interested in the temperature evolution of the Ohmic low–bias regime, we determine μ_{FE} at a drain voltage as low as possible. For the aGNR 5 device, we therefore use $V_D = 1\,\mathrm{V}$ and $V_D = 5\,\mathrm{V}$ for the aGNR 9 device. At 260 K, the charge carrier density is high with approximately $2\times10^{12}\,\mathrm{cm}^{-2}$ and $\approx 3\times10^{11}\,\mathrm{cm}^{-2}$ for the aGNR 5 device and the aGNR 9 device, respectively. This justifies the use of Eq. 2.29, which requires equal hopping steps through the device channel. For the aGNR 5 device, the charge carrier density remains constant from 260 K down to approximately 100 K. Only at lower temperatures, the carrier density seems to decrease. Measuring at lower temperatures however is impeded due to the low current levels. In the case of the aGNR 9 device, we find an activated behavior of the charge carrier density, allowing us to determine the activation energy with the help of an Arrhenius plot. We use an exponential model $n \propto \exp\left(-\frac{E_A}{2\,k_{\mathrm{B}}\,T}\right)$ to determine the activation energy as $E_A = (191 \pm 8)\,\mathrm{meV}$. Since we assume, that the charge carrier density is dominated by extrinsic charge carriers, we attribute this activation energy to the extrinsic dopants and not to intrinsic carriers from the valence band of the GNRs.

B.7 Doping and current annealing of GNR devices

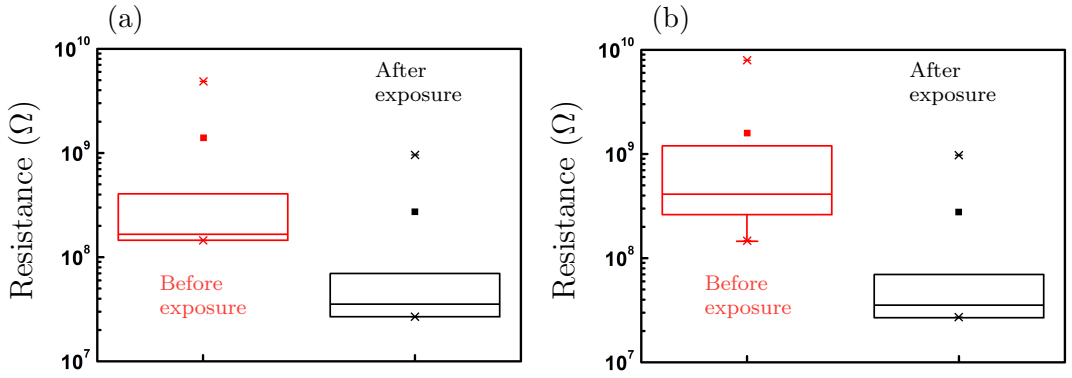

FIGURE B.6: Impact of the air exposure on day 15 of the experiments described in Sec. 5.2.2 presented in a box plot of the device resistances at $V_D = 5\,\mathrm{V}$. In (a) we summarize and compare four devices which have been tested immediately before and after the exposure to air, showing that the resistance of *all* these devices shifts systematically. These four devices are representative for all devices on the chip as demonstrated by only minimal changes of statistical parameters, when including eleven instead of four devices in the pre–exposure statistics in (b).

In Sec. 5.2.2, we exemplify the impact of unintentional doping by adatoms with measurements of a single device on chip 2 of the aGNR 9 series. Here, we show that the results are representative for all devices on the chip. We have measured the resistance (at $V_D = 5\,\mathrm{V}$) of four devices immediately before and after the 10–minute exposure on day 15. In Fig. B.6 (a), we present the measurement results in form of a box plot. The size of the box represents the interquartile range (IQR) between the 75th percentile and the 25th percentile. Whiskers to the box show the lowest data point still within 1.5 IQR of the lower quartile, and the highest data point still within 1.5 IQR of the upper quartile. The median is represented by a horizontal line inside the box and the square marker is the arithmetic mean. Asterisks mark the maximum and minimum values of the data set. All statistical parameters are shifted towards lower values (e.g. the median changes from approximately $290\,\mathrm{M}\Omega$ to $50\,\mathrm{M}\Omega$, demonstrating that the change introduced by the exposure is systematic for all devices. In Fig. B.6 (b), we include in total eleven devices which have been tested immediately before the exposure took place. The statistic is nearly unchanged as compared to the statistic based on only four devices, corroborating the assumption, that the previous four devices are representative for the whole chip.

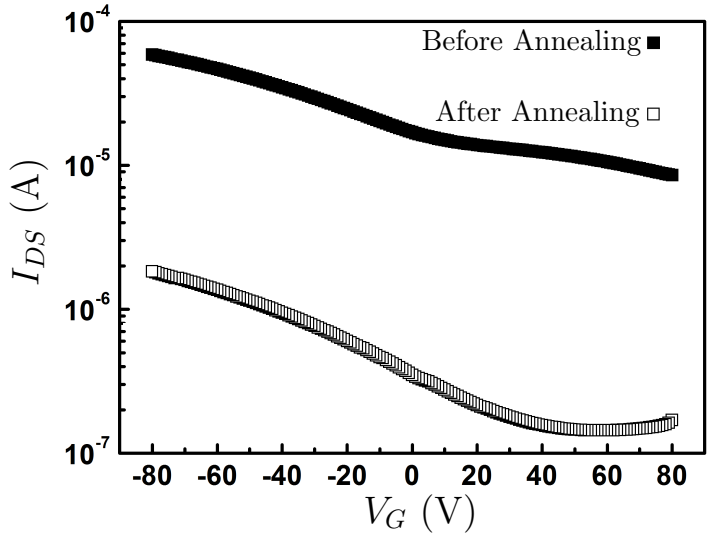

FIGURE B.7: Comparison of transfer curves ($V_D = 5\,V$) before and after current annealing. The current modulation is enhanced after the annealing process.

As mentioned in the main text of Sec. 5.2.2, such unintentional doping can (partly) be removed by annealing. Current annealing is one possible technique to reach this goal [231]. Here, we demonstrate, that our GNR devices can be subjected to current annealing in order to improve figures of merit of the device performance, such as the current modulation ratio. We choose an aGNR 5 device (chip 3 of the aGNR 5 series), since their lower resistance allows for larger currents. In five cycles of drain voltage sweeps, we increase the maximal bias from $V_D = 30\,\mathrm{V}$ up to $V_D = 60\,\mathrm{V}$, reaching maximal currents of 1 mA to 3 mA. After the procedure, the overall device resistance has increased. However as visible in the transfer curves shown in Fig. B.7, the current modulation is larger over the same gate voltage range. The current modulation ratio rises from $IM_{-80\mathrm{V},+80\mathrm{V}} \approx 6.8$ to $IM'_{-80\mathrm{V},+80\mathrm{V}} \approx 11$.

B.8 Gate voltage–dependence of the contact resistance

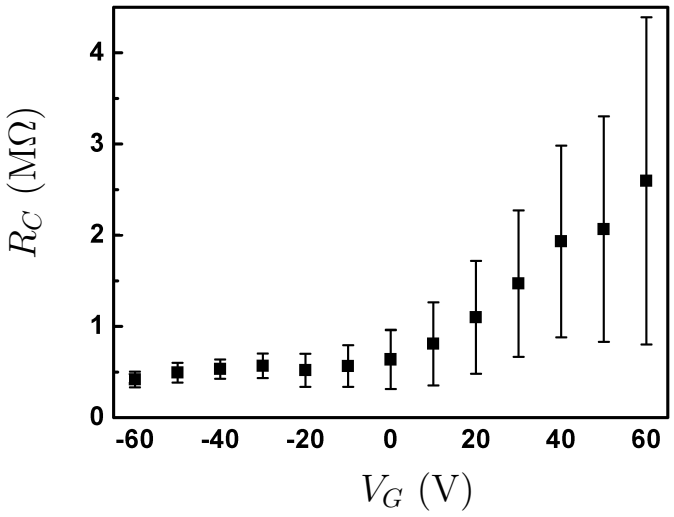

FIGURE B.8: Contact resistance as function of gate voltage measured on chip 5 of the aGNR 5 series. For large negative gate voltages, the contact resistance stays constant and begins to increase for gate voltages above $V_G \approx 0\,\mathrm{V}$.

The gate voltage dependent contact resistances were determined for a series of aGNR 5 devices by measuring charge transport at various channel lengths and using the transmission line method [232]. The total device resistance consists of the channel resistance and the contact resistance,

$$R_{on} = R_{\text{channel}} + R_C\,. \tag{B.3}$$

The channel resistance is a function of gate voltage and is proportional to the channel geometry L/W, with L the channel length and W, the channel width. The contact resistance R_C is expected to be a constant with respect to the gate voltage. However, due to current crowding effects a gate voltage dependence can be induced [283]. In Fig. B.8, we show the contact resistance as a function of gate voltage for chip 5 of the aGNR 5 series. We observe a decrease of R_C when the gate voltage is lowered from large positive values towards zero. When the gate voltage is further lowered towards large negative values, we gradually turn on the conducting channel and the contact resistance becomes constant. This behavior is typical for example in carbon nanotube network field effect transistors [233].

B.9 Conductance maps

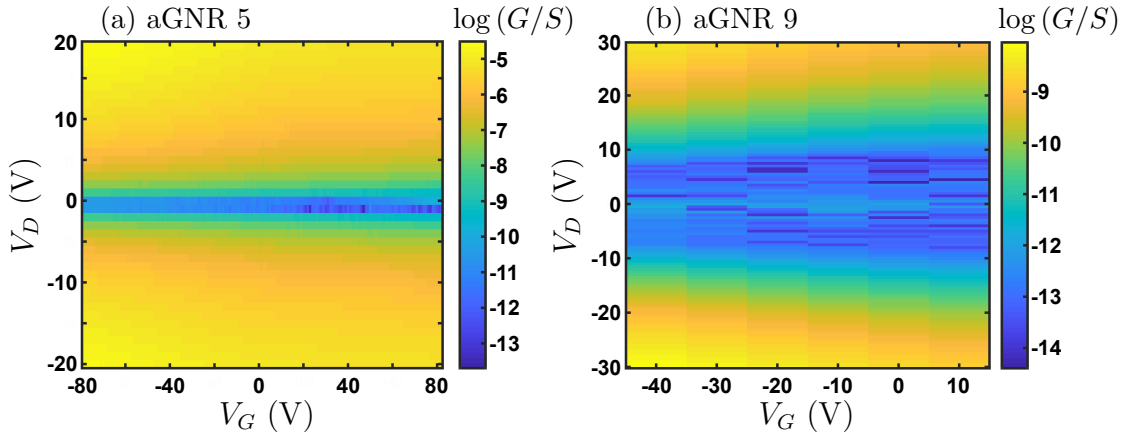

FIGURE B.9: (a) shows a conductance map at $T = 4\,\mathrm{K}$ for the aGNR 5 device on a logarithmic scale. (b) shows a conductance map at $T = 5\,\mathrm{K}$ for the aGNR 9 device. In both cases, the conductance is a monotonous function of drain voltage and gate voltage with no sign of Coulomb blockade in the form of Coulomb diamonds.

The scaling of current described by Eq. 2.29 is generally also compatible with devices dominated by Coulomb blockade [239]. Therefore, we map out the conductance, $G = I/V$, as a function of drain voltage and gate voltage. We used steps of $\Delta V_D = 1\,\mathrm{V}$ and $\Delta V_G = 1\,\mathrm{V}$ for the aGNR 5 device. In the case of the aGNR 9 device, we used $\Delta V_D = 0.5\,\mathrm{V}$ and $\Delta V_G = 10\,\mathrm{V}$. Both devices show no sign of Coulomb blockade, which is also not expected since the channel dimensions are large (see Tab. 4.1).

B.10 Temperature dependence of magnetotransport

Temperature (K)	a (T^{-2})
4	$(2060 \pm 4) \times 10^{-6}$
10	$(1131 \pm 5) \times 10^{-6}$
19	$(423 \pm 2) \times 10^{-6}$
28	$(247 \pm 2) \times 10^{-6}$
37	$(160 \pm 2) \times 10^{-6}$

TABLE B.7: Overview of the temperature dependence of the fitting parameter a in a fitting model $\Delta\rho/\rho = a\,B^2$, where $\Delta\rho/\rho$ is the relative change in resistivity and B is the magnetic field (see Sec. 5.3.2 for details).

Appendix C

Additional material for Chapter 7

C.1 Additional experimental details

Number	Species	Measurement Configuration	Mass (μg)	Mass error (μg)
1	CrI_3	$H \parallel c$	0.60	0.03
2	CrI_3	$H \parallel c$	0.6	0.1
3	CrI_3	$H \perp c$	1.05	0.04
4	$CrBr_3$	$H \parallel c$	3.2	0.1
5	$CrBr_3$	$H \parallel c$	1.4	0.1
6	$CrBr_3$	$H \perp c$	0.77	0.06
7	$CrCl_3$	$H \parallel c$	1.45	0.04
8	$CrCl_3$	$H \perp c$	0.66	0.10

TABLE C.1: Experimentally determined masses of CrX_3 crystals.

The mass densities of the CrX_3 compounds are $\rho_{CrI_3} = 5.33\,\mathrm{g/cm^3}$ [284], $\rho_{CrBr_3} = 4.60\,\mathrm{g/cm^3}$ [284] and $\rho_{CrI_3} = 2.95\,\mathrm{g/cm^3}$ [273].

C.2 Hysteresis loops of chromium trihalides

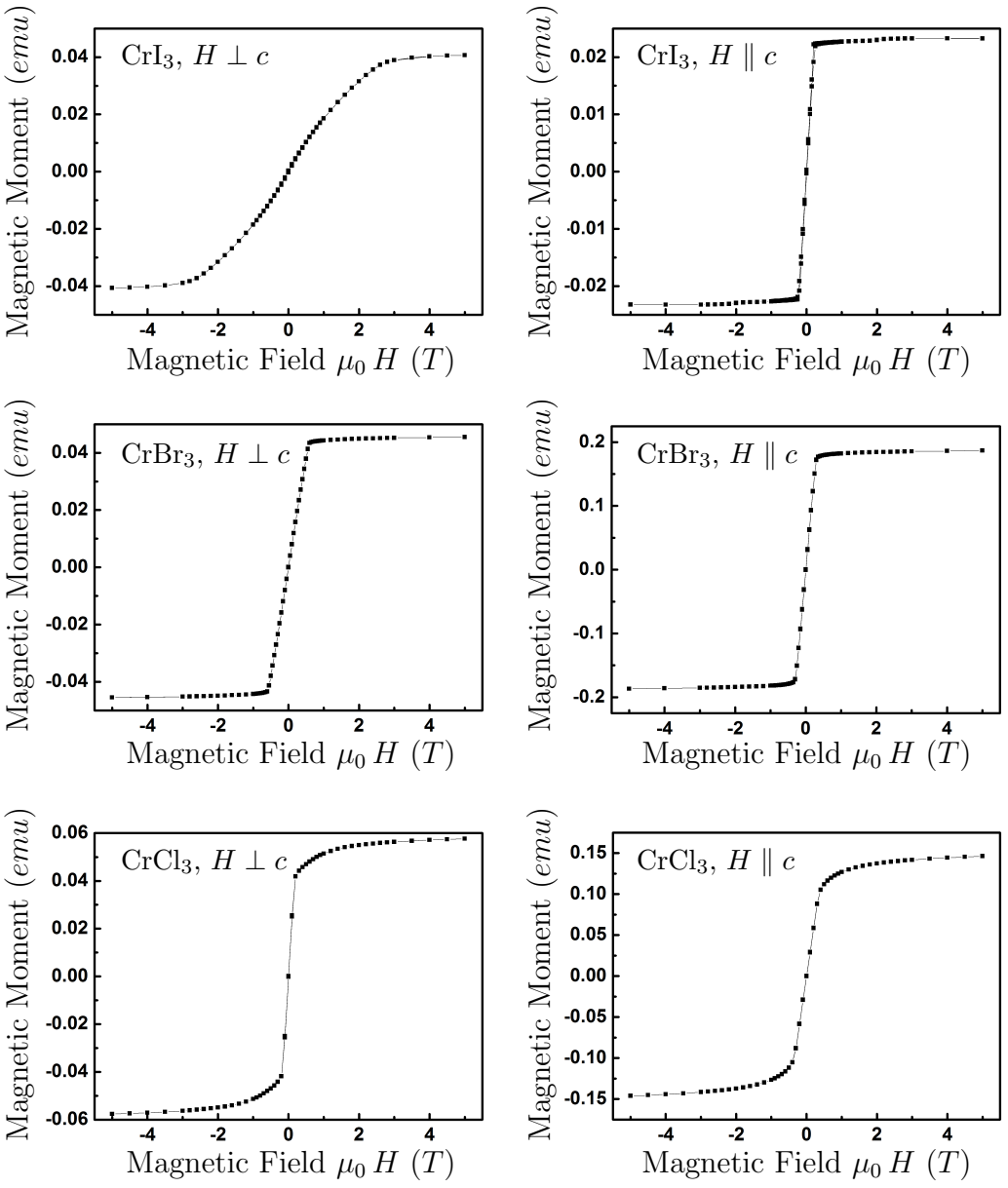

FIGURE C.1: Full hysteresis loops for all CrX_3 compounds at a temperature of 10 K in both measurement configurations. The error of the magnetic measurements are small as discussed in the main text in 7.4 and are not shown here in order to enhance the focus on the shape and features of the measurement curves. Lines are a guide for the eye.

C.3 Degradation of chromium bromide in air

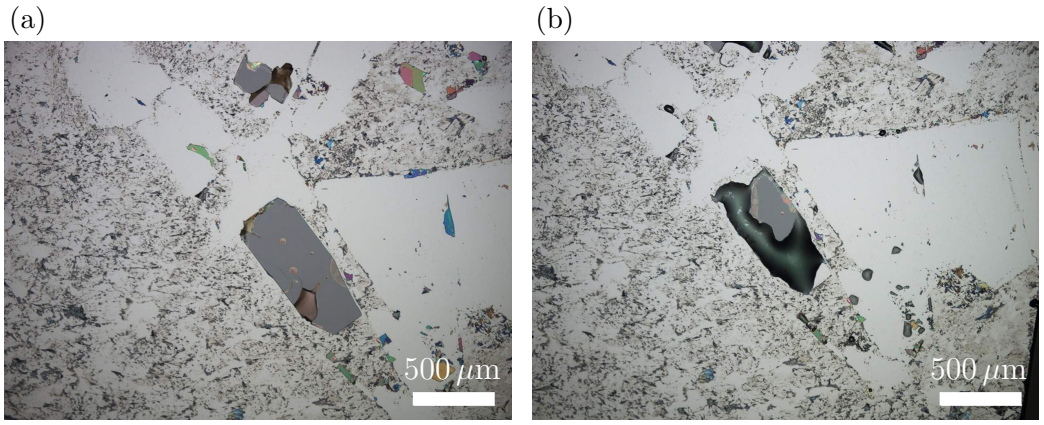

FIGURE C.2: Degradation of an exfoliated $CrBr_3$ crystal. In (a), the image was taken 5 min after exfoliation and in (b), the image was taken 30 min after exfoliation. Macroscopic changes are visible with a clear loss of the original crystal structure. I thank D. W. with whom the exfoliation experiments have been performed together.

Bibliography

[1] K. S. Novoselov, A. K. Geim, S. V. Morozov, D. Jiang, Y. Zhang, S. V. Dubonos, I. V. Grigorieva, and A. A. Firsov. Electric Field Effect in Atomically Thin Carbon Films. *Science*, 306(5696):666, 2004. doi: 10.1126/science.1102896.

[2] K. S. Novoselov, D. Jiang, F. Schedin, T. J. Booth, V. V. Khotkevich, S. V. Morozov, and A. K. Geim. Two-Dimensional Atomic Crystals. *Proceedings of the National Academy of Sciences of the United States of America*, 102(30):10451–10453, 2005. doi: 10.1073/pnas.0502848102.

[3] X. Li and H. Zhu. Two-dimensional MoS_2: Properties, Preparation, and Applications. *Journal of Materiomics*, 1(1):33, 2015. doi: 10.1016/j.jmat.2015.03.003.

[4] L. Li, Y. Yu, G. J. Ye, Q. Ge, X. Ou, H. Wu, D. Feng, Xian H. Chen, and Y. Zhang. Black Phosphorus Field-Effect Transistors. *Nature Nanotechnology*, 9 (5):372, 2014. doi: 10.1038/nnano.2014.35.

[5] K. Nakada, M. Fujita, G. Dresselhaus, and M. S. Dresselhaus. Edge State in Graphene Ribbons: Nanometer Size Effect and Edge Shape Dependence. *Physical Review B*, 54(24):17954, 1996. doi: 10.1103/PhysRevB.54.17954.

[6] L. Yang, C.-H. Park, Y.-W. Son, M. Cohen, and S. Louie. Quasiparticle Energies and Band Gaps in Graphene Nanoribbons. *Physical Review Letters*, 99(18):186801, 2007. doi: 10.1103/PhysRevLett.99.186801.

[7] O. V. Yazyev and M. I. Katsnelson. Magnetic Correlations at Graphene Edges: Basis for Novel Spintronics Devices. *Physical Review Letters*, 100(4):047209, 2008. doi: 10.1103/PhysRevLett.100.047209.

[8] F. Joucken, Y. Tison, P. Le Fèvre, A. Tejeda, A. Taleb-Ibrahimi, E. Conrad, V. Repain, C. Chacon, A. Bellec, Y. Girard, S. Rousset, J. Ghijsen, R. Sporken,

H. Amara, F. Ducastelle, and J. Lagoute. Charge Transfer and Electronic Doping in Nitrogen–Doped Graphene. *Scientific Reports*, 5:14564, 2015. doi: 10.1038/srep14564.

[9] L. D'Arsié, S. Esconjauregui, R. Weatherup, Y. Guo, S. Bhardwaj, A. Centeno, A. Zurutuza, C. Cepek, and J. Robertson. Stability of Graphene Doping with MoO_3 and I_2. *Applied Physics Letters*, 105(10):103103, 2014. doi: 10.1063/1.4895025.

[10] J. Meyer, P. R. Kidambi, B. C. Bayer, C. Weijtens, A. Kuhn, A. Centeno, A. Pesquera, A. Zurutuza, J. Robertson, and S. Hofmann. Metal Oxide Induced Charge Transfer Doping and Band Alignment of Graphene Electrodes for Efficient Organic Light Emitting Diodes. *Scientific Reports*, 4(5380), 2014. doi: 10.1038/srep05380.

[11] H. I. Wang, M.-L. Braatz, N. Richter, K.-J. Tielrooij, Z. Mics, H. Lu, N.-E. Weber, K. Müllen, D. Turchinovich, M. Kläui, and M. Bonn. Reversible Photochemical Control of Doping Levels in Supported Graphene. *The Journal of Physical Chemistry C*, 121(7):4083, 2017. doi: 10.1021/acs.jpcc.7b00347.

[12] H. Gao, L. Wang, J. Zhao, F. Ding, and J. Lu. Band Gap Tuning of Hydrogenated Graphene: H Coverage and Configuration Dependence. *The Journal of Physical Chemistry C*, 115(8):3236, 2011. doi: 10.1021/jp1094454.

[13] D. C. Elias, R. R. Nair, T. M. G. Mohiuddin, S. V. Morozov, P. Blake, M. P. Halsall, A. C. Ferrari, D. W. Boukhvalov, M. I. Katsnelson, A. K. Geim, and K. S. Novoselov. Control of Graphene's Properties by Reversible Hydrogenation: Evidence for Graphane. *Science*, 323:610, 2009. doi: 10.1126/science.1167130.

[14] B. R. Matis, J. S. Burgess, F. A. Bulat, A. L. Friedman, B. H. Houston, and J. W. Baldwin. Surface Doping and Band Gap Tunability in Hydrogenated Graphene. *ACS Nano*, 6(1):17, 2012. doi: 10.1021/nn2034555.

[15] S. Agnoli and M. Favaro. Doping Graphene with Boron: A Review of Synthesis Methods, Physicochemical Characterization, and Emerging Applications. *Journal of Materials Chemistry A*, 4(14):5002, 2016. doi: 10.1039/C5TA10599D.

[16] Y.-B. Tang, L.-C. Yin, Y. Yang, X.-H. Bo, Y.-L. Cao, H.-E. Wang, W.-J. Zhang, I. Bello, S.-T. Lee, H.-M. Cheng, and C.-S. Lee. Tunable Band Gaps and p-Type Transport Properties of Boron-Doped Graphenes by Controllable Ion Doping

Using Reactive Microwave Plasma. *ACS Nano*, 6(3):1970, 2012. doi: 10.1021/nn3005262.

[17] S. H. Park, J. Chae, M.-H. Cho, J. H. Kim, K.-H. Yoo, S. W. Cho, T. G. Kim, and J. W. Kim. High Concentration of Nitrogen Doped into Graphene using N_2 Plasma with an Aluminum Oxide Buffer Layer. *J. Mater. Chem. C*, 2(5):933, 2014. doi: 10.1039/C3TC31773K.

[18] Y. Xue, B. Wu, L. Jiang, Y. Guo, L. Huang, J. Chen, J. Tan, D. Geng, B. Luo, W. Hu, G. Yu, and Y. Liu. Low Temperature Growth of Highly Nitrogen-Doped Single Crystal Graphene Arrays by Chemical Vapor Deposition. *Journal of the American Chemical Society*, 134(27):11060, 2012. doi: 10.1021/ja302483t.

[19] J.-G. Park. Opportunities and Challenges of 2d Magnetic van der Waals Materials: Magnetic Graphene? *Journal of Physics: Condensed Matter*, 28(30):301001, 2016. doi: 10.1088/0953-8984/28/30/301001.

[20] B. Huang, G. Clark, E. Navarro-Moratalla, D. R. Klein, R. Cheng, K. L. Seyler, D. Zhong, E. Schmidgall, M. A. McGuire, D. H. Cobden, W. Yao, D. Xiao, P. Jarillo-Herrero, and X. Xu. Layer–Dependent Ferromagnetism in a van der Waals Crystal down to the Monolayer Limit. *Nature*, 546(7657):270, 2017. doi: 10.1038/nature22391.

[21] N. Richter, D. Weber, F. Martin, N. Singh, U. Schwingenschlögl, B. V. Lotsch, and M. Kläui. Temperature–dependent magnetic anisotropy in the layered magnetic semiconductors Cri_3 and $CrBr_3$. *Physical Review Materials*, 2(2):024004, 2018. doi: 10.1103/PhysRevMaterials.2.024004.

[22] M. A. McGuire, H. Dixit, V. R. Cooper, and B. C. Sales. Coupling of Crystal Structure and Magnetism in the Layered, Ferromagnetic Insulator CrI_3. *Chemistry of Materials*, 27(2):612, 2015. doi: 10.1021/cm504242t.

[23] I. Tsubokawa. On the Magnetic Properties of a $CrBr_3$ Single Crystal. *Journal of the Physical Society of Japan*, 15:1664, 1960. doi: 10.1143/JPSJ.15.1664.

[24] J. F. Dillon. Ferromagnetic Resonance in $CrBr_3$. *Journal of Applied Physics*, 33 (3):1191, 1962. doi: 10.1063/1.1728652.

[25] J. F. Dillon and C. E. Olson. Magnetization, Resonance, and Optical Properties of the Ferromagnet CrI_3. *Journal of Applied Physics*, 36(3):1259, 1965. doi: 10.1063/1.1714194.

[26] W. N. Hansen. Some Magnetic Properties of the Chromium (III) Halides at 4.2°K. *Journal of Applied Physics*, 30(4):304, 1959. doi: 10.1063/1.2185944.

[27] K. S. Novoselov, A. Mishchenko, A. Carvalho, and A. H. Castro Neto. 2D Materials and van der Waals Heterostructures. *Science*, 353(6298):9439, 2016. doi: 10.1126/science.aac9439.

[28] D. Zhong, K. L. Seyler, X. Linpeng, R. Cheng, N. Sivadas, B. Huang, E. Schmidgall, T. Taniguchi, K. Watanabe, M. A. McGuire, W. Yao, D. Xiao, K.-M. C. Fu, and X. Xu. Van der Waals Engineering of Ferromagnetic Semiconductor Heterostructures for Spin and Valleytronics. *Science Advances*, 3(5):e1603113, 2017. doi: 10.1126/sciadv.1603113.

[29] A. H. Castro Neto, F. Guinea, N. M. R. Peres, K. S. Novoselov, and A. K. Geim. The Electronic Properties of Graphene. *Reviews of Modern Physics*, 81(1):109, 2009. doi: 10.1103/RevModPhys.81.109.

[30] L. Onsager. Crystal Statistics. I. A Two-Dimensional Model with an Order–Disorder Transition. *Physical Review*, 65(3):117, 1944. doi: 10.1103/PhysRev.65.117.

[31] J. H. Davies. *The Physics of Low-dimensional Semiconductors: An Introduction*. Cambridge University Press, Cambridge, 1997. ISBN 978-0-521-48148-9. doi: 10.1017/CBO9780511819070.

[32] W. W. Chow and S. W. Koch. Basic Concepts. In W. W. Chow and S. W. Koch, editors, *Semiconductor-Laser Fundamentals: Physics of the Gain Materials*, pages 1–35. Springer Berlin Heidelberg, Berlin, Heidelberg, 1999. ISBN 978-3-662-03880-2. doi: 10.1007/978-3-662-03880-2_1.

[33] K. K. Ng. A Survey of Semiconductor Devices. *IEEE Transactions on Electron Devices*, 43(10):1760, 1996. doi: 10.1109/16.536822.

[34] L. Van Hove. The Occurrence of Singularities in the Elastic Frequency Distribution of a Crystal. *Physical Review*, 89(6):1189, 1953.

[35] A. Hirsch. The Era of Carbon Allotropes. *Nature materials*, 9(11):868, 2010. doi: 10.1038/nmat2885.

[36] P. R. Wallace. The Band Theory of Graphite. *Physical Review*, 71(9):622, 1947. doi: 10.1103/PhysRev.71.622.

[37] J. C. Slater and G. F. Koster. Simplified LCAO Method for the Periodic Potential Problem. *Physical Review*, 94(6):1498, 1954. doi: 10.1103/PhysRev.94.1498.

[38] C. Bena and G. Montambaux. Remarks on the Tight–Binding Model of Graphene. *New Journal of Physics*, 11(9):095003, 2009. doi: 10.1088/1367-2630/11/9/095003.

[39] E. Wigner and F. Seitz. On the Constitution of Metallic Sodium. *Physical Review*, 43(10):804, 1933. doi: 10.1103/PhysRev.43.804.

[40] M. O. Goerbig, J.-N. Fuchs, G. Montambaux, and F. Piéchon. Tilted Anisotropic Dirac Cones in Quinoid–Type Graphene and alpha-(BEDT-TTF)$_2$I$_3$. *Physical Review B*, 78(4):045415, 2008. doi: 10.1103/PhysRevB.78.045415.

[41] S. Reich, J. Maultzsch, C. Thomsen, and P. Ordejón. Tight–Binding Description of Graphene. *Physical Review B*, 66(3):035412, 2002. doi: 10.1103/PhysRevB.66.035412.

[42] R. S. Deacon, K.-C. Chuang, R. J. Nicholas, K. S. Novoselov, and A. K. Geim. Cyclotron Resonance Study of the Electron and Hole Velocity in Graphene Monolayers. *Physical Review B*, 76(8):081406(R), 2007. doi: 10.1103/PhysRevB.76.081406.

[43] G. W. Semenoff. Condensed–Matter Simulation of a Three–Dimensional Anomaly. *Physical Review Letters*, 53(26):2449, 1984. doi: 10.1103/PhysRevLett.53.2449.

[44] M. M. Grujic. Manifestations of Intrinsic and Induced Magnetic Properties of Graphene Nanostructures. PhD Thesis. University of Antwerp, 2015.

[45] J. C. Slonczewski and P. R. Weiss. Band Structure of Graphite. *Physical Review*, 109(2):272, 1958. doi: 10.1103/PhysRev.109.272.

[46] J. W. McClure. Theory of Diamagnetism of Graphite. *Phys. Rev.*, 119(2):606, 1960. doi: 10.1103/PhysRev.119.606.

[47] S. Shallcross, S. Sharma, E. Kandelaki, and O. A. Pankratov. Electronic Structure of Turbostratic Graphene. *Physical Review B*, 81(16):165105, 2010. doi: 10.1103/PhysRevB.81.165105.

[48] X. Zhang, O. V. Yazyev, J. Feng, L. Xie, C. Tao, Y.-C. Chen, L. Jiao, Z. Pedramrazi, A. Zettl, S. G. Louie, H. Dai, and M. F. Crommie. Experimentally Engineering the Edge Termination of Graphene Nanoribbons. *ACS Nano*, 7(1): 198, 2013. doi: 10.1021/nn303730v.

[49] M. Fujita, K. Wakabayashi, K. Nakada, and K. Kusakabe. Peculiar Localized State at Zigzag Graphite Edge. *Journal of the Physical Society of Japan*, 65(7): 1920, 1996. doi: 10.1143/JPSJ.65.1920.

[50] K. Wakabayashi, M. Fujita, H. Ajiki, and M. Sigrist. Electronic and magnetic properties of nanographite ribbons. *Physical Review B*, 59(12):8271, 1999. doi: 10.1103/PhysRevB.59.8271.

[51] L. Brey and H. A. Fertig. Electronic States of Graphene Nanoribbons Studied with the Dirac Equation. *Physical Review B*, 73(23):235411, 2006. doi: 10.1103/PhysRevB.73.235411.

[52] A. R. Akhmerov and C. W. J. Beenakker. Boundary Conditions for Dirac Fermions on a Terminated Honeycomb Lattice. *Physical Review B*, 77(8):085423, 2008. doi: 10.1103/PhysRevB.77.085423.

[53] K. Wakabayashi, Y. Takane, M. Yamamoto, and M. Sigrist. Electronic Transport Properties of Graphene Nanoribbons. *New Journal of Physics*, 11(9):095016, 2009. doi: 10.1088/1367-2630/11/9/095016.

[54] Y.-W. Son, M. L. Cohen, and S. G. Louie. Energy Gaps in Graphene Nanoribbons. *Physical Review Letters*, 97(21):216803, 2006. doi: 10.1103/PhysRevLett.97.216803.

[55] V. Barone, O. Hod, and G. E. Scuseria. Electronic Structure and Stability of Semiconducting Graphene Nanoribbons. *Nano Letters*, 6(12):2748, 2006. doi: 10.1021/nl0617033.

[56] Y. Miyamoto, K. Nakada, and M. Fujita. First–Principles Study of Edge States of H–Terminated Graphitic Ribbons. *Physical Review B*, 59(15):9858, 1999. doi: 10.1103/PhysRevB.59.9858.

[57] J. A. Vergés, G. Chiappe, and E. Louis. On the Forbidden Gap of Finite Graphene Nanoribbons. *The European Physical Journal B*, 88(8):200, 2015. doi: 10.1140/epjb/e2015-60389-5.

[58] L. Pisani, J. A. Chan, B. Montanari, and N. M. Harrison. Electronic Structure and Magnetic Properties of Graphitic Ribbons. *Physical Review B*, 75(6):064418, 2007. doi: 10.1103/PhysRevB.75.064418.

[59] J. Jung, T. Pereg-Barnea, and A. H. MacDonald. Theory of Interedge Superexchange in Zigzag Edge Magnetism. *Physical Review Letters*, 102(22):227205, 2009. doi: 10.1103/PhysRevLett.102.227205.

[60] H. Karimi and I. Affleck. Towards a Rigorous Proof of Magnetism on the Edges of Graphene Nanoribbons. *Physical Review B*, 86(11):115446, 2012. doi: 10.1103/PhysRevB.86.115446.

[61] O. V. Yazyev. Emergence of Magnetism in Graphene Materials and Nanostructures. *Reports on Progress in Physics*, 73(5):056501, 2010.

[62] F. Muñoz Rojas, J. Fernández-Rossier, and J. J. Palacios. Giant Magnetoresistance in Ultrasmall Graphene Based Devices. *Physical Review Letters*, 102(13):136810, 2009. doi: 10.1103/PhysRevLett.102.136810.

[63] Y.-W. Son, M. L. Cohen, and S. G. Louie. Half–Metallic Graphene Nanoribbons. *Nature*, 444(7117):347, 2006. doi: 10.1038/nature05180.

[64] N. D. Mermin and H. Wagner. Absence of Ferromagnetism or Antiferromagnetism in One– or Two–Dimensional Isotropic Heisenberg Models. *Physical Review Letters*, 17(22):1133, 1966. doi: 10.1103/PhysRevLett.17.1133.

[65] J. Jung and A. H. MacDonald. Carrier Density and Magnetism in Graphene Zigzag Nanoribbons. *Physical Review B*, 79(23):235433, 2009. doi: 10.1103/PhysRevB.79.235433.

[66] H. Raza and E. C. Kan. Armchair Graphene Nanoribbons: Electronic Structure and Electric–Field Modulation. *Physical Review B*, 77(24):245434, 2008. doi: 10.1103/PhysRevB.77.245434.

[67] H. Zheng, Z. F. Wang, T. Luo, Q. W. Shi, and J. Chen. Analytical Study of Electronic Structure in Armchair Graphene Nanoribbons. *Physical Review B*, 75 (16):165414, 2007. doi: 10.1103/PhysRevB.75.165414.

[68] A. V. Rozhkov, S. Savel'ev, and F. Nori. Electronic properties of armchair graphene nanoribbons. *Physical Review B*, 79(12):125420, 2009. doi: 10.1103/PhysRevB. 79.125420.

[69] K. Wakabayashi, K.-I. Sasaki, T. Nakanishi, and T. Enoki. Electronic States of Graphene Nanoribbons and Analytical Solutions. *Science and Technology of Advanced Materials*, 11(5):054504, 2010. doi: 10.1088/1468-6996/11/5/054504.

[70] J. Munárriz Arrieta. Tight-Binding Description of Graphene Nanostructures. In J. Munárriz Arrieta, editor, *Modelling of Plasmonic and Graphene Nanodevices*, page 13. Springer International Publishing, 2014. ISBN 978-3-319-07088-9. doi: 10.1007/978-3-319-07088-9_2.

[71] A. D. Zdetsis and E.N. Economou. Rationalizing and Reconciling Energy Gaps and Quantum Confinement in Narrow Atomically Precise Armchair Graphene Nanoribbons. *Carbon*, 116:422, 2017. doi: 10.1016/j.carbon.2017.02.006.

[72] D. Gunlycke and C. T. White. Tight–Binding Energy Dispersions of Armchair–Edge Graphene Nanostrips. *Physical Review B*, 77(11):115116, 2008. doi: 10. 1103/PhysRevB.77.115116.

[73] W. Jaskólski, A. Ayuela, M. Pelc, H. Santos, and L. Chico. Edge States and Flat Bands in Graphene Nanoribbons with Arbitrary Geometries. *Physical Review B*, 83(23):235424, 2011. doi: 10.1103/PhysRevB.83.235424.

[74] J. Liu, B.-W. Li, Y.-Z. Tan, A. Giannakopoulos, C. Sanchez-Sanchez, D. Beljonne, P. Ruffieux, R. Fasel, X. Feng, and K. Müllen. Toward Cove-Edged Low Band Gap Graphene Nanoribbons. *Journal of the American Chemical Society*, 137(18): 6097, 2015. doi: 10.1021/jacs.5b03017.

[75] C. Tao, L. Jiao, O. V. Yazyev, Y.-C. Chen, J. Feng, X. Zhang, R. B. Capaz, J. M. Tour, A. Zettl, S. G. Louie, H. Dai, and M. F. Crommie. Spatially Resolving Edge States of Chiral Graphene Nanoribbons. *Nature Physics*, 7(8):616, 2011. doi: 10.1038/nphys1991.

[76] O. V. Yazyev, R. B. Capaz, and S. G. Louie. Theory of Magnetic Edge States in Chiral Graphene Nanoribbons. *Physical Review B*, 84(11):115406, 2011. doi: 10.1103/PhysRevB.84.115406.

[77] A. R. Carvalho, J. H. Warnes, and C. H. Lewenkopf. Edge Magnetization and Local Density of States in Chiral Graphene Nanoribbons. *Physical Review B*, 89 (24):245444, 2014. doi: 10.1103/PhysRevB.89.245444.

[78] D. G. de Oteyza, A. García-Lekue, M. Vilas-Varela, N. Merino-Díez, E. Carbonell-Sanromà, M. Corso, G. Vasseur, C. Rogero, E. Guitián, J. I. Pascual, J. E. Ortega, Y. Wakayama, and D. Peña. Substrate–Independent Growth of Atomically Precise Chiral Graphene Nanoribbons. *ACS Nano*, 10(9):9000, 2016. doi: 10.1021/acsnano.6b05269.

[79] J. Cai, P. Ruffieux, R. Jaafar, M. Bieri, T. Braun, S. Blankenburg, M. Muoth, A. P. Seitsonen, M. Saleh, X. Feng, K. Müllen, and R. Fasel. Atomically Precise Bottom–Up Fabrication of Graphene Nanoribbons. *Nature*, 466(7305):470, 2010. doi: 10.1038/nature09211.

[80] T. H. Vo, M. Shekhirev, D. A. Kunkel, M. D. Morton, E. Berglund, L. Kong, P. M. Wilson, P. A. Dowben, A. Enders, and A. Sinitskii. Large–Scale Solution Synthesis of Narrow Graphene Nanoribbons. *Nature Communications*, 5(3189), 2014. doi: 10.1038/ncomms4189.

[81] E. C. Girão, L. Liang, E. Cruz-Silva, A. G. S. Filho, and V. Meunier. Emergence of Atypical Properties in Assembled Graphene Nanoribbons. *Physical Review Letters*, 107(13):135501, 2011. doi: 10.1103/PhysRevLett.107.135501.

[82] Z. Chen, W. Zhang, C-A. Palma, A. Lodi Rizzini, B. Liu, A. Abbas, N. Richter, L. Martini, X.-Y. Wang, N. Cavani, H. Lu, N. Mishra, C. Coletti, R. Berger, F. Klappenberger, M. Kläui, A. Candini, M. Affronte, C. Zhou, V. De Renzi, U. del Pennino, J. V. Barth, H. J. Räder, A. Narita, X. Feng, and K. Müllen. Synthesis of Graphene Nanoribbons by Ambient-Pressure Chemical Vapor Deposition and

Device Integration. *Journal of the American Chemical Society*, 138(47):15488, 2016. doi: 10.1021/jacs.6b10374.

[83] V. A. Saroka, K. G. Batrakov, V. A. Demin, and L. A. Chernozatonskii. Band Gaps in Jagged and Straight Graphene Nanoribbons Tunable by an External Electric Field. *Journal of Physics: Condensed Matter*, 27(14):145305, 2015. doi: 10.1088/0953-8984/27/14/145305.

[84] X. Wu and X. C. Zeng. Sawtooth–Like Graphene Nanoribbon. *Nano Research*, 1 (1):40, 2008. doi: 10.1007/s12274-008-8001-z.

[85] L. Kou, C. Tang, C. Chen, and W. Guo. Hybrid W–Shaped Graphene Nanoribbons: Distinct Electronic and Transport Properties. *Journal of Applied Physics*, 110(12):124312, 2011. doi: 10.1063/1.3669496.

[86] E. C. Girão, E. Cruz-Silva, L. Liang, A. G. S. Filho, and V. Meunier. Structural and Electronic Properties of Graphitic Nanowiggles. *Physical Review B*, 85(23): 235431, 2012. doi: 10.1103/PhysRevB.85.235431.

[87] W. Huang, J.-S. Wang, and G. Liang. Theoretical Study on Thermoelectric Properties of Kinked Graphene Nanoribbons. *Physical Review B*, 84(4):045410, 2011. doi: 10.1103/PhysRevB.84.045410.

[88] Y. Chen, T. Jayasekera, A. Calzolari, K. W. Kim, and M. Buongiorno Nardelli. Thermoelectric Properties of Graphene Nanoribbons, Junctions and Superlattices. *Journal of Physics: Condensed Matter*, 22(37):372202, 2010. doi: 10.1088/0953-8984/22/37/372202.

[89] H. Sevinçli, M. Topsakal, and S. Ciraci. Superlattice Structures of Graphene–Based Armchair Nanoribbons. *Physical Review B*, 78(24):245402, 2008. doi: 10.1103/PhysRevB.78.245402.

[90] A. Cresti and S. Roche. Edge–Disorder–Dependent Transport Length Scales in Graphene Nanoribbons: From Klein Defects to the Superlattice Limit. *Physical Review B*, 79(23):233404, 2009. doi: 10.1103/PhysRevB.79.233404.

[91] L. Esaki and R. Tsu. Superlattice and Negative Differential Conductivity in Semiconductors. *IBM Journal of Research and Development*, 14(1):61, 1970. doi: 10.1147/rd.141.0061.

[92] S. Ciraci and Inder P. Batra. Long-Range Order and Segregation in Semiconductor Superlattices. *Physical Review Letters*, 58(20):2114, 1987. doi: 10.1103/PhysRevLett.58.2114.

[93] L. Liang and V. Meunier. Electronic and Thermoelectric Properties of Assembled Graphene Nanoribbons with Elastic Strain and Structural Dislocation. *Applied Physics Letters*, 102(14):143101, 2013. doi: 10.1063/1.4800777.

[94] L. Liang and V. Meunier. Electronic Structure of Assembled Graphene Nanoribbons: Substrate and Many–Body Effects. *Physical Review B*, 86(19):195404, 2012. doi: 10.1103/PhysRevB.86.195404.

[95] M. Shishkin and G. Kresse. Self–Consistent GW Calculations for Semiconductors and Insulators. *Physical Review B*, 75(23):235102, 2007. doi: 10.1103/PhysRevB.75.235102.

[96] S. Wang and J. Wang. Quasiparticle Energies and Optical Excitations in Chevron-Type Graphene Nanoribbon. *The Journal of Physical Chemistry C*, 116(18):10193, 2012. doi: 10.1021/jp2125872.

[97] Heinz Bässler. Charge Transport in Disordered Organic Photoconductors a Monte Carlo Simulation Study. *physica status solidi (b)*, 175(1):15, 1993.

[98] Allen Miller and Elihu Abrahams. Impurity Conduction at Low Concentrations. *Physical Review*, 120(3):745, 1960.

[99] R. A. Marcus and N. Sutin. Electron Transfers in Chemistry and Biology. *Biochimica et Biophysica Acta (BBA)-Reviews on Bioenergetics*, 811(3):265, 1985.

[100] K. Asadi, A. J. Kronemeijer, T. Cramer, L. J. A. Koster, P. W. M. Blom, and D. M. de Leeuw. Polaron Hopping Mediated by Nuclear Tunnelling in Semiconducting Polymers at High Carrier Density. *Nature Communications*, 4:1710, 2013. doi: 10.1038/ncomms2708.

[101] N. J. van der Kaap, I. Katsouras, K. Asadi, P. W. M. Blom, L. J. A. Koster, and D. M. de Leeuw. Charge Transport in Disordered Semiconducting Polymers Driven by Nuclear Tunneling. *Physical Review B*, 93(14):140206(R), 2016. doi: 10.1103/PhysRevB.93.140206.

[102] M. P. A. Fisher and Alan T. Dorsey. Dissipative Quantum Tunneling in a Biased Double–Well System at Finite Temperatures. *Physical Review Letters*, 54(15): 1609, 1985.

[103] H. Grabert and U. Weiss. Quantum Tunneling Rates for Asymmetric Double-Well Systems with Ohmic Dissipation. *Physical Review Letters*, 54(15):1605, 1985.

[104] N. Ueno. Electronic Structure of Molecular Solids: Bridge to the Electrical Conduction. In *Physics of Organic Semiconductors*, page 65. Wiley-VCH Verlag GmbH & Co. KGaA, 2012. ISBN 978-3-527-65494-9. doi: 10.1002/9783527654949.ch3.

[105] C. Kittel. *Einführung in die Festkörperphysik*. Oldenbourg, München, Wien, 13. edition, 2002. ISBN 978-3-486-27219-2.

[106] S. Blundell. *Magnetism in Condensed Matter*. Oxford Master Series in Condensed Matter Physics. Oxford University Press, Oxford, 2001. ISBN 978-0-19-850591-4.

[107] E. C. Stoner. Collective Electron Ferromagnetism. *Proceedings of the Royal Society of London. Series A. Mathematical and Physical Sciences*, 165(922):372, 1938. doi: 10.1098/rspa.1938.0066.

[108] H. A. Kramers. L'interaction Entre les Atomes Magnétogènes dans un Cristal Paramagnétique. *Physica*, 1(1-6):182, 1934. doi: 10.1016/S0031-8914(34)90023-9.

[109] P. W. Anderson. Antiferromagnetism. Theory of Superexchange Interaction. *Physical Review*, 79(2):350, 1950. doi: 10.1103/PhysRev.79.350.

[110] P. W. Anderson. Generalizations of the Weiss Molecular Field Theory of Antiferromagnetism. *Physical Review*, 79(4):705, 1950. doi: 10.1103/PhysRev.79.705.

[111] P. W. Anderson. New Approach to the Theory of Superexchange Interactions. *Physical Review*, 115(1):2, 1959. doi: 10.1103/PhysRev.115.2.

[112] J. B. Goodenough. Theory of the Role of Covalence in the Perovskite–Type Manganites [La,M(II)]MnO_3. *Physical Review*, 100:564, 1955. doi: 10.1103/PhysRev.100.564.

[113] J. B. Goodenough. An Interpretation of the Magnetic Properties of the Perovskite-Type Mixed Crystals $La_{(1-x)}Sr_xCoO_{(3-lambda)}$. *J. Phys. Chem. Solids.*, 6:287, 1958. doi: 10.1016/0022-3697(58)90107-0.

[114] J. Kanamori. Superexchange Interaction and Symmetry Properties of Electron Orbitals. *J. Phys. Chem. Solids.*, 10:87, 1959. doi: 10.1016/0022-3697(59)90061-7.

[115] P. W. Anderson. Exchange in Insulators: Superexchange, Direct Exchange, and Double Exchange. In *Magnetism*, page 25. Academic Press, 1963. ISBN 978-0-12-575301-2. Edited by Rado, G. T. and Suhl, H.

[116] D. J. Gardiner and P. R. Graves. *Practical Raman Spectroscopy*. Springer, Berlin, Heidelberg, 1989. ISBN 978-3-540-50254-8.

[117] A. C. Ferrari and D. M. Basko. Raman Spectroscopy as a Versatile Tool for Studying the Properties of Graphene. *Nature Nanotechnology*, 8(4):235, 2013. doi: 10.1038/nnano.2013.46.

[118] C. V. Raman and K. S. Krishnan. A New Type of Secondary Radiation. *Nature*, 121:501, 1928. doi: 10.1038/121501c0.

[119] G. Landsberg and L. Mandelstam. Eine neue Erscheinung bei der Lichtzerstreuung in Krystallen. *Naturwissenschaften*, 16(28):557, 1928. doi: 10.1007/BF01506807.

[120] A. C. Ferrari, J. C. Meyer, V. Scardaci, C. Casiraghi, M. Lazzeri, F. Mauri, S. Piscanec, D. Jiang, K. S. Novoselov, S. Roth, and A. K. Geim. Raman Spectrum of Graphene and Graphene Layers. *Physical Review Letters*, 97(18):187401, 2006. doi: 10.1103/PhysRevLett.97.187401.

[121] S. Piscanec, M. Lazzeri, Francesco Mauri, A. C. Ferrari, and J. Robertson. Kohn Anomalies and Electron-Phonon Interactions in Graphite. *Physical Review Letters*, 93(18):185503, 2004. doi: 10.1103/PhysRevLett.93.185503.

[122] D. M. Basko, S. Piscanec, and A. C. Ferrari. Electron–Electron Interactions and Doping Dependence of the Two–Phonon Raman Intensity in Graphene. *Physical Review B*, 80(16):165413, 2009. doi: 10.1103/PhysRevB.80.165413.

[123] D. M. Basko. Calculation of the Raman G Peak Intensity in Monolayer Graphene: Role of Ward Identities. *New Journal of Physics*, 11(9):095011, 2009. doi: 10.1088/1367-2630/11/9/095011.

[124] M. Kalbac, A. Reina-Cecco, H. Farhat, J. Kong, L. Kavan, and M. S. Dresselhaus. The Influence of Strong Electron and Hole Doping on the Raman Intensity of

Chemical Vapor-Deposition Graphene. *ACS Nano*, 4(10):6055, 2010. doi: 10.1021/nn1010914.

[125] C.-F. Chen, C.-H. Park, B. W. Boudouris, J. Horng, B. Geng, C. Girit, A. Zettl, M. F. Crommie, R. A. Segalman, S. G. Louie, and F. Wang. Controlling Inelastic Light Scattering Quantum Pathways in Graphene. *Nature*, 471(7340):617, 2011. doi: 10.1038/nature09866.

[126] Y. M. You, Z. H. Ni, T. Yu, and Z. X. Shen. Edge Chirality Determination of Graphene by Raman Spectroscopy. *Applied Physics Letters*, 93(16):163112, 2008. doi: 10.1063/1.3005599.

[127] C. Casiraghi, A. Hartschuh, H. Qian, S. Piscanec, C. Georgi, A. Fasoli, K. S. Novoselov, D. M. Basko, and A. C. Ferrari. Raman Spectroscopy of Graphene Edges. *Nano Letters*, 9(4):1433, 2009. doi: 10.1021/nl8032697.

[128] L. G. Cançado, M. A. Pimenta, B. R. A. Neves, M. S. S. Dantas, and A. Jorio. Influence of the Atomic Structure on the Raman Spectra of Graphite Edges. *Physical Review Letters*, 93(24):247401, 2004. doi: 10.1103/PhysRevLett.93.247401.

[129] M. Begliarbekov, K.-I. Sasaki, O. Sul, E.-H. Yang, and S. Strauf. Optical Control of Edge Chirality in Graphene. *Nano Letters*, 11(11):4874, 2011. doi: 10.1021/nl2027316.

[130] I. A. Verzhbitskiy, M. De Corato, A. Ruini, E. Molinari, A. Narita, Y. Hu, M. G. Schwab, M. Bruna, D. Yoon, S. Milana, X. Feng, K. Müllen, A. C. Ferrari, C. Casiraghi, and D. Prezzi. Raman Fingerprints of Atomically Precise Graphene Nanoribbons. *Nano Letters*, 16(6):3442, 2016. doi: 10.1021/acs.nanolett.5b04183.

[131] J. Zhou and J. Dong. Vibrational Property and Raman Spectrum of Carbon Nanoribbon. *Applied Physics Letters*, 91(17):173108, 2007. doi: 10.1063/1.2800796.

[132] M. Yamada, Y. Yamakita, and K. Ohno. Phonon Dispersions of Hydrogenated and Dehydrogenated Carbon Nanoribbons. *Physical Review B*, 77(5):054302, 2008. doi: 10.1103/PhysRevB.77.054302.

[133] M. Vandescuren, P. Hermet, V. Meunier, L. Henrard, and P. Lambin. Theoretical Study of the Vibrational Edge Modes in Graphene Nanoribbons. *Physical Review B*, 78(19):195401, 2008. doi: 10.1103/PhysRevB.78.195401.

[134] R. Gillen, M. Mohr, and J. Maultzsch. Symmetry Properties of Vibrational Modes in Graphene Nanoribbons. *Physical Review B*, 81(20):205426, 2010. doi: 10.1103/PhysRevB.81.205426.

[135] C. J. Docherty, C.-T. Lin, H. J. Joyce, R. J. Nicholas, L. M. Herz, L.-J. Li, and M. B. Johnston. Extreme Sensitivity of Graphene Photoconductivity to Environmental Gases. *Nature Communications*, 3(1228):1228, 2012. doi: 10.1038/ncomms2235.

[136] C. F. Coombs. Impedance Measurement Instruments. In *Electronic Instrument Handbook, Third Edition*. McGraw Hill Professional, Access Engineering, 1972.

[137] L. J. van der Pauw. A Method of Measuring Specific Resistivity and Hall Effect of Discs of Arbitrary Shape. *Philips Research Reports*, 13(1), 1958.

[138] R. Chwang, B. J. Smith, and C. R. Crowell. Contact Size Effects on the van der Pauw Method for Resistivity and Hall Coefficient Measurement. *Solid-State Electronics*, 17(12):1217, 1974. doi: 10.1016/0038-1101(74)90001-X.

[139] B. D. Josephson. Possible New Effects in Superconductive Tunnelling. *Physics Letters*, 1(7):251, 1962. doi: 10.1016/0031-9163(62)91369-0.

[140] R. L. Fagaly. Superconducting Quantum Interference Device Instruments and Applications. *Review of Scientific Instruments*, 77(10):101101, 2006. doi: 10.1063/1.2354545.

[141] M. Tinkham. *Introduction to Superconductivity*. International Series in Pure and Applied Physics. McGraw-Hill, New York, 1975. ISBN 0-07-064877-8.

[142] Quantum Design Inc. Magnetic Property Measurement System – MPMS-XL data sheet, 2011.

[143] P. Stamenov and J. M. D. Coey. Sample Size, Position, and Structure Effects on Magnetization Measurements Using Second–Order Gradiometer Pickup Coils. *Review of Scientific Instruments*, 77(1):015106, 2006. doi: 10.1063/1.2149190.

[144] M. A. Mohammad, M. Muhammad, S. Dew, and M. Stepanova. Fundamentals of Electron Beam Exposure and Development. In M. Stepanova and S. Dew, editors, *Nanofabrication*, pages 11–41. Springer Vienna, Vienna, 2012. ISBN 978-3-7091-0423-1. doi: 10.1007/978-3-7091-0424-8_2.

[145] N. Richter. Spin and Charge Transport in Graphene Nanostructures. Diploma Thesis. Johannes Gutenberg–Universität Mainz, 2013.

[146] M. Ohring. *Materials Science of Thin Films*, volume 2. Academic Press, San Diego, CA, 2002. ISBN 978-0-12-524975-1.

[147] N. Richter, Y. R. Hernandez, S. Schweitzer, J.-S. Kim, A. K. Patra, J. Englert, I. Lieberwirth, A. Liscio, V. Palermo, X. Feng, A. Hirsch, K. Müllen, and M. Kläui. Robust Two–Dimensional Electronic Properties in Three-Dimensional Microstructures of Rotationally Stacked Turbostratic Graphene. *Physical Review Applied*, 7 (2):024022, 2017. doi: 10.1103/PhysRevApplied.7.024022.

[148] M. Bokdam, P. A. Khomyakov, G. Brocks, Z. Zhong, and P. J. Kelly. Electrostatic Doping of Graphene through Ultrathin Hexagonal Boron Nitride Films. *Nano Letters*, 11(11):4631, 2011. doi: 10.1021/nl202131q.

[149] Y. Ito, C. Christodoulou, M. V. Nardi, N. Koch, H. Sachdev, and K. Müllen. Chemical Vapor Deposition of N-Doped Graphene and Carbon Films: The Role of Precursors and Gas Phase. *ACS Nano*, 8(4):3337, 2014. doi: 10.1021/nn405661b.

[150] A. L. M. Reddy, A. Srivastava, S. R. Gowda, H. Gullapalli, M. Dubey, and P. M. Ajayan. Synthesis Of Nitrogen-Doped Graphene Films For Lithium Battery Application. *ACS Nano*, 4(11):6337, 2010. doi: 10.1021/nn101926g.

[151] D. Wei, Y. Liu, Y. Wang, H. Zhang, L. Huang, and G. Yu. Synthesis of N-Doped Graphene by Chemical Vapor Deposition and Its Electrical Properties. *Nano Letters*, 9(5):1752, 2009. doi: 10.1021/nl803279t.

[152] L. Ci, L. Song, C. Jin, D. Jariwala, D. Wu, Y. Li, A. Srivastava, Z. F. Wang, K. Storr, L. Balicas, F. Liu, and P. M. Ajayan. Atomic Layers of Hybridized Boron Nitride and Graphene Domains. *Nature Materials*, 9(5):430, 2010. doi: 10.1038/nmat2711.

[153] H. Wang, Y. Zhou, D. Wu, L. Liao, S. Zhao, H. Peng, and Z. Liu. Synthesis of Boron-Doped Graphene Monolayers Using the Sole Solid Feedstock by Chemical Vapor Deposition. *Small*, 9(8):1316, 2013. doi: 10.1002/smll.201203021.

[154] F. Hassani, H. Tavakol, F. Keshavarzipour, and A. Javaheri. A Simple Synthesis of Sulfur-Doped Graphene Using Sulfur Powder by Chemical Vapor Deposition. *RSC Advances*, 6(32):27158, 2016. doi: 10.1039/C6RA02109C.

[155] H. Gao, Z. Liu, L. Song, W. Guo, W. Gao, L. Ci, A. Rao, W. Quan, R. Vajtai, and P. M Ajayan. Synthesis of S–Doped Graphene by Liquid Precursor. *Nanotechnology*, 23(27):275605, 2012. doi: 10.1088/0957-4484/23/27/275605.

[156] J. Zhang, J. Li, Z. Wang, X. Wang, W. Feng, W. Zheng, W. Cao, and P. Hu. Low-Temperature Growth of Large-Area Heteroatom-Doped Graphene Film. *Chemistry of Materials*, 26(7):2460, 2014. doi: 10.1021/cm500086j.

[157] S. Some, J. Kim, K. Lee, A. Kulkarni, Y. Yoon, S. Lee, T. Kim, and H. Lee. Highly Air–Stable Phosphorus–Doped n–Type Graphene Field–Effect Transistors. *Advanced Materials*, 24(40):5481, 2012. doi: 10.1002/adma.201202255.

[158] R. Lv, M. C. dos Santos, C. Antonelli, S. Feng, K. Fujisawa, A. Berkdemir, R. Cruz-Silva, A. L. Elías, N. Perea-Lopez, F. López-Urías, H. Terrones, and M. Terrones. Large-Area Si-Doped Graphene: Controllable Synthesis and Enhanced Molecular Sensing. *Advanced Materials*, 26(45):7593, 2014. doi: 10.1002/adma.201403537.

[159] A. L. Friedman, C. D. Cress, S. W. Schmucker, J. T. Robinson, and O. M. J. van 't Erve. Electronic Transport and Localization in Nitrogen-Doped Graphene Devices using Hyperthermal Ion Implantation. *Physical Review B*, 93(16):161409(R), 2016. doi: 10.1103/PhysRevB.93.161409.

[160] L. Banszerus, M. Schmitz, S. Engels, J. Dauber, M. Oellers, F. Haupt, K. Watanabe, T. Taniguchi, B. Beschoten, and C. Stampfer. Ultrahigh-Mobility Graphene Devices from Chemical Vapor Deposition on Reusable Copper. *Science Advances*, 1(6):e1500222, 2015. doi: 10.1126/sciadv.1500222.

[161] H. C. Lee, W.-W. Liu, S.-P. Chai, A. R. Mohamed, C. W. Lai, C.-S. Khe, C. H. Voon, U. Hashim, and N. M. S. Hidayah. Synthesis of Single-layer Graphene: A

Review of Recent Development. *Procedia Chemistry*, 19:916, 2016. doi: 10.1016/j.proche.2016.03.135.

[162] T. Schiros, D. Nordlund, L. Pálová, D. Prezzi, L. Zhao, K. S. Kim, U. Wurstbauer, C. Gutiérrez, D. Delongchamp, C. Jaye, D. Fischer, H. Ogasawara, L. G. M. Pettersson, D. R. Reichman, P. Kim, M. S. Hybertsen, and A. N. Pasupathy. Connecting Dopant Bond Type with Electronic Structure in N-Doped Graphene. *Nano Letters*, 12(8):4025, 2012. doi: 10.1021/nl301409h.

[163] L. Zhao, R. He, K. T. Rim, T. Schiros, K. S. Kim, H. Zhou, C. Gutiérrez, S. P. Chockalingam, C. J. Arguello, L. Pálová, D. Nordlund, M. S. Hybertsen, D. R. Reichman, T. F. Heinz, P. Kim, A. Pinczuk, G. W. Flynn, and A. N. Pasupathy. Visualizing Individual Nitrogen Dopants in Monolayer Graphene. *Science*, 333 (6045):999, 2011. doi: 10.1126/science.1208759.

[164] F. Bonaccorso, A. Lombardo, T. Hasan, Z. Sun, L. Colombo, and A. C. Ferrari. Production and Processing of Graphene and 2D Crystals. *Materials Today*, 15 (12):564, 2012. doi: 10.1016/S1369-7021(13)70014-2.

[165] W. S. Hwang, P. Zhao, K. Tahy, L. O. Nyakiti, V. D. Wheeler, R. L. Myers-Ward, C. R. Eddy, D. K. Gaskill, J. A. Robinson, W. Haensch, H. Xing, A. Seabaugh, and D. Jena. Graphene Nanoribbon Field–Effect Transistors on Wafer–Scale Epitaxial Graphene on SiC Substrates. *APL Materials*, 3(1):011101, 2015. doi: 10.1063/1.4905155.

[166] B. Song, G. F. Schneider, Q. Xu, G. Pandraud, C. Dekker, and H. Zandbergen. Atomic-Scale Electron-Beam Sculpting of Near-Defect-Free Graphene Nanostructures. *Nano Letters*, 11(6):2247, 2011. doi: 10.1021/nl200369r.

[167] D. B. Shinde, M. Majumder, and V. K. Pillai. Counter-ion Dependent, Longitudinal Unzipping of Multi-Walled Carbon Nanotubes to Highly Conductive and Transparent Graphene Nanoribbons. *Scientific Reports*, 4(4363), 2014. doi: 10.1038/srep04363.

[168] D. V. Kosynkin, A. L. Higginbotham, A. Sinitskii, J. R. Lomeda, A. Dimiev, B. K. Price, and J. M. Tour. Longitudinal Unzipping of Carbon Nanotubes to Form Graphene Nanoribbons. *Nature*, 458(7240):872, 2009. doi: 10.1038/nature07872.

[169] J. Cai, C. A. Pignedoli, L. Talirz, P. Ruffieux, H. Söde, L. Liang, V. Meunier, R. Berger, R. Li, X. Feng, K. Müllen, and R. Fasel. Graphene Nanoribbon Heterojunctions. *Nature Nanotechnology*, 9(11):896, 2014. doi: 10.1038/nnano.2014.184.

[170] Y.-C. Chen, T. Cao, C. Chen, Z. Pedramrazi, D. Haberer, D.s G. de Oteyza, F. R. Fischer, S. G. Louie, and M. F. Crommie. Molecular Bandgap Engineering of Bottom–Up Synthesized Graphene Nanoribbon Heterojunctions. *Nature Nanotechnology*, 10(2):156, 2015. doi: 10.1038/nnano.2014.307.

[171] M. G. Schwab, A. Narita, Y. Hernandez, T. Balandina, K. S. Mali, S. De Feyter, X. Feng, and K. Müllen. Structurally Defined Graphene Nanoribbons with High Lateral Extension. *Journal of the American Chemical Society*, 134(44):18169, 2012. doi: 10.1021/ja307697j.

[172] L. Dössel, L. Gherghel, X. Feng, and K. Müllen. Graphene Nanoribbons by Chemists: Nanometer-Sized, Soluble, and Defect-Free. *Angewandte Chemie International Edition*, 50(11):2540, 2011. doi: 10.1002/anie.201006593.

[173] X. Yang, X. Dou, A. Rouhanipour, L. Zhi, H. J. Räder, and K. Müllen. Two-Dimensional Graphene Nanoribbons. *Journal of the American Chemical Society*, 130(13):4216, 2008. doi: 10.1021/ja710234t.

[174] A. Narita, X. Feng, Y. Hernandez, S. A. Jensen, M. Bonn, H. Yang, I. A. Verzhbitskiy, C. Casiraghi, M. R. Hansen, A. H. R. Koch, G. Fytas, O. Ivasenko, B. Li, K. S. Mali, T. Balandina, S. Mahesh, S. De Feyter, and K. Müllen. Synthesis of Structurally Well–Defined and Liquid–Phase–Processable Graphene Nanoribbons. *Nature Chemistry*, 6(2):126, 2013. doi: 10.1038/nchem.1819.

[175] A. Narita, I. A. Verzhbitskiy, W. Frederickx, K. S. Mali, S. A. Jensen, M. R. Hansen, M. Bonn, S. De Feyter, C. Casiraghi, X. Feng, and K. Müllen. Bottom-Up Synthesis of Liquid–Phase-Processable Graphene Nanoribbons with Near–Infrared Absorption. *ACS Nano*, 8(11):11622, 2014. doi: 10.1021/nn5049014.

[176] G. Li, K.-Y. Yoon, X. Zhong, X. Zhu, and G. Dong. Efficient Bottom–Up Preparation of Graphene Nanoribbons by Mild Suzuki–Miyaura Polymerization of Simple Triaryl Monomers. *Chemistry - A European Journal*, 22(27):9116, 2016. doi: 10.1002/chem.201602007.

[177] T. H. Vo, M. Shekhirev, D. A. Kunkel, F. Orange, M. J.-F. Guinel, A. Enders, and A. Sinitskii. Bottom–Up Solution Synthesis of Narrow Nitrogen-Doped Graphene Nanoribbons. *Chemical Communications*, 50(32):4172, 2014. doi: 10.1039/c4cc00885e.

[178] A. Kimouche, M. M. Ervasti, R. Drost, S. Halonen, A. Harju, P. M. Joensuu, J. Sainio, and P. Liljeroth. Ultra-Narrow Metallic Armchair Graphene Nanoribbons. *Nature Communications*, 6:10177, 2015. doi: 10.1038/ncomms10177.

[179] Y.-C. Chen, D. G. de Oteyza, Z. Pedramrazi, C. Chen, F. R. Fischer, and M. F. Crommie. Tuning the Band Gap of Graphene Nanoribbons Synthesized from Molecular Precursors. *ACS Nano*, 7(7):6123, 2013. doi: 10.1021/nn401948e.

[180] P. Ruffieux, S. Wang, B. Yang, C. Sánchez-Sánchez, J. Liu, T. Dienel, L. Talirz, P. Shinde, C. A. Pignedoli, D. Passerone, T. Dumslaff, X. Feng, K. Müllen, and R. Fasel. On-Surface Synthesis of Graphene Nanoribbons with Zigzag Edge Topology. *Nature*, 531(7595):489, 2016. doi: 10.1038/nature17151.

[181] R. R. Cloke, T. Marangoni, G. D. Nguyen, T. Joshi, D. J. Rizzo, C. Bronner, T. Cao, S. G. Louie, M. F. Crommie, and F. R. Fischer. Site–Specific Substitutional Boron Doping of Semiconducting Armchair Graphene Nanoribbons. *Journal of the American Chemical Society*, 137(28):8872, 2015. doi: 10.1021/jacs.5b02523.

[182] S. Kawai, S. Saito, S. Osumi, S. Yamaguchi, A. S. Foster, P. Spijker, and E. Meyer. Atomically Controlled Substitutional Boron–Doping of Graphene Nanoribbons. *Nature Communications*, 6:8098, 2015. doi: 10.1038/ncomms9098.

[183] G. D. Nguyen, F. M. Toma, T. Cao, Z. Pedramrazi, C. Chen, D. J. Rizzo, T. Joshi, C. Bronner, Y.-C. Chen, M. Favaro, S. G. Louie, F. R. Fischer, and M. F. Crommie. Bottom–Up Synthesis of $N = 13$ Sulfur–Doped Graphene Nanoribbons. *The Journal of Physical Chemistry C*, 120(5):2684, 2016. doi: 10.1021/acs.jpcc.5b09986.

[184] Z. Chen, H. I. Wang, J. Teyssandier, K. S. Mali, T. Dumslaff, I. Ivanov, W. Zhang, P. Ruffieux, R. Fasel, H. J. Räder, D. Turchinovich, S. De Feyter, X. Feng, M. Kläui, A. Narita, M. Bonn, and K. Müllen. Chemical Vapor Deposition Synthesis and Terahertz Photoconductivity of Low-Band-Gap $N = 9$ Armchair Graphene Nanoribbons. *Journal of the American Chemical Society*, 139(10):3635, 2017. doi: 10.1021/jacs.7b00776.

[185] Z. Chen, H. I. Wang, N. Bilbao, J. Teyssandier, T. Prechtl, N. Cavani, A. Tries, R. Biagi, V. De Renzi, X. Feng, M. Kläui, S. De Feyter, M. Bonn, A. Narita, and K Müllen. Lateral Fusion of Chemical Vapor Deposited $N = 5$ Armchair Graphene Nanoribbons. *Journal of the American Chemical Society*, 139(28):9483, 2017. doi: 10.1021/jacs.7b05055.

[186] L. Chen, Y. Hernandez, X. Feng, and K. Müllen. From Nanographene and Graphene Nanoribbons to Graphene Sheets: Chemical Synthesis. *Angewandte Chemie International Edition*, 51(31):7640, 2012. doi: 10.1002/anie.201201084.

[187] D. Weckbecker, S. Shallcross, M. Fleischmann, N. Ray, S. Sharma, and O. Pankratov. Low–Energy Theory for the Graphene Twist Bilayer. *Physical Review B*, 93 (3):035452, 2016. doi: 10.1103/PhysRevB.93.035452.

[188] S. Samaddar, I. Yudhistira, S. Adam, H. Courtois, and C.B. Winkelmann. Charge Puddles in Graphene near the Dirac Point. *Physical Review Letters*, 116(12): 126804, 2016. doi: 10.1103/PhysRevLett.116.126804.

[189] S. Lynum, J. Hugdahl, K. Hox, R. Hildrum, and M. Nordvik. Micro–Domain Graphitic Materials and Method for Producing the Same, 1998. WO Patent App. PCT/NO1998/000,093.

[190] G. Binnig, C. F. Quate, and Ch. Gerber. Atomic Force Microscope. *Physical Review Letters*, 56:930, 1986. doi: 10.1103/PhysRevLett.56.930.

[191] D. Tasis, N. Tagmatarchis, A. Bianco, and M. Prato. Chemistry of Carbon Nanotubes. *Chemical Reviews*, 106(3):1105, 2006. doi: 10.1021/cr050569o.

[192] Tetrahydrofuran. URL `http://www.sigmaaldrich.com/MSDS/MSDS/DisplayMSDSPage.do?country=DE&language=de&productNumber=401757&brand=SIAL&PageToGoToURL=Fsafety-center.html`. material safety data sheet [Online]; Sigma–Aldrich: St. Louis, Missouri (USA), Sep 1, 2016. url accessed May 12, 2017.

[193] 1-methyl-2-pyrrolidon. URL `http://www.sigmaaldrich.com/MSDS/MSDS/DisplayMSDSPage.do?country=DE&language=de&productNumber=78769&brand=SIAL&PageToGoToURL=http%3A%2F%2Fwww.sigmaaldrich.com%2Fcatalog%2Fproduct%2Fsial%2F78769%3Flang%3Dde`. material safety data

sheet [Online]; Sigma–Aldrich: St. Louis, Missouri (USA), Jun 17, 2015. url accessed May 12, 2017.

[194] A. N. Abbas, G. Liu, A. Narita, M. Orosco, X. Feng, K. Müllen, and C. Zhou. Deposition, Characterization, and Thin–Film-Based Chemical Sensing of Ultra-Long Chemically Synthesized Graphene Nanoribbons. *Journal of the American Chemical Society*, 136(21):7555, 2014. doi: 10.1021/ja502764d.

[195] U. Zschieschang, H. Klauk, I. B. Müller, A. J. Strudwick, T. Hintermann, M. G. Schwab, A. Narita, X. Feng, K. Müllen, and R. T. Weitz. Electrical Characteristics of Field-Effect Transistors based on Chemically Synthesized Graphene Nanoribbons. *Advanced Electronic Materials*, 1(3):1400010, 2015. doi: 10.1002/aelm.201400010.

[196] P. Fantuzzi, L. Martini, A. Candini, V. Corradini, U. del Pennino, Y. Hu, X. Feng, K. Müllen, A. Narita, and M. Affronte. Fabrication of Three Terminal Devices by ElectroSpray Deposition of Graphene Nanoribbons. *Carbon*, 104:112, 2016. doi: 10.1016/j.carbon.2016.03.052.

[197] P. B. Bennett, Z. Pedramrazi, A. Madani, Y.-C. Chen, D. G. de Oteyza, C. Chen, F. R. Fischer, M. F. Crommie, and J. Bokor. Bottom-Up Graphene Nanoribbon Field-Effect Transistors. *Applied Physics Letters*, 103(25):253114, 2013. doi: 10.1063/1.4855116.

[198] W. Regan, N. Alem, B. Alemán, B. Geng, Ç. Girit, L. Maserati, F. Wang, M. Crommie, and A. Zettl. A Direct Transfer of Layer-Area Graphene. *Applied Physics Letters*, 96(11):113102, 2010. doi: 10.1063/1.3337091.

[199] X. Li, Y. Zhu, W. Cai, M. Borysiak, B. Han, D. Chen, R. D. Piner, L. Colombo, and R. S. Ruoff. Transfer of Large–Area Graphene Films for High–Performance Transparent Conductive Electrodes. *Nano Letters*, 9(12):4359, 2009. doi: 10.1021/nl902623y.

[200] L. Gao, W. Ren, H. Xu, L. Jin, Z. Wang, T. Ma, L.-P. Ma, Z. Zhang, Q. Fu, L.-M. Peng, X. Bao, and H.-M. Cheng. Repeated Growth and Bubbling Transfer of Graphene with Millimetre-Size Single-Crystal Grains using Platinum. *Nature Communications*, 3:699, 2012. doi: 10.1038/ncomms1702.

[201] C. J. L. de la Rosa, J. Sun, N. Lindvall, M. T. Cole, Y. Nam, M. Löffler, E. Olsson, K. B. K. Teo, and A. Yurgens. Frame Assisted H2O Electrolysis Induced H2 Bubbling Transfer of Large Area Graphene Grown by Chemical Vapor Deposition on Cu. *Applied Physics Letters*, 102(2):022101, 2013. doi: 10.1063/1.4775583.

[202] Y. Cho, J.-M. Yang, D. V. Lam, S.-M. Lee, J.-H. Kim, K.-Y. Han, and J. Chang. Transmission Electron Microscopy Specimen Preparation for Layer-area Graphene by a Direct Transfer Method. *Applied Microscopy*, 44(4):133, 2014. doi: 10.9729/AM.2014.44.4.133.

[203] Y.-C. Lin, C.-C. Lu, C.-H. Yeh, C. Jin, K. Suenaga, and P.-W. Chiu. Graphene Annealing: How Clean Can It Be? *Nano Letters*, 12(1):414, 2012. doi: 10.1021/nl203733r.

[204] R. S. Sundaram, M. Steiner, H.-Y. Chiu, M. Engel, A. A. Bol, R. Krupke, M. Burghard, K. Kern, and P. Avouris. The Graphene-–Gold Interface and Its Implications for Nanoelectronics. *Nano Letters*, 11(9):3833, 2011. doi: 10.1021/nl201907u.

[205] C.-T. Chen, E. A. Casu, M. Gajek, and S. Raoux. Low–Damage High–Throughput Grazing–Angle Sputter Deposition on Graphene. *Applied Physics Letters*, 103(3):033109, 2013. doi: 10.1063/1.4813911.

[206] X. Shen, H. Wang, and T. Yu. How do the Electron Beam Writing and Metal Deposition Affect the Properties of Graphene during Device Fabrication? *Nanoscale*, 5(8):3352, 2013. doi: 10.1039/c3nr33460k.

[207] H. Park, A. K. L. Lim, A. P. Alivisatos, J. Park, and P. L. McEuen. Fabrication of Metallic Electrodes with Nanometer Separation by Electromigration. *Applied Physics Letters*, 75(2):301, 1999. doi: 10.1063/1.124354.

[208] M. L. Trouwborst, S. J. van der Molen, and B. J. van Wees. The Role of Joule Heating in the Formation of Nanogaps by Electromigration. *Journal of Applied Physics*, 99(11):114316, 2006. doi: 10.1063/1.2203410.

[209] A. K. Patra, A. von Bieren, S. Krzyk, J. Rhensius, L. J. Heyderman, R. Hoffmann, and M. Kläui. Magnetoresistance Measurement of Tailored Permalloy Nanocontacts. *Physical Review B*, 82(13):134447, 2010. doi: 10.1103/PhysRevB.82.134447.

[210] A. von Bieren, A. K. Patra, S. Krzyk, J. Rhensius, R. M. Reeve, L. J. Heyderman, R. Hoffmann-Vogel, and M. Kläui. Domain-Wall Induced Large Magnetoresistance Effects at Zero Applied Field in Ballistic Nanocontacts. *Physical Review Letters*, 110(6):067203, 2013. doi: 10.1103/PhysRevLett.110.067203.

[211] R. M. Reeve, A. Loescher, M.-A. Mawass, R. Hoffmann-Vogel, and M. Kläui. Domain Wall Pinning in Ultra–Narrow Electromigrated Break Junctions. *Journal of Physics: Condensed Matter*, 26(47):474207, 2014. doi: 10.1088/0953-8984/26/47/474207.

[212] F. Prins, A. Barreiro, J. W. Ruitenberg, J. S. Seldenthuis, N. Aliaga-Alcalde, L. M. K. Vandersypen, and H. S. J. van der Zant. Room–Temperature Gating of Molecular Junctions Using Few-Layer Graphene Nanogap Electrodes. *Nano Letters*, 11(11):4607, 2011. doi: 10.1021/nl202065x.

[213] H. S. J. van der Zant, Y.-V. Kervennic, M. Poot, K. O'Neill, Z. de Groot, J. M. Thijssen, H. B. Heersche, N. Stuhr-Hansen, T. Bjørnholm, D. Vanmaekelbergh, C. A. van Walree, and L. W. Jenneskens. Molecular Three-Terminal Devices: Fabrication and Measurements. *Faraday Discuss.*, 131:347, 2006. doi: 10.1039/B506240N.

[214] D. R. Strachan, D. E. Smith, D. E. Johnston, T.-H. Park, M. J. Therien, D. A. Bonnell, and A. T. Johnson. Controlled Fabrication of Nanogaps in Ambient Environment for Molecular Electronics. *Applied Physics Letters*, 86(4):043109, 2005. doi: 10.1063/1.1857095.

[215] R. Vincent, S. Klyatskaya, M. Ruben, W. Wernsdorfer, and F. Balestro. Electronic Read–Out of a Single Nuclear Spin Using a Molecular Spin Transistor. *Nature*, 488(7411):357, 2012. doi: 10.1038/nature11341.

[216] S. Thiele, F. Balestro, R. Ballou, S. Klyatskaya, M. Ruben, and W. Wernsdorfer. Electrically Driven Nuclear Spin Resonance in Single–Molecule Magnets. *Science*, 344(6188):1135, 2014. doi: 10.1126/science.1249802.

[217] S. Lumetti, A. Candini, C. Godfrin, F. Balestro, W. Wernsdorfer, S. Klyatskaya, M. Ruben, and M. Affronte. Single–Molecule Devices with Graphene Electrodes. *Dalton Trans.*, 45(42):16570, 2016. doi: 10.1039/C6DT02445A.

[218] K. N. Tu. Electromigration in Stressed Thin Films. *Physical Review B*, 45(3): 1409, 1992. doi: 10.1103/PhysRevB.45.1409.

[219] A. Loescher. Confined Domain Walls in Magnetic Nano Contacts. Diploma Thesis. Johannes Gutenberg–Universität Mainz, 2013.

[220] A. Candini, S. Klyatskaya, M. Ruben, W. Wernsdorfer, and M. Affronte. Graphene Spintronic Devices with Molecular Nanomagnets. *Nano Letters*, 11(7):2634, 2011. doi: 10.1021/nl2006142.

[221] A. Candini, N. Richter, D. Convertino, C. Coletti, F. Balestro, W. Wernsdorfer, M. Kläui, and M. Affronte. Electroburning of Few–Layer Graphene Flakes, Epitaxial Graphene, and Turbostratic Graphene Discs in Air and under Vacuum. *Beilstein Journal of Nanotechnology*, 6:711, 2015. doi: 10.3762/bjnano.6.72.

[222] J. P. Llinas, A. Fairbrother, G. Borin Barin, W. Shi, K. Lee, S. Wu, B. Yong Choi, R. Braganza, J. Lear, N. Kau, W. Choi, C. Chen, Z. Pedramrazi, T. Dumslaff, A. Narita, X. Feng, K. Müllen, F. Fischer, A. Zettl, P. Ruffieux, E. Yablonovitch, M. Crommie, R. Fasel, and J. Bokor. Short–Channel Field–Effect Transistors with 9–Atom and 13–Atom Wide Graphene Nanoribbons. *Nature Communications*, 8 (1), 2017. doi: 10.1038/s41467-017-00734-x.

[223] M. Affronte, M. Kläui, W. Wernsdorfer, K. Müllen, and M. Ruben. White Book on the Realization of Molecular Electrodes and Devices Fabrication, 2016. URL `http://www.moquas.eu/wp-content/uploads/2013/10/White-Book-on-fabrication-of-molecular-electrodes.pdf`.

[224] J. Bai, R. Cheng, F. Xiu, L. Liao, M. Wang, A. Shailos, K. L. Wang, Y. Huang, and X. Duan. Very Large Magnetoresistance in Graphene Nanoribbons. *Nature Nanotechnology*, 5(9):655, 2010. doi: 10.1038/nnano.2010.154.

[225] S. M. Sze and Kwok K. Ng. MOSFETs. In *Physics of Semiconductor Devices*, page 293. John Wiley & Sons, Inc., 2006. ISBN 978-0-470-06832-8. doi: 10.1002/9780470068328.ch6.

[226] A. Kokil, K. Yang, and J. Kumar. Techniques for Characterization of Charge Carrier Mobility in Organic Semiconductors. *Journal of Polymer Science Part B: Polymer Physics*, 50(15):1130, 2012. doi: 10.1002/polb.23103.

[227] J. S. Lee, S. Ryu, K. Yoo, I. S. Choi, W. S. Yun, and J. Kim. Origin of Gate Hysteresis in Carbon Nanotube Field-Effect Transistors. *The Journal of Physical Chemistry C*, 111(34):12504, 2007. doi: 10.1021/jp074692q.

[228] H. Wang, Y. Wu, C. Cong, J. Shang, and T. Yu. Hysteresis of Electronic Transport in Graphene Transistors. *ACS Nano*, 4(12):7221, 2010. doi: 10.1021/nn101950n.

[229] A. Tries, N. Richter, Z. Chen, K. Müllen, and M. Kläui. Hysteresis of Electronic Transport in Graphene Nanoribbon Transistors, 2017. *Manuscript in preparation.*

[230] T. Fang, A. Konar, H. Xing, and D. Jena. Carrier Statistics and Quantum Capacitance of Graphene Sheets and Ribbons. *Applied Physics Letters*, 91(9):092109, 2007. doi: 10.1063/1.2776887.

[231] S. Hertel, F. Kisslinger, J. Jobst, D. Waldmann, M. Krieger, and H. B. Weber. Current Annealing and Electrical Breakdown of Epitaxial Graphene. *Applied Physics Letters*, 98(21):212109, 2011. doi: 10.1063/1.3592841.

[232] D. Natali and M. Caironi. Charge Injection in Solution–Processed Organic Field–Effect Transistors: Physics, Models and Characterization Methods. *Advanced Materials*, 24(11):1357, 2012. doi: 10.1002/adma.201104206.

[233] S. P. Schießl, N. Fröhlich, M. Held, F. Gannott, M. Schweiger, M. Forster, U. Scherf, and J. Zaumseil. Polymer–Sorted Semiconducting Carbon Nanotube Networks for High–Performance Ambipolar Field-Effect Transistors. *ACS Applied Materials & Interfaces*, 7(1):682, 2015. doi: 10.1021/am506971b.

[234] Q. Cao, S.-H. Hur, Z.-T. Zhu, Y. G. Sun, C.-J. Wang, M. A. Meitl, M. Shim, and J. A. Rogers. Highly Bendable, Transparent Thin–Film Transistors That Use Carbon–Nanotube–Based Conductors and Semiconductors with Elastomeric Dielectrics. *Advanced Materials*, 18(3):304, 2006. doi: 10.1002/adma.200501740.

[235] S. H. Jin, J. Shin, I.-T. Cho, S. Y. Han, D. J. Lee, C. H. Lee, J.-H. Lee, and J. A. Rogers. Solution–Processed Single–Walled Carbon Nanotube Field Effect Transistors and Bootstrapped Inverters for Disintegratable, Transient Electronics. *Applied Physics Letters*, 105(1):013506, 2014. doi: 10.1063/1.4885761.

[236] T. J. Richards and H. Sirringhaus. Analysis of the Contact Resistance in Staggered, Top–Gate Organic Field-Effect Transistors. *Journal of Applied Physics*, 102(9): 094510, 2007. doi: 10.1063/1.2804288.

[237] K. P. Puntambekar, P. V. Pesavento, and C. D. Frisbie. Surface Potential Profiling and Contact Resistance Measurements on Operating Pentacene Thin–Film Transistors by Kelvin Probe Force Microscopy. *Applied Physics Letters*, 83(26): 5539, 2003. doi: 10.1063/1.1637443.

[238] M. Bockrath, D. H. Cobden, J. Lu, A. G. Rinzler, R. E. Smalley, L. Balents, and P. L. McEuen. Luttinger–Liquid Behaviour in Carbon Nanotubes. *Nature*, 397 (6720):598, 1999. doi: 10.1038/17569.

[239] E. B. Sonin. Tunneling into 1d and Quasi–1d Conductors and Luttinger-Liquid Behavior. *Journal of Low Temperature Physics*, 124(1):321, 2001. doi: 10.1023/A:1017598423240.

[240] A. S. Rodin and M. M. Fogler. Apparent Power–Law Behavior of Conductance in Disordered Quasi–One–Dimensional Systems. *Physical Review Letters*, 105(10): 106801, 2010. doi: 10.1103/PhysRevLett.105.106801.

[241] W. F. Pasveer, J. Cottaar, C. Tanase, R. Coehoorn, P. A. Bobbert, P. W. M. Blom, D. M. de Leeuw, and M. A. J. Michels. Unified Description of Charge–Carrier Mobilities in Disordered Semiconducting Polymers. *Physical Review Letters*, 94 (20):206601, 2005. doi: 10.1103/PhysRevLett.94.206601.

[242] A. J. Campbell, D. D. C. Bradley, and D. G. Lidzey. Space–Charge Limited Conduction with Traps in Poly(Phenylene Vinylene) Light Emitting Diodes. *Journal of Applied Physics*, 82(12):6326, 1997. doi: 10.1063/1.366523.

[243] B. Obradovic, R. Kotlyar, F. Heinz, P. Matagne, T. Rakshit, M. D. Giles, M. A. Stettler, and D. E. Nikonov. Analysis of Graphene Nanoribbons as a Channel Material for Field–Effect Transistors. *Applied Physics Letters*, 88(14):142102, 2006. doi: 10.1063/1.2191420.

[244] M. Kuik, G.-J. A. H. Wetzelaer, H. T. Nicolai, N. I. Craciun, D. M. De Leeuw, and P. W. M. Blom. 25th Anniversary Article: Charge Transport and Recombination in Polymer Light-Emitting Diodes. *Advanced Materials*, 26(4):512, 2014. doi: 10.1002/adma.201303393.

[245] J.-P. Jan. Galvamomagnetic and Thermomagnetic Effects in Metals. *Solid State Physics*, 5:1, 1957. doi: 10.1016/S0081-1947(08)60101-0.

[246] M. Y. Azbel. Variable-Range-Hopping Magnetoresistance. *Physical Review B*, 43 (3):2435, 1991. doi: 10.1103/PhysRevB.43.2435.

[247] A. S. Mayorov, R. V. Gorbachev, S. V. Morozov, L. Britnell, R. Jalil, L. A. Ponomarenko, P. Blake, K. S. Novoselov, K. Watanabe, T. Taniguchi, and A. K. Geim. Micrometer–Scale Ballistic Transport in Encapsulated Graphene at Room Temperature. *Nano Letters*, 11(6):2396, 2011. doi: 10.1021/nl200758b.

[248] M. Rein. Charge Transport in Graphene Nanostructures. Bachelor Thesis. Johannes Gutenberg-Universität Mainz, 2013.

[249] M. Rein, N. Richter, K. Parvez, X. Feng, H. Sachdev, M. Kläui, and K. Müllen. Magnetoresistance and Charge Transport in Graphene Governed by Nitrogen Dopants. *ACS Nano*, 9(2):1360, 2015. doi: 10.1021/nn5057063.

[250] T. Sundius. Computer Fitting of Voigt Profiles to Raman Lines. *Journal of Raman Spectroscopy*, 1(5):471, 1973. doi: 10.1002/jrs.1250010506.

[251] S. M. Abrarov and B. M. Quine. Efficient Algorithmic Implementation of the Voigt/Complex Error Function Based on Exponential Series Approximation. *Applied Mathematics and Computation*, 218(5):1894, 2011. doi: 10.1016/j.amc.2011.06.072.

[252] M. Kalbac, O. Frank, and L. Kavan. The Control of Graphene Double-Layer Formation in Copper-Catalyzed Chemical Vapor Deposition. *Carbon*, 50(10):3682, 2012. doi: 10.1016/j.carbon.2012.03.041.

[253] C. H. Lui, L. M. Malard, S. H. Kim, G. Lantz, F. E. Laverge, R. Saito, and T.F. Heinz. Observation of Layer–Breathing Mode Vibrations in Few–Layer Graphene through Combination Raman Scattering. *Nano Letters*, 12(11):5539, 2012. doi: 10.1021/nl302450s.

[254] Y. Zhang, Y.-W. Tan, H. L. Stormer, and P. Kim. Experimental Observation of the Quantum Hall Effect and Berry's Phase in Graphene. *Nature*, 438(7065):201, 2005. doi: 10.1038/nature04235.

[255] A. C. Ferrari and J Robertson. Interpretation of Raman Spectra of Disordered and Amorphous Carbon. *Physical Review B*, 61(20):14095, 2000. doi: 10.1103/PhysRevB.61.14095.

[256] L. G. Cançado, A. Jorio, E. H. Martins Ferreira, F. Stavale, C. A. Achete, R. B. Capaz, M. V. O. Moutinho, A. Lombardo, T. S. Kulmala, and A. C. Ferrari. Quantifying Defects in Graphene via Raman Spectroscopy at Different Excitation Energies. *Nano Letters*, 11(8):3190, 2011. doi: 10.1021/nl201432g.

[257] J. Heo, H. J. Chung, Sung-Hoon Lee, H. Yang, D. H. Seo, J. K. Shin, U-In Chung, S. Seo, E. H. Hwang, and S. Das Sarma. Nonmonotonic Temperature Dependent Transport in Graphene grown by Chemical Vapor Deposition. *Physical Review B*, 84(3):035421, 2011. doi: 10.1103/PhysRevB.84.035421.

[258] J. C. Prestigiacomo, A. Nath, M. S. Osofsky, S. C. Hernández, V. D. Wheeler, S. G. Walton, and D. K. Gaskill. Determining the Nature of the Gap in Semiconducting Graphene. *Scientific Reports*, 7:41713, 2017. doi: 10.1038/srep41713.

[259] N. F. Mott. Conduction in Non-Crystalline Materials: III. Localized States in a Pseudogap and near Extremities of Conduction and Valence Bands. *Philosophical Magazine*, 19(160):835, 1969. doi: 10.1080/14786436908216338.

[260] G. Jakob. Präparation, Charakterisierung der Struktur und Untersuchung der Transporteigenschaften von $YBa_2Cu_3O_7/PrBa_2Cu_3O_7$–Übergittern. PhD Thesis. Technische Hochschule Darmstadt, 1993.

[261] S. Cho and M. S. Fuhrer. Charge Transport and Inhomogeneity near the Minimum Conductivity Point in Graphene. *Physical Review B*, 77(8):081402(R), 2008. doi: 10.1103/PhysRevB.77.081402.

[262] Z.-M. Liao, Y.-B. Zhou, H.-C. Wu, B.-H. Han, and D.-P. Yu. Observation of both Classical and Quantum Magnetoresistance in Bilayer Graphene. *Europhysics Letters*, 94(5):57004, 2011. doi: 10.1209/0295-5075/94/57004.

[263] P. Willke, J. A. Amani, A. Sinterhauf, S. Thakur, T. Kotzott, T. Druga, S. Weikert, K. Maiti, H. Hofsäss, and M. Wenderoth. Doping of Graphene by Low-Energy Ion Beam Implantation: Structural, Electronic, and Transport Properties. *Nano Letters*, 15(8):5110, 2015. doi: 10.1021/acs.nanolett.5b01280.

[264] Y.-B. Zhou, B.-H. Han, Z.-M. Liao, H.-C. Wu, and D.-P. Yu. From Positive to Negative Magnetoresistance in Graphene with Increasing Disorder. *Applied Physics Letters*, 98(22):222502, 2011. doi: 10.1063/1.3595681.

[265] J. Moser, H. Tao, S. Roche, F. Alzina, C. M. Sotomayor Torres, and A. Bachtold. Magnetotransport in Disordered Graphene Exposed to Ozone: From Weak to Strong Localization. *Physical Review B*, 81(20):205445, 2010. doi: 10.1103/PhysRevB.81.205445.

[266] T. G. Rappoport, B. Uchoa, and A. H. Castro Neto. Magnetism and Magnetotransport in Disordered Graphene. *Physical Review B*, 80(24):245408, 2009. doi: 10.1103/PhysRevB.80.245408.

[267] S. Fujita. Negative Magnetoresistance in Carbons and Diffuse Scattering at Crystallite Boundaries. *Carbon*, 6(5):746, 1968. doi: 10.1016/0008-6223(68)90022-5.

[268] X. Zhang, Q. Z. Xue, and D. D. Zhu. Positive and Negative Linear Magnetoresistance of Graphite. *Physics Letters A*, 320(5-6):471, 2004. doi: 10.1016/j.physleta.2003.11.050.

[269] Vladimir I. Fal'ko, K. Kechedzhi, E. McCann, B.L. Altshuler, H. Suzuura, and T. Ando. Weak Localization in Graphene. *Solid State Communications*, 143(1-2):33, 2007. doi: 10.1016/j.ssc.2007.03.049.

[270] E. McCann, K. Kechedzhi, Vladimir I. Fal'ko, H. Suzuura, T. Ando, and B. L. Altshuler. Weak-Localization Magnetoresistance and Valley Symmetry in Graphene. *Physical Review Letters*, 97(14):146805, 2006. doi: 10.1103/PhysRevLett.97.146805.

[271] W.-B. Zhang, Q. Qu, P. Zhu, and C.-H. Lam. Robust Intrinsic Ferromagnetism and Half Semiconductivity in Stable Two–Dimensional Single–Layer Chromium Trihalides. *J. Mater. Chem. C*, 3(48):12457, 2015. doi: 10.1039/C5TC02840J.

[272] H. Wang, V. Eyert, and U. Schwingenschlögl. Electronic Structure and Magnetic Ordering of the Semiconducting Chromium Trihalides $CrCl_3$, $CrBr_3$, and CrI_3. *Journal of Physics: Condensed Matter*, 23(11):116003, 2011. doi: 10.1088/0953-8984/23/11/116003.

[273] B. Morosin and A. Narath. X-Ray Diffraction and Nuclear Quadrupole Resonance Studies of Chromium Trichloride. *The Journal of Chemical Physics*, 40(7):1958, 1964. doi: 10.1063/1.1725428.

[274] L. J. De Jongh and A. R. Miedema. Experiments on Simple Magnetic Model Systems. *Advances in Physics*, 50(8):947, 2001. doi: 10.1080/00018730110101412.

[275] J. W. Cable, M. K. Wilkinson, and E. O. Wollan. Neutron Diffraction Investigation of Antiferromagnetism in $CrCl_3$. *Journal of Physics and Chemistry of Solids*, 19 (1):29, 1961. doi: 10.1016/0022-3697(61)90053-1.

[276] E. C. Stoner and E. P. Wohlfarth. A Mechanism of Magnetic Hysteresis in Heterogeneous Alloys. *Philosophical Transactions of the Royal Society of London. Series A, Mathematical and Physical Sciences*, 240(826):599, 1948. doi: 10.1098/rsta.1948.0007.

[277] Jr. F. Dillon, J. Ferromagnetism and Anisotropy of Chromium Tribromide. *Journal of the Physical Society of Japan*, 19(9):1662, 1964. doi: 10.1143/JPSJ.19.1662.

[278] C. Zener. Classical Theory of the Temperature Dependence of Magnetic Anisotropy Energy. *Physical Review*, 96(5):1335, 1954. doi: 10.1103/PhysRev.96.1335.

[279] W. J. Carr. Temperature Dependence of Ferromagnetic Anisotropy. *Journal of Applied Physics*, 29(3):436, 1958. doi: 10.1063/1.1723171.

[280] H. Wang, F. Fan, S. Zhu, and H. Wu. Doping Enhanced Ferromagnetism and Induced Half-Metallicity in CrI $_3$ Monolayer. *EPL (Europhysics Letters)*, 114(4): 47001, 2016. doi: 10.1209/0295-5075/114/47001.

[281] V. Shautsova, A. M. Gilbertson, N. C. G. Black, S. A. Maier, and L. F. Cohen. Hexagonal Boron Nitride Assisted Transfer and Encapsulation of Large Area CVD Graphene. *Scientific Reports*, 6(1), 2016. doi: 10.1038/srep30210.

[282] X. Wu, X. Li, Z. Song, C. Berger, and W. A. de Heer. Weak Antilocalization in Epitaxial Graphene: Evidence for Chiral Electrons. *Physical Review Letters*, 98 (13):136801, 2007. doi: 10.1103/PhysRevLett.98.136801.

[283] H. Karimi-Alavijeh. Modeling the Gate-Bias Dependence of Contact Resistance in Staggered Organic Field Effect Transistors Based on Carrier-Concentration

Dependent Mobility. *Journal of Applied Physics*, 119(10):105501, 2016. doi: 10.1063/1.4943532.

[284] L. L. Handy and N. W. Gregory. Structural Properties of Chromium(III) Iodide and Some Chromium(III) Mixed Halides. *Journal of the American Chemical Society*, 74(4):891, 1952. doi: 10.1021/ja01124a009.

Acknowledgements

Removed in the electronic version of this thesis due to data protection regulations.

In der elektronischen Version entfernt aufgrund datenschutzrechtlicher Bestimmungen.

Publications List

N. Motzko, B. Burkhardt, **N. Richter**, R. Reeve, P. Laczkowski, W. Savero Torres, L. Vila, J.-P. Attané, and M. Kläui, *Pure spin current-induced domain wall motion probed by localized spin signal detection*, Phys. Rev. B **88**, 214405 (2013).

N. Motzko, **N. Richter**, B. Burkhardt, R. Reeve, P. Laczkowski, L. Vila, J.-P. Attané, and M Kläui, *Spin relaxation in Cu and Al spin conduits*, physica status solidi **211**, 986 (2014).

M. Rein, **N. Richter**, K. Parvez, X. Feng, H. Sachdev, M. Kläui, and Klaus Müllen, *Magnetoresistance and Charge Transport in Graphene Governed by Nitrogen Dopants*, ACS Nano **9**, 1360 (2015).

A. Candini, **N. Richter**, D. Convertino, C. Coletti, F. Balestro, W. Wernsdorfer, M. Kläui, and M. Affronte, *Electroburning of few-layer graphene flakes, epitaxial graphene, and turbostratic graphene discs in air and under vacuum*, Beilstein Journal of Nanotechnology **6**, 711 (2015).

Z. Chen, W. Zhang, C.-A. Palma, A. Lodi Rizzini, B. Liu, A. Abbas, **N. Richter**, L. Martini, X.-Y. Wang, N. Cavani, H. Lu, N. Mishra, C. Coletti, R. Berger, F. Klappenberger, M. Kläui, A. Candini, M. Affronte, C. Zhou, V. De Renzi, U. del Pennino, J. V. Barth, H. J. Räder, A. Narita, X. Feng, and K. Müllen, *Synthesis of Graphene Nanoribbons by Ambient-Pressure Chemical Vapor Deposition and Device Integration*, Journal of the American Chemical Society **138**, 15488 (2016).

A. Pfeiffer, R. M. Reeve, M. Voto, W. Savero-Torres, **N. Richter**, L. Vila, J.-P. Attané, L. Lopez-Diaz, and M. Kläui, *Geometrical control of pure spin current induced domain wall depinning*, Journal of Physics: Condensed Matter, **29**, 085802 (2017).

H. Wang, M.-L. Braatz, **N. Richter**, K.-J. Tielrooij, Z. Mics, H. Lu, N.-E. Weber, K. Müllen, D. Turchinovich, M. Kläui, and M. Bonn, *Reversible Photochemical Control of Doping Levels in Supported Graphene*, The Journal of Physical Chemistry C, **121**, 4083 (2017).

N. Richter, Y. R. Hernandez, S. Schweitzer, A. K. Patra, J. Englert, I. Lieberwirth, A. Liscio, V. Palermo, X. Feng, A. Hirsch, K. Müllen, and M. Kläui *Robust two-dimensional electronic properties in three-dimensional microstructures of rotationally stacked turbostratic graphene*, Physical Review Applied **7**, 024022 (2017).

N. Richter, Z. Chen, M.-L. Braatz, F. Musseau, N.-E. Weber, A. Narita, K. Müllen, and M. Kläui, *Dimensional confinement in carbon-based structures – From 3D to 1D*, Annalen der Physik **529**, 1700051 (2017).

N. Richter, D. Weber, F. Martin, N. Singh, U. Schwingenschlögl, B. V. Lotsch, and M. Kläui, *Temperature–dependent magnetic anisotropy in the layered magnetic semiconductors CrI_3 and $CrBr_3$*, Physical Review Materials **2**, 024004 (2018).